STUDY ON OSSIFICATION AROUND MACRO-TEXTURED IMPLANT TOPOGRAPHIES

A Thesis submitted to

Indian Institute of Technology Guwahati

in partial fulfilment of the requirements for the award of the degree

of

Doctor of Philosophy

by

Rajdeep Ghosh

under the supervision of

Dr Debabrata Chakraborty

and

Dr Souptick Chanda

DEPARTMENT OF MECHANICAL ENGINEERING

INDIAN INSTITUTE OF TECHNOLOGY GUWAHATI

February 2023

DECLARATION

I declare that

a. the work contained in this thesis is original and has been done by me under the guidance of my supervisors.

b. the work has not been submitted to any other Institute for any degree or diploma.

c. I have followed the guidelines provided by the Institute in preparing the thesis.

d. I have conformed to the norms and guidelines given in the Ethical Code of Conduct of the Institute.

e. whenever I have used materials (data, theoretical analysis, figures, and text) from other sources, I have given due credit to them by citing them in the textof the thesis and giving their details in the references. Further, I have taken permission from the copyright owners of the sources, whenever necessary.

Rajdeep Ghosh

Department of Mechanical Engineering
Indian Institute of Technology Guwahati
Guwahati-781039, Assam, India

CERTIFICATE

This is to certify that the thesis entitled "**Study on ossification around macro-textured implant topographies**", submitted by Rajdeep Ghosh in the *Department of Mechanical Engineering, Indian Institute of Technology Guwahati*, for the award of the degree of Doctor of Philosophy, is a record of an original research work carried out by him under our supervision and guidance. The thesis has fulfilled all requirements as per the regulations of the institute and in our opinion has reached the standard needed for submission. The findings embodied in this thesis have not been submitted to any other university or institute for the award of any degree or diploma.

(Dr Debabrata Chakraborty)
Professor
Department of Mechanical Engineering
Indian Institute of Technology
Guwahati
Guwahati-781039, Assam, India

(Dr Souptick Chanda)
Assistant Professor
Department of Biosciences and
Bioengineering
Indian Institute of Technology Guwahati
Guwahati-781039, Assam, India

Dedicated to...

The Almighty

&

my beloved parents

Acknowledgements

I would like to start by thanking the Almighty and continuous blessings from my spiritual guru for keeping me mentally fit. I would like to extend my sincere thanks to all those who are involved in nurturing me from childhood and beyond and also to those who has directly or indirectly helped me in various ways during the tenure of my doctoral study at Indian Institute of Technology Guwahati. I am grateful to all of them.

I wish to express my sincere gratitude and respect to my enthusiastic supervisors, Prof. Debabrata Chakraborty and Dr. Souptick Chanda, for guiding and mentoring me throughout the period of the doctoral research study. I am extremely grateful for their valuable advice, critical comments, continuous support, encouragement and motivation. I have been immensely benefited by their knowledge and experience, which eventually helped me enormously to conduct the research work. There were phases of ups and downs during this long tenure of doctoral studies where I was stuck many times while formulating algorithms to getting results. The unprecedented time of the pandemic was a bolt from the blue in the midst which not only affected by family badly but took away a lot of precious moments to cherish during this doctoral study. However, constant encouragement, support, friendly and stimulating discussions in both the academic and the personal matters from both the supervisors actually helped me in sailing through this tough period. These discussions are greatly appreciated since it motivated me and helped me to focus on my doctoral research and to finish my dissertation successfully. It was truly a great honour and privilege to work under their direct supervision.

I would like to acknowledge the Doctoral Committee members, Prof. S.K. Dwivedy, Prof. S. M. Hazarika, and Prof. S. K. Deb, for their suggestions, constructive criticism and insightful comments at various stages of the research study. I am also grateful to the former and present heads of the Department of Mechanical Engineering for providing a congenial academic and research environment, necessary infrastructure and laboratory facilities in the Department for smooth completion of my doctoral program. I sincerely acknowledge the financial support provided by the institute during the entire period of the doctoral research study. The help of the office and laboratory staff members of the department is thankfully acknowledged. Special thanks to Mr. Sanjib Sarma, Senior Technical Superintendent, Strength of Materials Laboratory, Indian Institute of Technology Guwahati

for extending the computational infrastructure required for this study. The support provided by the Scheme for Promotion of Academic and Research Collaboration (SPARC), MHRD (Presently, Ministry of Education), Government of India (through grant: SPARC/P705) funded project entitled “Investigation on the Influence of Ferromagnetic Coating on Bone Ingrowth in Hip Stems Made of Composite Titanium-Tantalum (Ti-Ta) Foam” is greatly acknowledged.

I wish to sincerely thank the Agartala Government Medical College, Agartala, Tripura, India for providing the CT scan of the femur of the patient for conducting the final stages of my thesis work. Special thanks to my cousin Dr. Rupesh Banik, Agartala Government Medical College, Agartala without whom the arrangement of CT data was a daunting task.

I express my gratefulness to Dr. Tapan Das, Orthopaedic Surgeon, Agartala Government Medical College, Agartala for sharing his clinical experiences related to the study. I would also like to thank Prof. Damien Lacroix, The University of Sheffield, Dr. Alex Dickinson, University of Southampton and Dr. Kaushik Mukherjee, Indian Institute of Technology Delhi for sharing their invaluable and critical inputs during the early phases of my dissertation.

I would like to convey my sincere thanks to Ankan, Atchuta, Sasanka, Sukanya and Dr. Debabrata Gayen, my friends and colleagues in the laboratory, for supporting me in various ways and maintaining a friendly working environment. I would like to specially mention the contributions from Ankan for his critical insights into the work. I also wish to thank all of my friends, especially Antaripa, Suman, Kaustabh, Faladrum, Pratik, Adeline and many more, who helped me in different ways and encouraged me during the critical phases of the study.

Last but by no means the least, I express my sincere gratitude and my heartfelt love to my mother Mrs. Tapati Banik and father Mr. Gautam Narayan Ghosh, for their patience, understanding, love and affection. It would never have been possible to accomplish my goal without their moral support and constant encouragement. They are the most important people in my world and this thesis is dedicated to them.

Indian Institute of Technology Guwahati

Date: 08-02-2023 **Rajdeep Ghosh**

Table of Contents

Abstract

Surface topography on implant surface at different length-scales are known to provide either mechanical stability or promote bone growth. Macro-textured surfaces are primarily provided to enhance mechanical stability to the implant. However, there is a scarcity of studies investigating the influence of macro-textured implant surfaces on bone-growth. Combining finite element analysis (FEA) and a mechanoregulatory tissue differentiation algorithm, a study has been performed to investigate the influence of three distinct macro-textured implant surfaces on bone growth. Results indicate that higher levels of bone-implant tangential micromotion inhibits formation of bone and promotes formation of fibrous tissue and cartilage. Furthermore, it was observed that textures containing filleted and chamfered edges reduce the formation of fibrous tissue. Thereafter the combined influence of sliding and gap distances on bone growth considering two macro-textured implant surfaces has been studied. In addition, the influence of texture density on bone growth was also analysed. Results show that higher values of both gap and sliding distances promote fibrous tissue formation. Nevertheless, the directional component of micromotion with lower magnitude plays the deciding role in formation of tissue phenotypes. Additionally, the study indicates that there is no linear relationship between the texture density and amount of tissue formed at the bone-implant interface gap. Further, Neural Network (NN) schemes have been formulated to establish predictive models of bone growth with given surface topographical dimensions. In a follow-up study, an integrated approach combining the FEA, NN and genetic algorithm (GA) was attempted to find optimally designed macro-textures to enhance the formation of bone growth. Finally, a comparative study to investigate the influence of textured and non-textured implant surface on bone growth has been studied on femoral implants under routine activities and fibrous tissue is observed to have formed while climbing stairs compared to that in normal walking. This study suggests that climbing stairs just after a hip replacement surgery is detrimental to the patient compared to normal walking. Furthermore, non-textured implants produce more fibrous tissue compared to textured implants under similar musculoskeletal loading conditions which might promote aseptic loosening of implant.

Keywords: macro-texture, uncemented, tissue differentiation, mechanobiology, finite element analysis, optimization, genetic algorithm, neural network, femoral implant.

Nomenclature

Symbols

E	elastic modulus
ρ_{app}	apparent density
K	constant ranging from 3,000 to 30,000
Q	constant ranging from 1.14 to 1.62
C	compression
T	tension
S	Octahedral shear
D	Dilatational hydrostatic stress
σ_1, σ_2, σ_3	principal stresses
I	Osteogenic index
λ	total number of load cases
n_i	number of loading cycles in a load case
β	empirical constant
Z	Combined stimulus
γ	shear strain
v	relative solid/fluid velocity
k	diffusion constant
c	cell concentration at each finite element
$\Psi(x,t)$	mechanical stimulus represents 2^{nd} invariant of deviatoric strain tensor
Y	site-specific elastic modulus
D	site-specific coordinate of the bone surface perpendicular to the surface
S_{ij}	actual strain tensor and
S_{ij}^0	strain-tensor at equilibrium
P_{ij}, Q_{ij}	matrix formed by remodelling coefficients
X_i	internal remodelling rate
X_e	external remodelling rate
ξ	actual SED
ξ_{ref}	site-specific SED at homeostatic equilibrium

s	threshold level of initiation of remodelling
R	a constant in the equation of bone adaptation
S_m	mechanical stimulus influencing the adaptation process
π	threshold value of the mechanical stimulus
$\sigma_{average}$	Hydrostatic pressure
$\varepsilon_{deviatoric}$	Deviatoric strain
c_{max}	maximum cell concentration
c_{tissue}	element specific cell concentration of newly formed tissue
Π_c	rate of transfer of cells in direction Ω
$\mho$	thermal conductivity
ρ	density of the material through which heat flows
Ψ	specific heat of the material
$\rho\Psi$	heat capacity of the material
θ	temperature
Π_θ	rate of transfer of heat in direction Ω
O_{Im}	output of the m^{th} neuron lying on the input layer
a_1	constant of activation function I
I_{Im}	input of m^{th} neuron
b	constant bias value
I_{Hn}	input of the n^{th} neuron lying on the hidden layer
v_{mn}	weight connects m^{th} neuron of input to n^{th} neuron of hidden layer
O_{Hn}	output of n^{th} neuron of the hidden layer
w_{nz}	weight connects n^{th} neuron of hidden to z^{th} neuron of output layer
I_{Oz}	input of the output neuron
a_2	constant of activation function II
O_{Oz}	output of the output neuron
a_3	constant of activation function III
E	Mean squared error
ζ	number of training cases
T_{Oz}^{ζ}	target output corresponding to ζ^{th} training case
O_{Oz}^{ζ}	computed output corresponding to ζ^{th} training case

α	learning rate
μ	momentum constant
$I_{RVM\#}$	input vector for training RVM#
$O_{RVM\#}$	output vector for training RVM#
$X_{\#}$	input vector for training MODEL#
$O_{\#}$	output vector for training MODEL#

Acronyms

THA	Total Hip Arthroplasty
NSA	neck-shaft angle
FNA	femoral neck anteversion
EMG	electromyography
BW	body weight
RBC	Red Blood Corpuscle
WBC	White Blood Corpuscle
HA	hydroxyapatite
BSP	bone sialoprotein
EMA	effective mechanical advantage
MSC	Mesenchymal Stem Cell
ECM	extracellular matrix
LFA	low friction arthroplasty
PMMA	polymethyl methacrylate
AML	anatomic medullary locking
3D	Three dimensional
OA	Osteoarthritis
RA	Rheumatoid arthritis
ON	Osteonecrosis
AVN	avascular necrosis
MRI	Magnetic resonance imaging
BMD	bone mineral density
VTE	venous thromboembolism
DVT	deep vein thrombosis
PE	pulmonary embolism
RNA	Ribonucleic acid
FE	Finite element
NN	Neural network
GA	Genetic algorithm

2D	Two dimensional
SED	Strain energy density
FEM	Finite element method
NSO	numerical shape optimization
NLP	non-linear programming
CPU	Central processing unit
TKA	total knee arthroplasty
MLT	Machine learning technique
ANN	Artificial neural network
SVM	Support vector machine
RSM	Response surface methodology
NCGA	Neighbourhood cultivation genetic algorithm
NSGA-II	Nondominated sorting genetic algorithm-II
IoI	Index of Instability
BMF	Bone mass fraction
HTO	high tibial osteotomy
DoE	design of experiment
KIGA	Kriging interpolation method and genetic algorithm
ML	Machine learning
CT	Computed tomography
BPNN	Backpropagation neural network
MSE	Mean squared error
ISO	International Organization for Standardization
DOS	Disk operating system
UHMWPE	Ultra-high molecular weight polyethylene
BIC	bone-to-implant contact
BHR	Birmingham Hip Resurfacing
RVIM #	Representative Volume Interface Model ‘Number’
BMP	bone-morphogenetic protein
BR	Bayesian regularization

LM	Levenberg–Marquardt
RVM#	Representative Volume Model ‘Number’
ANOVA	Analysis of Variance
BG	percentage of bone growth
DF	degrees of freedom
SS	sum of squares
MS	mean squares
AI	Artificial intelligence
DFM	Design for manufacturability
$OMT_{\#}$	Osseointegration-maximized-texture for MODEL#
HU	Hounsfield Units
GSV	Gray Scale Value
TFS	Textured femoral stem
NTFS	Non-textured femoral stem
STL	Stereolithography
CAD	Computer aided design
APDL	Ansys Parametric Design Language
ALA	Augmented Langrangian Algorithm
NTNW	Non-textured implant on normal walking
TNW	Textured implant on normal walking
TSC	Textured implant on stair climbing
GZ	Gruen zones
AV	Anterior view
PV	Posterior view

List of Figures

List of Tables

CHAPTER 1

Introduction

This chapter briefly introduces the broad area of the present work on influence of macroscopic surface morphology over commercial femoral implants on bone growth with a detailed discussion on hip anatomy and related musculoskeletal loading conditions at the hip joint. A quick note on total hip arthroplasty, tissue level mechanobiology involved during bone growth and remodelling have also been discussed. Based on those discussions, the motivation behind undertaking the present research is presented. At the end of this chapter, the chapterwise organization of the thesis is also presented.

1.1 Backdrop behind the research

Twentieth and 21st centuries have been witnessing incredible advancements in biology and medicine. This generation and henceforth will have higher life expectancy than our predecessors. Development in healthcare integrated with core principles of science and state-of-the-art technology has made human life easier by improving its quality in various formats. One such advancement is the innovation in hip replacement procedure, as known as, Total Hip Arthroplasty (THA). THA is a conventional surgical hip reconstruction surgery that helps patients with degenerative bone diseases such as osteoarthritis (arthrosis), rheumatoid arthritis, congenital abnormalities, and post-traumatic disorders by improving joint function and thus relieving discomfort. The hip joint is a ball-and-socket synovial joint that consists of a ball-shaped femoral head that articulates in an acetabular cavity (acetabulum) of the pelvic girdle and rotates with regard to the acetabulum (Fig.1.1). A standard hip replacement surgical intervention involves replacing the proximal section of the femur with an implant (femoral stem), and attaching a hemispherical cup (acetabular component) to the acetabulum on the pelvic side.

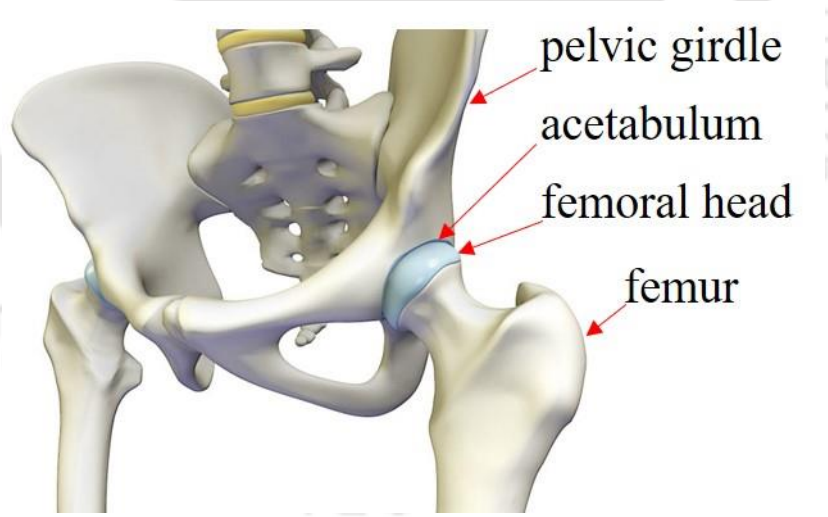

Figure 1.1 Anatomy of hip joint (https://tinyurl.com/rajdeep-thesis-1)

Depending on the mode of fixation technique, any joint arthroplasty can be broadly classified into two major surgical procedures: cemented and uncemented joint arthroplasty. In cemented arthroplasty, a polymeric bone-cement is used to adhere the implant and the bone, whereas, in uncemented arthroplasty, a press-fit fixation combined with the utilization of friction between the bone and the implant helps in achieving the biologic bone-implant fixation through a sequential post-

operative process of angiogenesis followed by bone growth in and around the implants that remain adhere to it. Most surgeons worldwide prefer uncemented prosthesis owing to its natural fixation with the host bone (Yamada et al., 2009) without recourse to the complications that arise with the bone cement.

The last few decades have witnessed an exponential growth in hip replacement surgeries worldwide. Between 2003 to 2014, almost 708,311 hip replacement procedures have been reported in England and Wales (National Joint Registry for England and Wales, 12th Annual Report, 2015) alone. This number in Sweden has increased from nominal 6 in 1976 to an exorbitant 16330 in 2013 (The Swedish National Hip Arthroplasty Register Annual Report. 2013). Australia saw a hike of 6.3% in hip replacements in the year 2015 (Australian Orthopaedic Association National Joint Replacement Registry 2015). However, the proportion of revision surgery has dwindled continuously from 12.9% in 2003 to 10.2% in 2014 (Australian Orthopaedic Association National Joint Replacement Registry 2015). Scotland saw 80% increase in hip replacement procedures between 2001 and 2013 (The Scottish Arthroplasty Project, Biennial Report 2014). Scientists predicted three times increase in the number of hip arthroplasties in US from 2005 to 2030 (Kurtz et al., 2007). The rise in hip arthroplasty almost tripled in 2014 back then 2013 in New Zealand (The New Zealand Joint Registry: Sixteen Year Report January 1999 to December 2014, 2015). The number of hip replacements reported in 2013 was also double the number reported in 1999 (The New Zealand Joint Registry: Sixteen Year Report January 1999 to December 2014, 2015; The New Zealand Joint Registry: Thirteen Year Report January 1999 to December 2011, 2012). According to reports (National Joint Registry for England and Wales, 12th Annual Report, 2015; The New Zealand Joint Registry: Sixteen Year Report January 1999 to December 2014, 2015), uncemented or cementless implant fixation procedure gained popularity over the cemented implant fixation. In Indian scenario, approximately 470,000 hip replacements are intervened annually (Source: The American National Institute of Arthritis and Musculoskeletal and Skin Diseases). Noteworthy, the annual rate of hip replacement surgeries in India is also expected to rise (Pachore et al., 2013). Unlike Swedish orthopaedic surgeons who prefer cemented joint surgeries for women and uncemented ones for men, a recent report (Vaidya et al., 2021) recorded a stellar 93% of the hip arthroplasties in India which

were performed using uncemented fixation procedure. Such modality of uncemented procedure has been replicated in similar other prominent joint registries known globally. Uncemented cup and femoral stem are used in almost 60% to 90% of arthroplasties performed in the United States each year (Dunbar, 2009; Lombardi et al., 2009).

Nevertheless, the success of hip replacement surgeries with around 75% of the hip replacements lasting for 15-20 years and 58% of such procedures last for 25 years (Evans et al., 2019), the global failure rate is still on the higher side. As a result of the continual increase in such occurrences, there has been a noticeable increase in the absolute number of joints that have failed despite the surgeons' best efforts, necessitating revision surgery. Although all such failures have been due to variety of controllable and uncontrollable reasons, the lion's share may be attributed to the biomechanical causes.

Failure of the femoral stems are found to be more common in initial decade of primary hip replacement as compared to the acetabular component (Crawford and Murray, 1997). Two important biomechanical failure mechanisms that may impair the longevity of uncemented implants are implant-induced unfavourable bone remodelling and inadequate osseointegration. The success of an uncemented prosthesis is also influenced by a lack of primary stability caused by excessive interfacial micromotion. Surgical protocols and bone quality of the patients play an important role on deciding long term success of hip implants. The lone or cumulative effect of all of these mechanisms may lead to aseptic loosening of the implant which require revision surgeries which in most of the cases are not successful due to physiological conditions of the patient and due to age related degradation of bone quality. Besides all these key aspects, the design of the femoral components through geometric or material changes also affects the success of hip arthroplasty to a major extent (Huiskes and Boeklagen, 1988; Viceconti et al., 2001). Despite the availability of a variety of commercially accessible uncemented femoral components with various porous coating designs, many of the design outcomes and their impact on osseointegration and bone adaptation remain unexplored, owing to a lack of clinical data, and thus need to be investigated.

1.2 Anatomy and biomechanics of hip joint

Gross anatomy or simply, anatomy is the study of structure and function of the body at macroscopic level as revealed by dissection. There are two types of anatomical study to be done viz. 'clinical anatomy' that is mostly related to the practice of medicine and 'basic anatomy' that gives us a minimal idea about the structure and function of the body.

1.2.1 Anatomical planes

Any joint biomechanics requires an understanding of the basic human anatomy. All anatomic planes of the human body are based on the assumption that the person is standing erect, with the upper limbs by the sides of the body and the face and palms directed forward, which is also termed as 'anatomic position' (Snell, 2011). Fig. 1.2 shows the typical orientations of different anatomical planes of a human body and are discussed as follows:

- **Median Sagittal Plane**: Vertical plane passing across the centre of the human body, equally bifurcating into right and left halves is known as median sagittal plane. Any section of the human body that lie towards proximal to the median plane is known to be medial while that lies farther away from the median plane is known as lateral section.
- **Coronal Plane**: The anatomic plane that is hypothetical vertical plane perpendicular to the medial sagittal plane is the coronal plane.
- **Transverse Plane**: Horizontal plane that is mutually perpendicular to both the median sagittal as well as the coronal planes is known as transverse plane.

  The “anterior” and “posterior” terminologies are used to indicate the frontal and backward of the body, respectively. To describe the positions of two different body structures at different anatomic positions, one is said to be anterior or posterior to the other considering their individual proximity to the anterior or posterior body surface. “Proximal” and “distal” describe the relative distances from the torso. The terms “superior” and “inferior” denote positions of structures with reference to the upper and lower ends of the body. The term “ipsilateral” refers to same (from Latin *ipse*) side of the body, whereas “contralateral” refers to opposite (from Latin *contra*) sides. The “supine” position referenced to lying on one's back, whereas, “prone” position means lying face downward.

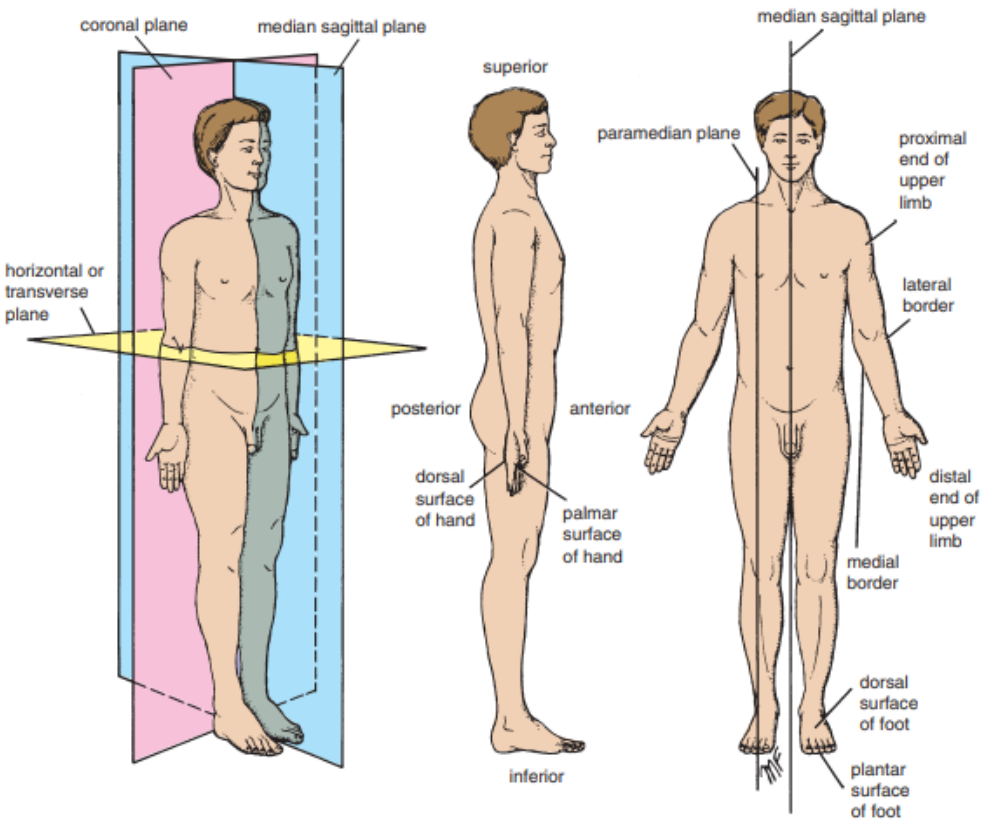

Figure 1.2 Anatomical Planes of reference along with the anatomic positions of a basic human anatomy (Snell, 2011)

1.2.2 Anatomy of hip

The hip joint, also known as the acetabulofemoral joint, is the principal connection between the pelvic girdle (hip bone) and the lower limb of the appendicular skeleton (Fig. 1.3a). The hip joint bears the weight of the body and distributes load from the axial and upper appendicular skeleton to the lower limb. The hip bone, also known as innominate bone or *os coxae*, is made up by synostosis of three bones – ilium, ischium and pubis (Fig. 1.3b). The ilium is large, flat with a subtle curvature, and pointed upwards. The pubis and ischium bones lie inferiorly. The pubis lies more anteromedially, whereas, the ischium resides more posterolaterally.

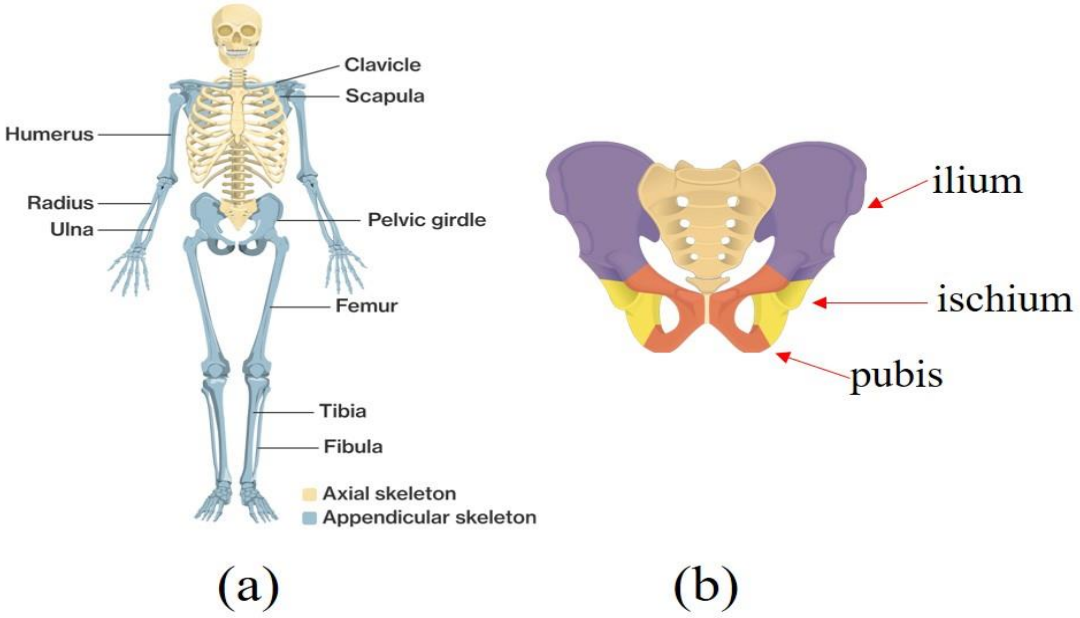

Figure 1.3 (a) Human Skeletal System differentiated into axial and appendicular system (https://tinyurl.com/rajdeep-thesis-2) (b) Major bones of pelvic girdle (https://tinyurl.com/rajdeep-thesis-3)

1.2.2.1 Articulation at hip joint

The joint between the femoral head and the acetabulum of the hip bone is known as the hip joint. The existence of a fibro cartilaginous rim called the "acetabular labrum" fills the acetabular cavity. The hyaline cartilage covers the articular surfaces.

1.2.2.2 Hip Joint

The hip joint is a synovial ball-and-socket joint with a synovial membrane that produces synovial fluid for lubrication and to reduce frictional resistance in a healthy hip joint.

1.2.2.3 Hip capsule

The hip capsule (Fig. 1.4a) is attached to the acetabular labrum medially and encloses the hip joint. It connects to the intertrochanteric line at the front and midway along the posterior aspect of the bone's neck behind.

1.2.2.4 Hip ligaments

Hip capsule is surrounded by three major hip ligaments viz. iliofemoral ligament, ischiofemoral ligament and pubofemoral ligament (Fig. 1.4b). The “iliofemoral ligament”, also known as ligament of Bigelow, is a strong, inverted Y-shaped ligament, which prevents overextension during standing. The triangular

"pubofemoral ligament" limits extension and abduction. The spiral-shaped "ischiofemoral ligament," which inhibits extension, is attached to the ischium's body near the acetabular edge. The ligament of the femoral head, which lies deep within the joint, is flat and triangular and is ensheathed by synovial membrane.

1.2.2.5 Synovial membrane

The hip capsule is lined by synovial membrane, which is linked to the margins of articular surfaces. It protects the part of the femur's neck that is inside the joint capsule. It encloses the femoral head ligament and covers the lipid-containing pad inside acetabular fossa (Fig. 1.4a).

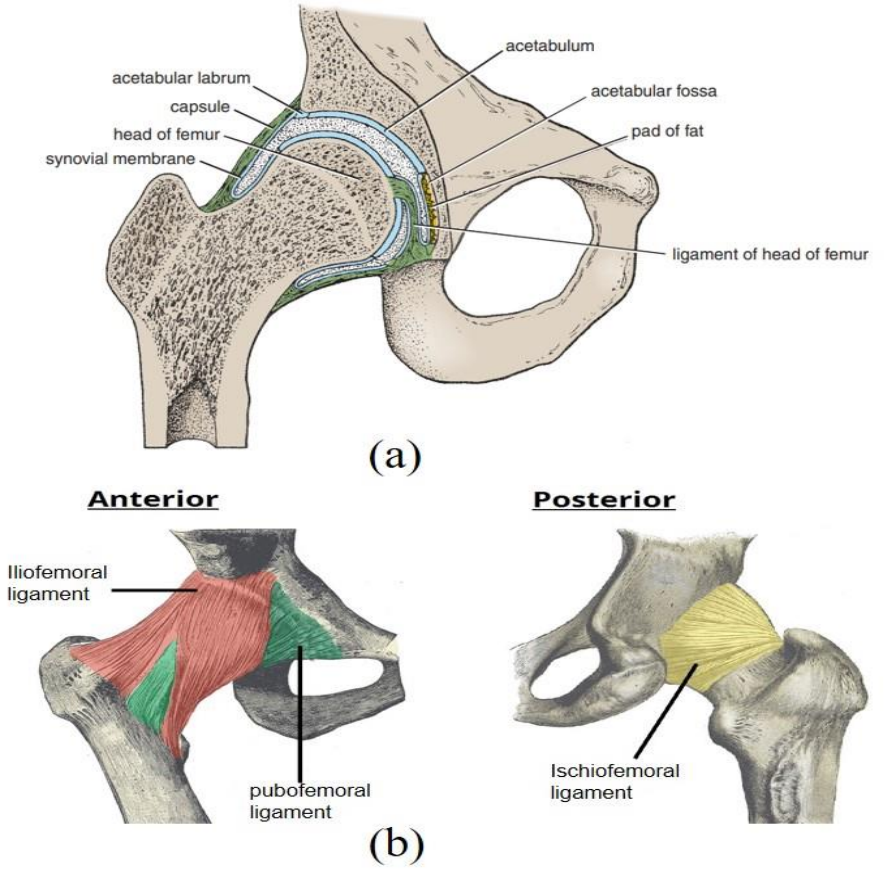

Figure 1.4 (a) Coronal Section of right hip joint anatomy (Snell, 2011) (b) Anterior and posterior view of hip joint showing major hip ligaments (https://tinyurl.com/rajdeep-thesis-4)

1.2.3 Anatomy of femur

The femur (thigh bone) is known to be the longest as well as strongest bone in the skeletal system of human. The femur (thigh bone) is the human skeleton's longest and strongest bone. It is divided into three sections viz. a middle femoral shaft, called diaphysis; two broader bulges, named epiphyses, at the two extreme ends (Fig. 1.5); and each epiphysis is joined to the diaphysis at metaphysis. The epiphysis comprises

of the epicondyles (medial and lateral) and finally ends with the condyles (medial and lateral). The proximal tibia articulates distally with the condyles. The diaphysis is generally made up of strong cortical bone with a little spongy core, whereas the epiphysis and metaphysis are mostly made up of cancellous bone with a thin cortical bone shell. There is a spherical head, a frustum-shaped neck, a greater trochanter, and a lesser trochanter on the proximal femoral portion (Fig. 1.5). The surface of the femoral head of a healthy femur is generally smooth and is coated with cartilaginous tissue, except over the pit on the head of the femur to attach the ligament of the head, clinically known as *fovea capitis*. The inclination angle of neck to the shaft in the frontal plane is known as "neck-shaft angle (NSA)". While the angle of inclination of the femoral neck to the proximal metaphysis in transverse plane is known as the "femoral neck anteversion (FNA)". Muscle attachment points can be found on the greater trochanter, which is located at the junction of the neck and the upper half of the central shaft. In a healthy adult, it is positioned laterally and backward about 10 mm below the femoral head (Gray, 1918; Snell, 2011). On the other hand, the lesser trochanter has a conical anatomy and lies on the medial side of the femur. In addition, a ridge that runs longitudinally on the posterior aspect of a femur, clinically known as *linea aspera* acts as a muscle attachment site.

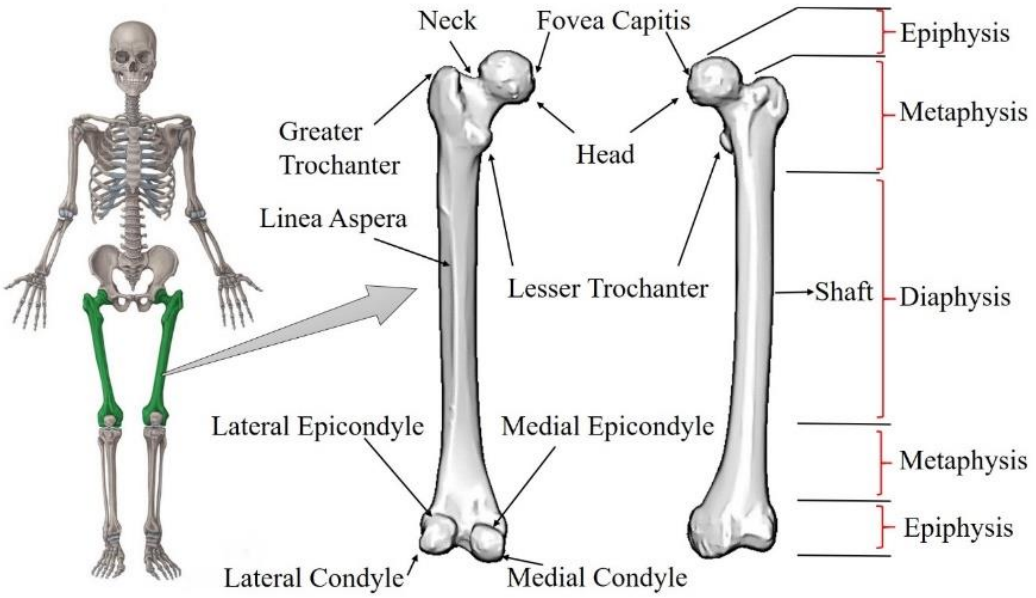

Figure 1.5 Basic anatomy of human femur (https://tinyurl.com/rajdeep-thesis-5)

1.2.4 Kinematics of human gait

Gait cycle is a periodic sequence of locomotion of a single foot during forward propulsion of the body (Fig. 1.6) It follows a common pattern for any healthy human with no locomotor disability. Gait pattern also maintains the proper stability of the skeletal structure during movement. Implant biomechanics generally addresses this issue to stabilize the normal gait pattern of a human with any kind of locomotor disability. Human gait kinematics are bipedal and biphasic. The gait kinematics of the human body are divided into two distinct but interconnected phases viz. i) a stance phase that regulates about 60% of the normal gait cycle, and ii) a swing phase that regulates the remaining 40% of the cycle. Both the above-mentioned phases can be further split into eight distinct events (Fig.1.6). The stance phase comprises of the following movements of the same foot:

a. **Initial contact (heel strike):** The stance phase is initiated by initial contact of the heel of the reference foot that strikes the ground. It is also a duration of initial double support period when both the feet remain in contact with the ground.

b. **Foot flat:** This event is characterized by slow transfer of the body-weight to the reference foot. It completes the initial double support period and starts with the single support period.

c. **Mid stance:** Only the reference foot touches the ground and the total body weight is stabilized on it.

d. **Terminal stance:** This event is marked by the rising of the heel of the reference foot with its toe touching the ground. Terminal stance completes the end of single support period and marks the inception of the second double support period.

e. **Toe off:** It marks the end of the stance phase with the toe of the reference foot is taken off the ground. It also completes the second double support duration.

The swing phase contains three periodic movements of the reference foot viz. initial swing, mid swing and terminal swing all going through in sequence. The same pattern repeats itself for the other leg as well with a phase difference to provide support and propulsion during movement.

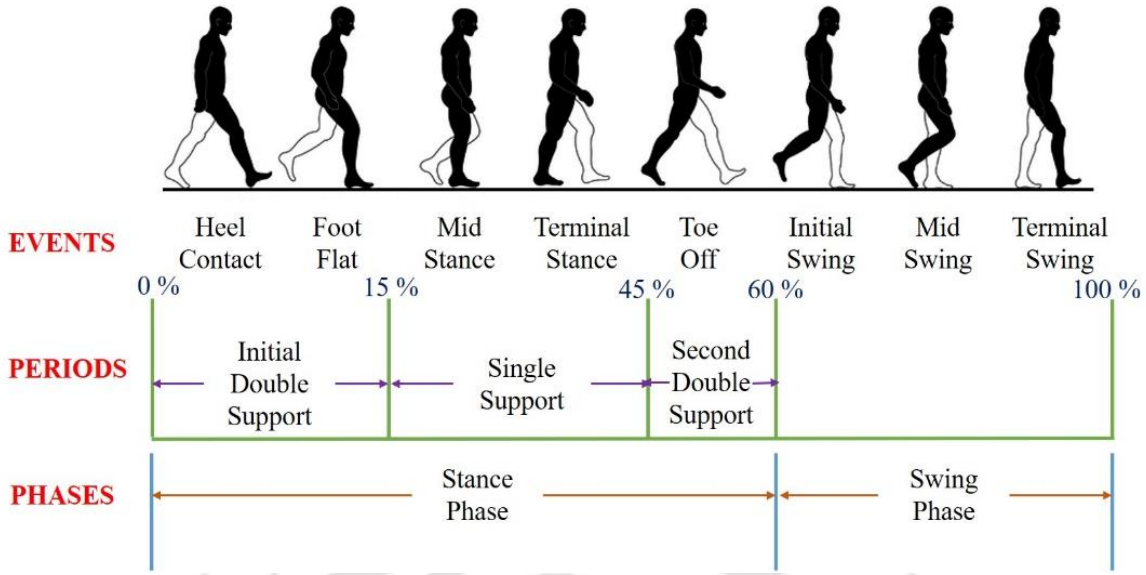

Figure 1.6 Gait cycle representing normal walking pattern (https://tinyurl.com/rajdeep-thesis-6)

1.2.5 Musculoskeletal loading of hip joint

Musculoskeletal loading plays an important role in influencing the process of bone growth and bone adaptation. Twenty-one muscle forces facilitate the movement of hip joint. Depending upon the movement the muscles produce, they are grouped as: flexors, extensors, abductors, adductors and deep hip external rotators. The point of origin along with the insertion of the dominant hip joint muscles are listed in Table 1.1. It is however to be noted that, not each and every muscle significantly influence in transfer of load from axial to appendicular skeleton (Nordin and Frankel, 2001). Besides these muscular forces, the hip contact force plays a significant role in load transfer to the lower extremities (Dalstra et al., 1995).

Several researchers used force plate devices and kinematic data paired with electromyography (EMG) based on the theory of inverse dynamics (Crowninshield et al., 1978; van den Bogert et al., 1999) or instrumented hip implants to measure hip contact force (Bergmann et al., 1993; 2016; Taylor et al., 1997). Inter-patient variability was also accounted in these studies while measuring the hip joint reaction force. Bergmann et al. (2001) evaluated the hip joint forces in a cohort study using four patients while considering normal walking and stair climbing. The study reported a mean peak hip joint force around 238% of body weight (BW) during

normal walking. However, the same was reported to be 251% BW during stair climbing and 260% BW while going downstairs.

Table 1.1 Principle actions of major hip muscles with their site of origin and insertion site. The abbreviation m. stands for muscle. (Source: Dowson et al., 1981)

Movement	Muscle Involved	Site of Origin	Insertion Site
Flexion	m. gracilis	Pubic bone	Anterior medial tibial condyle
	m. pectineus	Pubic bone	Pectineal line
	m. iliopsoas	Iliac fossa, anterior lumbar spine	Lesser Trochanter
	m. sartorius	Anterior superior iliac spine	Anterior medial tibial condyle
	m. rectus femoris	Anterior superior iliac spine	Tibial tuber via patellar tendon
Extension	m. gluteus maximus	Posterior ilium, sacrum	Iliotibial band and gluteal tuberosity
	m. biceps femoris	Ischial tuberosity, linea aspera	Fibular head
	m. semitendinosus	Ischial tuberosity	Anterior medial tibial condyle
	m. semimembranosus	Ischial tuberosity	Medial tibial condyle
Abduction	m. tensor fascia latae	Lateral to anterior superior iliac spine	Inserts into iliotibial band
	m. gluteus medius	Gluteal lines on posterior ilium	Greater Trochanter
	m. gluteus minimus	Gluteal lines on posterior ilium	Greater Trochanter
Adduction	m. adductor magnus	Inferior pubis and ischium	Adductor tuberosity, linea aspera
	m. adductor longus	Pubic Bone	Linea aspera
	m. adductor brevis	Pubic Bone	Upper linea aspera
Deep Hip External Rotators	m. piriformis m. gemellus inferior m. gemellus superior m. obturator externus m. obturator internus m. quadratus femoris	Sacrum, Obturator membrane, Ischium	Greater Trochanter

To avoid the ethical issues that come with employing invasive procedures with instrumented hip prostheses, appropriately validated mathematical optimization algorithms were created to estimate the complicated distribution of in vivo muscle forces (Pedersen et al., 1997; Duda et al., 1998; Heller et al., 2001). Heller et al. (2001) computed the magnitude of muscle forces and the hip contact force, which agreed with the measured values (Bergmann et al. 2001). Throughout the gait cycle, however, there were considerable differences in measured and calculated values (Fig. 1.7).

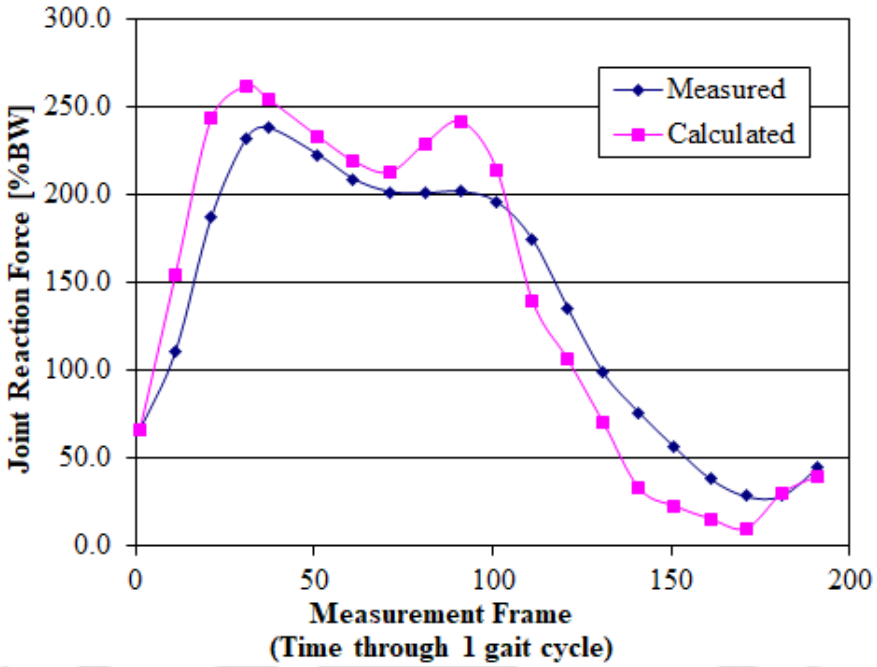

Figure 1.7 Comparison between measured and calculated hip joint reaction force for a normal walking gait cycle (Bergmann et al. 2001; Heller et al. 2001)

On six femoral specimens, a digitising method was used to identify the site of muscle attachment, the centroidal location of the attachment site, and the muscle volume for biomechanical assessments of long bones (Duda et al., 1996). Typical primary muscle attachment locations of the hip joint are shown in Fig. 1.8 (Bergmann et al., 2001; Heller et al., 2001). Although hip joint reaction force and the forces from the abductor muscle plays a major role on the load distribution over the proximal femur, other subsidiary muscles also influence the load transfer significantly. Hip loading conditions during normal walking take into account the abductor, tensor fascia latae (proximal and distal), and vastus lateralis muscle forces, as well as the hip contact force (Bergmann et al., 2001; Heller et al., 2001). In representing the musculoskeletal loading conditions while climbing stairs, the iliotibial tract (proximal and distal) and vastus medialis muscle forces are also included.

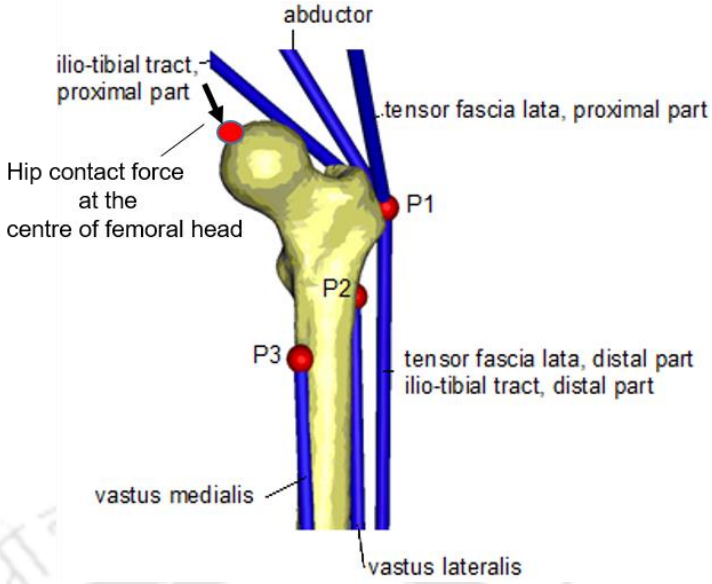

Figure 1.8 Major hip muscles with their site of attachment and hip contact force (Bergmann et al., 2001; Heller et al., 2001)

1.3 Bone

Bone, a highly hierarchical composite connective tissue, is a structural element of the human skeletal system, which acts as a shield to the soft tissues, and other internal organs of the body. It helps in movement while keeping body shape by transmitting weight and muscle forces from one section of the body to another during daily activities.

1.3.1 Bone histology

From engineering point of view, bone is considered as an anisotropic, non-homogeneous and viscoelastic composite material (Currey, 1984). Bones are adaptable tissue, which means they change shape and composition to meet the physiological demands of the body. Bone marrow inside the bone is the progenitor of different types of cells inside the human body like Red Blood Corpuscles (RBCs), White Blood Corpuscles (WBCs), adipocytes and fibroblasts, in medicos the process is known as 'Haematopoiesis'. Mineral homeostasis and triglyceride accumulation in adipocytes of the adipose tissue are also regulated by bone.

Macroscopically, bone is found in two primary architectures based on strength and volume fraction and thus are classified into compact or cortical and trabecular or cancellous (Gibson, 1985). The cortical bone is the extremely hard, dense lamellar outer shell. When compared to the inner spongy cancellous bone, cortical bone has a substantially higher volume fraction (Fig. 1.9a). Cancellous bone

reduces the stress by increasing the bearing area while still being a load bearing structural member of the skeletal system. The architectural distribution of these two types of bones depends on varied factors including anatomic-site, patient-variability and load transfer capability thus making it a highly anisotropic composite material. The mineral and organic composition of bone determines its mechanical properties. The tiny hydroxyapatite (HA) (chemical name: hydrated calcium phosphate, $Ca_{10}(PO_4)_6(OH)_2$) crystals (2-5 nm thick × 15 nm wide × 20-50 nm long plates) containing impurities such as potassium, magnesium, sodium, strontium, carbonate and chloride/fluoride contributes greatly to the cortical bone's stiffness, whilst the proteinaceous collagen determines its ductility (Guo, 2008). A distinctive cellular structure of interconnected network of low density, open cell rods and high density, closed cell plates is found in cancellous or trabecular bone (Gibson, 1985). Cortical bone, on the other hand, is a solid mass with only microscopic channels.

Bone is composed of 65% mineral, 35% organic matrix, water, and cells at the molecular level. The mineral content is largely impure HA, which is found inside and between the organic matrix in the form of small needles, plates, and rods. The organic matrix is composed of 90% collagen with 10% noncollagenous proteins such as osteocalcin, osteopontin, osteonectin, and bone sialoprotein (BSP). Bone can be further categorized into woven and lamellar bone. Woven bone is immature or pathologic bone and is a temporary phase of bone which is later resorbed and replaced by much stronger lamellar bone. It grows rapidly and typically form during embryogenesis, post-fetal fracture healing and ectopic ossification (Jee, 2001). The collagen fibres of woven bone are loosely packed and randomly oriented in comparison to lamellar bone. The growth rate of lamellar bone is not as high as in woven bone. Lamellar bone is divided into two types viz. primary and secondary lamellar bone. In certain chambers known as haversian canal, small cavities (lacunae) holding osteocytes are present throughout the woven and lamellar bone and are connected by tubular canals (canaliculi). Canaliculi houses the cell processes for the osteocytes. Volkmann's canal connects haversian canals. Fig 1.9b shows the histological sectional views of a human bone showing bone components.

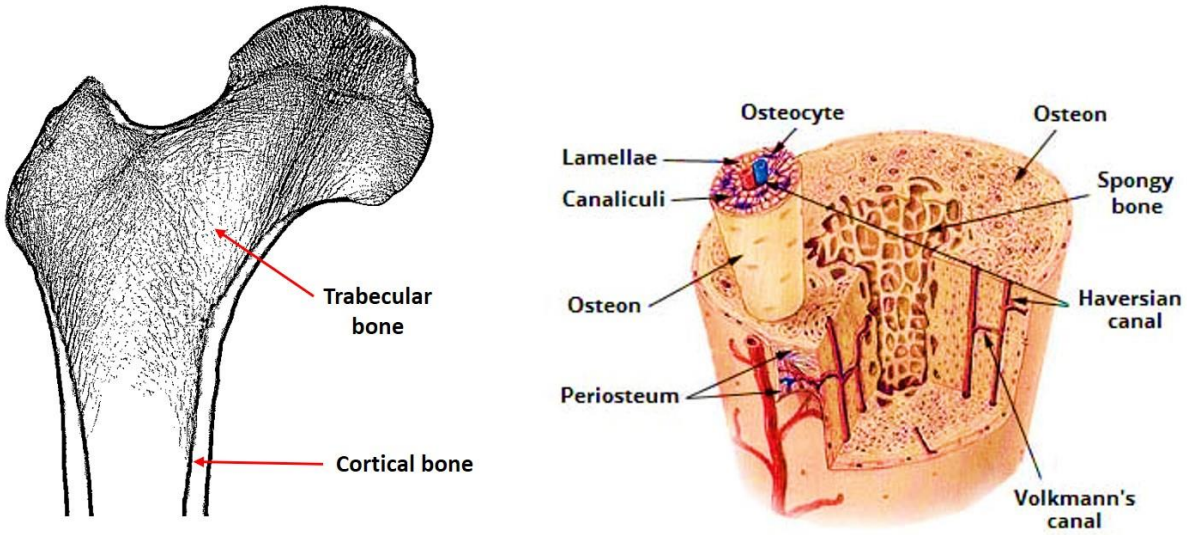

Figure 1.9 (a) Coronal section of proximal region of an adult femur (https://tinyurl.com/rajdeep-thesis-7) (b) Cross-sectional view of bone microstructure showing compact and spongy bone (https://tinyurl.com/rajdeep-thesis-8)

1.3.2 Types of bone

Bones in human skeletal system are broadly classified as follows:

- Long bone;
- Short bone;
- Flat bone;
- Sesamoid bone; and
- Irregular bone.

1.3.2.1 Long bone

Bones with longer length and shorter width are generally known as 'long bones'. These bones have a long strong shaft with broad ends or epiphyses. Long bones have a subtle curvature to uniformly distribute the load through them so as to minimize the chance of fracture. Long bones are primarily cortical in diaphyses and cancellous at their epiphyses. Bones of the thigh (femur), lower legs (tibia and fibula), arm (humerus), forearm (radius and ulna) falls under the category of long bones.

1.3.2.2 Short bone

Cube-shaped bones with almost equal length and breadth. They are primarily spongy at the core with a thin cortical layer at the surface. Bones of wrist (carpals) and ankles (tarsals) are short bones.

1.3.2.3 Flat bone

Generally thin, flat and parallel bones with oppositely faced cortical bone plates and a cancellous centre forming a sandwich like structure are known as flat bones. Apart from support, flat bones provide sufficient areas of attachment for muscles. Examples include bones of the brain (cranium), breastbone (sternum), ribs, and the shoulder blades (scapulae).

1.3.2.4 Sesamoid bone

Few bones are found embedded in certain tendons, which are generally the locations of considerable stress, wear and friction. The number of such bones are subject-specific and not always observable in completely ossified form. The patellae and sesamoid bones of the quadriceps femoris tendon, which are found in every human, are exceptions. They not only preserve tendons against excessive wear and tear, but they also improve a joint's effective mechanical advantage (EMA) by shifting the direction of pull of the tendons.

1.3.2.5 Irregular bone

Bones that cannot be categorized in any of the above types of bones and are having complex morphology falls under irregular bone category. They serve different unique purposes of support like in pharynx and trachea, protection of nerve tissue (vertebrae) and attachment of bones (hyoid bone of tongue) and muscles (sacrum).

1.3.2.6 Sutural bone

Sutural bones or wormian bones are irregular, isolated, accessory bones that occur within the joints or sutures of certain cranial bones. They are most commonly observed in lambdoid sutures of the cranium. The factors that influence the development of such bones in human body is still controversial to the practitioners of medicine as well as researchers.

1.3.3 Mechanical characteristics of cortical bone

Cortical bone accounts for around 80% of the body's bone mass but just 20% of the total bone volume in a normal adult human skeleton. Cortical bone has a higher ultimate strength and modulus in the longitudinal direction than those in the transverse direction demonstrating anisotropic material behaviour. Furthermore, it is stronger in compression than tension. The longitudinal elastic moduli of cortical bone were found to vary from 12-24 GPa (Ashman et. al., 1984; Carter et al., 1981; Dong and Guo, 2004) whereas, the radial moduli vary from 6-14 GPa (Ashman et al., 1984; Dong and Guo, 2004). This means that the cortical bone becomes 1.5–2 times stronger in the longitudinal direction than in the radial orientations. Despite its inherent anisotropy, any orthotropic or transversely isotropic constitutive correlation accurately describes the cortical bone elastic properties (Guo, 2008). However, the reported elastic moduli and strengths (Carter et al. 1981) are only indicative, as they may change based on the subject characteristics.

According to a study, the stiffness and strength of a bone specimen are affected by the strain rate it is subjected to, indicating the bone's viscoelastic nature (Özkaya and Nordin, 1999). Further inspection demonstrated that the orientation of the bone in regard to the loading direction affected its stress-strain behaviour.

1.3.4 Mechanical characteristic of cancellous bone

Depending on the mode of loading, the mechanical characteristics of cancellous or spongy bone varies significantly. Trabecular bone has a compressive behaviour comparable to that of cellular solids (Gibson, 1985). Under compressive load, the stress-strain diagram of cancellous bone shows an initial linearly elastic region up to a strain of about 5%, followed by a flat region of constant stress until the point of fracture (Özkaya et al., 2017). The yielding of material tends to occur as the fracture in the trabeculae has just incepted, marking a ductile behaviour of the material. Contrary to this, the trabeculae behave as a brittle material under tensile loads (Özkaya et al., 2017). However, the mechanical yield properties of trabeculae vary with anatomic site (Morgan and Keaveny, 2001; Morgan et al., 2003). Strain energy of trabecular bone is considerably higher under compressive loading regime than under tensile loading regime (Gibson, 1985; Özkaya et al., 2017).

The apparent or relative density (volume fraction of solid) of trabecular bone, as well as its manner of loading, influence its material properties and stress-strain

behaviour. The Young's modulus of anisotropic heterogeneous cancellous bone varies with the power of the relative density (Gibson, 1985). Keeping this proposition in mind, an empirically fitted power-law relationship between elastic modulus (E) with relative density (ρ_{app}) has been proposed by a number of research groups each having their different values for constants (Morgan and Keaveny, 2001; Morgan et al., 2003) as follows:

$$E = K\rho_{app}^{Q} \quad (1.1)$$

Here, constant *K* (in MPa g^{-1} cc) values ranged from 3,000 to 30,000 depending on anatomic site, while constant *Q* values were determined to be between 1.14 and 2.62. (Morgan et al., 2003). (Table 1.2) However, differences in the yield strain results in different anatomical sites were found to be minimal. It clearly suggests that uniform strain criterion will be found to be useful to reproduce realistic density distributions in the proximal femur and was applicable to other bones. Morgan and Keaveny (2001) also suggested that strain-based criteria for human trabecular bone might be mathematically simpler and statistically powerful.

Table.1.2 Mechanical properties of cancellous bone based on anatomic site and mode of loading C: Compression; T: Tension (Morgan and Keaveny 2001; Morgan et al. 2003)

Anatomic Site	Apparent Density (ρ_{app}) in $g.cm^{-3}$		$E = K\rho_{app}^{Q}$ K (95% CI)	Q (95% CI)		Yield Strain (%)	Yield Stress (MPa)
Vertebra (T10-L5)	Mean	0.18	4730	1.56	C	0.77±0.06	2.02±0.92
	Range	0.11-0.35	3050-7320	1.31-1.81	T	0.70±0.05	1.72±0.64
Proximal Tibia	Mean	0.23	15520	1.93	C	0.73±0.06	5.83±3.42
	Range	0.09-0.41	10830-22230	1.70-2.16	T	0.65±0.05	4.50±3.14
Greater Trochanter	Mean	0.22	15010	2.18	C	0.70±0.05	3.21±1.83
	Range	0.14-0.28	7590-29690	1.74-2.62	T	0.61±0.05	2.44±1.26
Femoral Neck	Mean	0.56	6850	1.49	C	0.85±0.10	17.45±6.15
	Range	0.26-0.75	5440-8630	1.14-1.84	T	0.61±0.03	10.93±3.08
Pooled	Mean	0.27	8920	1.83	----------		----------
	Range	0.09-0.75	7540-10550	1.72-1.94			

1.3.5 Bone Cells – Types, Structure and Functions

1.3.5.1 Osteogenic cells

Osteogenic or osteoprogenitor cells are unspecialized bone stem cells of mesenchymal origin. Due to their mesenchymal origin, they are also known as Mesenchymal Stem Cells (MSCs). These cells are the only pluripotent bone cells that undergo cellular differentiation upon acted by different mechanical signals

through the process of mechanotransduction. These cells are commonly available in the inner lining of periosteum, in the endosteum and inside the vascular regions of the bone canals (Snell 2011).

1.3.5.2 Osteoblasts

Osteoblasts are large, round, organelle-rich bone-forming cells that synthesis and produce collagen fibres and other organic material that are involved in the formation of extracellular matrix (ECM) (Puthumanapully 2010). Osteoblasts are found as contiguous cells with diverse morphology of diameter 20-50 µm (Snell 2011).

1.3.5.3 Osteocytes

Osteoblasts getting trapped in the ECM secreted by them differentiates and form mature stellate shaped bone cells called osteocytes. These cells making up the bulk of the bone tissue (around 90-95%) are long-lived and helps in maintaining the daily metabolic activities of the bone. Osteocytes coordinates the activities of other bone cells by releasing certain proteins that signal other cells to act to the environmental variations. They also help in maintaining mineral homeostasis, undergoing morphogenetic and restructuring processes (Snell 2011). Average size of osteocytes ranges from 5-20 µm in diameter. The premature death of osteocytes may present as osteoporosis, osteoarthritis and osteonecrosis to the subjects.

1.3.5.4 Osteoclasts

Bone resorbing large multi-nucleated cells that are formed from the fusion of precursor cells in the myeloid or monocyte lineage are generally referred to as osteoclasts (Snell 2011). They are primarily concentrated at the "Howship's Lacunae" of the endosteum and appear foamy in appearance due to the large number of cellular organelles present on the surface of the cells (Jee 2008). Average size of osteoclasts ranges from 150-200 µm. To breakdown the protein and mineral components of the surrounding ECM, these cells secrete lysosomal enzymes and acids. Osteoclasts by the stimulation of parathyroid hormone (PTH) are also responsible to regulate blood calcium levels and are primarily used as target cells to treat diseases like osteoporosis (Puthumanapully 2010).

1.3.6 Bone Formation

Bone formation or ossification occurs through two processes: intramembranous ossification and endochondral ossification.

1.3.6.1 Intramembranous Ossification

In this mode of bone formation, the bone is formed directly from a connective tissue membrane. This method is considerably simpler method in comparison to the mode of endochondral ossification. The process starts with the gathering of MSCs in ossification centres to form *nidus* which then differentiate into osteoblasts. ECM is secreted by the osteoblasts followed by calcification and hardening of the matrix (Martini and Bartholomew 2016). Osteoid or non-mineralized portion of the bone forms progressively along with angiogenesis to form trabecular or cancellous bone. Remodelling of cancellous bone into thin layer of compact bone occurs at the periphery of cancellous bone (Martini and Bartholomew 2016). The bones of the skull, the mandible and the clavicles are formed by the process of intramembranous ossification.

1.3.6.2 Endochondral Ossification

In this mode of bone formation, the bone is formed from hyaline cartilage. The long bones of the human limbs are developed by following the process of endochondral ossification. On contrary to intramembranous ossification, MSCs gather to form chondroblasts which secret cartilage matrix thus form a hyaline cartilage model (Puthumanapully 2010; Martini and Bartholomew 2016). A layer of perichondrium is formed around the cartilage model. Chondrocytes upon differentiation from chondroblasts are surrounded by the cartilaginous matrix. Continuous cellular division by the osteocytes help in further growth of the cartilage model which promotes hypertrophic growth of chondrocytes at the mid-region and burst. All these phenomena change the pH of the cartilage model that set off the process of calcification (Martini and Bartholomew 2016). Formation of a lacunae takes place with the death of chondrocytes. Thereafter, a primary centre of ossification is formed when a nutrient artery penetrating into the perichondrium at the mid-region stimulates the perichondrial osteogenic cells to differentiate into osteoblasts (Martini and Bartholomew 2016). Perichondrium thus develops into a periosteum. Periosteal capillaries develop into the disintegrating calcified cartilage at the core of the cartilage model, forming the primary ossification centre. Bone is replaced by the cartilage at this stage. Trabeculae are formed when bone matrix is deposited over the remaining cartilage (Martini and Bartholomew 2016). A medullary cavity is formed as the trabeculae is resorbed further by the osteoclasts. During the time of

birth in humans, a secondary ossification centre is formed at each of the end of the epiphysis. Meanwhile, ossification progresses from centre of the bone towards the outer surface. Articular cartilage is formed from the hyaline cartilage at the epiphysis, while epiphyseal growth plate is formed from the hyaline cartilage at the metaphysis that promotes longitudinal growth of the bone (Martini and Bartholomew 2016).

1.4 Brief history of Total Hip Arthroplasty (THA)

Hip arthroplasty has a clinical history of more than a century. The hip components as well as the procedure has however experienced incremental changes and adjustments throughout. Themistocles Gluck, a German surgeon, was the first to attempt hip replacement in 1891. Clinicians studied many paths for interpositional arthroplasty in the late nineteenth and early twentieth centuries, including adding various tissues (fascia lata, skin, pig bladder submucosa) between the articulating hip surfaces of an arthritic hip (Learmonth et. al., 2006). Surgeon Marius Smith-Petersen is known for developing the first glass-made 'mold arthroplasty' in 1923. The prosthesis was made up of a hollow hemispherical cup that could be fitted over the femoral head to provide an additional smooth articulating surface. However, the success of the implant was limited as the articulated surface was unable to bear the extremely high hip joint forces and failed. Later, Marius Smith-Petersen as well as Philip Wiles individually studied the cobalt-chromium (Co-Cr) implant, which became a significant advancement of arthroplasty, during the first hip reconstruction surgery using fasteners (Smith-Petersen, 1948; Wiles, 1958). Despite its success, the actual resurfacing approach was discovered to be insufficient in the long run. Frederick R. Thompson and Austin T. Moore each produced reconstructive models for the entire femoral head to address the problem of femur fracture as well as arthritic femoral head (hemi-arthroplasty). Despite its widespread use in the 1950s, there was doubt about the effects and acetabulum injury. Moreover, until then, no convincing approach for attaching the component to the host bone had been discovered.

By replacing the Thompson stem with a new one-piece Co-Cr socket as the new acetabular cavity in 1953, British surgeon George McKee became the first to use a metal-on-metal hip prosthesis. McKee and Watson-Farrar injected much more creativity to this design. According to a clinical trial, this prosthesis showed a 74

percent survival rate after a 28-year follow-up period (Brown et. al., 2002). The technique's popularity faded by the mid-1970s, owing to strong frictional resistance, which produces wear debris (McKellop et al., 1996), which can lead to osteonecrosis, osteosarcoma, and other complications.

While working at the Manchester Royal Infirmary in 1962, surgeon Sir John Charnley invented the Charnley hip, the highest quality level of primary hip reconstruction. Following the unsuitability of Teflon cups (1959-62), Sir Charnley unveiled the earliest low friction arthroplasty (LFA) (Charnley, 1970), that was virtually identical to the prostheses used today on a fundamental basis. It was made up of three parts viz. a metal femoral stem, an acetabular portion made of very dense polyethylene, and acrylic bone cement. By the 1960s, this cutting-edge research had completely overtaken the available commercial designs. It was dubbed 'low friction arthroplasty' because Charnley campaigned for the adoption of a small femoral head, which resulted in a significant reduction in wear due to the smaller surface area. A 35-year follow-up on Charnley LFA revealed a 78 percent chance of survival, despite the design's poor joint stability. Nonetheless, the Charnley hip was quite well acknowledged femoral stem for more than two decades. Moreover, the first Charnley prosthesis has experienced further design alterations since 1969 to additionally diminish the failures of the THA (Fig. 1.10). Due to the long-term contribution in the field of artificial hip, Sir Charnley is regarded as the father of the modern hip arthroplasty.

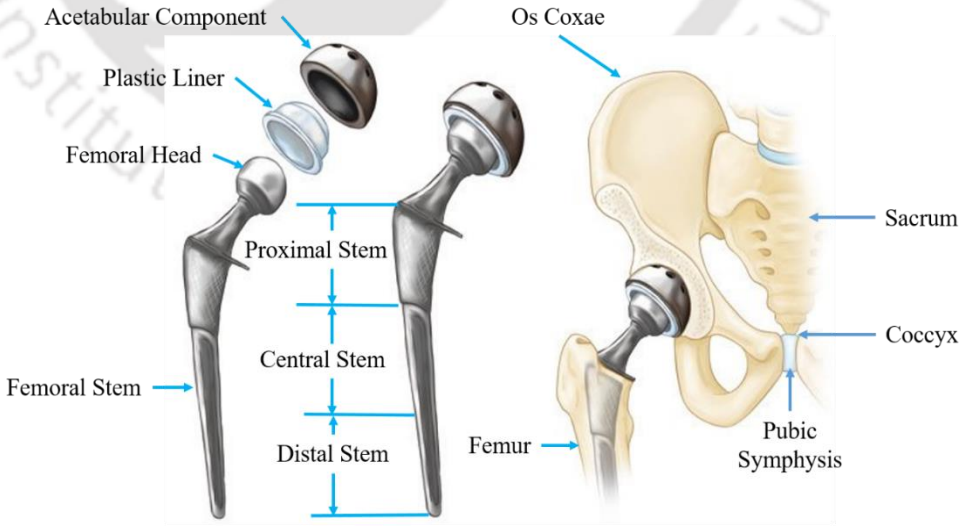

Figure 1.10 Components of the hip implant used in primary THA (Left); Assembled hip implant (Center); Implant after implantation (Right) (https://tinyurl.com/rajdeep-thesis-9)

1.4.1 Cemented THA versus Uncemented THA

Until towards the end of 20th century, cement-based fixation technique (Fig. 1.11a) was the dominating surgical procedure utilized for THA. Despite the fact that the Charnley LFA had a successful cemented design and procedure, the other cemented THA methods performed poorly, with a high and premature loosening rate (Yamada et. al., 2009). Initially, infection was assumed to be the main reason of these failures (Charnley, 1970). Histological examinations of diseased tissue removed from these isolated foci of osteolysis, on the other hand, revealed the presence of 'polymethyl methacrylate (PMMA)' debris (Harris et. al., 1976). This led the researchers to believe that the premature loosening of the cemented prosthesis was caused by a pathologic condition known as "cement disease" (Jasty et al., 1986; Maloney et al., 1990), in which PMMA particles induce a biologic response by osteoclasts, resulting in bone atrophy and progressive bone loss. These prompted scientists to look for alternative way of fixating in hip arthroplasty.

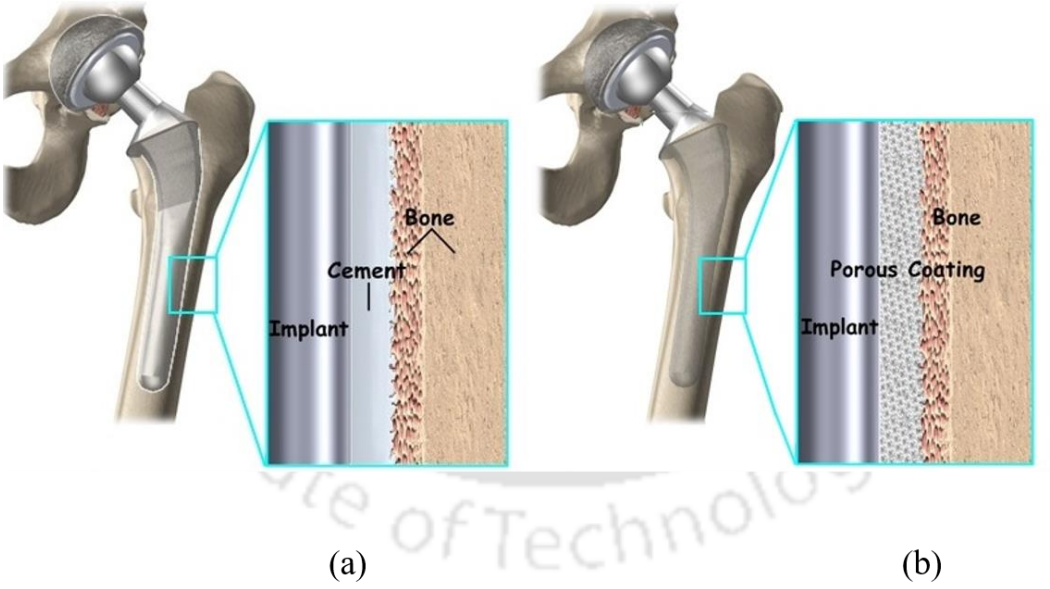

Figure 1.11 (a) Cemented THA (b) Uncemented THA (https://tinyurl.com/rajdeep-thesis-10)

Further investigations reported that cemented implants have certain cons; the most prominent among them being osteonecrosis (Mont et. al., 2006). Furthermore, cement is strong in compression but not in tension. Bone cement, however, does not adhere bone to cement or cement to implant; rather, it fills gaps during surgical interventions and comes with a slew of drawbacks. The implant-cement interface is

said to be the most vulnerable part of the implanted bone, causing debonding. All of these issues may have contributed to the development of uncemented intramedullary fixation systems that rely on implant press-fitting (Fig. 1.11b). The standards of uncemented fixation have advanced drastically over a recent period since the initial phases of outcomes were accounted for. The goal of the design was to achieve a balance of implant stability and biological anchoring at the bone-implant interface. However, a number of factors affect osseointegration like implant design, surface treatment, primary mechanical stability and quality of the bone. Thus, there is a wide range of area towards the research community to develop and improve the osseointegrity and osteoconductivity of the hip stems. The AML stem (anatomic medullary locking) was the first uncemented femoral prosthesis approved in the United States. Despite a 20-year survival rate of up to 98 percent (Belmont et al., 2008), the implant was taken off the market due to proximal stress shielding and infrequent thigh inflammation related to distal cortical hypertrophy.

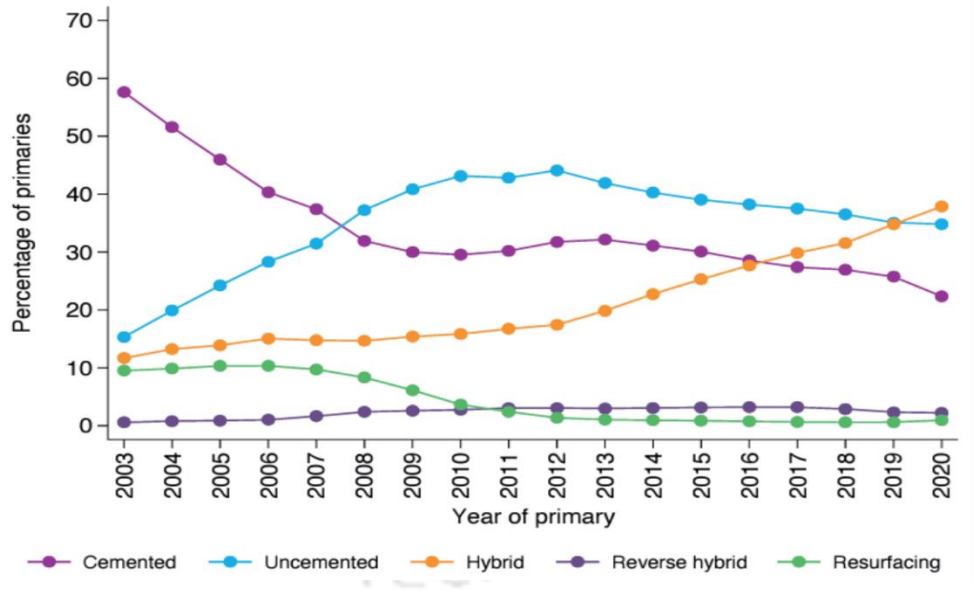

Figure 1.12 A Brief History of Time-dependent use of each fixation procedure used in primary hip arthroplasty.
Source: UK National Joint Registry 18th annual report, 2021

Although the relative superiority between cemented and uncemented arthroplasty remained a concern for argument in the domain of THA, a recent trend of preference for surgeons towards uncemented and hybrid (cemented stem with uncemented acetabular component) hips in the UK National Joint Registry 18th annual report 2021 (Fig. 1.12) still clearly shows the importance of uncemented fixations in the present scenario. Furthermore, current advances in computing power, micro-

precision 3D printing technology, and image processing techniques have enabled researchers to delve deeper into the know-how of uncemented implant performance.

1.4.2 Primary reasons for hip arthroplasty

The major symptoms of a degenerative hip joint is pain, swelling, joint stiffness and reduced mobility, which, in initial stages can be prevented from further augmentation by lifestyle changes and other therapies but in extreme cases, calls for hip arthroplasty. Though arthroplasty cannot mimic the natural joint native to the patient but still it can improve mobility and reduce pain and inflammation to considerable extent. The most common reasons that in extreme cases can lead to surgical interventions in the hip are as follows:

1.4.2.1 Osteoarthritis (OA)

Osteoarthritis (OA) is the most often cause for undergoing hip arthroplasty. Osteo meaning "bone", arthr means "joint or articulation" and itis meaning "pain or inflammation", which means that OA is a degenerative bone joint inflammation and not restricted to hip. Almost 75% - 90% (Swedish Hip Arthroplasty Register, Annual Report, 2004; Finnish Arthroplasty Register, 2006; National Joint Registry for England and Wales, 2008) of the THAs performed worldwide is due to OA. Cartilage being soft and smooth act as a bearing and cushioning surface between bones in a joint. This cartilaginous layer wears off with age and increased mobility, exposing the bone surfaces to come into direct contact with one other, generating more frictional mobility. Exercises, analgesics and reduction of body weight (for obese patients) are some of the basic preventive cure for patients whose natural joints did not suffer much wearing out and can be kept as it is for longer period whereas, surgical intervention is a must for extreme cases of osteoarthritic hip. Fig. 1.13 shows the difference between clinical condition in osteoarthritic and rheumatoid arthritis joint.

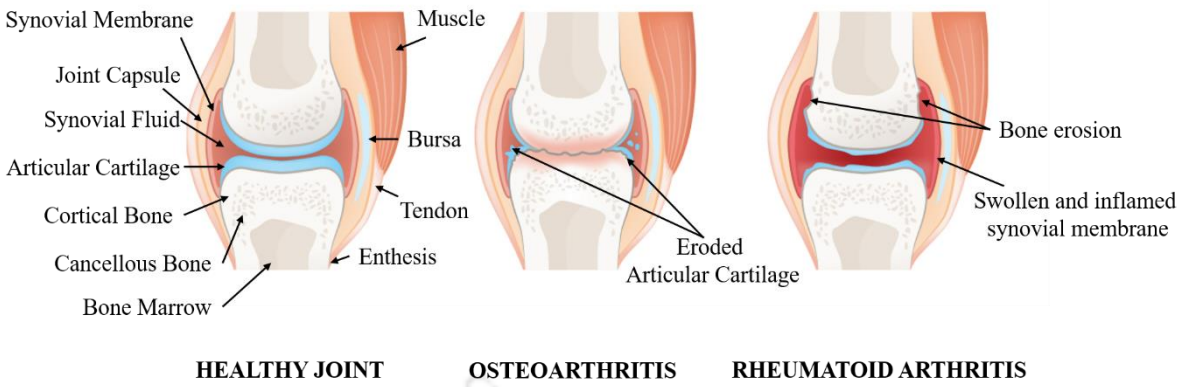

Figure 1.13 Difference between healthy, osteoarthritic and rheumatoid arthritis joint (https://tinyurl.com/rajdeep-thesis-11)

1.4.2.2 Rheumatoid Arthritis (RA)

Rheumatoid Arthritis (RA) (Fig. 1.10), also known as "inflammatory arthritis" is a chronic inflammatory autoimmune disease that affects not only joints but also other bodily systems like eyes, cardiovascular and respiratory systems etc. and so also known as "systemic disease" in medical fraternity. RA is believed to occur when self-immune system attacks the synovial membrane, which leads to thickening of the membrane with the formation of a fibrovascular tissue called pannus and thus eventually undergoes progressive bone and cartilage degeneration at the joints. RA in the long run can lead to osteoarthritis, due to loss of articular cartilage. "Rheumatoid factor" which is an antibody is found to be present in almost 80% of the patients suffering from RA. RA is an incurable disease but lifestyle changes along with medications and surgery in extreme cases may be beneficial. A population based study revealed that, about 4% of hip arthroplasties are performed due to RA (Swedish Hip Arthroplasty Register, Annual Report, 2004; Finnish Arthroplasty Register, 2006).

1.4.2.3 Osteonecrosis (ON)

Osteonecrosis (ON) (Fig. 1.14), also known as avascular necrosis (AVN), aseptic necrosis or ischemic bone necrosis, is a disorder where the bone cells die due to lack of oxygen supply and other essential nutrients. It occurs due to decreased blood flow in those bony areas. Although it can occur at any bony regions but it is generally found to occur at epiphysis of long bones like femur and upper humerus. ON can eventually lead to osteoarthritis at the joints, especially hip and knee joints. Early

stages of ON hardly come up with any symptoms but at later stages, patient suffers from mild to extreme joint pain. Imaging technologies like X-rays and MRIs are generally preferred to diagnose the disease at advanced stages though it is hard to detect ON at initial stages. Biopsy can be an option but still is not preferred. However, no acceptable preventive drugs or treatments for ON have yet been reached. Given the sex, age, and severity of ON, surgical intervention such as joint replacement, osteotomy, core decompression of the bone, and bone grafting become the primary course of ON treatment.

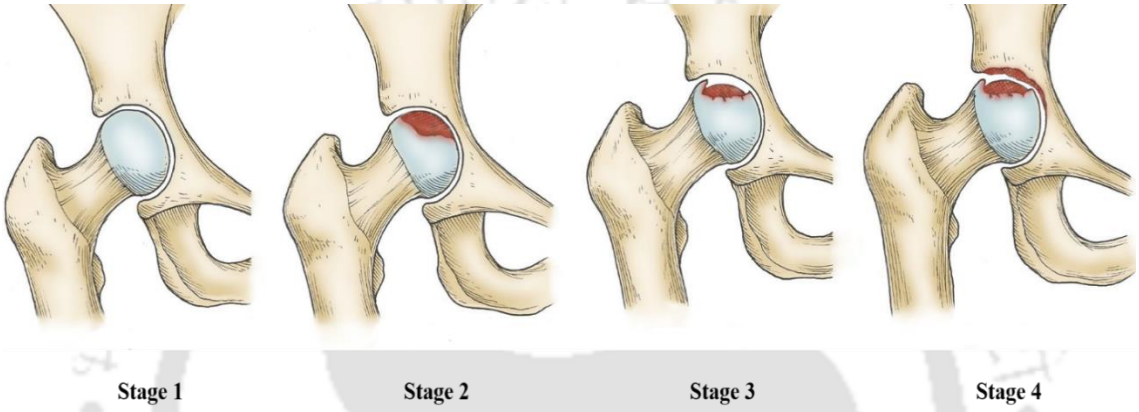

Figure 1.14 Stages of Osteonecrosis at hip from a healthy joint to a collapsed joint (https://tinyurl.com/rajdeep-thesis-12)

In addition to the reasons mentioned above, traumatic femoral neck and inter-trochanteric fractures, dysplasia, poor bone quality, increasing loss of bone mineral density (BMD) leading to osteoporosis are also few reasons for hip surgery/arthroplasty.

1.4.3 Failure scenarios in THA

A hip prosthesis is said to fail when either patient is suffering from excessive pain and impaired function and need for a revision or radiological images show signs of implant loosening and migration (Huiskes, 1993). Although the failure of a hip prosthesis can be caused by a variety of factors, mechanical events can trigger the failure process. Major failure scenarios for restored hip joints are as follows:

1. ***Accumulated damage failure scenario*:** Due to long-term repetitive dynamic loading, owing to daily physiological activities, mechanical damage gets progressively accumulated in the materials and bone-implant interfaces. These mechanical damages eventually escalate and leads to damage of implant-bone

interface, change in micromotion to unstable values, bone resorption, fibrogenesis and finally gross loosening of the implant (Huiskes,1993). Moreover, stresses generated at the implant-bone interface may exceed the implant-bone bonding and initiate failure.

2. ***Particulate-reaction failure scenario*:** This is caused due to wear debris from implant parts or from any other parts of the body that get accumulated at the joint, thus activate macrophages which creates osteolysis or inflammatory response of local bone resorption. This process weakens the bone-implant interface and might lead to potential implant migration and gross loosening of the component. In addition, venous thromboembolism (VTE) which is a combined after-effect of deep vein thrombosis (DVT) and pulmonary embolism (PE) can also occur due to occlusion of wear debris in the veins and capillaries of the body. Blood clots due to VTE can not only damage heart and lungs of the body but also inhibit angiogenesis at the bone-implant interface leading to poor bone growth. Blood thinners are therefore prescribed after a successful THA to minimize the chance of VTE.

3. ***Debonding due to poor osseous integration*:** The long-term stability of uncemented porous-coated femoral stem depends on biologic bonding through bone growth. A poor biologic bonding often enhances the chance of implant migration. Inadequate osseointegration and fibrous encapsulation at the bone-implant interface have often been associated with high bone-implant micromotion more than 150μm (Engh et al., 1992).

4. ***Stress/Strain shielding and bone remodelling*:** The stress-shielding scenario occurs at the cortical part of the bone in any intermedullary reconstruction. For example, it primarily occurs at the femoral stem in THA where there is a sharing (Huiskes,1993) of load that takes place between the host bone and the implant. The stiffer implant carries a bulk of the load and changes the load sharing pattern across the implanted bone. Consequently, a significant portion of bone, which was exposed to loads in intact condition, is shielded from the load by the stiff prosthesis in implanted condition. This sudden stress/strain shielding in mechanical environment increases osteoclastic activities causing bone resorption or gradual decrease in bone

density (Huiskes et al., 1992). This long-term bone adaptation phenomenon is known as strain adaptive bone remodelling. Such adverse bone remodelling reduces the support to the implant eventually leading to the failure of the implant-bone construct. Moreover, such prolonged bone resorption also poses a challenge during the revision surgery.

5. ***Stress bypass*:** The stiff implant transfers the joint reaction force to the bone via a novel pathway in the implanted bone. The surrounding bone reacts to this new pathway of stress transfer by apposition or an increase in bone density, according to Wolff's law (Wolff, 1892). This is a common case for uncoated press-fitted femoral implants, when distal load transmission is favoured over proximal load transfer due to proximal fit issues. As a result, the proximal femur continues to be understressed, resulting in adaptive bone resorption. The apposition of bone around the distal tip of the femoral implant, on the other hand, causes stem jamming in the distal canal (van Rietbergen et al., 1993).

6. ***Destructive wear*:** The generation of wear particles is caused by continual fretting between modular prosthesis and abrasion of bearing surfaces, which may lead to a situation where the mechanical integrity of those components is no longer maintained. Despite the fact that the annual wear rate of the articular surface is rather low (Amstutz et al., 1992), it is unlikely that the prosthesis will be able to withstand heavy fatigue loading over a long time (at least 20 years) (Saikko, 1993).

1.5 Tissue differentiation and bone formation around orthopaedic implants

The biology of bone formation is a complicated biological process that resembles the well-defined sequential process of various cellular activity and tissue differentiation that occurs during primary bone fracture repair (Davies, 1996, 2003). Mesenchymal stem cells, or MSCs, are multipotent nonhaematopoetic stromal cells that play a crucial role in the repair of primary bone fractures. A phenomenon known as mechanotransduction occurs in the meantime. This phenomenon converts mechanical stimulus to corresponding biochemical responses by which MSCs can undergo their cellular activities like cell proliferation, differentiation, cellular maintenance, functioning, apoptosis etc. Cell is a visco-elastic material and ECM

that supports cells contains proteins collagen and elastin which provides tensile strength and stiffness to the cells as well as hinders strain due to compaction. Cells and their ECM give signals to each other by which they can manifest different cellular processes. Individual cells often receive many signals of different types simultaneously which they integrate into an information for a unified action plan. The type of signals cells receive may be biochemical like growth factors, hormones, neurotransmitters etc. or mechanical like hydrostatic pressure, deviatoric strain, fluid velocity due to interstitial fluid flow etc. The progenitor cells develop into various connective tissue cells based on the proper signalling, which leads to the formation of new tissue (Barry et al.,2003). MSCs from yellow bone marrow (Fig. 1.15) migrate to the site of bone healing and differentiate into fibroblasts (tendon/ligament cells), osteoblasts (bone cells), chondrocytes (cartilaginous cells), myoblasts (muscle cells), adipocytes (fat cells for the formation of bone marrow fat), and other cell types through a cellular differentiation mechanism. An equilibrium between different types of stimuli (mechanical, biochemical like growth factors and physiological) is a need to facilitate growth and differentiation of a connective tissue (Matsuda et al., 1998).

To study implant biomechanics, knowledge of mechanical stimulus influencing biological process of cell differentiation, also known as "bone adaptation" is paramount. Bone adaptation is characterized by a sequence of events (Weinbaum et al., 1994; Stoltz et al., 2018) as follows:

a) **Mechanocoupling**: *conversion of mechanical stimulus to biological input signals to act on the cells.*

b) **Mechanotransduction**: *conversion of the biological input signals to electrical, chemical or biochemical signals.*

c) **Transduction**: *Intracellular conversion of the mechanotransducted signals into final signals for the cells to act upon.*

d) **Cell response**: *cell differentiation, proliferation etc.*

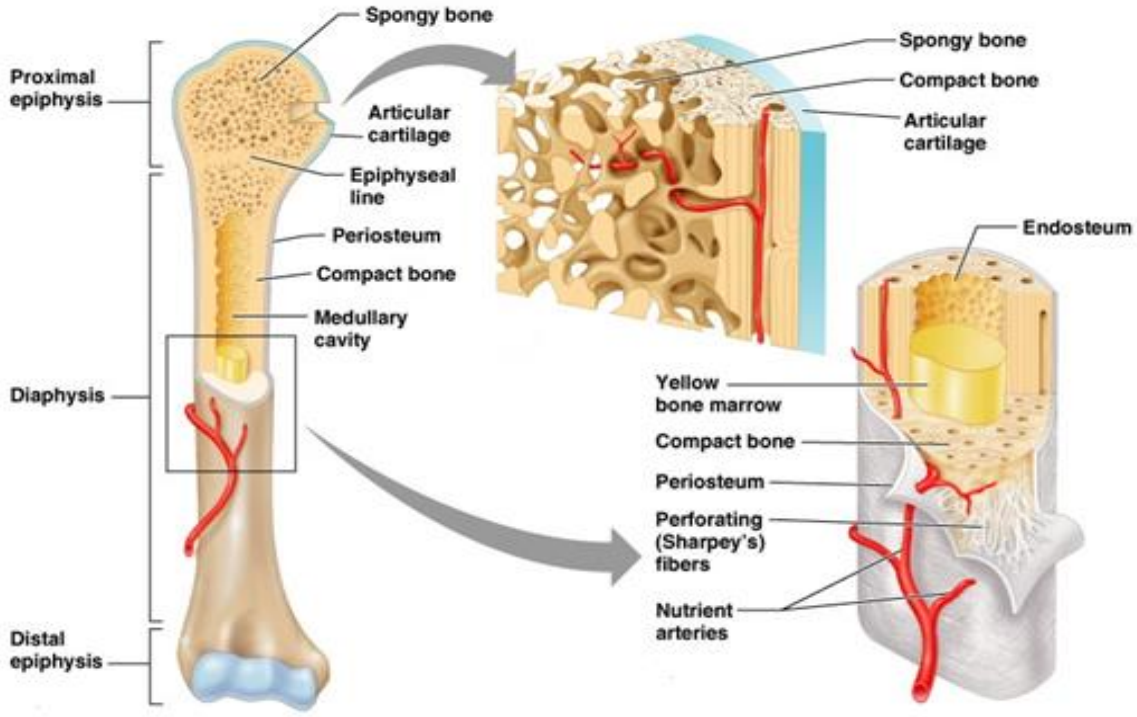

Figure 1.15 Internal architecture of bone showing yellow bone marrow (Marieb and Hoehn, 2013)

A model known as "mechanostat of bone adaptation"(Frost,1987) was proposed to get an idea to get the optimum level of bone strain for physiological growth of bone. It suggests that lower level of strains promote bone resorption by formation of osteoclasts whereas moderate level is considered physiological. Studies revealed that static loading prohibited bone formation and promoted bone resorption along with decreasing of RNA and synthesis of proteins, whereas, cyclic loading promotes osteogenesis (Stolz et al.,2018). Studies showed that mechanical stimuli itself could regulate cellular differentiation process in a cartilageneous medium and in dearth of any growth factor (Angele et al., 2003; Altman et al., 2002). One such example is the fact that differentiation of progenitor cells influenced by local mechanical environment such as deviatoric and hydrostatic stresses (Pauwels, 1960; Carter et al., 1988). However, both of these stimuli are heavily reliant on relative interfragmentary micromotion (Speirs et al., 2000).

1.6 Bone remodelling around orthopaedic implants

"Large animals need stronger and bigger and harder supports, especially those of them that are particularly violent in their habits" as written by Aristotle. This shows the relationships between size of an animal body and its activity level that were being

appreciated even in ancient years. Much later, scientists took interest in investigating any correlation of mechanical stimulus on tissue formation. Bone is capable to adapt its structure, both externally and internally, in response to change in mechanical loading by bone apposition (formation) and bone resorption (loss) through the activities of cells called osteoblasts and osteoclasts, respectively. This process is known as bone remodelling. Internal bone remodelling refers to changes in internal morphology, whereas external remodelling is described relative to periosteal geometry. Internal remodelling, thus, is expressed as a change of density or porosity of the cancellous bone (Carter et al., 1989; Huiskes et al., 1987), whereas the geometric (or shape) changes of the cortical bone are referred to as external remodelling (Hart et al., 1984). For an adult, the cancellous bone usually has a higher rate of metabolic activity and hence, appears to respond more rapidly to changes in mechanical loads than the cortical bone. Therefore, the geometry changes are considerably less in comparison to internal adaptation or internal remodelling of the bone. The combined effect of internal and external remodelling models has been investigated by several researchers (Beaupré et al., 1990; García et al., 2001; Huiskes et al., 1987; Weinans et al., 1993).

No net changes in bone morphology was observed in the natural bone, since the rate of bone resorption and that of bone apposition remain in equilibrium (Frost, 1964; Parfitt, 1984). However, any mechanical intervention disturbs the normal state of equilibrium between apposition and resorption processes, and subsequently, the bone tries to reach a new state of equilibrium. Surgical reconstruction of bone with prosthesis alters the mechanical environment within the bone by changing the load transfer mechanism. As a result, the prosthesis starts to share the joint load in the implanted situation, which was otherwise carried exclusively by the bone in the pre-operative stage.

Bone remodelling process is known to be regulated by external loading condition (Huiskes et al., 1989; Mullender et al., 2004). Way back in the 17th century, Galileo Galilei first observed a certain relationship between mechanical forces (body weight) and bone morphology (Carter, 1984). Considerable scientific interest developed thereafter to describe the relation between the bone structure and its function. A notable contribution came from Wolff (1892), who further developed the theory of functional adaptation originally conceived by Roux (Roux, 1881).

These studies concluded the combination of bone apposition and resorption to be a biological control process dependent on the local state of stress (Roux, 1881). According to Wolff's hypothesis, every change in the form and the function of a bone is followed by certain definite changes in their internal architecture and equally definite secondary alterations in their external geometry, based on certain mathematical laws (Wolff, 1892). This 'law of bone transformation' by Wolff was later referred to as 'Wolff's Law'. A series of investigations followed to describe this law in terms of mathematical formulation and to further quantify the process of bone remodelling (Beaupré et al., 1990; Cowin and Hegedus, 1976; Doblaré and García, 2002; Fyhrie and Carter, 1986; Hart et al., 1984; García et al., 2001; Huiskes et al., 1987; Jacobs et al., 1997).

1.7 Need for in silico simulations in mechanobiology

Mechanobiology is an emerging highly interdisciplinary field that uses the knowledge of cell biology, developmental biology, bioengineering, biochemistry and biophysics (Jansen et al., 2015) to understand the influence of both internal and external mechanical signals (stress/strain) to cell growth, proliferation, migration, differentiation etc. It deals with an extremely important concept that both mechanics and biology are inter-dependent on each other at four levels of geometric scale viz. organ level, tissue level, cellular level and molecular level. Macro-scale loading history represents the mechanical signals at organ level that promotes cell differentiation at cellular level. Whereas stress and strain variants are treated as mechanical stimulus at tissue level for mechanotransduction. At the cellular scale, cell pressure, cell-matrix interactions, cellular morphology, temperatrure, nutrient supply, oxygenation etc. acts as mechanical cues for mechanobiological changes in cells. And finally, at the molecular level which is perhaps the most important level to look into the domain of mechanobiology, changes in cytoskeleton, growth factors, inflammatory cytokines, integrins, stretch activated ions etc. act as mechanical signals.

The human body including the skeletal bones and joints is a biomechanical formation. The pre-natal and post-natal skeletal development and joint morphogenesis in humans can be owed to the external mechanical loading that contributes to the change in structural and cellular phenotypes in the bones and joints within. The external macroscopic loading is transferred at a microscopic cellular

level through a mechanosensing mechanism. Local mechanical cues have a direct effect on the stimulation of cells and therefore dictates the type of tissue formation through cellular differentiation (Jansen et al., 2015; Mukherjee and Gupta, 2016).

Different *in vitro* studies were performed to study the influence of different mechanical stimulus on tissue adaptation but still now there is no common agreement regarding the precise mechanism of mechanotransduction. However, the potential of experimental studies to provide solution to many problems regarding mechanoregulation is constrained due to the complexity of cellular behaviour and the application of different biochemical factors that governs the cell/matrix interaction. With the advent of advanced computational power, *in silico* methods came up as alternative approaches to the research community for scientific investigation. It has used tools like finite element method (FEM) that can explore domains and provide solutions to those scientific problems which were thought to be impossible to solve. It has provided the capability to analyse any structure through rigorous finite element (FE) simulations.

Pre-clinical testing of a bone-implant system such as in THA which involves the use of both fundamental concepts of structural mechanics as well as mechanobiology of the biological system can be suitably addressed with the use of computer simulations. However, due to numerical limitations and incomplete information on loading and tissue properties, simplified assumptions are often made that have been found to provide fruitful solutions in the field of biomechanics and mechanobiology.

1.8 Motivation of the present work

Intramedullary implant fixation is a common surgical procedure for re-establishing fractured bones and joints, as well as for treating various joint illnesses like osteoarthritis (OA), rheumatoid arthritis (RA), and femoral fractures. Because of sedentary lifestyles among youngsters, a rise in road accidents, and an ageing population in wealthy countries, the global demand for joint replacements is skyrocketing. Bone cement used in cemented surgeries, is however less trustworthy due to its exothermic polymerization, high rigidity, and short-term reliability. On the other hand, long-term fixation of uncemented implants relies on biologic fixation of the bone with the prosthesis. However, due to higher safety and reliability, demand for uncemented implants continue to rise in the coming decades.

Aseptic loosening of an uncemented implant is characterised by fibroplasia at the bone-implant interface, resulting in inadequate fixation and component mobility. According to clinical evidence, mechanical factors appear to have a significant impact on aseptic loosening of uncemented implants. Maintaining adequate implant-to-bone fixation is critical for the long-term stability and success of intramedullary implant fixation. The implant design, the patient's bone quality, and the spatial orientation of the implant all have their role in the initial fixation of the uncemented prosthesis. The osseointegration or biologic fixation of the porous coated prosthesis with the host bone is required for long-term fixation. Although the failure mechanisms of uncemented implants are still unknown (Chanda et al., 2016), the most common reason is poor design of prosthesis (Huiskes and Boeklagen, 1988; Viceconti et al., 2001; Sánchez et al., 2021a). Surface roughness, which includes both micro- and macro-textures (Mukherjee and Gupta, 2016), has been shown to affect biologic attachment and mechanical interlocking between the implant and the host bone, respectively.

Numerous mechanoregulation models were developed to assess the influence of different mechanical stimuli on tissue growth and morphogenesis. Some of these models were implemented with FE analysis to predict the amount of bone growth during fracture healing or bone-implant fixation. Furthermore, many bone-remodelling approaches were also developed to assess post-operative bone adaptation. With this motivation, a thorough literature review on currently developed mechanoregulatory models and bone-remodelling approaches has been done. Since bone growth around uncemented implants is primarily governed by design of implants, literature review on studies involving design optimization of orthopaedic implants has also been done to understand the state-of-the-art in the area of implant design. The inference from the literature helped to find suitable gaps in the existing knowledge as well as to decide the objectives of the present thesis. The literature review is broadly presented in the next chapter.

1.9 Organization of the thesis

This thesis contains 8 chapters.

Chapter 1 briefly introduces the readers on backdrop behind the present study followed by basics of hip anatomy and functionality, anatomical planes and

directions, the anatomy of femur, gait kinematics while normal walking to musculoskeletal loading of hip joint. Additionally, structure, properties and functionalities of different types of bones and bone formation were also presented in brief. Thereafter, a brief history of THA with the reasons for performing the same has been mentioned with different failure scenarios involving THA. Moreover, an idea of mechanobiology at tissue level and bone remodelling that is responsible for bone growth and adaptation around orthopaedic implants is discussed briefly. Finally, the chapter ends with the organization of the thesis.

Chapter 2 presents a literature review on different mechanoregulation models, bone remodeling approaches and their applications in design optimization of orthopaedic implants. Subsequently, research motivation has been documented for carrying out this present study and based upon the voids in the literature, the objectives of the dissertation are outlined.

Chapter 3 presents the methodology applied to assess bone growth at the macroscopic bone-implant interface. Thereafter, a generalized methodology that has been used to assess design optimization of implant macro-textures has been discussed.

Chapter 4 presents a study on the influence of three distinct macro-textured implant surfaces on formation of new tissue phenotypes with emphasis on bone growth. Combining FE based structural and diffusion analysis followed by mechanoregulatory tissue differentiation algorithm, a numerical framework has been formulated to predict the amount and spatial distribution of bone growth qualitatively.

Chapter 5 further presents a study on the combined influence of both tangential displacement (sliding distance) and radial displacement (gap distance) on bone growth over macro-textured surfaces. Additionally, effect of texture density on bone growth has also been studied as a part of the next objective of the study.

Chapter 6 initially presents a pilot study to assess the variation in amount of bone growth with the change in significant dimensions of a macro-textured surface. Subsequently, a neural network (NN) scheme has been developed to predict amount of bone growth with implant surface design parameters as inputs.

Following the work in the earlier chapter, Chapter 7 highlights an integrated approach combining the FE analysis, NN and genetic algorithm (GA) to find optimally designed macro-textures to enhance osteogenesis. Custom NN scripts have been trained and validated in MATLAB for each of the tested macro-textures and optimal NN architectures were developed based on pre-defined NN regulating parameters.

Chapter 8 presents a study on the influence of textured and non-textured femoral implant on growth and distribution of bone and associated connective tissues. This study has been performed considering the musculoskeletal loading conditions under normal walking. Thereafter, a comparative analysis on the influence of different routine activities on formation and distribution of bone and other tissue type has been performed on the textured femoral stem.

Chapter 9 concludes the present dissertation with the key conclusions drawn from this current research work. The recommendations for future studies that might be performed as possible extensions of this study are also presented.

CHAPTER 2

Background and Literature Review

Mechanoregulatory tissue-differentiation and adaptive bone remodelling approaches are presented in this chapter in a systematic way. First, popular tissue-differentiation models and their applications in few pre-clinical biomechanical problems are thoroughly reviewed and discussed. Then, a brief insight into the background of mathematical formulation of bone remodelling approaches is discussed and thereafter presented a state-of-the-art in the field of bone remodelling approaches along with few of their most recent applications in fracture healing and bone-implant systems. In addition, importance of shape-optimization methods towards development of optimal orthopaedic implants is discussed along with some relevant literature in the area. Finally, based on the presented literature, suitable research gaps have been highlighted and specific objectives and scope of the thesis have been presented.

2.1 Mechanoregulatory models and few of their applications

Several attempts were undertaken from time to time to quantify the effect of different mechanical stimuli on tissue differentiation and bone adaptation (Carter et al., 1988; Claes and Heigele, 1999; Prendergast et al., 1997; Huiskes et al., 1997). In most of the models, fibrogenesis is more prominent by the tensile or shear stresses at their higher side (Fig. 2.1) whereas, formation of mature bone was considered where in the models have profound vascularity and lower magnitudes of stresses.

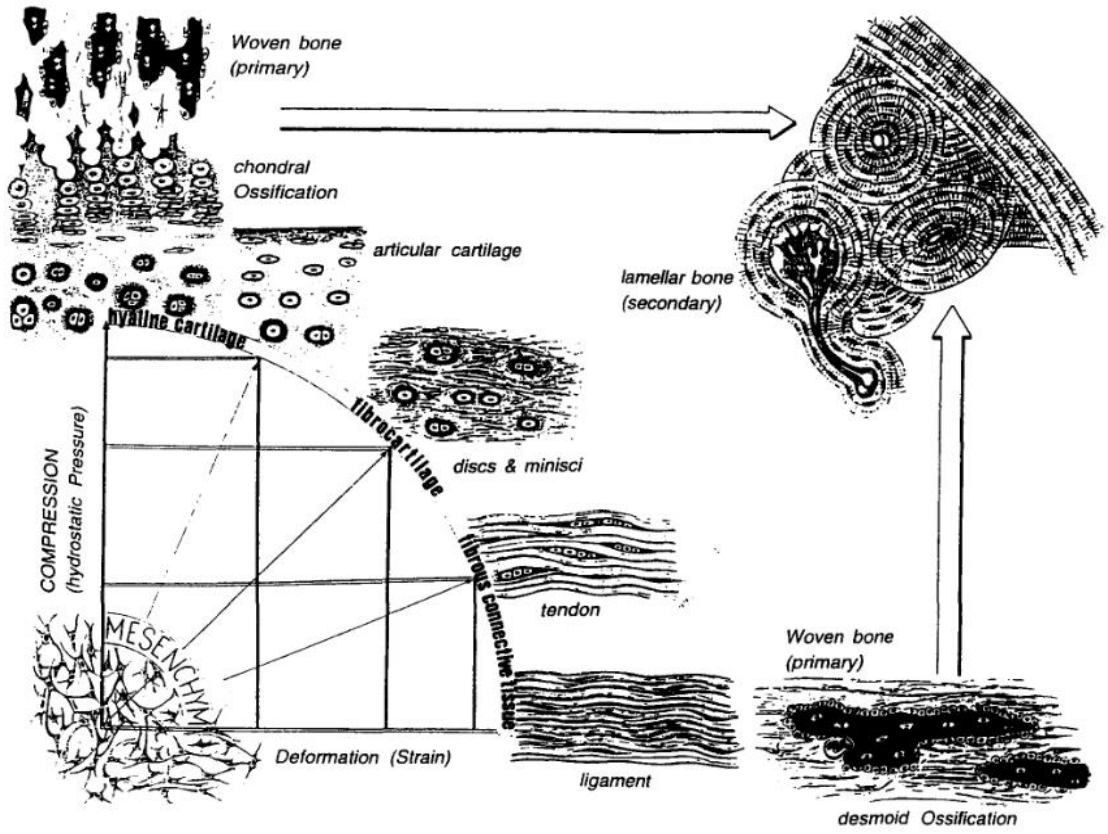

Figure 2.1 Influence of biophysical stimuli on formed tissue phenotype (Weinans and Prendergast, 1996)

2.1.1 Mechanoregulation models of fracture healing and evolutionary tissue differentiation

A handful of mechanoregulatory models have been proposed to quantify the cell/tissue differentiation phenomenon (Carter et al., 1988; Prendergast and Huiskes, 1996; Prendergast et al., 1997; Huiskes et al., 1997; Claes and Heigele, 1999). Almost all these algorithms implemented two mechanoregulatory stimuli for assessment of bone growth: octahedral shear (*S*) and dilatational hydrostatic (*D*) stresses as:

$$S = (1/3)\sqrt{[(\sigma_1 - \sigma_2)^2 + (\sigma_2 - \sigma_3)^2 + (\sigma_3 - \sigma_1)^2]} \tag{2.1}$$

$$D = (1/3)[\sigma_1 + \sigma_2 + \sigma_3] \tag{2.2}$$

where, σ_1, σ_2, σ_3 are the cyclic principal stresses.

2.1.1.1 Mechanoregulation model by Carter and co-workers

Based on Pauwels' theory (Pauwels, 1960) of mechanoregulation, Carter et al. (1988) (Carter et al., 1988) were the first to integrate these two stress stimuli into a single quantitative measure called the "Osteogenic Index" to analyse endochondral growth and ossification (Carter et al., 1988) (Figure 2.2) as:

$$I = \sum_{i=1}^{\lambda} n_i (S_i + \beta D_i) \tag{2.3}$$

where, *i* denotes the specific load case, λ denotes the total number of load cases, n_i represents number of loading cycles in a specific load case, β is an empirical constant which is dependent upon two defined mathematical models (linear and bilinear). Intermittent compressive hydrostatic pressure limits cartilage development and ossification, but intermittent strain or shear stresses accelerate both the processes according to this mechanoregulation model. In addition, this model advocated the influence of blood supply or vascularization to the prediction of tissue phenotype. Poor vascularization promotes fibrocartilage at lower stresses. Conversely, a proper blood supply with similar mechanical environment promotes ossification.

Although osteogenic index approach was formulated based on two-dimensional (2-D) FE-models, this formulation had been a success in prediction of early trends of tissue differentiation in cases of initial fracture fixation (Carter et al., 1988), embryonic morphogenesis (Carter and Wong, 1988) and around implant-bone interfaces (Giori et al., 1995; Prendergast and Huiskes, 1996). However, subsequent research into the quantification of tissue differentiation suggests that as cell/tissue differentiation progresses, the osteogenic index-based technique fails to predict tissue differentiation (Gardner et al., 2004).

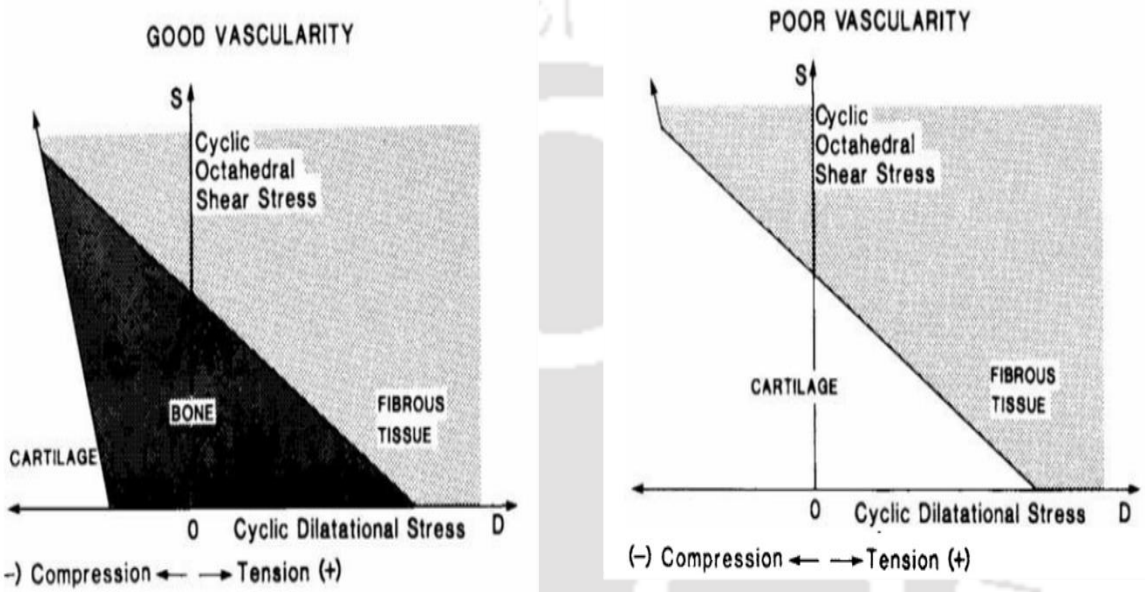

Figure 2.2 Mechanoregulatory tissue differentiation algorithm implemented by Carter et al., (1988)

2.1.1.2 Mechanoregulation model by Claes and Heigele

Although there may be many more mechanical stimuli affecting mechanobiological process of tissue differentiation, interestingly, Claes and Heigele (1999) developed a kind of a different mechanoregulatory model, wherein the local (longitudinal and radial) strains and hydrostatic stresses were considered as two mechanical stimuli governing the tissue differentiation process for a fracture healing study validated on an ovine model (Fig. 2.3). For strains less than 5% and hydrostatic pressures between ±0.15 MPa, the theory predicted threshold limits for intramembranous bone formation. Furthermore, endochondral ossification is linked to compressive hydrostatic pressures greater than 0.15 MPa and strains less than ±15%.

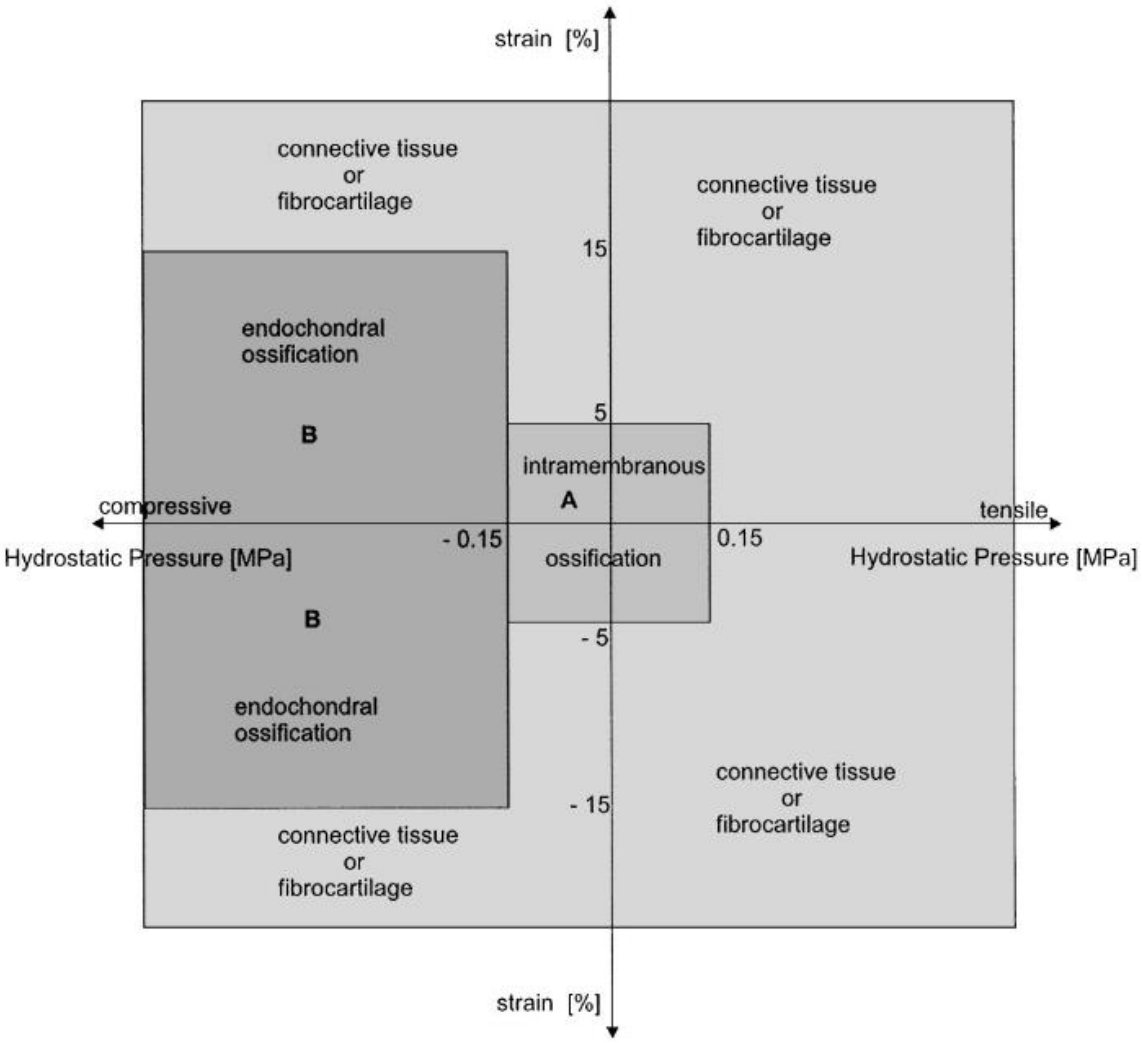

Figure 2.3 Mechanoregulatory algorithm implemented by Claes and Heigele (1999)

2.1.1.3 Mechanoregulation model by Prendargast and co-workers

On the basis of push-out experiments of the bone-implant interface gap performed by Søballe et al. (1993) on canine model, a novel mechanoregulatory model was formulated by Prendergast et al. (1997) (Prendergast et al., 1997a) considering bone as a biphasic poroelastic tissue. The conceptualization of considering a biphasic model is attributed to the fact that, soft tissues at the bone-implant interface primary comprises of collagenous solid phase and a fluid media. This model was therefore postulated on the hypothesis that, biophysical stimuli experienced by the regenerative cells at the bone-implant interface were not only reliant on the stresses acting at the ECM but also on the drag forces experienced by the interstitial fluid flow. Thus, a combined effect of octahedral strain of the solid phase of the tissue

and interstitial fluid velocity were studied in the model (Fig. 2.4). Similar to Claes and Heigele (1999) theory, the quantitative limits (Prendergast et al., 1997b) on the mechanical stimuli i.e. shear strain and interstitial fluid velocity in the biphasic model were also obtained through an empirical fit to a canine model (Huiskes et al., 1997).

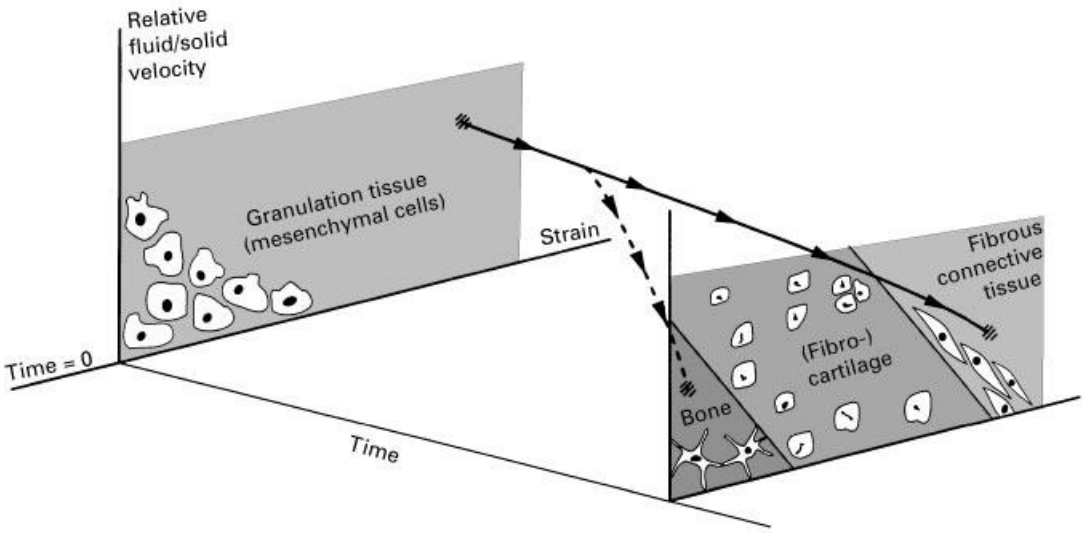

Figure 2.4 Schematic diagram of mechanoregulatory tissue differentiation algorithm of Prendargast et al. (1997)

According to this model (Fig. 2.5), a combined stimulus (Z) has been developed by combining magnitudes of shear strain (γ) and relative solid/fluid velocity (v) that regulates the tissue differentiation as:

$$Z = \frac{\gamma}{a} + \frac{\upsilon}{b} \tag{2.4}$$

where a (=0.0375) and b (= 3μm s^{-1}) are constants (Huiskes et al., 1997). Woven bone is found to develop for Z < 1 whereas, any magnitude of Z > 3 promotes fibrous tissue formation.

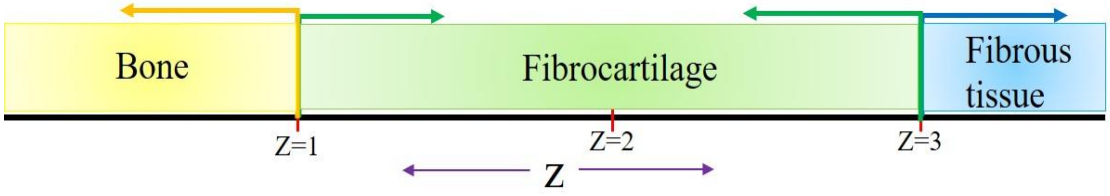

Figure 2.5 Influence of combined stimulus (Z) on tissue differentiation

2.1.1.4 Mechanoregulation model by Lacroix and co-workers considering cellular phenomenon

The biphasic model was later on implemented in a computational framework to simulate fracture healing considering cell differentiation and dispersal, followed by a diffusion based poroelastic model (Eqn. 2.5) to study the cell migration (Lacroix et al., 2002; Lacroix and Prendergast, 2002a, 2002b):

$$k\nabla^2 c = \frac{dc}{dt} \tag{2.5}$$

where, k is the diffusion constant, and c denotes the cell concentration at each finite element at the fracture callus. However, considering diffusion model to simulate cellular dispersal is a simplified version of the biological phenomena of cellular migration. A homogeneity in the cellular migration is assumed to have been achieved by the cells at the interface. In addition, migration of intermediate regenerating cellular phenotypes which might interfere with the healing process was not modelled in the study. Furthermore, such a model does not take into account cellular mitosis and necrosis/apoptosis. However, such an adaptive model was found to satisfactorily mimic the periosteal bone formation, endochondral ossification, bone bridging at the callus followed by bone formation.

2.1.2 Modifications and applications of primary mechanoregulatory algorithms

A number of research groups across the globe have used these approaches of mechanoregulatory models to analyse fracture healing (Isaksson et al., 2006,2008a, 2008b, 2009), osteochondral defect healing (Kelly and Prendergast, 2005; Kelly and Prendergast, 2006) and implant-bone interfacial tissue differentiation (Liu and Neibur, 2008; Chou and Müftü, 2013, Dickinson et al., 2012, Mukherjee and Gupta, 2016; Li et al., 2020; Irandoust and Muftu, 2020) with subtle modifications such as in obtaining the influence of micro texture over implant surface on bone growth (Chou and Müftü, 2013; Mukherjee and Gupta, 2016; Mathai and Gupta, 2022). Inclusion of cellular events such as cell proliferation, cell necrosis/apoptosis (Kelly and Prendergast, 2005; Kelly and Prendergast, 2006; Isaksson et al., 2008a; Andreykiv et al.,2008a), formation of ECM and tissue degradation (Mukherjee et

al.,2017) were formulated based on this mechanobiological model. However, although the complexity of computational model increases for cell-phenotype specific algorithms they are found to provide almost similar results while predicting spatial distribution of new tissue (Mukherjee et al.,2017) when compared with the simpler diffusion-based phenomenological algorithms. The mechanoregulatory algorithm of Prendargast et al., 1997(Prendergast et al., 1997a) was further modified in various other problems such as by including angiogenesis (Checa and Prendargast,2009), understanding the influence of mechanical environment on the collagen architecture in regenerative soft-tissues (Nagel and Kelly, 2010) and also assessing the influence of mechanical stimuli in predicting tissue phenotype in a Calcium Phosphate (CaP) scaffold under compressive load and perfusion flow (Sandino and Lacroix, 2011).

2.1.3 Mechanoregulatory models not used frequently

Apart from the mechanoregulatory models mentioned above, a few other modelling algorithms were developed during the past decade. Gómez-Benito et al. (2005) (Gómez-Benito et al.,2005) developed a novel mathematical model to mimic the influence of mechanical stimuli on the majority of cellular events occuring during the healing process. They modelled bone healing as a response to a defined mechanical stimulus, $\Psi(x,t)$ supposed to represent the deviatoric strain tensor's second invariant. Ambard and Swider (2006) (Ambard and Swider,2006) developed a predictive mechanobiological formulation through a multiphasic porous model focussing primarily on the bone formation by osteoblastic differentiation. However, this model did not take into account the initial inflammatory phase of the callus and proliferation and differentiation of the precursor cells. Puthumanapully and Browne (2010) (Puthumanapully and Browne, 2010) modified the mechanoregulatory model of Carter et al. (1988) (Carter et al., 1988) to study tissue differentiation around short-stemmed metaphyseal loading femoral prosthesis by incorporating an iterative time-stepping combined with a temporal smoothing method to simulate the progressive healing at bone-implant interface. The results of tissues differentiation were found to be consistent with prior animal studies thus providing confidence to their model. However, all these mechanoregulatory models are not used frequently

as they were modified specifically to the problems they address and have not been tested under different types of biomechanical problems.

2.1.4 Studies on efficacy of primary mechanoregulatory models

Later, the efficacy of few primary mechanoregulatory models to predict tissue adaptation were also studied by Isaksson et al. (2006) (Fig. 2.6) and they came to conclusion that all the algorithms were capable of predicting similar trends of tissue adaptation (Isaksson et al., 2006) under axial loading conditions. In addition, it was also predicted that deviatoric strain (Isaksson et al., 2006; Tarlochan et al,2018; Mehboob et al.,2020; Mohandes et al.,2021) at the bone-tissue interface region itself could predict similar trends of tissue differentiation and bone resorption than those predicted by other mechanoregulative stimuli (Lacroix et al., 2002) but in a different iterative pseudo-time scale. Under torsional loads, none of the modelling approaches could predict bone healing entirely similar to animal experiments (Isaksson et al., 2005). Nevertheless, those were employed to predict qualitative assessment of fracture healing and bone growth considering a combination of deviatoric strain and interstitial fluid velocity growth (Mukherjee and Gupta, 2016; Tarlochan et al,2018;

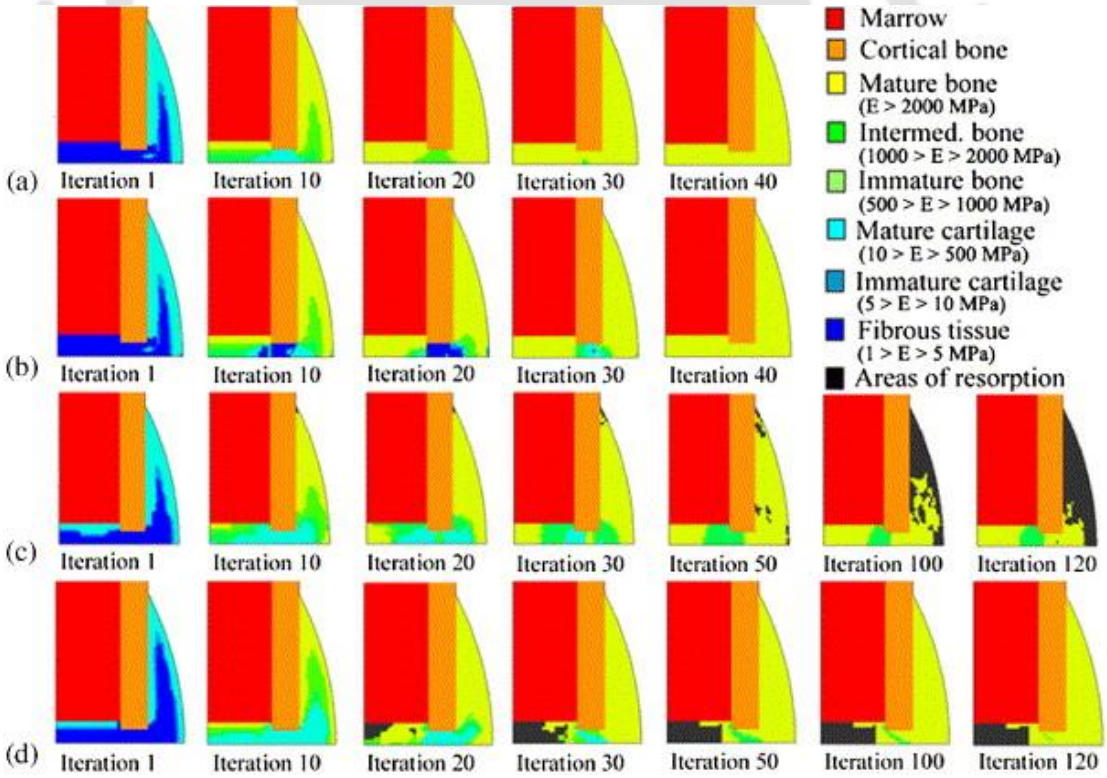

Figure 2.6 Predicted tissue differentiation study with mechanoregulatory algorithms of (a) Carter et al., 1988 (b) Claes and Heigele, 1999 (c) Lacroix and Prendergast, 2002 (d) Deviatoric strain

Source: Isaksson et al.,2006

2.2 Different modelling approaches on bone remodelling

The mathematical formulations of bone remodelling were based on the common assumption that bone has certain sensing capability to measure the change in internal mechanical conditions (stimulus) within it and respond to that change (combined with other biological factors) by the action of osteoblasts and osteoclasts. Although most of these models considered apparent density (ρ_{app}) as variable to represent the remodelling state, the choice of mechanical stimulus varied depending on the model. Several diverse mechanical stimuli have been defined as a function of strain (Cowin and Hegedus, 1976; Turner et al., 1997; Fernandes et al., 1999; Wang et al., 2016), stress (Beaupré et al., 1990; Goda et al.,2016), strain energy density (SED) (Huiskes et al., 1987; Weinans et al., 1992; Waizy et al., 2017), mechanical tissue damage (McNamara et al., 1992; Prendergast and Taylor, 1994; Prendergast and Huiskes, 1995; Hambli et al.,2011) and proliferation of bone forming cells (Pivonka et al.,2008; Bonfoh et al.,2011).

2.2.1 Bone remodelling approach by Cowin and Hegedus

'Adaptive elasticity' approach as proposed by Cowin and Hegedus (1976) is a 'site-specific' remodelling theory primarily to describe the adaptive nature of cortical bone. It can be described as a normalisation of the active local state of strain to the strain state occurring under daily physiological activities at the same locations. According to this model, the amount of local bone resorption or apposition depends on the local differences in strains between an actual and the corresponding normal situation. Adaptation model by Cowin and Hegedus (1976) proposed internal remodelling of bone as expressed in Eqn 2.6:

$$\frac{dY}{dt} = P_{ij}(S_{ij} - S_{ij}^{0}) \tag{2.6}$$

where, Y is the site-specific elastic modulus, S_{ij} and S_{ij}^{0} are the actual site-specific strain tensor and strain-tensor at equilibrium respectively and P_{ij} is the matrix formed by remodelling coefficients. Conversely, external remodelling of bone can be expressed as in Eqn 2.7:

$$\frac{dD}{dt} = Q_{ij}(S_{ij} - S_{ij}^{0}) \tag{2.7}$$

where, D is the site-specific coordinate of the bone surface perpendicular to the surface, S_{ij} and S_{ij}^0 are the actual site-specific strain tensor and strain-tensor at equilibrium respectively and Q_{ij} is the matrix formed by remodelling coefficients.

2.2.2 Bone remodelling approach by Huiskes and co-workers

Huiskes et al. (1987) came up with an alternative formulation to the already proposed theory of 'adaptive elasticity' by using the local SED, instead of strain tensors (Cowin and Hegedus, 1976) as the remodelling stimulus for peri-prosthetic bone adaptation. Bone, however, does not respond to small deviations in the mechanical stimulus. A bare minimum threshold value of the inhibitory signal, the difference between the mechanical stimuli for altered and natural situations, is required for the bone remodelling process to initiate (Huiskes et al., 1987). The range of values of mechanical stimuli, where bone does not respond, is known as the 'dead zone' or 'lazy zone'. Figure 2.7 illustrates the remodelling phenomena as proposed.

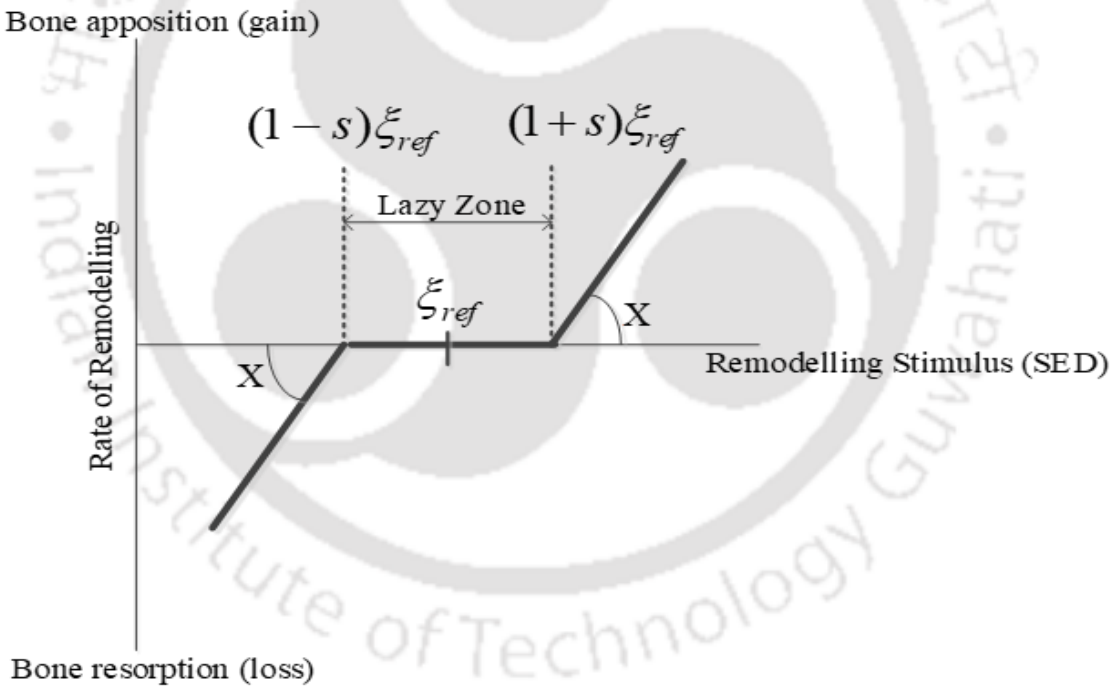

Figure 2.7 Trilinear relationship of adaptive remodelling rate as a function of remodelling stimulus (SED)

Huiskes et al. (1987) accounted for an inclusion of the 'dead zone' in their mathematical formulation for bone remodelling. The model proposed by Huiskes et al. (1987) for internal bone adaptation, can be further expressed as:

$$\frac{dY}{dt} = \begin{bmatrix} X_i(\xi - (1+s)\xi_{ref}), & \xi > (1+s)\xi_{ref} \\ 0, & (1-s)\xi_{ref} \le \xi \le (1+s)\xi_{ref} \\ X_i(\xi - (1-s)\xi_{ref}), & \xi < (1-s)\xi_{ref} \end{bmatrix} \quad (2.8)$$

where, X_i denotes the internal remodelling rate, ξ and ξ_{ref} denote the actual SED and site-specific SED at homeostatic equilibrium and s represents the threshold level of initiation of remodelling. Similarly, the mathematical formulation for external bone remodelling is expressed as Eqn 2.9:

$$\frac{dD}{dt} = X_e(\xi - \xi_{ref}) \quad (2.9)$$

where, X_e denotes the external remodelling rate.

Such a formulation of adaptive bone remodelling is fundamentally a rule-based optimization process (Weinans et al., 1992) of achieving a pre-set SED by adapting the apparent density of bone. In the model proposed by Huiskes et al. (1987) and Weinans et al. (1992), the change in bone apparent density(porosity) was expressed as a function of mechanical signal responsible for bone adaptation as:

$$\frac{d\rho_{app}}{dt} = R(S_m - \pi),\ 0 < \rho_{app} \le \rho_{\max} \quad (2.10)$$

where, ρ_{app} represents the site-specific apparent bone density, R denotes a constant, S_m represents the mechanical stimulus influencing the adaptation process and π denotes the threshold value of the mechanical stimulus.

2.2.3 Bone remodelling approach by Beaupré and co-workers

Beaupré et al. (1990) proposed a remodelling approach based on a proposed idea that adaptability of the bone due to external stimulus depends on systemic influence and site-specific biochemical influence of neighbouring bone tissues. They extended the 'bone-maintenance theory' by Carter et al. (1989) that considers the influence of 'effective stress' to a temporal adaptive theory (Garijo et al.,2014). Iterative computer-simulation procedures, in combination with the FE analysis, were described to predict adaptive bone remodelling around prostheses (Huiskes et al. 1987; van Rietbergen et al. 1993). Nevertheless, these theories were based on an assumption that bone is an isotropic material.

2.2.4 Modifications and applications of primary bone remodelling approaches

Resorption of host bone due to implantation (Huiskes et al.,1987; Cilla et al., 2017) of prosthesis is a major setback in the development of joint arthroplasty across the globe. Once bone fracture occurs, techniques like gypsum casts and implants are used to stabilize the fracture. However, metallic implants are very effective in stabilizing osteoporotic and transverse fractures requiring more support and compression which cannot be provided by gypsum casts. But, metallic implants lead to associated undesirable stress shielding (Cilla et al., 2017; Ansari et al., 2017) causing bone loss. The changed mechanical environment is considered to trigger an adaptative response in the bone, causing the bone structure and density to cater to its mechanical needs (Huiskes et al.,1987). Such a remodelling phenomenon occurs due to a response to underload at bone tissue. Figure 2.8a shows the stress-shielding phenomenon due to underload at the bone surface. However, overload induced high stresses (Li et al., 2007; Behrens et al., 2009; Bouguecha et al., 2011) at the bone-implant interface has also been found responsible for bone resorption. Figure 2.8b shows the remodelling zones in between the growth zone separated by critical resorption stress curves.

Li et al. (2007) modified the remodelling approach by Huiskes et al. (1987) to include a quadratic term to the generalized equation of bone adaptation to incorporate the overload induced bone resorption. Behrens et al. (2009) had also made slight modification to the Huiskes model (Huiskes et al., 1987) to include the bone loss due to high stresses. The proposed model assumed that rate of bone apposition must not exceed the maximum value of bone loss rate and thus bone necrosis occurred due to severe overload at the bone-implant interface (Behrens et al., 2009).

Andreaus et al. (2009) proposed shear strains at the bone-stem interface as a precursor of micromotion and changes in strain energy density with respect to physiological state as indicators of atrophy and hypertrophy of bone tissue. Giorgio et al. (2019) proposed a model to describe the diffusive nature of mechanically driven biological stimulus responsible for bone remodelling.

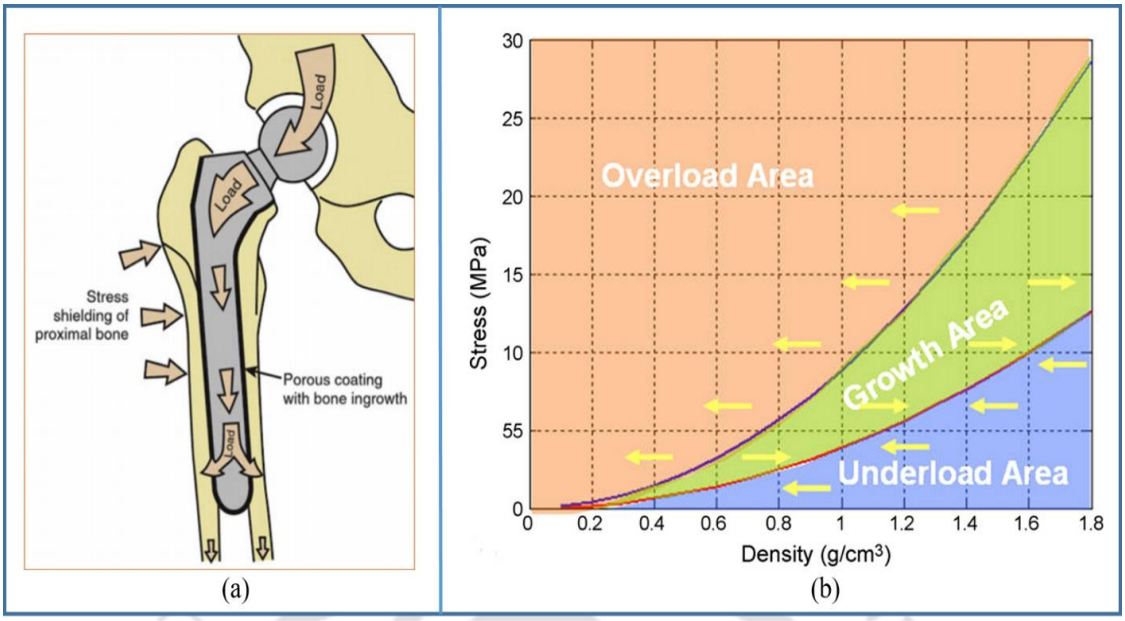

Figure 2.8 (a) Pictorial representation to stress-shielding phenomenon in the proximal femur due to the implanted prosthesis (Ansari et al., 2017). (b) Bone remodelling zones (overload and underload induced) in between the growth zone separated by critical resorption stress curves (Li et al., 2007).

2.2.5 Some problem specific bone remodelling approaches

Trabecular bone is heterogeneous as well as anisotropic. Using anisotropic strain data reported by Carter (1978), Beaupré et al. (1990) defined a daily tissue level stress stimulus as the equilibrium state for a time dependent remodelling theory. The fabric tensor, a symmetric and positive definite second order tensor (Cowin,1986; Doblaré and García,2002) that describes the principal values and directions of bone mass distribution, is used by Cowin (1986) to characterise bone anisotropy. An anisotropic model was developed by Jacobs et al. (1997) based on density adaptation and anisotropy reorientation, considering the principal stresses as the mechanical stimulus. Damage-based theoretical models have also proved to be capable of successfully predicting some aspects of bone remodelling (Prendergast and Taylor, 1994; Prendergast and Huiskes, 1995). Doblaré and García (2002) proposed an anisotropic bone remodelling theory based on damage repair theory, where microdamage in the bone surface was considered to be the remodelling stimulus. Moreover, combined strain and microdamage has also been proposed as remodelling stimulus (McNamara and Prendergast, 2007). Several studies have investigated structural topology optimization for bone remodelling simulation (Hollister et al., 1994; Fernandes et al., 1999; Bagge, 2000; Jang and Kim, 2008; Jang et al., 2009).

Geraldes and Phillips (2014) proposed a 3-D orthotropic adaptation model and further implemented on an FE model of femur, wherein bone was modelled as optimised strain-driven continuum with local orthotropic symmetry (Geraldes and Phillips, 2014). Andreaus et al. (2012) developed an optimal control procedure combined with FE analysis for functional adaptation of the bone tissue subjected to a mechanical stimulus where two conflicting objectives of structural efficiency i.e. minimum bone mass with maximum stiffness were used.

Giorgio et al. (2016) addressed the problem of bone interaction with grafts of bioresorbable materials by formulating a poro-viscoelastic model of the bone tissue and the material while proposing a linear combination of deformation energy and viscous dissipation to simulate the mechanical stimulus for bone remodelling. Very recently, Mathai et al. (2021) has developed an orthotropic bone remodelling approach for the assessment of peri-prosthetic adaptation of an uncemented implanted femur bone and thus compared with the already existing isotropic bone remodelling algorithm (Huiskes et al., 1987; Weinans et al., 1992) and reported that no significant difference in the quantative prediction of bone resorption was observed in the proximal femur while using both the adaptive models.

2.2.6 Internal bone remodelling and external bone remodelling approaches

To date, most of the bone-remodelling approaches are developed for internal adaptation and a very few models cater to the external adaptation (Huiskes et al., 1987; Huiskes et al., 2000; Chen et al., 2007) of bone surfaces. Lack of studies driven in the field of external remodelling approaches might be attributed to its delayed occurrence (Goda et al.,2016) as compared to internal adaptation of bone. Studies on design on artificial bone grafts primarily rely on the external surfaces of the bone and thus external adaptation becomes a necessity to address such problems. Nonetheless, both internal and external bone remodelling is important to get a comprehensive overview of the remodelling process due to mechanical perturbations at the bone tissue. In addition, since the time, the theory of SED based bone remodelling approach (Huiskes et al., 1987; Ghosh et al.,2013; Mondal and Ghosh,2019; Ghaziani et al.,2021) came into existence, there has been very little development in the remodelling approaches. However, most of the models developed since then are mostly need based subtle modifications (van Rietbergen et al. 1993; Li et al., 2007; Lin et al.,2009; Ghosh et al.,2013; Cheong et al., 2018;

Moghaddam et al.,2018; Calvo-Echenique et al.,2019; Kung et al.,2020) of the existing formulation of Huiskes and coworkers (Huiskes et al., 1987; Weinans et al., 1992) and the Stanford model (Beaupré et al.,1990; Garijo et al.,2014; Saeidi et al.,2020) of bone adaptation.

2.3 Design optimization of orthopaedic implants

The stability (primary and secondary) at the bone-implant interface in a joint arthroplasty relies on magnitude and orientation of applied loads under daily activities (Mukherjee and Gupta, 2016), material properties of the implant as well as on the shape (or geometry) of the implant (Huiskes and Boeklagen, 1988; Huiskes and Boeklagen, 1989). The choice of a proper design philosophy towards improvement in implant design seems to be an arduous task than it seems. Earlier manipulations in design of implants by the industry had sometimes created a massive resentment among the medical community due to the failure of the implants resulting from erroneous design changes. Design modifications done without systematic evaluations in Capital Hip prosthesis marketed by 3M Health Care Ltd. in the early 1990s was taken off from the market due to high failure rates registered (Pandit et al.,2000).

Finite Element Method (FEM) has been extensively used towards improvement of the shape (or geometry) of the prosthesis to enhance the primary or secondary stability of the prosthesis (Huiskes and Boeklagen, 1989; Mukherjee and Gupta, 2017a). Such improvements in designs of implants are primarily based on systematic parametric alterations which is not only computationally expensive but also a cumbersome process owing to the large number of design variables that need to be incorporated in a prosthesis (Huiskes and Boeklagen, 1989). All these factors have prompted the scientific community to invoke for shape optimization techniques on orthopaedic implants.

2.3.1 Design optimization studies with single objective function

In a landmark study on shape optimization of a cemented hip implant, Huiskes and Boeklagen (1989) implemented a numerical shape optimization (NSO) procedure to minimize the peak stresses at the cement layer as well as bone-cement interface (Huiskes and Boeklagen, 1989). This investigation employed the NSO technique to minimize strain energy density (SED) distribution of the cemented interface considered under varied loading conditions. Using the values of the objective

function, the geometric parameters were manually adjusted during the iterative phase. Biomet®, an improved design of cemented femoral prosthesis, was commercialised as a result of this investigation. Regardless of how primitive the model was, it was the preliminary step toward optimally-designed orthopaedic implants which provided significant insights for future research. Yoon et al. (1989) have also implemented a gradient projection technique to optimize the shape of the cemented hip stem by minimizing stress concentration in the cemented layer. However, the stresses acting on the bone and the prosthesis were kept within permissible limits, and the geometric constraints of the stem were considered commercially and physiologically feasible (Yoon et al., 1989). Perforated reinforcing shells are funicular metallic shells attached to the inner surface of the proximal femoral cortex in total hip arthroplasty (THA) to support its structure and conceal any defects so as to reduce the complications of revision surgery. Beus et al. (1990) used a non-linear programming (NLP) technique to optimize the shape (or geometry) of perforated reinforcing shells on cemented hip stems by minimizing an objective function that penalized stress concentration so as to achieve a smooth transfer of physiological loads between the components. It is however noted that, the NLP methods could not guarantee a globally optimized solution in many real-life problems without the use of certain specific mathematical constraints (Beus et al., 1990). These investigations on shape optimization of cemented prosthesis were focussed primarily on reducing interfacial stresses at the bone-implant interface and thereby neglected the phenomenon of bone adaptation under physiological loading conditions.

Kuiper and Huiskes (1992) used an optimization scheme to achieve an optimal stiffness characteristic of an uncemented hip prosthesis by minimizing the probability of failure at the interface while keeping the amount of bone resorbed under defined permissible limits. To reduce the computational time, underload induced bone resorption was employed in the optimization scheme (Kuiper and Huiskes, 1992) without implementing the total bone remodelling algorithm developed earlier (Huiskes et al., 1987; Weinans et al., 1992). This was perhaps the earliest ever study on shape optimization for uncemented orthopaedic implants. In a further investigation on hip prosthesis, Evans and Gregson (1994) numerically implemented an optimization method to improve the design of a coated uncemented

hip prosthesis by minimizing the stress-shielding across the bone-implant interface. By keeping the stresses at the bone-implant interface within permissible limits, stress-shielding was minimized to a considerable extent compared to the initial design (Evans and Gregson, 1994). Hedia et al. (1996) had proposed another method of shape optimization of cemented hip stem with the objective of maximizing the fatigue life of the bone cement while minimizing the fatigue notch factor (Hedia et al., 1996) in the cemented layer. In their 2D study (Hedia et al., 1996), the CPU time for computation was found to be much lesser compared to that of an earlier study (Yoon et al., 1989) due to the use of fatigue notch factor in the objective function as well as in the constraints instead of stress or stress concentration factor. In an another study (Hedia et al., 1996) on Charnley hip stem, NSO was again implemented to achieve an optimized shape of the implant based on minimizing the fatigue notch factor. In a further study by Hedia et al. (2000) on cemented acetabular component, NSO methodology was implemented to optimize the design of a metal backing shell by minimizing the fatigue notch factor in the cement layer at the cement-bone and cement-backing shell interfaces while maximizing the fatigue notch factor in the acetabulum center so as to prevent stress-shielding. Chang et al. (1999) implemented a "robust optimization" scheme for optimizing the shape and geometry of hip prosthesis incorporating various environmental variables such as different loading conditions and properties of bone. The goal of their study was to minimize an objective function dependent on structural response and distribution of environmental variables by using an efficient analytical, statistical predictor (Chang et al. 1999). However, all these studies did not take into account the 3D shape and properties of bone and the prosthesis along with spatial load distribution (Huiskes and Boeklagen, 1989; Evans and Gregson, 1994).

To incorporate the versatility of the spatial optimization, the investigation by Katoozian and Davy (2000) implemented a numerical method for a 3D shape optimization of both cemented and uncemented femoral components in a THA. For defining component geometry in terms of longitudinal and cross-sectional shape variables, a parametric framework was developed. A 3-D FE analysis and a numerical optimization technique were combined with the 3-D design model. The influences of two distinct musculoskeletal loading conditions and a variety of objective functions such as minimization of SED, minimization of von Mises stress,

and minimization of maximum shear stress were investigated separately. The loading condition, rather than the objective function used, was found to have a greater influence on the outcome. Chang et al. (2001) has further extended their earlier study (Chang et al. 1999) of "robust optimization" formulation by including relevant constraint equations and a 3D non-linear FE model. Minimization of the difference in SED of the intact and implanted femur was conducted in the study employing a reduced midstem implant design. The bone remodelling signal predicted in this study (Chang et al. 2001) corroborated well with the results predicted using 1D beam on elastic foundation (BOEF) model used in their previous investigation (Chang et al. 1999). The study presented by Kowalczyk (2001) looked at the post-operative short-term failure possibilities related with uncemented femoral stems. The post-operative variables that led to insufficient osseointegration into the porous-coated implant surface, resulting in the formation of permanent gap encapsulate with loose fibrous tissue, were evaluated in the study (Kowalczyk, 2001). In this study, the etiology was assumed to be either an inadequate initial fit of the implant into the medullary cavity or excessive micromotions at the bone-implant interface. As a result, the study was conducted with the intention of minimizing micromotions between the internal surface of the bone and the porous-coated section of the implant surface. For the investigation, a gradient-based optimization technique (Kowalczyk, 2001) was used. Petrie and Williams (2002) performed a shape optimization of dental implant using a subproblem approximation method by minimizing average von Mises strain at most superior and most inferior location of the peri-implant cortical bone. Nicolella et al. (2006) implemented a shape optimization method to minimize the square of von Mises stress in the cement layer in a cemented femur-implant system. The accumulation of polyethylene wear debris is one of the leading cause of aseptic loosening of femoral prosthesis. The wear debris can lead to osteolysis and degradation of host bone (Matsoukas and Kim,2009).

A study by Matsoukas and Kim (2009) implemented an optimization scheme to hunt for optimal design parameters of prosthesis to minimize the volumetric wear at the articulating surface of the femoral head and the polymeric liner of an uncemented femoral stem. A similar study (Willing and Kim, 2009) of shape

optimization while perturbing the design parameters of prosthesis to minimize wear reduction was performed on a total knee arthroplasty (TKA).

Nobari et al. (2010) hunted for an optimized femoral plate using a remodelling algorithm developed earlier (Huiskes et al., 1987; Weinans et al., 1992). The primary goal of the optimization problem (Nobari et al.,2010) was to minimize the sum of local differences between the actual and normal reference values of SED. Willing and Kim (2011) implemented their early method (Willing and Kim, 2009) of optimization to achieve an optimized shape of components of TKA by minimizing a kinematic objective function formulated to improve constraint and flexion kinematics. This was perhaps the first of the kind of investigations which have used a rigorous design optimization scheme to achieve optimal shapes of TKA components involving kinematics.

Machine learning techniques (MLTs) have been used extensively used in medical analysis to improve efficiency of radio-diagnosis, disease prognosis based on relevant symptoms etc. with reduction in overhead expenses (Cilla et al.,2017; Chanda et al., 2016a). A single objective based shape optimization of short-stem hip implant was studied by Cilla et al. (2017) using artificial neural networks (ANNs) and support vector machines (SVM). Once the MLTs were developed, a numerical pattern-search minimization model was implemented to obtain the optimal shapes of the implant. The optimization algorithm minimizes a loss function (Cilla et al.,2017) which is defined as the average difference of maximal absolute principal strain between the intact and the implanted models. Roy et al. (2018) implemented a hybrid model of NN and a defined desirability function as the objective function for the shape optimization of a patient specific dental implant using genetic algorithm (GA). The optimized shape as obtained from the hybrid NN-GA modelling was further validated by FE models. Based on the fact that proper amount of micro-strain (Roy et al.,2018) at the bone-implant interface is responsible for better bone remodelling, the goal of the optimization model thus was to achieve a desired value of micro-strain at the bone-implant interface. GA has been extensively used in optimization of such problems with large number of parameters or a need for detailed solution is sought (Ishida et al.,2011; Chanda et al.,2015). Very recently, a similar study (Chatterjee et al.,2019) on combined NN-desirability function-GA

methodology was implemented to study shape optimization of femoral implant by minimizing the strain deviation between the intact and implanted prosthesis.

2.3.2 Design optimization studies with multi-objective function

So far, all of the shape optimization models discussed have been formulated considering a single-objective function. However, it was clear that the evaluation of implant design must take into consideration more than one failure criterion. As a result, multi-criteria optimization models appeared to be a more effective design method to address such problems.

Fernandes et al. (2004) presented a 2-D FE model for shape optimization of uncemented femoral stems by minimizing relative displacement and stress on the bone-implant interface under routine activities. This was perhaps the first ever multi-objective shape optimization study on orthopaedic implants in general, and hip prosthesis in particular. The optimization scheme employed a steepest-descent method to search for the desired shape of the implant.

Ruben et al. (2012) formulated a 3-D shape optimization technique to design implants with greater initial stability and reduced proximal bone resorption in a more sophisticated investigation on shape optimization of uncemented stems. The proposed method employed a multi-criteria framework to minimize three important parameters for uncemented prosthesis viz. relative tangential displacement, contact stress, and proximal bone loss. However, shape of the optimized hip stems, thus obtained, were found to be contradictory due to contradiction in different criteria. Nonetheless, when compared to the initial prosthesis geometry, the trade-off designs were found to predict improved performance.

Geramizadeh et al. (2018) implemented a response surface methodology (RSM) to obtain an optimal value of thread depth and pitch of a dental implant by minimizing maximum von Mises stress and maximum von Mises strain so as to determine optimal stress distribution pattern around the implant. In their study, von Mises strain was used as a measure of deviatoric strain component in the material without accounting for the hydrostatic strain component. This investigation indicated that threaded or textured morphologies (Geramizadeh et al.,2018; Mukherjee and Gupta,2017) on implant surface have a significance influence on the local stress/strain values around them.

Very recently in a similar study by Elleuch et al. (2021), multi-objective shape optimization of dental implants was performed so as to enhance the primary stability of the bone-implant system. Multiple implant geometrical parameters were taken as the input design variables and von Mises stresses around the prosthesis as the output. Following the approach of RSM, response surfaces were generated after FE simulations. Desirability function method was formulated to solve this optimization problem (Elleuch et al.,2021) by maximizing the overall desirability in a formulated desirability function that combined desirability of cortical bone, cancellous bone, implant and the abutment. Among all the input design variables, diameter of the implant was found to influence significantly on the interfacial stress around the prosthesis.

Ishida et al. (2011) were the first to apply GA to solve a shape optimization problem for a cemented implant. The peak maximum principal stress of the cement layer at proximal and distal hip stem were considered as two independent objective functions to be minimized in the multi-objective formulation. Further, walking and stair-climbing load cases were also considered in the problem formulation making it an optimization problem with four objective functions. The neighbourhood cultivation genetic algorithm (NCGA), developed by Watanabe et al. (2002), was introduced to solve the multi-objective optimization. The designs of the implants so obtained might not be the "best" one but of course were improved versions of the existing initial designs taken in the study. However, their study incorporated a primitive version of the prosthesis with isotropic material properties of bone only to showcase the efficacy of using GA to address such multi-objective optimization problems.

Further incremental development in the area was performed by utilising GA in uncemented hip stem (Chanda et al.,2015; Chanda et al.,2016a; Chanda et al.,2016b), cemented hip stem (Corso et al.,2016), uncemented acetabular component (Ghosh et al.,2016), high tibial osteotomy plates (Koh et al.,2019) and dental implants (Cheng et al.,2019).

Chanda et al. (2015) effectively utilised nondominated sorting genetic algorithm-II (NSGA-II) optimization module (Deb et al.,2002) in performing shape optimization of uncemented femoral stem. Their study was arguably the first of its

kind, where GA has been employed to study a multi-objective optimization problem for uncemented implants. Minimization of interface stress and implant induced bone-resorption were taken as objective functions for the optimization study. They further employed a NN to predict the primary stability of the implant through a defined parameter referred to as "Index of Instability (IoI)" and further minimizes IoI using GA to achieve optimal implant shapes (Chanda et al.,2016a). Multi-objective formulation using NN-NSGA-II was thereafter implemented to study the influence of interface conditions on shape optimization of uncemented femoral implants. The study (Chanda et al.,2016b) introduced two other objective functions, one based on proximal resorbed bone mass fraction (BMF) and another one total bone-implant interface area, along with IoI to incorporate into the optimization module.

Unlike earlier investigation (Ishida et al.,2011) that looked for minimization of the maximum principal stresses at defined locations in a cemented prosthesis, Corso et al. (2016) employed bone-remodelling algorithm to minimize stem induced bone resorption while utilising GA as the optimization module. However, a few studies were performed considering a bonded interface between the bone and the implant (Chanda et al.,2015; Corso et al.,2016), while a few others implemented contact simulations at the interface (Chanda et al.,2016a; Chanda et al.,2016b; Ghosh et al.,2016; Koh et al.,2019; Cheng et al.,2019) considering the fuzzy nature of the interface. Ghosh et al. (2016) implemented NSGA-II module to study shape optimization of uncemented acetabular component with the goal of minimizing implant induced bone loss as well as volumetric wear.

A study by Koh et al. (2019) implemented the well-known NSGA-II technique to optimize the shape of high tibial osteotomy (HTO) plates by minimizing von Mises stress on the plates as well as obtaining the required level of bone-implant micromotions at two different load-bearing locations. A sensitivity analysis based on a design of experiment (DoE) was used to sort out the most significant design factors and later on GA was implemented to achieve optimal shapes of the tibial plates (Koh et al.,2019).

Very recently, a study (Cheng et al.,2019) to minimize the micromotion between the implant and the bone was used as an objective function to study the

optimal shape of dental implant. A novel hybrid optimization model using a DoE technique to study the influence of geometric design parameters on bone-implant micromotion, followed by a Kriging interpolation method (Matheron, 1973) and genetic algorithm (KIGA) in tandem to optimize the shape of one-piece dental prosthesis.

2.4 Summary of the literature review- gaps and unaddressed issues

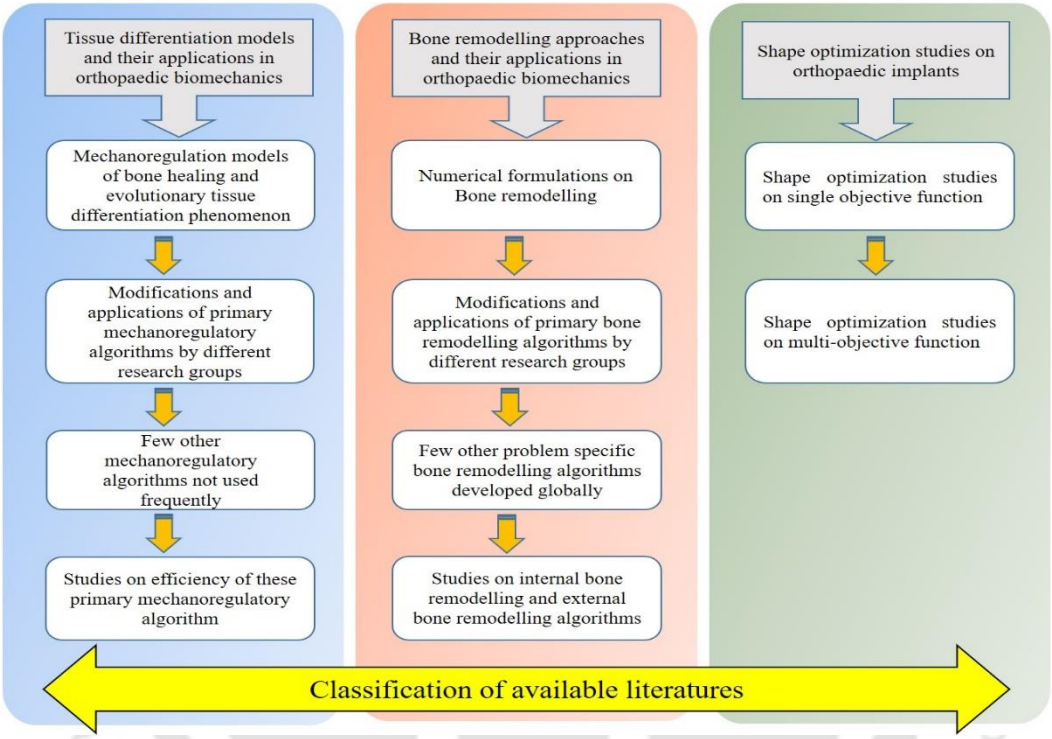

Figure 2.9 A flowchart to highlight the classification of available literature

The extensive literature review as classified above (Fig. 2.9) can be summarized as follows:

- Different mechanoregulation models were developed either to address the phenomenon of fracture healing or to predict formation of different connective tissues with particular emphasis on bone growth at the bone-implant interface.
- Surface roughness on implant surfaces, which includes both micro- and macro-textures, has been shown to affect biologic attachment by altering the local mechanical environment at the bone-implant interface or by mechanical interlocking between the bone and the rough ridges of the implant surface. The impact of micro-textures on bone development and osseointegration has been extensively studied (Liu and Neibur, 2008; Chou

and Müftü, 2013; Mukherjee and Gupta, 2016; Mathai and Gupta, 2022).

- Lower press-fit may result in implant loosening and, as a result, inadequate primary fixation. Increased press-fit fixation, on the other hand, may provide higher compressive stresses (contact forces) at the bone-implant interface, allowing for additional frictional movement.
- The non-primitive nature of most design features of implants, together with a variety of important design considerations, might result in complex non-linear correlations with ossification levels. NNs have previously been used to evaluate biomechanical design on a variety of prostheses (Kayri 2016; Chanda et al., 2016a; Cilla et al. 2017; Roy et al. 2018; Chatterjee et al. 2019).
- Despite the fact that several shape optimization approaches and ideal implant designs have been developed, the focus of these studies has been on primary stability and bone adaptation (Huiskes and Boeklagen, 1989; Kuiper and Huiskes, 1992; Yoon et al., 1989; Fernandes et al., 2004; Chanda et al., 2015; Cilla et al., 2017).

Based on the exhaustive literature review in the broad area of mechanoregulation models of tissue differentiation and bone remodelling with particular emphasis on their applications in FE based biomechanical problems of fracture healing, bone growth and design optimization of orthopaedic implants, some of the important issues in this area which have not been addressed are as follows:

- Macro-textures were regarded to be primarily beneficial for providing primary stability between the implant surface and the bone. Previously, it was assumed that the dimensions of such macro-textures (in the order of millimeters) were too large for cells to sense in order to promote bone development. Due to this, there have been very few works that have examined the impact of such macro-textures on bone development.
- Mechanoregulation models were extensively used to predict bone growth at bone-implant interface at micro-scale (in the order of microns). But very few works have been done to predict bone growth at bone-implant interface at macro-scale (in the order of millimeters).

- The contact forces at the bone-implant interface could cause abrasion and irreversible micro bone damage resulting in gaps between the bone and the implant despite meticulous operating techniques (Huiskes and Boeklagen, 1988; Viceconti et al., 2001). These gaps might open and close sequentially due to mobility caused by daily routine activities. Such mobility at the bone-implant interface towards the direction of bone might influence bone growth at the interface. However, there have been no such studies performed to predict influence of this radial mobility on bone growth.
- Although NNs have been used to predict primary implant stability, no research has been performed to create such NN frameworks to assess secondary implant stability by predicting bone growth at the bone-implant interface depending upon the surface topological parameters.
- Shape optimization studies of textured geometry were undertaken on dental implants (Geramizadeh et al., 2018; Elleuch et al., 2021), but none has been performed on micro or macrotextured surfaces of other implants or surrogate implant models.
- Different types of objective functions were studied in performing design optimization of orthopaedic implants. However, there is a dearth of studies that included bone growth as an optimization function. Therefore, there is a need of such an investigation that incorporate qualitative assessment of bone growth as an optimization function to pre-clinically search for trade-off implant design features.
- Although influence of textured geometry on bone growth was evaluated on dental implants, the comparative assessments of textured and non-textured implant geometries on bone growth were never been investigated.

2.5 Objectives of the present work

In view of this, the specific objectives of the present study have been laid down as under:

1. Influence of macro-textured implant surface on bone growth.
    - Influence of multiple textures over implant surface on bone growth under constant bone-implant micromotion using a

mechanoregulation based tissue-differentiation algorithm.

- Use of the tissue differentiation algorithm to assess the influence of different magnitudes of intermittent micromotion on bone growth over macro-textured surfaces.

2. Influence of interface gaps and texture density on bone growth
    - Influence of opening/closing of interface gap on bone growth over distinct macro-textured implant surfaces.
    - Influence of texture density on bone growth over macro-textured implant surface.
    - Combined influence of sliding and gap distances towards bone growth over macro-textured implant surfaces.
3. Artificial neural network (ANN) based prediction of bone growth over textured implant surfaces with change in surface design parameters.
    - To assess possible relationship between macro-texture design parameters and bone growth.
    - To formulate predictive models based on NN to establish relationship between macro-textured design parameters and amount of bone growth.
4. Predictions of bone growth over optimally designed macro-textured implant surfaces using neural network (NN) and genetic algorithm (GA)
    - To select significant design parameters and corresponding geometric constraints for the chosen macro-textured surfaces.
    - To develop set of FE models and thereafter predicting bone growth for each of the textured surface to use them to train NNs.
    - To develop NN schemes for each of the textured surfaces in order to predict bone growth for unlabeled datasets of implant surfaces with similar surface morphology.
    - To implement GA to search for optimal designs for the surface morphologies over a set of tested data.

5. Qualitative assessment of growth of connective tissues on femoral stem with macro-textures

    - To develop FE models of implanted patient-specific femur using a CT-scan dataset.
    - A comparative study to assess the influence of textured and non-textured femoral stems on tissue growth under normal walking.
    - Study the influence of distinct daily activities viz. normal walking and stair climbing on bone growth over textured femoral stems.

CHAPTER 3

Methodology

This chapter explains the methodology implemented in the present work to assess the bone growth at the bone-implant interface. Thereafter, the methodology implemented for design optimization of implant macro-texture is also explained in detail.

3.1 Introduction

This chapter presents the general methodology implemented to carry out the present work on qualitative assessment of bone growth at macroscale bone-implant interface. In addition, numerical methodology implemented to study design optimization of implant macro-textures is also explained in detail. The present work combined the computational scheme developed earlier by Lacroix and Prendargast (2002a) to predict tissue differentiation on a fracture healing with the mechanoregulation based tissue differentiation model by Claes and Heigele (1999). Furthermore, optimal designs for chosen macro-textures were developed by combining FE, backpropagation neural networks (BPNNs) and GA. Hence, the current chapter is divided into three major sections. First section elucidates the computational algorithm used in the present study. Then, a diffusion model used in the computational scheme and the tissue-differentiation model used thereafter is explained. Finally, methodology of formation of NNs and GA is mentioned in brief.

3.2 Computational framework to assess bone growth

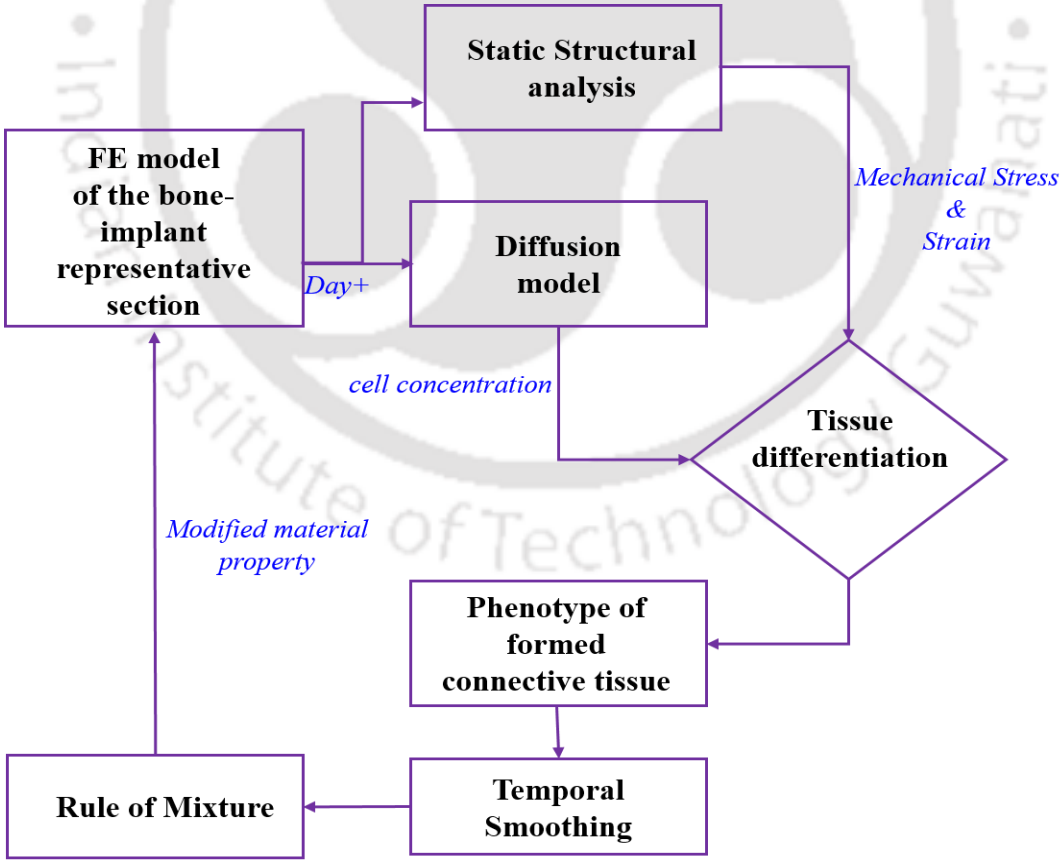

Figure 3.1 Schematic view of the computational framework used to assess bone formation at macro-scale bone-implant interface

This methodology assumed equal probability of formation of bone, cartilage and fibrous matrix depending upon the mechanical stimuli. The iterative implementation of the algorithm was performed over a thin domain of granulation tissue between the bone and the implant. The computational steps to study bone growth in the present study are as follows:

- Step 1: Develop FE models of bone-implant-interface representative models

FE models of bone-implant-interface models with few macro-textures on implant surface have been developed in ANSYS FE software (ver 14.5 ANSYS Inc., Canonsburg, PA, USA). Uniform meshing has been adopted in the present study to eliminate discretization error.

SOLID185 is used for three-dimensional modelling of solid structures. It is made up of eight nodes, each of which has three degrees of freedom at each node: translation in the nodal X, Y, and Z axes. SOLID185 comes in two different types viz. homogeneous and layered structural solids. For modelling of homogeneous isotropic materials assumed in the sectional studies of bone-implant-interface geometries, homogeneous structural solid element has been used primarily. Figure 3.2 represents the homogeneous structural solid FE geometry.

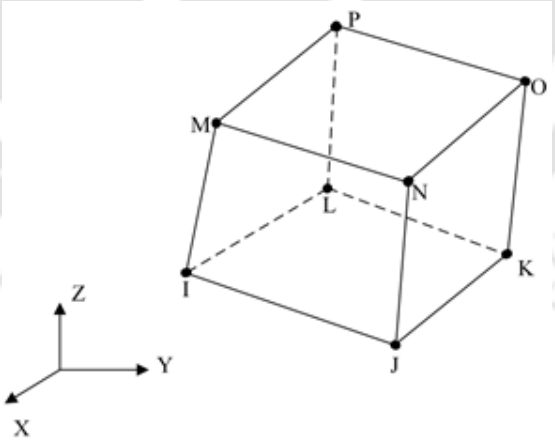

Figure 3.2 Homogeneous structural solid 8-noded hexahedral finite element (FE) geometry (https://tinyurl.com/rajdeep-phd-8)

However, SOLID187 is used to model finite element structures in full-scale bone-implant-interface model due to higher geometric complexity in the model. SOLID187 is a higher order three dimensional ten noded element (Fig. 3.3) with three degrees of freedom at each node.

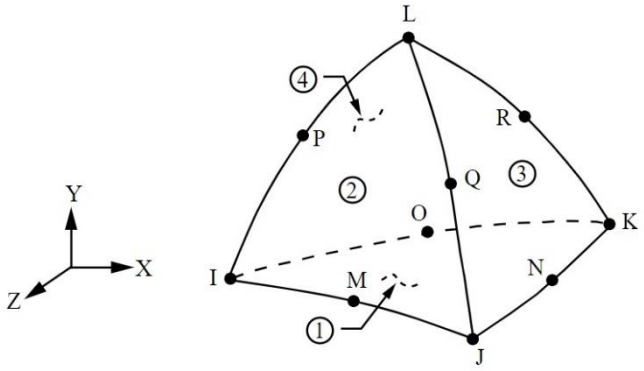

Figure 3.3 Homogeneous structural solid 10-noded tetrahedral finite element (FE) geometry (https://tinyurl.com/rajdeep-phd-9)

- Step 2: Apply suitable loading and boundary conditions

Suitable structural loads and boundary conditions have been applied to catch the mechanical stress-strain history at the granulation tissue. Small intermittent micromotion has been provided to simulate the relative displacement between the bone and the implant. However, musculoskeletal loading conditions have been applied to full-scale bone-implant-interface model considering different routine activities viz. normal walking and stair climbing.

Diffusion equation has been run parallel to the structural analysis under thermal analogy. The detailed explanation of diffusion model in thermal analogy has been presented in section 3.2.1. Diffusion equation mimic the migration of MSC from bone interface towards the implant interface. Concentration of MSCs has been assumed to be maximum towards the bone-granulation tissue interface and zero at the tissue-implant interface. Thermal solid elements viz. SOLID70 (8-noded hexahedral thermal element for the representative bone-implant-interface models) and SOLID87 (10-noded tetrahedral thermal element for the full-scale model) have been considered to discretize the geometric domain under consideration.

- Step 3: Run structural and diffusion analysis.

Structural FE analysis has been run under static loading to catch local hydrostatic pressure and deviatoric strain. In addition, diffusion analysis provides element specific concentration of MSC at iterative time-frame.

⊙ Step 4: Implement tissue-differentiation algorithm

Tissue-differentiation algorithm (Claes and Heigele, 1999) has been developed in MATLAB (Matlab 2017a, The MathWorks Inc., Natick, MA, USA) that runs on a logical model to assess different connective tissue phenotypes depending upon the combination of magnitude of hydrostatic and deviatoric terms as obtained after structural FE analysis. Hydrostatic pressure ($\sigma_{average}$) can be calculated as:

$$\sigma_{average} = \frac{\sigma_1 + \sigma_2 + \sigma_3}{3} \tag{3.1}$$

where $(\sigma_1, \sigma_2, \sigma_3)$ are 3 principal stresses. Whereas, deviatoric strain ($\varepsilon_{deviatoric}$) can be computed as:

$$\varepsilon_{deviatoric} = \frac{1}{1+\nu}\sqrt{\frac{(\varepsilon_1 - \varepsilon_2)^2 + (\varepsilon_2 - \varepsilon_3)^2 + (\varepsilon_3 - \varepsilon_1)^2}{2}} \tag{3.2}$$

where $(\varepsilon_1, \varepsilon_2, \varepsilon_3)$ are 3 principal strains and ν is the effective Poisson's ratio. The tissue differentiation model implemented in the present study has been mentioned in brief in section 3.2.2.

⊙ Step 5: Use temporal smoothing to minimize numerical instability

A smoothing technique has been implemented that minimizes numerical instability caused due to sudden changes in material properties in each finite element at the granulation tissue. For example: It is practically infeasible for the MSCs to differentiate and develop as bone after 1st day of surgery. So, the smoothing technique ensures a smooth transition of tissue-differentiation by averaging local material properties over "*n*" previously estimated material properties over "*n*" iterations as in Eqn. 3.1. In the present model, each iteration has been considered as a single post-operative day. However, it should be noted that there has been no direct relation of such iterative time-steps with the real-time. These computational time-steps can be thought of as in proportion to physical time.

$$(\text{Material property})_{n+1,smoothed} = \frac{1}{n}\sum_{iteration=n}^{n-9}(\text{Material property})_{iteration} \tag{3.3}$$

- Step 6: Implementation of Rule of Mixture to incorporate biological phenomenon

  In a physically realizable geometric domain, there would be a probability of simultaneous presence of granulation tissue as well as the predicted tissue phenotype in a single finite element. However, mechanoregulation based tissue-differentiation scheme fails to implement such a realistic picture in a finite element. In order to address this issue, a rule of mixture is implemented combining element specific cell concentration obtained during diffusion analysis and the material properties so predicted by tissue differentiation algorithm in the form of a mathematical equation as:

$$(\text{Material property})_{n+1} = \left(\frac{c_{\max} - c_{tissue}}{c_{\max}} \right)\Bigg|_n (\text{Material property})_{granulation} + \left(\frac{c_{tissue}}{c_{\max}} \right)\Bigg|_n (\text{Material property})_{tissue} \quad (3.4)$$

- Step 7: The material property of each finite element in the granulation tissue is updated and assigned with the final material property so obtained after the end of numerical procedures until step 6.

  This ends one single iteration of the computational scheme. Iterations are continued over next cycle of loading and boundary conditions till the end of simulation time frame.

3.2.1 Implementation of cell migration through diffusion model

Mathematicians are well aware that heat flow and diffusion are essentially the same phenomena. However, the change in notations required to describe both the phenomena is discussed in details for a diffusion equation used widely in this dissertation to describe the dispersal of MSC throughout the region of granulation tissue.

Diffusion of mass (MSCs) across a region in a particular direction is based upon Fick's Law of diffusion as described below:

$$k\nabla^2 c = \frac{dc}{dt} \quad (3.5)$$

$$\Pi_c = -k\frac{\partial c}{\partial \Omega} \quad (3.6)$$

where k = diffusion coefficient, c = concentration of undifferentiated MSCs, Π_c = rate of transfer of cells in direction Ω.

Corresponding heat flow equation is based upon Fourier Law of Conduction as described below:

$$\left(\frac{\mho}{\rho\psi}\right)\nabla^2\theta = \frac{d\theta}{dt} \tag{3.7}$$

$$\Pi_\theta = -\mho\frac{\partial\theta}{\partial\Omega} \tag{3.8}$$

where $\mho$ = thermal conductivity, ρ = density of the material through which heat flows, Ψ = specific heat of the material, $\rho\Psi$ = heat capacity of the material, θ = temperature, Π_θ = rate of transfer of heat in direction Ω.

Finding correlation between concentration, c with temperature, θ in all the above equations and comparing both the equations (3.5) and (3.7),

$$k \equiv \frac{\mho}{\rho\psi} \tag{3.9}$$

Similarly, comparing both the equations (3.6) and (3.8),

$$\Pi_c \equiv \Pi_\theta \tag{3.10}$$

From Equation (3.8),

$$k \equiv \mho \tag{3.11}$$

Now comparing both the equations (3.9) and (3.11),

$$\rho\psi = 1 \tag{3.12}$$

In thermal diffusion, heat conduction takes place and not temperature. In physical significance, $\rho\Psi$ being the heat capacity of the material is an important factor in heat equation that is responsible to convert temperature, θ into the amount of heat per unit volume. However, this factor has no significance in mass diffusion since in mass

diffusion, the term "concentration, c" represents diffusion of mass per unit volume and hence, $\rho\Psi$ becomes unity (1.0).

3.2.2 Mechanoregulation based model to predict tissue phenotype

Mechanoregulation based tissue differentiation algorithm is formulated considering hydrostatic stress and deviatoric strain as the mechanical signals responsible for changing cell type and morphology. Deviatoric strain less than 5% and hydrostatic pressure between ±0.15 MPa promotes development of mature bone (Claes and Heigele 1999). Whereas deviatoric strains less than ±15% and dilatational stress less than 0.15 MPa promotes immature bone with endochondral ossification. Cartilage is formed either when strain is more than 15% with stress magnitude less than -0.15 MPa or compressive strain is greater than 15% with dilatational stress less than -0.15 MPa. Fibrous tissue although not a desirable tissue to be formed at the bone-implant interface still forms and promote aseptic loosening either due to local stress of more than 0.15 MPa or strain magnitudes of either greater than 5% or compressive strain greater than 5% with stress values above -0.15 MPa. Table 3.1 shows the mechanoregulatory algorithm implemented in the present study.

Table 3.1 Mechanoregulatory algorithm implemented in the present study (Mukherjee and Gupta, 2016; Claes and Heigele, 1999; Lacroix and Prendergast, 2002a; Chou and Müftü, 2013; Dickinson et al., 2012; Isaksson et al., 2006b; Hori and Lewis, 1982; Jurvelin et al., 1997).

Tissue phenotypes	Young's Modulus (in MPa)	Poisson's Ratio	Deviatoric Strain (in %)	Hydrostatic Stress (in MPa)
Granulation Tissue	1	0.167	-	-
Fibrous Tissue	2	0.167	-	>0.15
			>5	>-0.15
			<-5	>-0.15
Cartilage	10	0.167	>15	<-0.15
			<-15	<-0.15
Immature Bone	1000	0.3	-15 to +15	<-0.15
Mature Bone	6000	0.3	-5 to +5	-0.15 to +0.15

3.3 Mathematical formulation to develop NN

The underlying mathematical formulations used to develop the NN scheme used to predict bone growth is presented below. Forward propagation and backward propagation are two core processes of NNs.

Forward propagation in a NN represents the process of taking up the input data and thereby passing them through hidden layer of neural net where they are processed by suitable activation functions and passed successively either towards next hidden layer or output layer. When more than one hidden layer is used to develop a NN, it is known as "deep learning" NN. In the present study, only one hidden layer was considered for framing the NNs for each macro-textured surface morphology. Such a forward propagation methodology is generally known as "feed-forward network". Each neuron in the hidden and outer layer has two functions to process input data fed to them viz. pre-activation and activation. Pre-activation calculates the weighted sum of the outputs from a previous layer. However, bias neuron added as a bias value is added to the weighted sum so as to form a linear function with a bias intercept. Bias is added in both pre-activation and activation functions so as to provide flexibility to the network for proper curve fitting. Finally, activation function adds non-linearity to the network and provides the output signal.

Back-propagation is the cornerstone of any NN. It is the process of tweaking the weights of the NN based on the loss (error) from the preceding epoch (iteration). Backward propagation ensures lesser error between the targeted output signal and computed output signal thus boosting the flexibility of the model and making it more reliable. The mathematical formulations adopted to model feed-forward and back-propagation NN in the present study is outlined in the next sub-section.

3.3.1 Forward step computations

***Computations in Input layer*:** The output of the m^{th} neuron lying on the input layer was determined using the following expression:

$$O_{\mathrm{Im}} = a_1(I_{\mathrm{Im}} + b), a_1 > 0 \text{ and } -\infty < (I_{\mathrm{Im}} + b) < \infty \tag{3.13}$$

where a_1 is the constant of activation function; I_{Im} represents the input of m^{th} neuron; b denotes the constant bias value.

***Computations in Hidden layer*:** The input of the n^{th} neuron lying on the hidden layer was determined using the following expression:

$$I_{Hn} = \sum_{m=1}^{M} O_{Im} v_{mn} + b \tag{3.14}$$

where v_{mn} is the weight that connects m^{th} neuron of the input and n^{th} neuron of the hidden layer.

The output of n^{th} neuron of the hidden layer can be determined as:

$$O_{Hn} = \frac{1}{1-e^{-a_2(I_{Hn}+b)}}, a_2 > 0 \text{ and } -\infty<(I_{Hn}+b)<\infty \tag{3.15}$$

where a_2 is the constant of non-linear activation function.

***Computations in Output layer*:** The input of the output neuron can be determined as follows:

$$I_{Oz} = \sum_{n=1}^{N} O_{Hn} w_{nz} + b \tag{3.16}$$

where w_{nz} is the weight that connects n^{th} neuron of the hidden and z^{th} neuron of the output layer.

The output of the output neuron can be computed as follows:

$$O_{Oz} = \frac{1}{1-e^{-a_3(I_{Oz}+b)}} \tag{3.17}$$

where a_3 is the constant of activation function.

The forward step computation for a batch run terminates here.

3.3.2 Backward step computations

***Computation of Cost Function*:** Mean Squared Error (MSE) Cost function was chosen for this algorithm which is computed after each batch run (epoch) as follows:

$$E = \frac{1}{\zeta} \sum_{k=1}^{\zeta} \frac{1}{2} (T_{Oz}^{\zeta} - O_{Oz}^{\zeta})^2 \tag{3.18}$$

where ζ denotes number of training cases; T_{Oz}^{ζ} represents target output corresponding to ζth training case; O_{Oz}^{ζ} represents computed output corresponding to ζth training case.

The goal of the learning process is to adjust initial weights in order to fine-tune the network for better performance. At every epoch, connecting weights [V] and [W] were updated in order to minimize the cost, *E*.

***Computation of adjustment in [W]*:**

The adjustment in weights connecting hidden and output layers, [W] at every epoch was computed as follows:

$$\Delta w_{nz}(epoch) = -\alpha \frac{\partial E}{\partial w_{nz}}(epoch) + \mu \Delta w_{nz}(epoch-1) \tag{3.19}$$

where α denotes the learning rate, which is a tuning parameter which is updated after each epoch while moving towards minimum cost function, and μ denotes the momentum constant which helps in preventing the learning process from terminating in a local minimum thus providing a stabilizing effect to the network.

Sensitivity factor, $\frac{\partial E}{\partial w_{nz}}$ can be further expressed and computed as:

$$\frac{\partial E}{\partial w_{nz}} = \frac{\partial E}{\partial E^{\xi}} \frac{\partial E^{\xi}}{\partial O_{Oz}} \frac{\partial O_{Oz}}{\partial I_{Oz}} \frac{\partial I_{Oz}}{\partial w_{nz}} \tag{3.20}$$

***Computation of adjustment in [V]*:**

The adjustment in weights connecting input and hidden layers, [V] at every epoch was computed as follows:

$$\Delta v_{mn}(epoch) = -\alpha \frac{\partial E}{\partial v_{mn}}(epoch) + \mu \Delta v_{mn}(epoch-1) \tag{3.21}$$

Sensitivity factor, $\frac{\partial E}{\partial v_{mn}}$ can be further expressed and computed as:

$$\frac{\partial E}{\partial v_{mn}} = \frac{\partial E}{\partial E^{\xi}} \frac{\partial E^{\xi}}{\partial O_{Oz}} \frac{\partial O_{Oz}}{\partial I_{Oz}} \frac{\partial I_{Oz}}{\partial O_{Hn}} \frac{\partial O_{Hn}}{\partial I_{Hn}} \frac{\partial I_{Hn}}{\partial v_{mn}} \tag{3.22}$$

However, it is to be noted that the optimal number of nodes in the hidden layer, learning rate and the momentum constant have been chosen based on a parametric study by varying each parameter at a time keeping other two parameters constant. Such a methodology would provide an optimum NN architecture in the present study.

3.4 Methodology to implement GA

The GA search heuristic is based on the natural evolution theory of Charles Darwin. This algorithm mimics natural selection, in which the fittest individuals are chosen for reproduction in order to create the offspring/children of the subsequent generation. If parents are physically active (fit), their offspring will be fitter than they are and have a greater chance of survival. This procedure will continue to iterate until a generation of the fittest individuals is identified. GA has been implemented in five phases to reflect this evolutionary process: starting population, computation of fitness function, selection, crossover and mutation.

3.4.1 Populate the initial population

Significant design variables of the textured morphology are chosen with their upper and lower bounds based upon clinical admissibility and manufacturing feasibility of the implant. Strings of chromosome, known as individuals, are formed by different combinations of values of design variables. All the individuals are populated in random to form the initial set of population.

3.4.2 Computation of fitness function

NN acts as the mathematical model for the fitness in the present study. Optimal NN obtained after training and validation is set as the optimization function in the GA module. The fitness function calculated through a trained NN determines the ability of each individual string to satisfy the objective function. Rank scaling of objective function determines the values of fitness function.

3.4.3 Selection of fittest individuals

Selection of fittest individuals is performed to pass the best individuals to the next generation. There have been many selection methods available to date. But few of them are used extensively in different problems such as stochastic-uniform selection, tournament selection, roulette wheel selection, rank selection etc.

Stochastic-uniform selection has been chosen as the selection algorithm in the present work. Although stochastic-uniform selection is modified form of roulette wheel selection, it provides a better chance for the highly fit individuals to be selected at least once with no bias and minimal spread.

3.4.4 Crossover and mutation

This is perhaps the most important phase in GA. A cross-over point in the individual string is chosen randomly and thereafter genes are exchanged to form offspring. The scattered crossover fraction chosen in the present work is the percentage of offspring produced by crossing over without considering the elite individuals. The remaining individuals are created by mutation. Mutation is provided to maintain diversity in the next generation of individual to avoid early convergence. Throughout all generations, the elite count was set at two.

The GA implemented in the present study is said to be terminated after a selected number of generations. However, optimal values of GA parameters have been determined through a parametric study where crossover fraction, initial population size and maximum number of generations are varied from a chosen lower bound to an upper bound one at a time keeping other parameters constant. With the near optimal GA parameters, the final GA has been run to obtain optimal design variables of the implant macro-textures.

3.5 Summary

In this chapter, methodology of studying tissue-differentiation at the bone-implant interface is presented in detail. An FE based approach is shown that is used to catch mechanical stress and strain responsible for tissue-differentiation. Thereafter, numerical procedures such as smoothing techniques and rule of mixtures are explained in detail on the context of simulating a biophysical model in a more practical way. In addition, mathematical formulation of migration of MSCs

simulated through a diffusion model under thermal analogy is also presented in detail. FE based approach is also undertaken to solve the diffusion model with suitable end conditions. Then, detailed mathematical formulation of NN involving feed-forward and backpropagation methods are presented in detail. This formulation has not only helped to predict bone growth for a chosen macro-textured surface but also been used as an optimization function to run a GA. Finally, steps involving GA has been described in details which has been further used to obtain optimal designs for the chosen macro-textured implant surfaces.

CHAPTER 4

Influence of macro-textured implant surface on bone growth

The long term secondary stability of an uncemented implant depends primarily on the quality and extent of bone in-growth or on-growth at the bone-implant interface. Investigations are warranted to predict the influences of implant macro-textures on bone growth pattern. Mechanoregulatory tissue differentiation algorithms can predict such patterns effectively. This chapter presents a study that assess the influence of macro-textured implant surfaces on changes in tissue formation at the bone-implant interface by carrying out a mechanoregulation based 3D finite element (FE) analysis. The numerical scheme developed in this chapter can further be used as a template for more rigorous parametric and multi-scale studies.

4.1 Importance of textured implant surface

For biological acceptance of a load-bearing orthopaedic implant, e.g. hip stem, a long-term adherence of the implant to the host bone is required. The primary bone-implant adherence can be achieved either by using bone-cement (commercially known as poly-methyl methacrylate or PMMA) between bone and the implant (cemented implants) or by press-fitting the implant into the host bone canal and thereby utilising the interference-fit and coefficient of friction between them (uncemented implants). In the uncemented implants, the implant gradually integrates with the host bone by means of mechanical interlocking through osseointegration, thereby attaining secondary stability (Sánchez et al., 2021a). The success of uncemented implants, therefore, demands proper biologic fixation of the bone and intermediate soft tissues in and around the implant (Yamada et al., 2009). Notwithstanding the stupendous success of uncemented prostheses all across the globe and despite high surgical precautions, there have been notable inflation in the absolute number of failed joints, leading to the necessity of revision surgery. Although the reason behind such failure incidences may be multifactorial, the lion's share of it may be attributed to the biomechanical causes. One such biomechanical failure scenario is the lack of primary stability arising due to excessive interfacial micromotion. Results of clinical studies reported that interfacial micromotion of below 40 µm was observed to be optimum for bone growth at the bone-implant interface (Sánchez et al., 2021a; Sánchez et al., 2021b). On the contrary, higher micromotions of 150 µm and above was observed to promote fibrous tissue formation near the implant surface which is detrimental to biologic fixation, thus leading to aseptic loosening of the prosthesis (Sánchez et al., 2021a; Sánchez et al., 2021b). Any compromise on primary stability thus may eventually lead to insufficient long-term secondary stability (biologic fixation) of the implanted construct. By incorporating minor to profound design changes, these failure situations may be averted (Huiskes and Boeklagen, 1988; Viceconti et al., 2001).

Bone growth around the uncemented implants can be achieved by bone in-growth and on-growth. Bone in-growth indicates a bone-implant fixation by bone growth into the porous coated surface or porous implant surface. Conversely, bone on-growth is the fixation of bone and the implant by bone growth on the surface of the implant (Yamada et al., 2009; Kim and Yoo, 2016). Commercially, a variety of

implant surface features is in existence with a core objective of promoting bone on-growth. These surface features can either be microscopic or macroscopic (Pilliar, 1998; Kienapfel et al., 1999). Although there exists no clear technical definition of micro and macro-textures, a new standard (ISO 14607:2018) on mammary implants (Munhoz et al., 2019) has classified implants with surface features of the order 10-50 μm as micro-textures and those above 50 μm as macro-textures. Investigations suggested that micro-textured surfaces could promote cell differentiation (Andreykiv et al., 2008; Olivares-Navarrete et al., 2010) and osseointegration (Andreykiv et al., 2008; Cochran et al., 1998) even without the use of any osteogenic factors. Recent studies have also explored the possibility of enhancing osteoblastic differentiation and maturation, followed by implant osseointegration by nanoscopic surfaces (Mendonca et al., 2008; Gittens et al., 2014).

4.2 State-of-the-art in textured implant surface

Although earlier studies investigated the influence of implant micro-textures (Andreykiv et al., 2008; Mukherjee and Gupta, 2016) and microscopic threads (Chou and Müftü, 2013) and vents on osseointegration, there has been no volumetric *in silico* study to assess the influence of macro-textures on bone growth. A recent histological study on the influence of macroscopic grooves has been reported on dental implants (Kuroshima et al., 2017). However, such histological studies are not capable of predicting the spatial distribution of peri-prosthetic osseointegration (Mukherjee and Gupta, 2016). Moreover, the dimensions of these grooves are not convincing to be treated as fully macroscopic grooves. In a recent investigation, the influence of macro-textured grooves on implant-induced strain shielding for three commercial hip stem models was studied, and a trade-off design of the texture was proposed (Heyland et al., 2019). Besides no comparative study of multiple discernible textures on commercially viable implants and osseointegration thereof has not been reported till date, even though similar comparison was performed on stress-shielding phenomenon in femoral implants (Heyland et al., 2019).

4.3 Objective of this investigation

The primary objective of this investigation is to develop a finite element (FE) based framework to pre-clinically assess the mechanoregulatory influences of macro-textures on bone growth patterns at the bone-implant interface region and over the implant surface.

4.4 Problem Definition

Having understood the importance of textured implant surface, in this study three different types of macro-morphologies have been considered to investigate the comparative influence of these textures on bone growth with varying tangential bone-implant relative displacements (micromotion). In the present FE based scheme, it is hypothesised that the bone growth around the implant surface depends directly on the levels of micromotion (in the form of relative displacements) at the bone-implant interface. This hypothesis may lead to conclude further on the optimal nature of the implant surface texture favourable for bone growth. The outcome of this study may be helpful for further clinical research on the study of macro-textures and osseointegration thereof.

4.4.1 Development of bone-implant sectional models

Three novel 3D macro-textured models (**MODEL A**, **MODEL B** and **MODEL C**) of the bone-implant interface were developed using CATIA® V5R20 software (Dassault Systèmes, France), as shown in Fig. 4.1. The primitive surface textures on **MODEL A**, **MODEL B** and **MODEL C** were developed loosely based on the discernible textures on commercial hip stems, e.g. CLS Spotorno, CORAIL and SP-CL stems, respectively. All the commercial hip stems considered for generating the primitive 3D models of the macro-textures (present on the proximal region of these stems) are clinically proven to be successful prostheses based on long-term results (Heyland et al., 2019). **MODEL A**, which resembles the proximal region of CLS Spotorno (Zimmer Biomet, UK, Product Brochure), has ribs of different height to enhance bone compression that provides a higher stimulus for bone growth. **MODEL B**, which resembles the proximal region of CORAIL (DePuy Synthes, Johnson & Johnson Medical Devices, USA, CORAIL® HIP System Design Rationale), is characterized by rectangular grooves to provide primary stability.

Similarly, **MODEL C**, which resembles a comparable region of SP-CL stems (Waldemar Link GmbH & Co. KG, Germany, LINK SP- CL product brochure), has semi-circular grooves. These macro-textures were chosen to predict the effect of these patterned metallic surfaces on bone growth.

Each model contains a cast-in macroscopic textured implant on one end, granulation tissue at the middle and bone at the other end of the model (Fig. 4.1). A base implant height of 10 mm and a maximum bone-implant gap of 5 mm for all three models were considered to provide a trade-off thickness for the granulation tissue. It may be noted that 'base' of an implant refers to the region on which the novel textures were developed on the model. Dimensions, such as the heights from the implant 'base', inter-spacing of the grooves/ribs and width of the implant bed, were chosen following some qualitative inputs from experienced orthopaedic surgeons. It may, however, be noted that neither the full femur-implant model nor the coating on the surface of the implant was modelled in the present study.

The present analysis is premised on the assumption that an ideal osteogenic environment is prevalent and identical across all the bone-implant interface models. A rigorous multi-scale assessment employing a full-scale femur-implant model integrated with a mechanobiological algorithm of the present scale is warranted for better insight into osseointegration. However, such schemes may involve a significantly large number of finite elements (Liu and Niebur, 2008) with complex, continuously adapting contact conditions. A program of such complexity demands parallel computing for better efficiency and hence, will be prohibitively expensive.

4.4.2 FE modelling and analysis

FE discretization of each of the 3D models was performed using coupled linear elastic eight-noded hexahedral elements, with a maximum edge length of around 0.9 mm for **MODEL A** and **MODEL B** and 1 mm for **MODEL C** using ANSYS FE software (ver 14.5 ANSYS Inc., Canonsburg, PA, USA) as shown in Figure 4.2. Uniform meshing was adopted to eliminate discretization error in the models. All the three components of the model, i.e. host bone, implant and granulation tissue, were assumed to have linear, elastic, homogeneous and isotropic material properties.

The host bone tissue is assumed to have Young's modulus of 500 MPa (Puthumanapully, 2010; Mukherjee and Gupta, 2014). The Young's moduli of the implant and the granulation tissue were considered to be 210 GPa and 1 MPa, respectively. Poisson's ratio for all materials was taken as 0.3. The two interfaces (bone-granulation tissue and implant-granulation tissue) in all three models were assumed to be perfectly bonded.

4.4.3 Loading and boundary conditions

In order to predict the effect of micromotion on bone growth, relative motion between the implant and the host bone was simulated by applying displacements (Fig. 4.2) following the loading conditions from a previously investigated study (Simmons et al. 2001). Since the granulation tissue was assumed to adhere to the host bone, the displacements of the top surface of the bone were restricted in all the three directions. To prevent the initial debonding of the implant from the interface tissue and to represent a press-fit condition at the bone-implant interface, a normal displacement of 20 μm (Mukherjee and Gupta, 2014) was provided in the positive Y direction (Fig. 4.2). A tangential displacement of 20 µm was applied at the bottom surface of the implant relative to the bone in the positive X direction. It is worth noting that physiological loading around the bone-implant model was not considered since the main goal of the study was to predict the relative influence of patterned macro-textures on bone growth. Although physiological loads and muscle forces were not considered in the study, such loading and boundary conditions provide a simplified mechanical environment observed in generalised tissue-interfacing implants.

4.4.4 Analysis-combining FEA and mechanobiological model

Conditions for different tissue phenotypes corresponding to mechanical stimuli used in the progressive mechanoregulatory algorithm to simulate the tissue growth process in the present study are discussed in Table 3.1, Chapter 3. The numerical scheme (Fig. 4.3) comprises of two main segments: mechanical and biological. The mechanical component of the model estimates mechanical stimuli sensed by the stem cells that migrate in the interfacial tissue. In contrast, the biological part accounts for the cellular process such as cell migration. Initially, the gap between the bone and the implant is assumed to be filled with granulation tissue, that is filled

with sufficient blood vessels formed by angiogenesis to supply nutrients to the newly formed cells and inflammatory cells to remove injured portion of the tissue. Therefore, the concentration of MSCs at this point of time in the tissue region is zero. However, the normalized concentration of MSCs at the bone-granulation tissue interface was considered as unity (1.0).

The precursor cells from bone-granulation tissue interface migrate towards the region of bone healing to repair the bone defect. Depending upon the local mechanical stimulus (hydrostatic pressure and deviatoric strain), the migrated stem-cells differentiate into different cellular phenotypes (Isaksson et al., 2006b; Barry, 2003), e.g. fibroblast, chondrocyte, osteoblast (Claes and Heigele, 1999). Upon attaining maturity, all these new cell phenotypes would transform into fibrous tissue, cartilage and bone (Claes and Heigele, 1999). Independent of the mechanical component of the numerical model, migration and proliferation of MSCs within the region of interfacial tissue was modelled as a diffusive phenomenon (Lacroix et al., 2002; Lacroix and Prendergast, 2002a, 2002b), following Eq. 4.1:

$$k\nabla^2 c = \frac{dc}{dt} \tag{4.1}$$

where k is diffusion constant (0.1 mm^3/day) and c is the element-specific concentration of cells. The value of k was chosen judiciously, such that the process of MSC migration and proliferation can be completed within 16 weeks (Lacroix and Prendergast, 2002b). A zero-diffusion boundary condition was imposed on the peripheral boundaries of the granulation tissue layer, representing no cell loss from the granulation tissue during the diffusion process.

The bone growth was simulated following the mechanoregulatory tissue differentiation algorithm. The temporal development of mechanoregulated tissue phenotypes would prompt the simultaneous presence of granulation tissue as well as newly differentiated tissue at any instant of time. In this regard, the effective material properties (Young's modulus, E and Poisson's ratio, υ) of the new tissues were computed through a rule of mixture as:

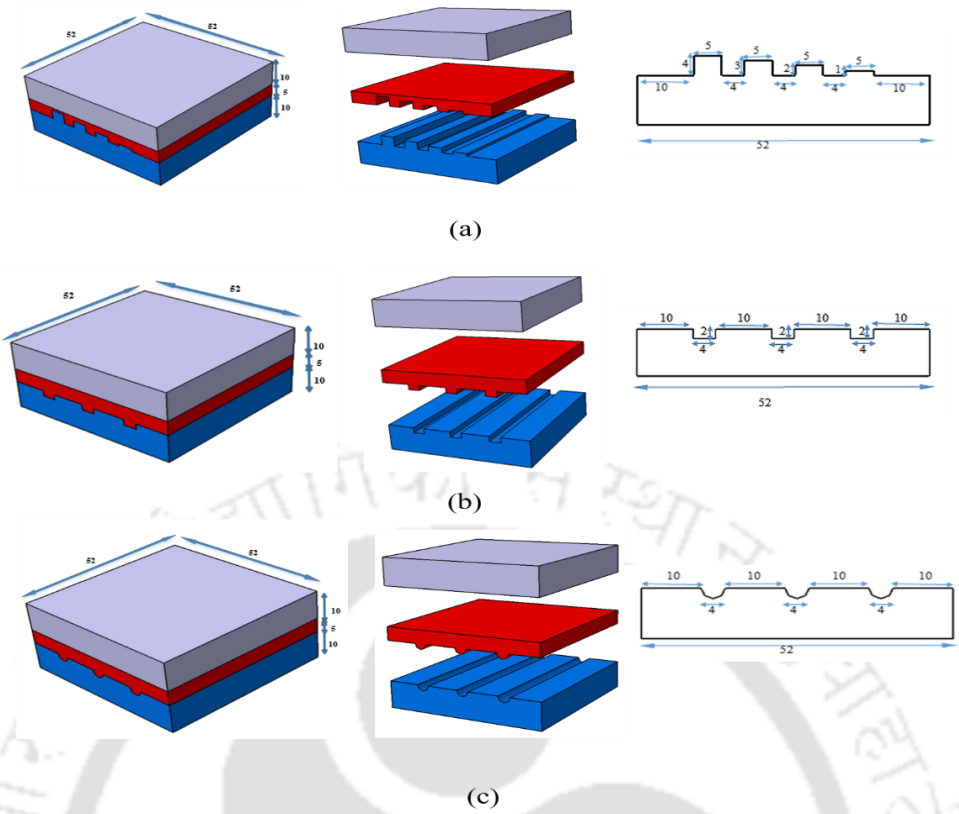

Figure 4.1 Representative macro-textured CAD models (52 mm × 52 mm × 25 mm) of the three bone-implant interfaces: (a) MODEL A, (b) MODEL B and (c) MODEL C. (Colour Map: Blue for Implant; Red for granulation tissue; Grey for Host Bone). All dimensions are in mm.

$$E_{n+1} = \left(\frac{c_{max} - c_{tissue}}{c_{max}} \right)\Bigg|_n E_{granulation} + \left(\frac{c_{tissue}}{c_{max}} \right)\Bigg|_n E_{tissue} \tag{4.2}$$

$$\nu_{n+1} = \left(\frac{c_{max} - c_{tissue}}{c_{max}} \right)\Bigg|_n \nu_{granulation} + \left(\frac{c_{tissue}}{c_{max}} \right)\Bigg|_n \nu_{tissue} \tag{4.3}$$

where, E_{n+1} and ν_{n+1} are the resulting Young's modulus and Poisson's ratio of the new tissue respectively after n^{th} iteration; $E_{granulation}$ (also $\nu_{granulation}$) and E_{tissue} (also ν_{tissue}) are the material properties of the granulation tissue and the newly evolved tissue, respectively; c_{max} and c_{tissue} are the maximum cell concentration and the actual element-specific concentration of cells, respectively.

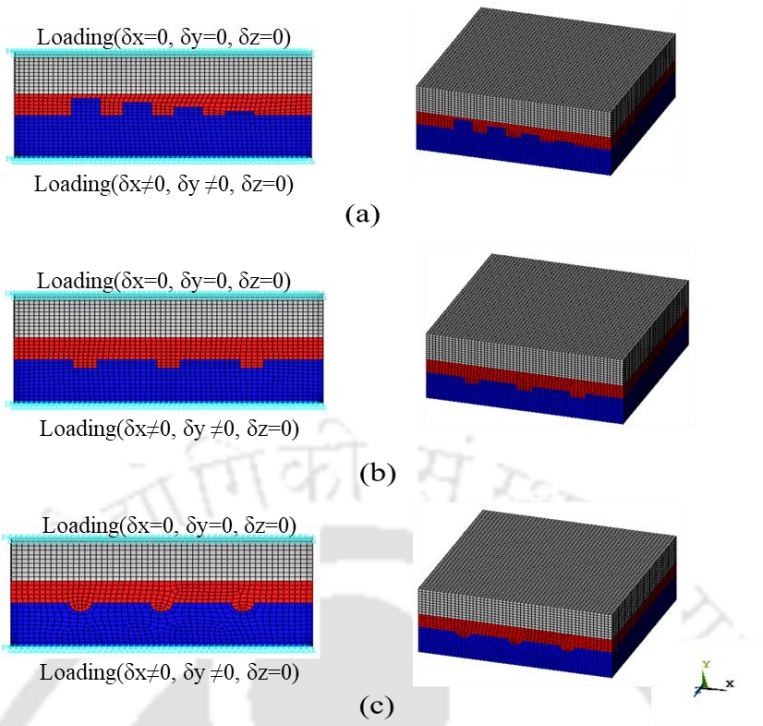

Figure 4.2 3D FE models of the three macro-textured bone-implant interfaces with loading and boundary conditions: (a) MODEL A, (b) MODEL B and (c) MODEL C. (Colour Map: Blue for Implant; Red for granulation tissue; Grey for Host Bone).

In order to avoid numerical instability owing to a sudden change in material properties after each iteration and artificial fast tissue differentiation, a temporal smoothing method was implemented (Lacroix and Prendergast, 2002a, 2002b). The method updates the material properties of the newly formed tissue layer by averaging local material properties over ten previously estimated values of material properties, following Eq. 4.4 and Eq. 4.5:

$$E_{n+1,smoothed} = \frac{1}{10}\sum_{i=n}^{n-9} E_i \tag{4.4}$$

$$\nu_{n+1,smoothed} = \frac{1}{10}\sum_{i=n}^{n-9} \nu_i \tag{4.5}$$

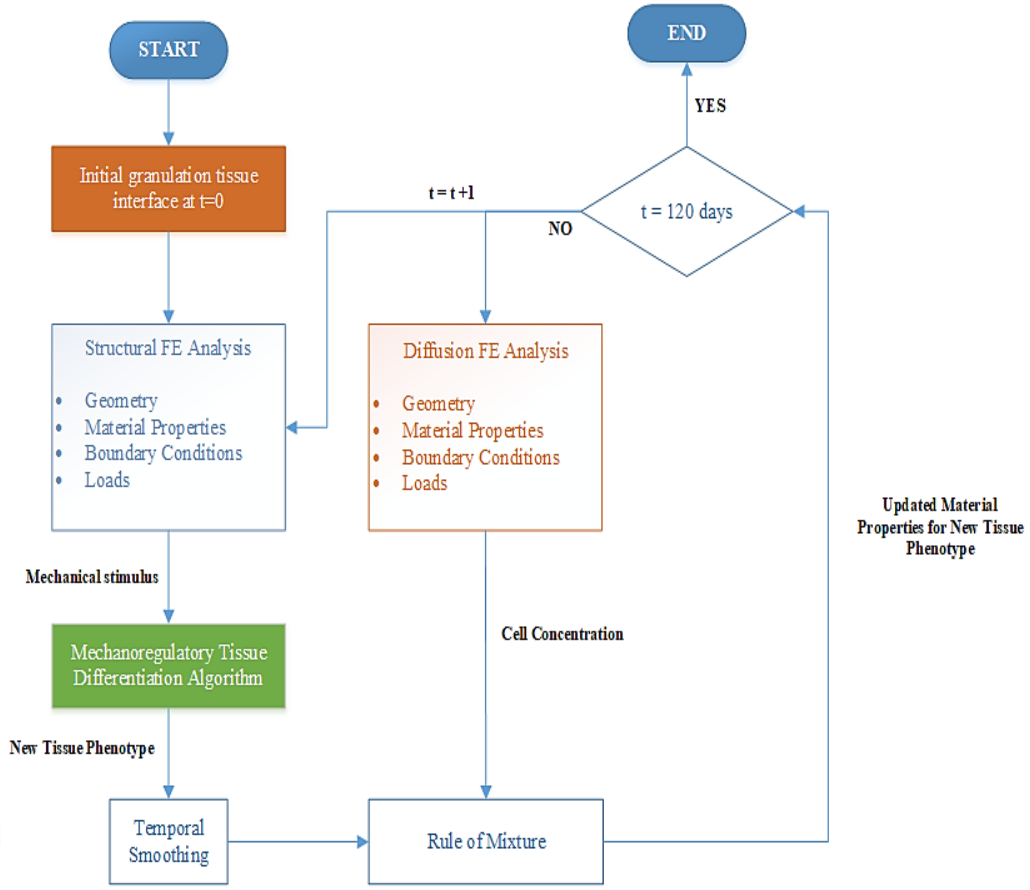

Figure 4.3 Flowchart of the Mechanoregulation based scheme for tissue differentiation algorithm.

A custom MATLAB script (Matlab 2017a, The MathWorks Inc., Natick, MA, USA) was developed separately to implement the mechanoregulatory tissue-differentiation model. A masterbatch script (DOS) was employed to sequentially launch ANSYS module for structural FE analysis and MATLAB module for tissue differentiation calculations, in each iteration. In this computational framework, each iteration was supposed to represent one postoperative day. The complete scheme was set to run for 120 iterations (~120 days), representing 16 weeks or equivalent 4 months' postoperative period. The simulation was run in batch mode in a Windows 10 Pro platform with Intel® Core™ i7-4510U 2-core CPU powered by 8 GB RAM.

4.5 Results and Discussion

The present numerical investigation has been aimed at predicting the mechanoregulatory influences of implant surface macro-textures on bone growth patterns at varying levels of interfacial micromotion. Three distinct 3D macro-textured surface models of the implant have been considered for comparative evaluation of the growth behaviour. The FE based study relied upon a mechanobiology based tissue-differentiation algorithm (Lacroix et al., 2002; Lacroix and Prendergast, 2002a, 2002b), which provides a better agreement with controlled animal studies of bone-fracture healing (Isaksson et al., 2006a).

4.5.1 Mesh convergence

A mesh independence test was performed for the three macro-texture models based on maximum von-Mises stress developed within the interfacial tissue to achieve a reasonable level of accuracy on the predicted results. Each of the three models was subjected to 60 µm tangential displacement and 20 µm normal displacement. Mesh refinement was carried out varying element size from 1 mm to 0.5 mm in steps. Consistent and stable stress values (up to a stress magnitude of order 2) were predicted from element size of 0.9 mm for **MODEL A** (16,356 interface finite elements) and **MODEL B** (23,664 interface finite elements). In comparison, the same was predicted corresponding to element size of 1 mm for **MODEL C** (16,016 interface finite elements)**.** Accordingly, the refined mesh was used for further computational analyses. Figure 4.4 shows the mesh convergence study for the present study.

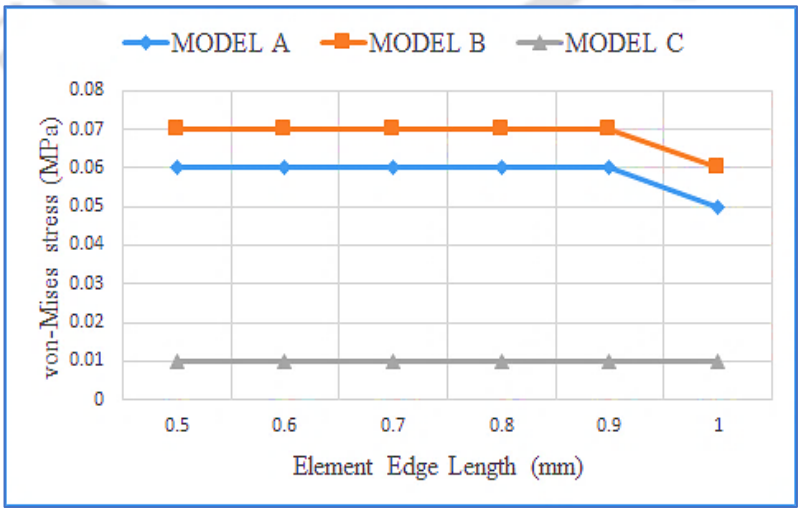

Figure 4.4 Mesh convergence study based on von-Mises stress (MPa) predictions of the three FE models: Model A, Model B and Model C.

4.5.2 Influence of macro-textured implant surface on tissue growth

The variation in the percentage of tissue growth over three distinct implant surfaces for a constant level of micromotion (20 µm) is presented in Fig. 4.5. The amount of bone growth for both **MODEL B** and **MODEL C** was found to be similar (~15%) up to 12 weeks. However, **MODEL B** predicted a higher rate of bone growth with nearly 25% osteoblast formation in nearly 16 weeks. **MODEL A,** on the other hand, predicted slightly lower osteogenesis (~11%) after 16 weeks of the healing period. The formation of chondrocytes (cartilaginous cells) was predicted to be higher in all three models. The amount of cartilage tissue for **MODEL A**, **MODEL B** and **MODEL C** was predicted to be ~70%, ~67% and ~74%, respectively. Mesenchymal Stem Cells (MSCs) and fibroblasts were found to be slightly lower in case of **MODEL B** (2%, 11%) and **MODEL C** (1.3%, 9.7%), as compared to **MODEL A** (3%, 14%), over the full healing period.

This finding implies that **MODEL B** and **MODEL C** are more favourable candidates for bone growth as compared to **MODEL A**. A clinical relevance can also be attributed to the difference in outcomes as observed in different commercial implants, based on which the macro-textures were developed in the present study. These differences in macro- textured surface designs might be one of the possible explanations for long-term survival (Heyland et al., 2019) of CORAIL (**MODEL B**) as compared to CLS Spotorno (**MODEL A**).

Fibrous tissue and immature cartilage formation were more prominent at the edges of the grooves/ribs (Fig. 4.6) primarily due to high stress-concentration at the region, as compared to other regions in the interface tissue layer which favours the growth of fibroblasts and immature chondrocytes. A recent finding (Tan et al., 2017) also corroborates our results, predicting softer connective tissues and relatively lesser bone growth at the bone-implant interface with an increase in stress-concentration around the implant. The formation of fibrous tissue in **MODEL C** was less prominent around the curvature as compared to that around the stepped design in **MODEL B** (Fig. 4.6). This finding suggests that filleting and chamfering of edges of macro-textures may reduce the formation of fibrous tissue, thereby enhancing the formation of bone.

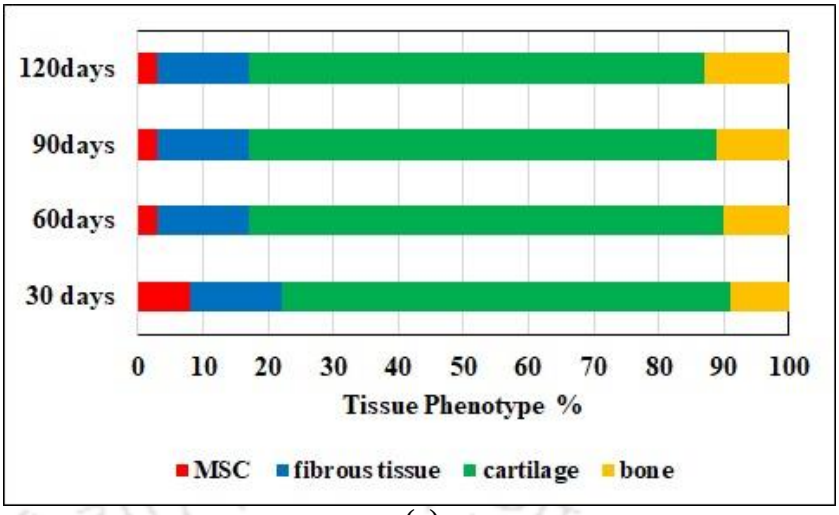

(a)

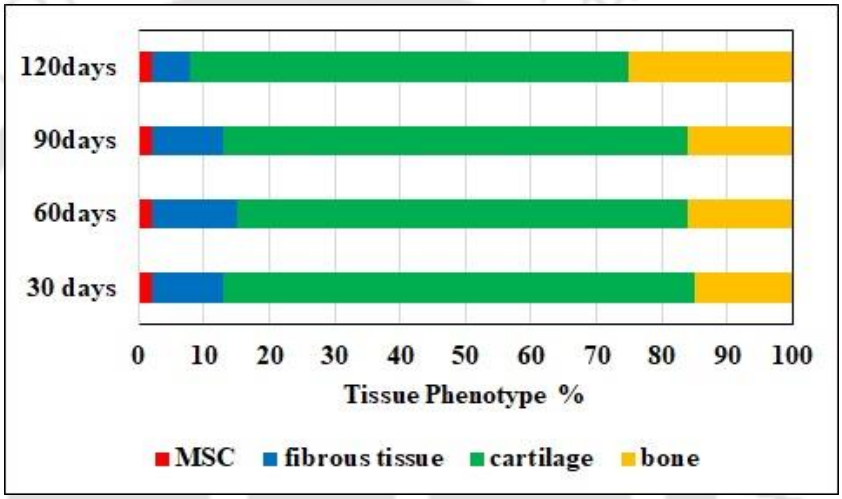

(b)

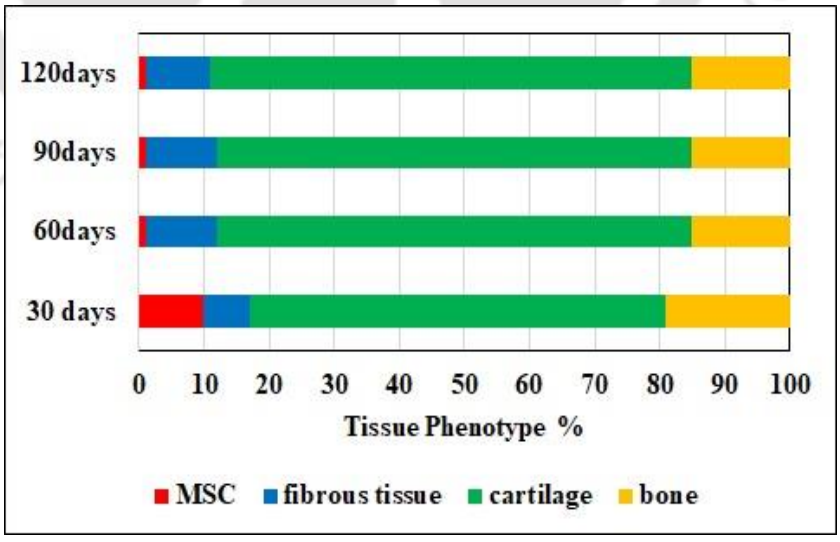

(c)

Figure 4.5 Percentage of tissue phenotype over the three macro-textured implant surfaces for a constant micromotion of 20 µm: (a) MODEL A; (b) MODEL B; (c) MODEL C.

Fibrous tissue and immature cartilage formation were more prominent at the edges of the grooves/ribs (Fig. 4.6) primarily due to high stress-concentration at the region, as compared to other regions in the interface tissue layer which favours the growth of fibroblasts and immature chondrocytes. A recent finding (Tan et al., 2017) also corroborates our results, predicting softer connective tissues and relatively lesser bone growth at the bone-implant interface with an increase in stress-concentration around the implant. The formation of fibrous tissue in **MODEL C** was less prominent around the curvature as compared to that around the stepped design in **MODEL B** (Fig. 4.6). This finding suggests that filleting and chamfering of edges of macro-textures may reduce the formation of fibrous tissue, thereby enhancing the formation of bone.

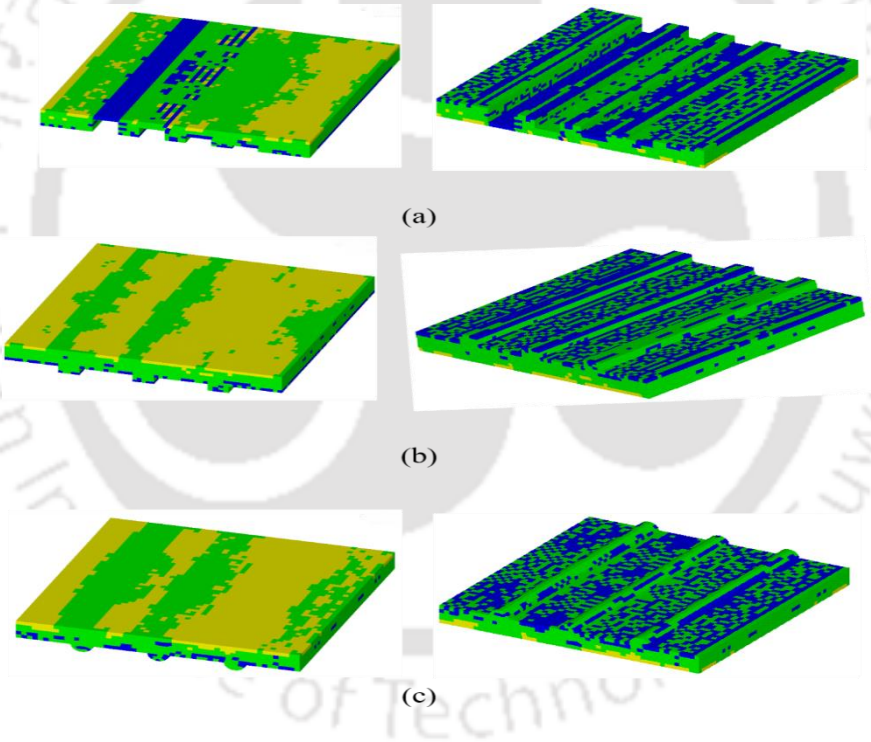

Figure 4.6 Distribution of major tissue growth over the three macro-textured designs on implant surface after 16 weeks healing period: (a) MODEL A, (b) MODEL B and (c) MODEL C (Colour Map: Blue for fibrous tissue; Green for cartilaginous tissue; Yellow for Bone).

There has been a decline in the bone formation in the middle of the implant surface in **MODEL A**, away from the boundaries that might inhibit bone bridging across the interface tissue (Fig. 4.6a). Inhibition of bone bridges might lead to implant instability (Isaksson et al., 2006b) in the central region of the implant

surface. This finding can be substantiated by the amount of fibrous tissue that was prominent around deeper grooves as compared to shallower ones (Fig. 4.6). This further indicates that shallower grooves promote isolated bone bridges across the bone and implant surface, resulting in faster osseointegration. A previous *in silico* study suggested that an increase in the bone-implant gap may enhance the formation of softer tissues within the gap (Mukherjee and Gupta, 2014).

The variation in tissue stiffness with the number of postoperative days (in healing time-scale) is plotted in Fig. 4.7, while keeping the micromotion constant at 20 µm. Although higher stiffness values (Fig. 4.7) were predicted for **MODEL B** up to 6 weeks, a gradual decline was observed afterwards, which was followed by a constant stiffness curve from 10th weeks onwards. The average Young's modulus at the bone-implant interface after 16 weeks for **MODEL B** and **MODEL C** was found to be ~214 MPa. The same for **MODEL A** was predicted to be ~130 MPa.

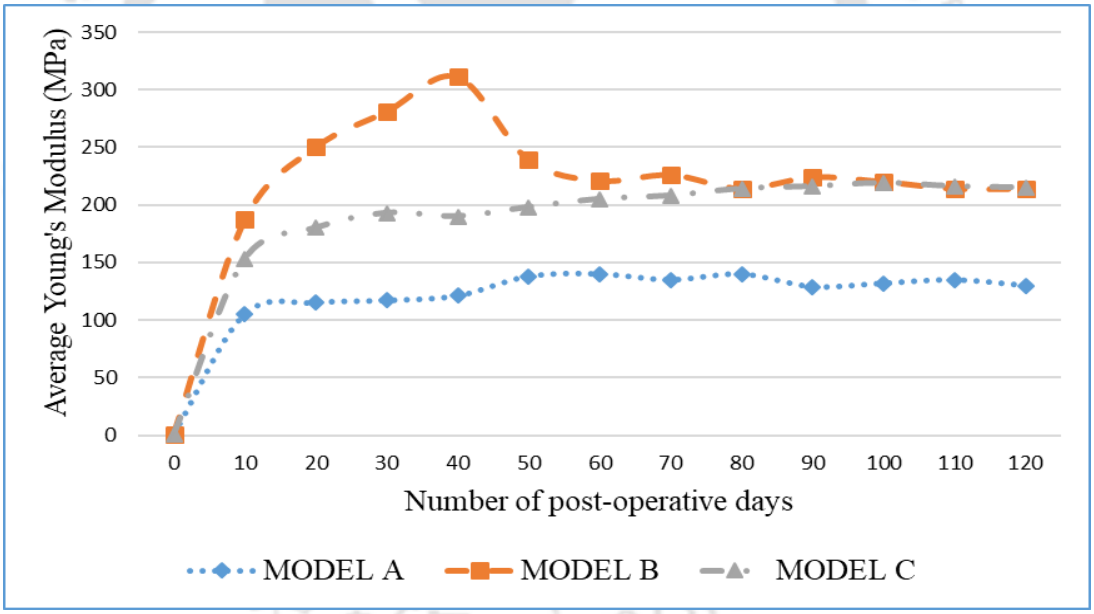

Figure 4.7 Variation in tissue stiffness at the bone-implant interface for the three macro-textured designs on implant surface throughout the healing period corresponding to 20 µm tangential micromotion.

4.5.3 Influence of micromotion at the bone-implant interface on tissue growth

Fig. 4.8 shows the variation of tissue growth for each of the models for different levels of micromotion, e.g. 20 µm, 60 µm and 100 µm. For lower tangential micromotion of 20 µm, **MODEL A** predicted a steady decrease in the amount of

MSCs from 100% to nearly 8% in the first postoperative month (Fig. 4.8a). This trend was followed by a further reduction to nearly 3% at the end of the fourth month of surgical intervention. Similar trends were predicted for micromotion values of 60 µm and 100 µm as well. However, the concentration of stem-cells (after cell proliferation, migration and differentiation) for higher micromotion value (100 µm) was found to be higher (by ~67 %) as compared to that for a lower value of micromotion (20 µm). Similar trends were predicted for model **MODEL B** and **MODEL C,** as well. Fibrogenesis was observed for all the three models but in a very less proportion ranging from 6% to 14%. However, the fibroblasts formation leading to fibrous tissue was generally more detectable corresponding to higher micromotion values (60 µm and 100 µm) for all models.

Each model exhibited the formation of new bone cells (or osteoblasts) in the gap between the implant and the host bone, along with a gradual reduction of deviatoric strains in bone-implant interface tissue. At a micromotion of 20 µm, **MODEL A**, **MODEL B** and **MODEL C** predicted the new bone formation of approximately 13 %, 25% and 15%, respectively, after 120 postoperative days. At a micromotion of 60 µm, the three models exhibited new bone formation of approximately 8%, 10% and 10% respectively (Fig. 4.8a, 4.8b, 4.8c). However, at higher micromotion of 100 µm, the formation of new bone was found to be relatively lower, at ~6-7% for all the three models. The micromotion at the interfacial callus between the host bone and the prosthesis was found to influence the progressive temporal transformation (through a series of phase transformation) of precursor cells or MSCs towards the formation of bone cells or osteoblasts (Fig. 4.8). All the three designs of the implant surface predicted an identical qualitative nature towards tissue growth. This prediction suggests that higher the bone-implant interfacial micromotion, lower is the rate of formation of osteoblasts. Higher levels of bone-implant relative displacement were found to prohibit bone growth. This result is also supported by some of the earlier findings (Mukherjee and Gupta, 2016; Liu and Niebur, 2008). However, a higher volume of fibrous tissue formation is observed over a long period, which may lead further to aseptic loosening of the implant. When bone-implant interfacial micromotions were applied, the present scheme resulted in softer tissues at the bone-implant interface, which is in consistent with a previous *in silico* study (Liu and Niebur, 2008).

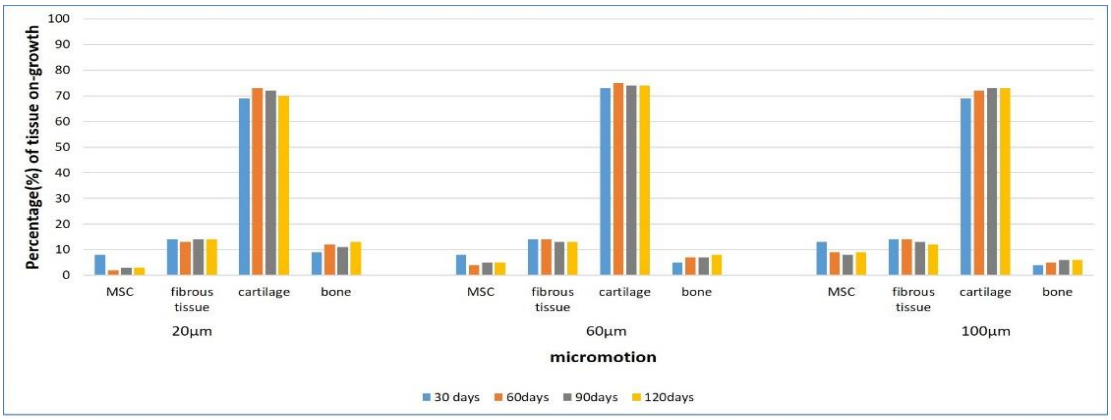

(a)

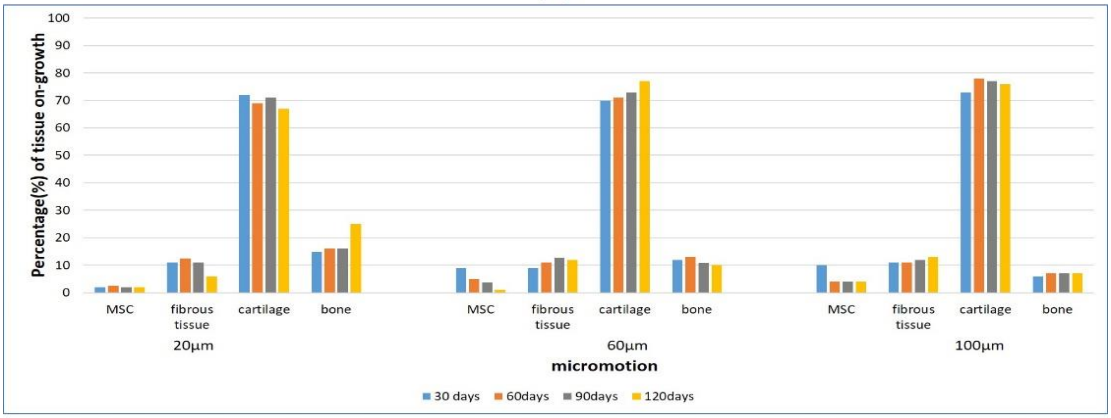

(b)

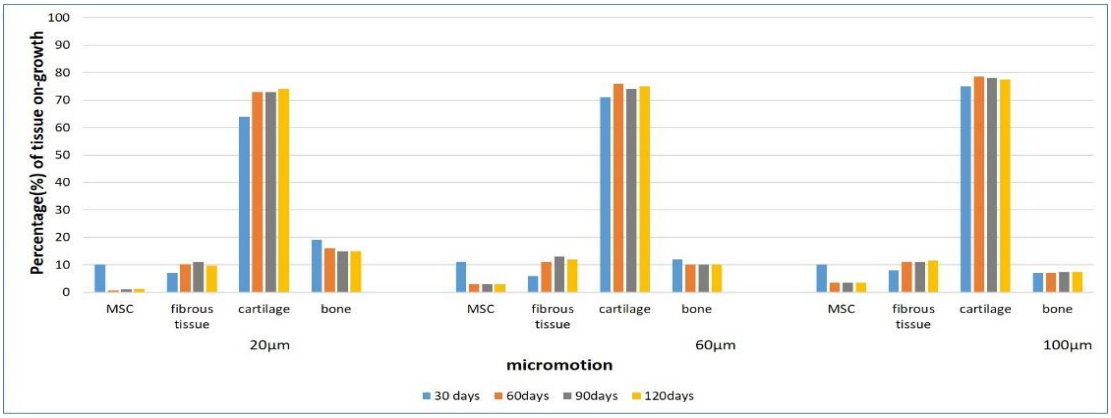

(c)

Figure 4.8 Tissue differentiation corresponding to different levels of micromotion over the entire healing period (120 days) at the bone-implant interface for the three macro-textured designs on implant surface: (a) MODEL A, (b) MODEL B and (c) MODEL C.

Figure 4.9 shows the variation in tissue stiffness (in MPa) at the interface for each of the macro-textured implant designs. At lower micromotion values, the average Young's modulus at the bone-implant interface tissue was predicted to be higher, as compared to that observed for higher micromotion. For **MODEL A**, for a micromotion of 20 µm, the average Young's modulus was found to be nearly 130

MPa, whereas, the same is lower (~82 MPa) for micromotion of 100 µm (Fig. 4.9a). Similar trends were observed for models **MODEL B** (214 MPa at 20 µm and 129 MPa at 100 µm) and **MODEL C** (214 MPa at 20 µm and 120 MPa at 100 µm) (Fig. 4.9b, 4.9c) as well. The values of interfacial average Young's modulus were predicted to have an increasing trend (Mukherjee and Gupta, 2014,2016) with peaks and valleys in between (Fig. 4.9), implying bone resorption and cartilage degeneration (Isaksson et al., 2006a) in the intermediate stages of bone formation. The formation of a stable interface at lower levels of bone-implant relative displacement is well-supported by the previous experimental observations (Qin et al., 1996), which concluded that higher levels of micromotion could lead to failure of an implant.

The predicted spatial distribution of the tissue for different micromotion values is shown through the contour plots in Figure 4.10, for a qualitative depiction of the bone growth pattern. It is evident from the figure that higher levels of micromotion (60 µm and 100 µm) at the bone-implant interface resulted in the formation of relatively softer tissues, i.e. cartilage and immature bone, and a relatively high volume of fibrous tissue (Fig. 4.10); whereas lower levels of micromotion (20 µm) yielded stiffer bone growth over the implant (Fig. 4.10).

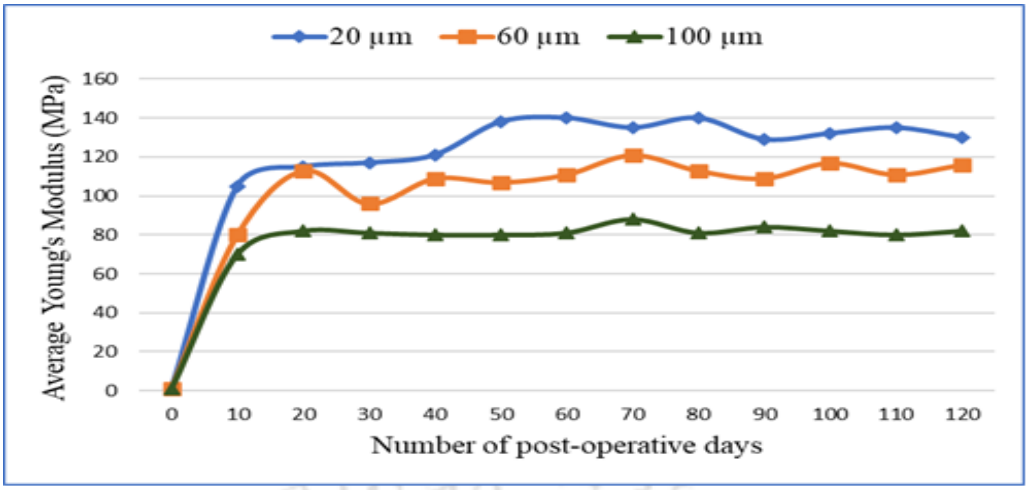

(a)

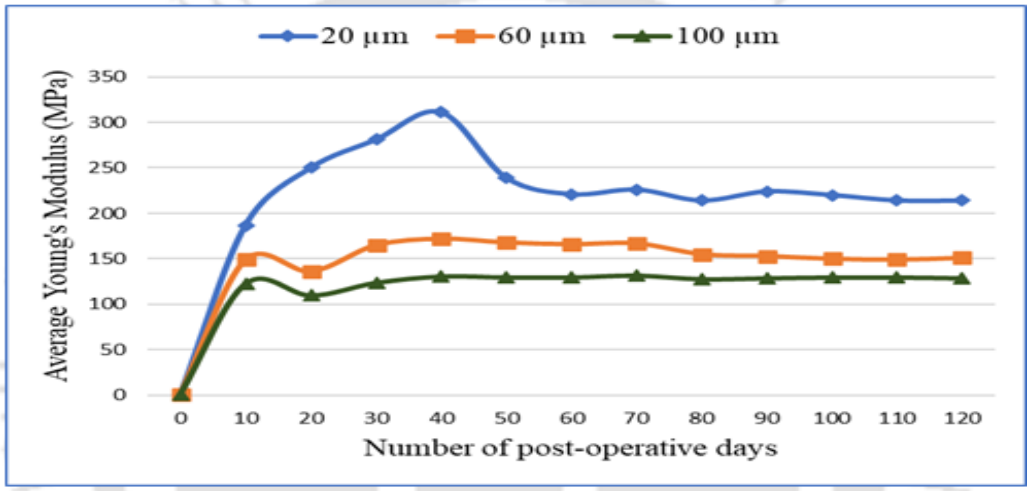

(b)

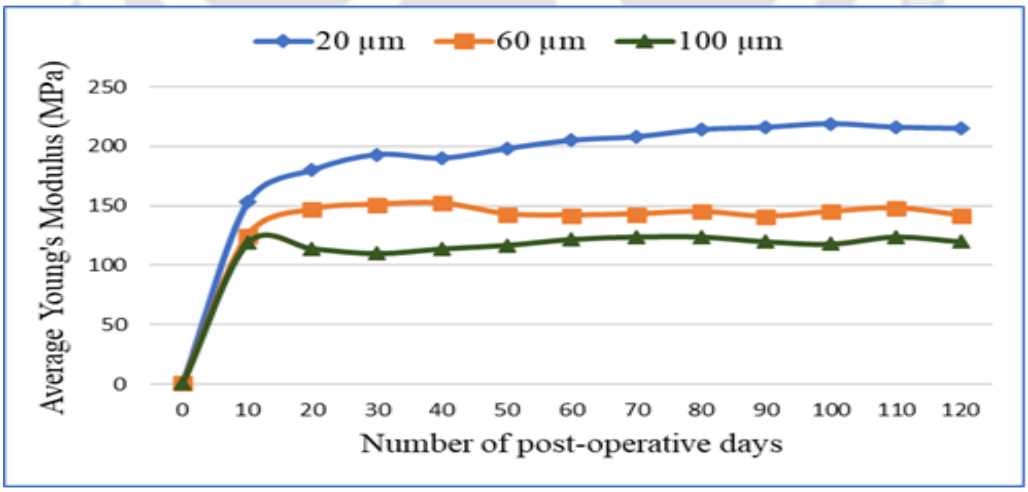

(c)

Figure 4.9 Variation in tissue stiffness over the entire healing period (120 days) for different levels of micromotion at the bone-implant interface for the three macro-textured designs on implant surface: (a) MODEL A, (b) MODEL B and (c) MODEL C.

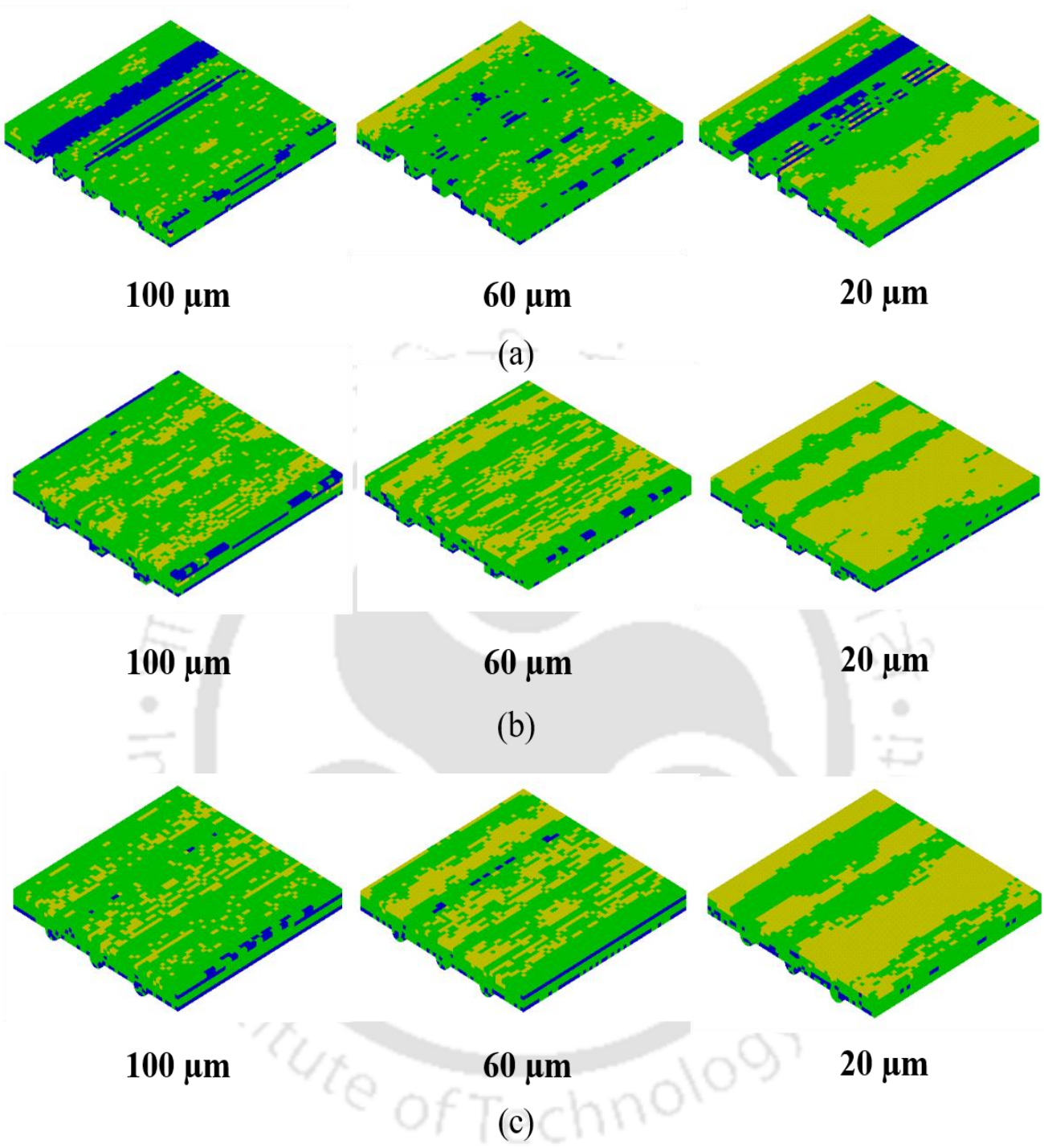

Figure 4.10 Influence of different levels of bone-implant micromotion on tissue growth distribution after full healing period (120 days) corresponding to the three macro-textured models: (a) MODEL A, (b) MODEL B and (c) MODEL C (Colour Map: Blue for fibrous tissue; Green for cartilaginous tissue; Yellow for Bone).

4.6 Clinical significance of the present work

From clinical significance, distance osteogenesis (Fig. 4.6) was observed in the present study indicating attainment of secondary stabilization of the implant (Kuzyk and Schemitsch, 2011). Results indicated the mineralization of woven bone at the periphery of the host bone site and gradual progression towards the smooth implant surface as was observed in few other *in silico* studies (Puthumanapully, 2010; Liu and Niebur, 2008; Sennerby et al., 1993). The previous study shows that distance and contact osteogenesis are not independent of each other (Choi et al., 2017). However, due to the absence of micro-roughness over the smooth macro-textures, contact osteogenesis was not observed in the present study. It was observed from the FE results that, the elements in the inter-groove spaces were subjected to higher levels of mechanical stimuli as compared to those at the host bone periphery. Following the mechanoregulatory model (Claes and Heigele, 1999; Liu and Niebur,2008) used in the present study, the mechanical stimuli at the periphery of the old host bone were found to be favourable for osteogenesis as compared to that in the vicinity of the implant surface, thereby resulting in distance osteogenesis.

The mechanoregulation based tissue-differentiation algorithm largely depends upon the variability in the geometric designs of implants and the amount of relative displacement at the bone-implant interface which further dictates the magnitude and distribution of stress/strains at the interface. Studies (Andreykiv et al. 2008; Mukherjee and Gupta, 2016; Mathai and Gupta, 2022) pertaining to implant design changes with relevance to mechanoregulation based tissue differentiation studies were employed to micro-topographical changes on the implant surface rather than macro-textured surfaces presently studied. Micro-textured surfaces produce robust local changes in mechanical environment in the length scale of microns favoring the mechanical stimulus (hydrostatic pressure and deviatoric strain) towards ossification. However, macro-textured surfaces in the length scale of millimeters produce higher magnitude of stresses/strains favoring more cartilage formation.

Moreover, the present scheme may serve as a substantial and powerful tool for any implant manufacturer and orthopaedic surgeon in choosing a trade-off implant texture on an implant surface. Such pre-clinical schemes further help in consolidating knowledge and understanding of how macro-textured designs on implant surfaces influence bone growth critical for proper biologic fixation. These

models may further be used as templates for more exhaustive parametric optimisation study (Chanda et al., 2015) resulting in novel bone interfacing implants.

4.7 Validation of the study

There is, however, a paucity of previous experimental as well as clinical data to validate the prognosis of the present mechanobiological simulation. In order to predict volumetric bone growth with the applied loading regime, it is necessary to study the 3D model of the bone-implant interface. Since experimental and clinical studies were not readily available, the prognosis on tissue growth at the bone-implant interface was compared with the results from a previous numerical study on osteogenesis around a micro-scale model on pore spaces of a beaded porous coated implant, assuming similar physiological environment (Puthumanapully, 2010). The percentage of bone growth predicted for 20 µm micromotion for the present models in this study was around 19% ± 3%. This result corroborates the findings of the previous study (16%) (Puthumanapully, 2010). A similar agreement was noted in the case of 100 µm micromotion value, for which the present study predicted bone growth of around 7%, as against 4% reported in the erstwhile work (Puthumanapully, 2010). Nevertheless, a slightly higher magnitude of predicted bone growth in the present study may be ascribed to variation in models concerning design morphology and dimensions. It may be worth noting that the morphology of the macro-textured designs in the present study is clinically relevant, although the dimensions may not be. However, the present scheme is flexible enough to incorporate variable dimensions in a future investigation.

It may further be noted that there is no clear relationship till date between the real postoperative time and the computational time step. Owing to the unavailability of clinical or histological data, the time frame for the simulation was considered as 16 weeks (~120 days) which was reported as the maximum time for precursor cells to reach maximum cell-density at the tissue in the interface (Lacroix et al., 2002; Isaksson et al., 2006b; Frost, 1989). Thus, the trends of the predicted results in the present study were found to be analogous to that of the previous numerical studies, thereby providing further confidence in the present methodology.

4.8 Limitations

The present computational scheme though could provide reasonably well-prediction on the bone growth over macro-textures on the implant surfaces; however, it is a simplification of the realistic postoperative bone growth condition which is also

affected by bone adaptation through remodelling and other parameters, e.g. physiological loading conditions, bone-implant gap, the porosity of bone, a surface coating on the implant as well as biochemical and patient-specific factors. Besides, a fully bonded interfacial condition is considered in the present investigation, thereby disregarding the fuzzy nature of the interface. However, a comparison between bonded and non-bonded interfacial condition in a previous study (Mukherjee and Gupta, 2016) reports that there is no significant difference in tissue growth and stiffness of the interface tissue layer. A more sophisticated and realistic model could consider continuous adaptive contact conditions, considering combined bone growth and remodelling phenomena to assess the growth patterns of new bone tissue around the implant (Fernandes et al., 1999; Chanda et al., 2020), albeit at the cost of relatively much higher computational load.

4.9 Summary

The present study will be useful as a pre-clinical assessment tool for implant manufacturers and orthopaedic surgeons while choosing a trade-off implant texture over the implant surface. The developed framework could predict the influence of commercially discernible macro-textured grooves/ribs on changes in tissue formation at the bone-implant interface. Some of the important conclusions drawn from this investigation are:

- Higher levels of micromotion (60 μm and 100 μm), leads to a higher rate of fibrogenesis and chondrogenesis followed by a lower rate of osteogenesis resulting in weak bone-implant interface strength.
- It could be inferred that changes in the bone-implant contact area with large surfaces through grooves or macro-textures might alter the mechanical environment required for optimum ossification and adherence to the implant surface.
- Unlike prior studies on micro-roughened surface that observed contact ostegenesis, this study concluded the presence of distance osteogenesis from the bone site towards the implant site.
- This may further infer that, smooth macro-textured implant surfaces trigger distance osteogenesis which might assist in formation of quicker bone bridges in presence of porous coated surface.

- A realistic optimisation study may lead to minor modifications in the design parameters of the proposed models for improved bone growth outcome.
- Nevertheless, a rigorous clinical assessment is also warranted to gain further insight into the tissue growth pattern on various implant surface textures.

CHAPTER 5

Influence of interface gaps and implant texture density on bone growth

Intramedullary implant fixation is achieved through a press-fit between the implant and the host bone. A stronger press-fit between the bone and the prosthesis often introduces damage to the bone canal creating micro-gaps. This chapter presents an investigation to study the influences of simultaneous opening/closing of gaps on bone growth over macro-textured implant surfaces. Models based on textures available on CORAIL and SP-CL hip stems have been considered and 3D finite element analysis has been carried out in conjunction with mechanoregulation based tissue differentiation algorithm. Additionally, using a full-factorial approach, different combinations of sliding and gap distances at the bone-implant interface were considered to understand their combined influences on bone growth.

5.1 Implant Fixation

Intramedullary implant fixation is a standard surgical procedure which is extensively used in re-establishing fractured bones and joints, further aiding to the treatment of various joint diseases such as osteoarthritis (OA), rheumatoid arthritis (RA), femoral fractures etc. The importance of uncemented fixation has already been discussed in Chapter 4. A proper combination of both primary stability and secondary fixation is crucial for long term success of such intramedullary fixation devices (Ghosh et al. 2020).

As discussed earlier in Chapter 4, failure mechanisms of such implants are still not precise (Chanda et al. 2016) and the major cause is attributed to the improper design of prosthesis (Huiskes and Boeklagen 1988; Viceconti et al. 2001; Sánchez et al. 2021a). Surface roughness, comprising of both micro-textures (Mukherjee and Gupta 2016) and macro-textures (Ghosh et al. 2020) are known to influence biologic fixation as they influence the local mechanical environment at the bone-implant interface.

5.2 State of the art

Improper press-fit may lead to implant loosening and thus insufficient primary fixation. Proper press-fit fixation induces higher compressive stresses at the bone-implant interface which further allows increased frictional movement (Sánchez et al. 2021a). However, these contact forces might cause abrasion and irreversible bone damage, severely affecting the interference-fit (Gebert et al. 2009; Berahmani et al. 2018; Sánchez et al. 2021a; Sánchez et al. 2021b). Surgical protocols ensure a complete contact between the bone and the implant to ensure long-term biologic fixation. In spite of careful operative procedures, the micro bone incisions, on the other hand, do not always match the implant surface, resulting in gaps between the bone and the implant (Huiskes and Boeklagen 1988; Viceconti et al. 2001; Sánchez et al. 2021a). These gaps are not static and may open and close with the variation in physiological loads applied during daily human activities, thus interfering with the primary as well as jeopardizing the secondary stability of the implant (Sánchez et al. 2021a). Figure. 4.1 shows the loading conditions at the bone-implant interface for a total knee arthroplasty (TKA). Shear displacement at interface represents the bone-implant relative micromotion (Ghosh et al. 2020; Sánchez et al. 2021a) also known as “sliding distance” (Bougherara et al. 2007; Cristofolini et al.

2007; Ghavidelnia et al. 2020), whereas, normal displacement, also referred as "normal micromotion or gap distance" (Bougherara et al. 2007; Cristofolini et al. 2007; Ghavidelnia et al. 2020) simulates the opening and closing of gaps (Sánchez et al. 2021a; Sánchez et al. 2021b). Very few studies (Bougherara et al. 2007; Gebert et al. 2009; Berahmani et al. 2018; Sánchez et al. 2021a; Sánchez et al. 2021b) have been performed on the influence of interference-fit and opening/closing gap on primary stability of the implant. Sánchez et al. (2021a) reported the influence of two different levels of press-fitting on primary stability of uncemented femoral component in a TKA. A recent study by Sánchez et al. (2021b) also reported the effect of interference-fit on primary fixation of tibial component. Gebert et al. (2009) investigated the influence of interference-fit on the primary stability of cementless femoral resurfacing prosthesis. An earlier investigation by Berahmani et al. (2018) studied the influence of press-fit and induced bone damage to the mechanical fixation of knee implant. Bougherara et al. (2007) designed a novel biomimetic polymer-composite femoral stem which minimizes the sliding and gap distances to a considerable extent as compared to a similar metallic stem. However, hardly any studies were performed to assess the biologic fixation or secondary stability of the implant considering opening/closing interface gap as the primary criteria of loading.

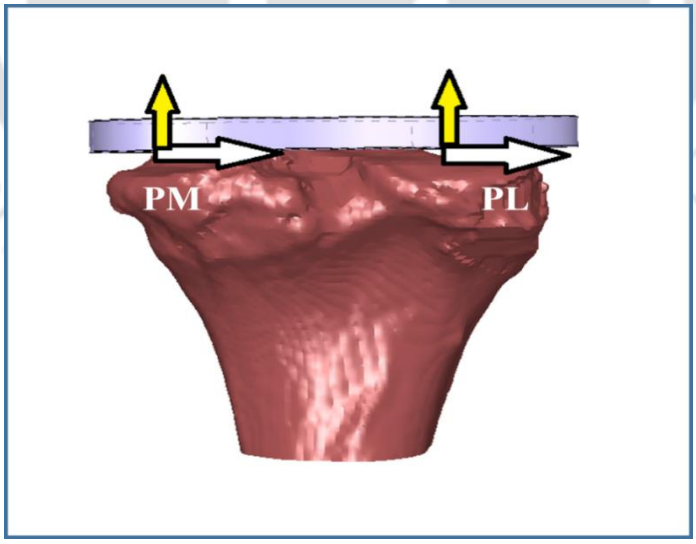

Figure 5.1 Loading conditions at bone-implant interface around a tibial component in Total Knee Arthroplasty (TKA). Acronyms: Posterior Medial (PM), Posterior Lateral (PL). Color Map: Brown segment (Bone part of Tibia), Grey component (Tibial Component), White Arrows (bone-implant relative micromotion) and Yellow Arrows (normal loading responsible for opening/closing of interface gap)

Texture density is defined as the number of similar micro or macro-textures on unit implant surface area (Allen and Raeymaekers 2021). Most of the earlier investigations (Nishimura et al. 1993; Zhang et al. 2013) on texture density were focussed on the tribological aspects and bearing surface of the implant surface. Nishimura et al. (1993) reported optimum texture density to enhance lubrication of the bearing surfaces of artificial joints by Pin-On-Disk experiments. Zhang et al. (2013) also investigated the influence of surface texture density on two different engineered surfaces of steel and UHMWPE. Similar to thread pitch of a dental screw, texture density also plays a major role in enhancing bone-to-implant contact (BIC) and biomechanical distribution of applied loads (Chun et al. 2002; Geng et al. 2004; Steigenga et al. 2004). Higher density of such macro-textures and threads increases BIC, thus enhancing primary stability of the implant by achieving proper mechanical interlocking (Ryu et al. 2014). Earlier investigation on a hemispherical surface micro-texture on Birmingham Hip Resurfacing (BHR) cup reported the influence of texture density on osseointegration (Mukherjee and Gupta 2017a). However, none of the studies investigated the influence of surface texture density of macro-textured implant surfaces on bone growth.

5.3 Objective of this investigation

The purpose of this investigation thus is to study the influence of differential opening/closing gap between the implant and the bone on bone growth over two different macro-textured implant surfaces at constant micromotion. Further investigation has been performed on the influence of texture density on bone growth over such macro-textured surface topologies.

5.4 Problem definition

In Chapter 4, the study on bone growth over macro-textured surface morphologies of implants were restricted to loading conditions with constant normal micromotion and variable tangential micromotion. Having understood the importance of normal micromotions, in this investigation two similar macro-textured surfaces as discussed in Chapter 4 have been considered to study the influence of variation in interface gap on bone growth. Furthermore, realizing the usefulness of texture density, bone growth has been evaluated with a change in texture density for a single macro-textured implant surface. The estimation of qualitative trends of bone and other tissue growth with the mechanoregulatory algorithm as shown in Chapter 4, Table 4.1 might provide further insight for future clinical investigations on the influence

of different macro-texture parameters and variable loading conditions on secondary stability of implant.

5.4.1 Representative bone-implant interface models

Two distinct 3D macro-textured representative bone-implant interface models namely, **RVIM 1** and **RVIM 2** were modelled in CATIA® V5R20 software (Dassault Systèmes, France) as shown in Figure 5.2. **RVIM #** denotes Representative Volume Interface Model 'Number'. The surface topography was modelled with suitable macro textures that can be seen on widely available femoral prosthesis. Textures on the implant surface of **RVIM 1** contains uniformly spaced prismatic rectangular ribs that is roughly based on the surface topology of anterior-posterior surfaces of proximal regions of a CORAIL stem. Conversely, **RVIM 2** contains equally spaced channels with hemispherical grooves as mimicking the anterior-posterior surfaces of proximal and central areas in SP-CL stems.

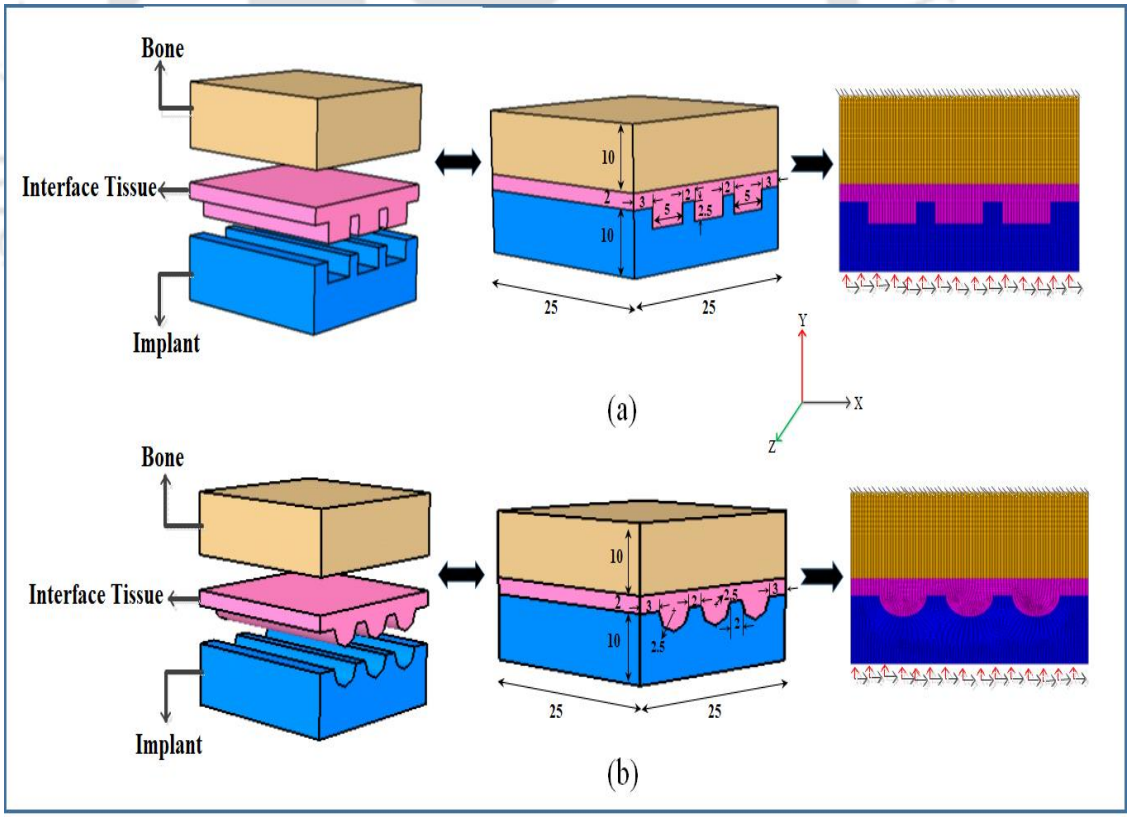

Figure 5.2 3D CAD model and FE model of representative bone-implant interface for (a) RVIM 1; (b) RVIM 2. Color Map: Black Arrows (bone-implant relative micromotion) and Red Arrows (normal loading responsible for opening/closing of interface gap. All dimensions are in mm.

The significant dimensions (height of ribs/grooves, rib thickness, bone-implant interface gap) of the models were chosen from a radiographic image of CLS Spotorno stem extracted using an open source image processing program, ImageJ v1.53a (National Institutes of Health and Laboratory for Optical and Computational Instrumentation, University of Wisconsin, USA) considering the clinical reliability and manufacturing feasibility of the surface topologies. Properly fabricated macroscopic textures covers the implant surface in both the models. As shown in Figure 5.2, the mid-section in the models were designed so as to represent a granulation tissue, while the remaining section of the model illustrates healthy bone. Although 1-2 mm interface thickness is sufficient for proper biologic fixation, a bone-implant interface gap of 2 mm was maintained in each of the representative bone-implant interface models in the present investigation. A suitable osteogenic environment with growth factors, surface coating and micro-roughened surfaces on implant surface, proper vascularisation etc. was assumed to be prevalent during qualitative estimation of bone growth over each of the implant surfaces.

5.4.2 FE models, loading and boundary conditions

The 3D CAD models so generated were imported to ANSYS V14.5 FE software (ANSYS Inc., Canonsburg, PA, USA) for further analysis. Each models were meshed (Fig. 5.2) using coupled linear elastic eight-noded hexahedral elements (SOLID 185). Mesh sensitivity study was performed for obtaining good accuracy to the FE results.

5.4.2.1 Material properties

All the volumetric sections of the models i.e. implant, granulation tissue and bone possess linear elastic and isotropic material properties. A high-nitrogen stainless steel alloy M30NW (Aubert & Duval, France) with Young's modulus, E = 195 GPa was considered for the implant. Young's modulus of healthy parent bone was taken as 500 MPa (Puthumanapully 2010), while that for soft granulation tissue was taken as 1 MPa (Mukherjee and Gupta 2016; Puthumanapully 2010) as obtained from literatures. The bone and the implant possess a Poisson's ratio of 0.3 (Mukherjee and Gupta 2016; Puthumanapully 2010), while granulation tissue has a Poisson's ratio of 0.167 (Mukherjee and Gupta 2016; Puthumanapully 2010). Bonded contact was considered at the bone-tissue and implant-tissue interfaces (Mukherjee and Gupta 2016). Node-sharing method was used while creating the

contact between the bone-tissue and implant-tissue interfaces.

5.4.2.2 Loading and boundary conditions

Similar to the loading situation (Sánchez et al. 2021a; Sánchez et al. 2021b) as shown in Figure 5.1, shear displacement in the global X direction (Fig. 5.2) was provided at the bottom surface of the implant to simulate the micromotion (or sliding distance) at the bone-implant interface. Conversely, to simulate the opening/closing of the interface, a normal displacement in the global Y direction was provided as shown in Figure 5.2. Normal micromotion eventually leads to opening and closing of the bone-implant interface leading to increase and decrease of the interface gap and the whole mechanical procedure occurs at the same time progressively over the initial post-operative healing period (Sánchez et al. 2021a). In the present study, a constant shear displacement of 20 µm was provided at the bottom surface of implant, while, normal displacements of 5 µm, 10 µm, 20 µm and 40 µm were provided in each case study to simulate the opening/closing of interfaces (Sánchez et al. 2021a). It is assumed that higher levels of normal displacement (or higher gap distance) will decrease the interfacial gap while undergoing daily activities. The upper surface of the bone was restricted in all global coordinates (Puthumanapully 2010; Mukherjee and Gupta 2017a).

Additionally, to study the combined influence of sliding and gap distances in a qualitative assessment of bone-growth over macro-textured implant surface, RVIM 1 was chosen for the analysis. Realistic data for micromotion (both tangential and normal) were selected by varying the bone-implant relative micromotion (displacement in X: 5 µm,10 µm,15 µm) and normal micromotion (displacement in Y: 5 µm,10 µm,15 µm). Three values of each micromotion parameters were considered that combined to result in 9 combinations of micromotions (3^2 = 9 combinations of FE analyses) based on a full-factorial approach. Full-factorial approach was implemented to make use of all the possible combinations of tangential and normal micromotions while assessing their influence on bone growth. Tangential and normal displacement are represented as (X displacement in µm, Y displacement in µm).

5.4.3 Mechanoregulation based tissue differentiation algorithm

The interfacial gap between the host bone and the implant was primarily assumed to be filled with a soft homogeneous medium, known as "granulation tissue" (Gardner et al. 2000; Lacroix et al. 2002; Ghimire et al. 2020). It should be emphasized, however, that when tissue differentiation occurs on the iterative timeframe, the initial state of granulation tissue homogeneity will cease out. Granulation tissue is filled with sufficient blood vessels formed by angiogenesis to supply nutrients to the newly formed cells and inflammatory cells to remove injured portion of the tissue. The progressive bone growth phenomenon was simulated using a mechanoregulatory scheme as discussed in Chapter 3, Figure 3.1 that simulated the migration of multipotent stromal cells, also referred as mesenchymal stem cells (MSCs), from the bone site within the region of soft granulation tissue using a transient-diffusion model as mentioned in Chapter 4, Equation 4.1.

A constant healing phase of T′=120 days or approximately four months was chosen for the migration of stromal cells for all the analysis in the present study. No-flux condition was considered at the peripheral surfaces of the tissue, which represents no cellular loss from the tissue. The concentration of other cells, insignificant for tissue-differentiation, in the granulation tissue is assumed to be zero (Andreykiv et al. 2008a; Puthumanapully 2010; Mukherjee and Gupta 2017a). The concentration of stromal cells at the bone interface (c_{max}) was assumed to be unity (1.0).

Assuming sufficient vascularisation, local mechanical signals (dilatational hydrostatic pressure and deviatoric strain) determine the differentiation of stromal cells into various osteogenic cells (Barry 2006; Isaksson et al. 2006a). These new cellular phenotypes, on sufficient maturation, would manifest into bone, cartilage, and fibrous tissue (Claes and Heigele 1999). The conditions for formation of various tissue phenotypes in response to mechanical stimuli utilized in the progressive mechanoregulatory algorithm has been discussed in Chapter 3, Table 3.1.

To simulate the co-existence of granulation tissue and new tissue phenotype in an element at any instant, the effective tissue material properties (elastic modulus, E and Poisson's ratio, υ) were numerically computed using a rule of mixture as discussed in Chapter 4, Equations. 4.2 and 4.3.

To avoid computational instability after each iteration, a temporal smoothing methodology was implemented to update the material properties in each finite element, following Equations. 4.4 and 4.5 as mentioned in Chapter 4.

To implement the mechanoregulatory based tissue differentiation algorithm, a custom script written in MATLAB environment (Matlab 2017a, The MathWorks Inc., Natick, MA, USA) was developed separately. A master batch (DOS) script was developed to consecutively launch ANSYS module for FE analysis and MATLAB module for prediction of tissue differentiation, in every iteration. Every iteration in this numerical framework represents one post-surgical day. The entire simulation was set to run in batch mode in a high-performance workstation (Windows 10 Pro, 8-core AMD Ryzen 7 3700X CPU, 64 GB RAM, speed 3.59 GHz).

5.5 Results and Discussion

The goal of this *in silico* study has been to anticipate how a macro-textured implant surface affects tissue development patterns at different magnitudes of normal micromotion at the bone-implant interface. For a comparative examination of the implant's growth behaviour, two geometrically distinct 3D macro-textured surface topologies have been investigated. The numerical study is based on a mechanoregulation based tissue-differentiation algorithm, which is consistent with controlled animal investigations of fracture healing of long bones (Isaksson et al. 2006b). Using the developed FE models in conjunction with mechanoregulatory algorithm, results have been generated to study the influence of variation in interface gap and texture density on bone growth over macro-textured implant surfaces.

5.5.1 Mesh convergence

Since the interfacial tissue is the primary site of bone-growth between the host bone and the implant, peak von Mises stress at the bone-implant interface region was studied to check the numerical convergence on the predicted results. Three different FE meshes ~2,375 elements (coarse mesh), ~13,062 elements (medium mesh), ~37,358 elements (fine mesh) for **RVIM 1** and ~3,975 elements (coarse mesh), ~17,849 elements (medium mesh), ~37,988 elements (fine mesh) for **RVIM 2** were chosen to predict the peak Von Mises stress at the interface. Interestingly, the maximum difference in peak Von Mises stress was found to be 33.33% and 14.28% between the coarse mesh and the medium mesh for **RVIM 1** and **RVIM 2** respectively, whereas, the same is observed to be 6.25% and 5.25% between the

medium mesh and fine mesh for **RVIM 1** and **RVIM 2** respectively. Considering the computational cost and efficiency, the medium mesh with element sizes of 0.6 mm for **RVIM 1** and 0.5 mm for **RVIM 2** are found to be threshold values for further numerical simulations with sufficient accuracy.

5.5.2 Influence of interface gap on bone growth

Figure 5.3 shows the percentage of tissue development over two different macro-textured implant surfaces with varying opening/closing gap and a consistent degree of micromotion (20 µm). The qualitative prediction of bone growth for **RVIM 1** and **RVIM 2** was found not to vary significantly with variation in opening/closing interface gap over the healing period. The predicted levels of bone growth ranges from 12.05% to 13.00% with variation in normal displacement from 20 µm to 5 µm in **RVIM 1**. Similar findings were observed in **RVIM 2** with predicted bone growth levels ranging from 11.4% to 12.52 % with decrease in normal displacement from 20 µm to 5 µm. Interestingly, both the models predicted a higher levels of bone growth with nearly 16.67% (**RVIM 1**) and 14.15% (**RVIM 2**) formation of osteoblast for normal displacement of 40 µm. Conversely, a sharp decline in the percentage of softer cartilaginous tissue from 75.64% to 53.94% was observed with increasing levels of interface normal micromotion in **RVIM 1**. A similar observation was recorded for **RVIM 2**, where a declining trend of cartilage formation ranged from 76.02% for 5 µm to 53.60% for 40 µm over the entire healing phase. A higher percentage of formed fibrous tissue was observed for both the models with increasing levels of normal displacement. **RVIM 1** predicted a steep jump of 10.96% to 29.38% in the formed fibrous tissue with increased levels of normal displacement. Similar records were noted for **RVIM 2** with decreasing levels of fibrous tissue from 32.25% to 11.45% with reduced levels of normal displacement.

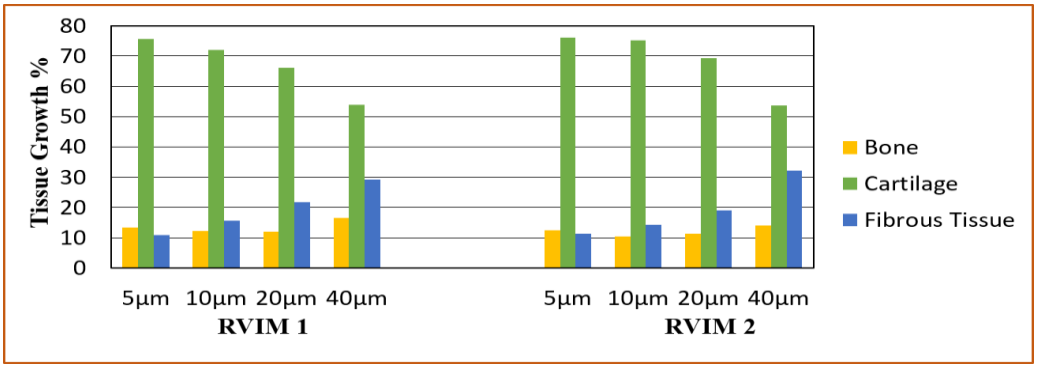

Figure 5.3 Percentage of formed tissue over two different macro-textured implant surfaces with varying opening/closing gap

The regional distribution of tissue phenotypes at the interface due to macro-textured surfaces is shown in Figure 5.4. Bone growth decreased further from the interfacial boundaries in the centre of the interface area. Soft cartilaginous tissue was prominent throughout the interface with higher levels at the mid-region. Formation of cartilaginous tissue was higher at lower values of normal micromotion. This is due to the fact that, lowered values of normal displacement produces successive opening and closure of interface with increased gap. Higher interfacial gap thus produces lesser stress regime over the interface region which favours formation of cartilage. Higher formation of softer cartilage might promote endochondral ossification thus forming mature bone. This finding is clinically attributable towards formation of bone from cartilage through hypertrophic modifications of the chondrocytes (Breeland et al. 2021) followed by further calcification of the extra cellular matrix (ECM).

Conversely, as shown in Figure 5.4, fibrous tissue development was more evident along the margins of the ribs and inter-rib corners in **RVIM 1** and groove corners in **RVIM 2** due to higher stress concentration in the region compared to other places in the interface tissue layer, which favours fibroblast growth. This finding is supported by a previous study (Tan et al. 2017), anticipating weaker connective tissues and less bone development at the implant-bone interface due to an increase in stress concentration surrounding the implant. Moreover, higher deposition of fibrous tissue towards the implant surface was prominent at higher normal displacement. The formation of bulky fibrous matrix for higher normal displacement (or higher gap distance) for both the models might be attributed to the daily uniform oscillations and decreased interface gaps which produces higher stress

regime around the implant which facilitates fibrous encapsulation (He et al. 2017) over the implant surface.

Fibrous encapsulation (Abu-Amer et al. 2007; He et al. 2017) around the implant surface reduces the chances of contact osteogenesis (Berglundh et al. 2003) thus inhibiting formation of bone bridges. Inhibition of bone bridges might reduce the strong bony fixation across the interface region, thus leading to implant instability (Barry 2003; Abu-Amer et al. 2007).

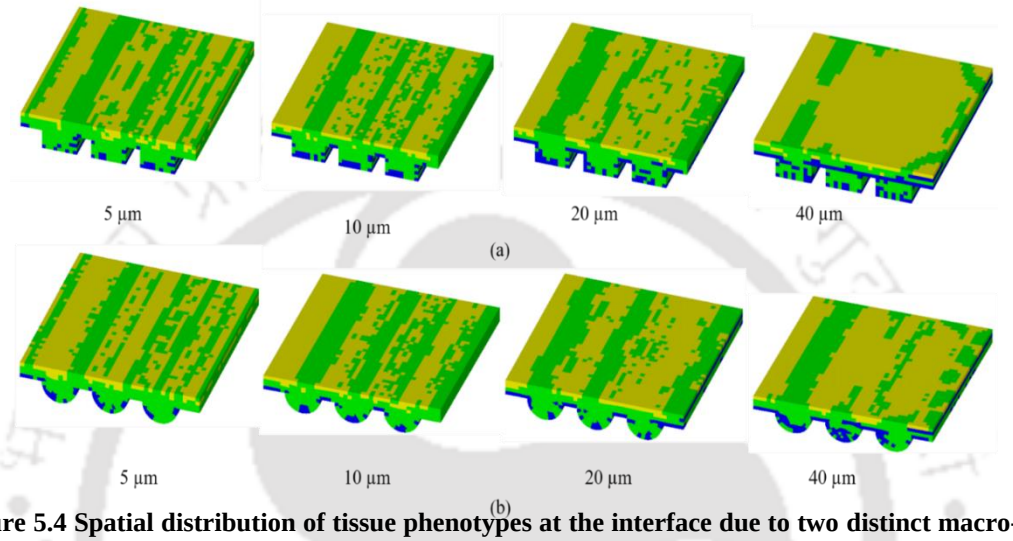

Figure 5.4 Spatial distribution of tissue phenotypes at the interface due to two distinct macro-textured surfaces (a) RVIM 1 (b) RVIM 2 at different normal displacement with constant shear micromotion (20 µm). Color Map: Blue represents fibrous tissue, Green represents cartilaginous tissue, Yellow represents bone

5.5.3 Influence of texture density on bone growth

The differential tissue formation with the variation in texture density for **RVIM 1** for varied levels of normal displacement is shown in Figure 5.5. In the present investigation, three different number of ribs from the **RVIM 1** on same implant base area (25 x 25 cm^2) was chosen to study the influence of texture density on tissue differentiation over macro-textured surface morphology. **RVIM 1.1** represents implant with 2 ribs, **RVIM 1.2** comprises of 3 ribs while, **RVIM 1.3** contains implant surface with 4 ribs over it. Rest of the other dimensional parameters (initial interface gap of 2 mm, bone surface area and volume) were kept fixed.

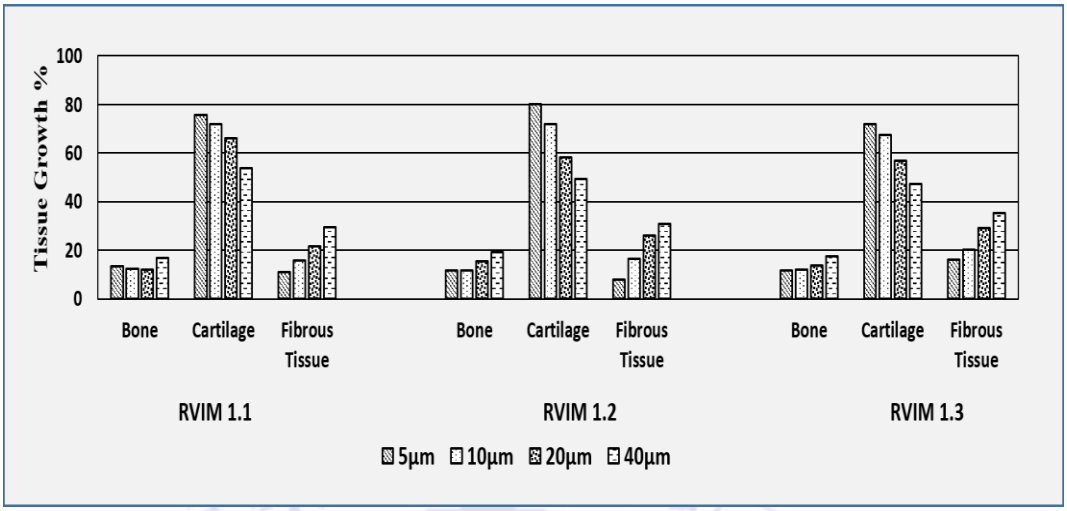

Figure 5.5 Percentage of formed tissue with variation in texture density with varying opening/closing gap

The levels of bone growth for **RVIM 1.1** ranged from 12.05% at 20 µm normal displacement to 16.67% at 40 µm. Whereas, the levels of bone growth were relatively higher (13.40%) at 5 µm as compared to higher normal micromotion of 10 µm (12.26%) and 20 µm (12.05%). Conversely, amount of bone growth shows a significant pattern for the other two case scenarios. Bone growth was relatively lesser at lower normal displacement and higher for the higher values of normal micromotion for rest of the two models. **RVIM 1.2** predicted a bone growth of 11.71% at 5 µm and a gradual increase to 19.48% at 40 µm normal displacement. Similar findings were reported for **RVIM 1.3** which predicted a bone growth of 11.73% at 5 µm and a steady increase to 17.58% at 40 µm normal micromotion. This prediction suggests that there is no linear relationship between the texture density and the amount of bone-growth. The present finding is well-supported by an earlier study (Mukherjee and Gupta 2017a) on surface micro-texture on BHR cups. Although an earlier study (Mukherjee and Gupta 2017a) reported that geometric parameters of the texture such as texture height, diameter, inter-rib/groove spacing have an influence over tissue growth, investigation by Mukherjee et al. (2017a) reveals that there is no significant linear correlation between number of identical textures and bone growth.

Similar to the earlier findings on the influence of interface gap on bone growth, formation of soft cartilaginous tissue was higher (75.64% in **RVIM 1.1**, 80.17% in **RVIM 1.2**, 71.96% in **RVIM 1.3**) at lower normal displacement (5 µm) and a steep decrease of formed cartilage was observed with gradual increase in

normal micromotion values. Similarly, fibrous tissue formation was relatively higher (29.38% in **RVIM 1.1**, 31.00% in **RVIM 1.2**, 35.27% in **RVIM 1.3**) at higher normal displacement (40 μm) as compared to lesser values of displacement. The current approach thus resulted in softer fibro-cartilage at the bone-implant interface when interfacial displacements were applied, which is in agreement with earlier investigation (Liu and Niebur 2008). Although there is a dearth of *in silico* and clinical studies to assess the influence of normal micromotion on secondary implant stability, however, previous experimental findings (Qin et al. 1996), which indicated that greater levels of shear micromotion might lead to implant failure, support the development of a stable interface at lower levels of normal displacement at bone-implant gap. In addition, it is clear from the Figure 5.6 that, increase in the number of identical surface texture with grooves/ribs will increase the probability of deposition of fibrous tissue at those grooved/ribbed basins by fibrous encapsulation (Abu-Amer et al. 2007; He et al. 2017) thus further inhibiting the interface strength. However, the distribution of immature bone was found to be identical for similar loading condition. The present investigation on influence of texture density of macro-textured implant surface on bone growth thus reports a complex non-linear relationship between texture density and bone growth which might be further analysed using a machine learning based predictive tool (Chanda et al. 2016) over a large dataset.

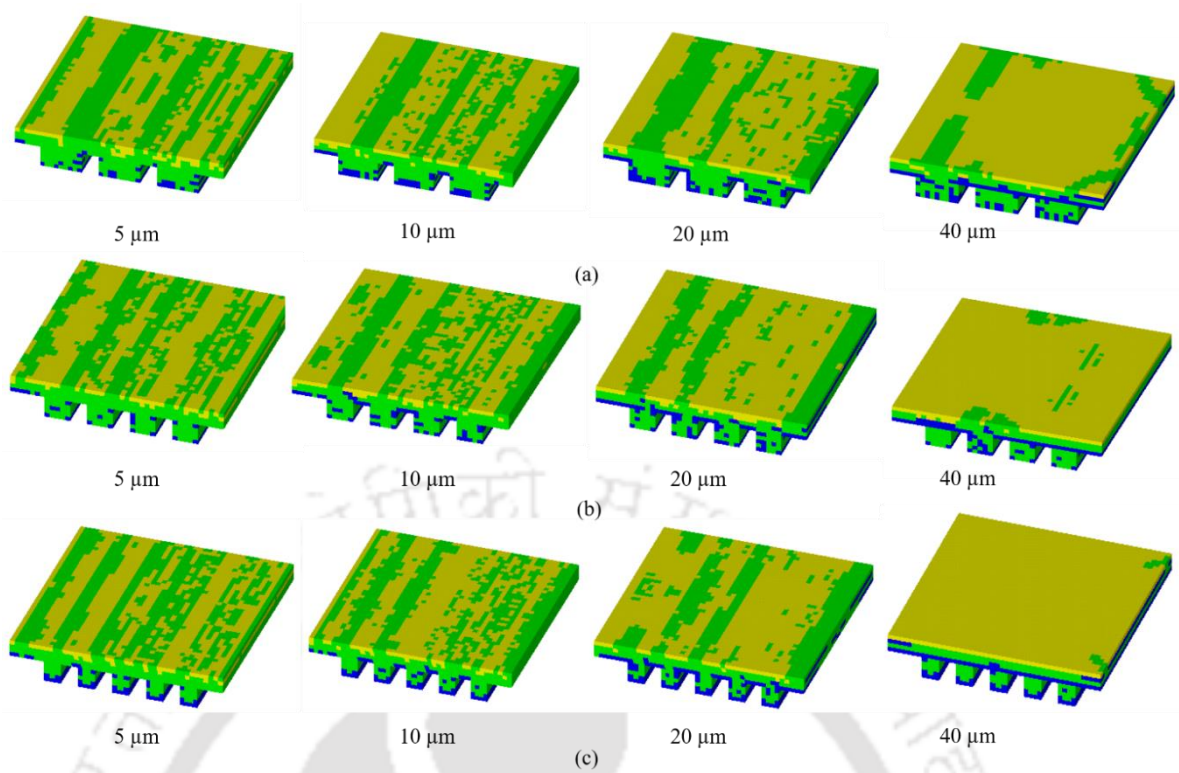

Figure 5.6 Spatial distribution of formed tissues at the interface with variation in texture density in RVIM 1 at different normal displacement with constant shear micromotion (20 µm). (a) RVIM 1.1 (b) RVIM 1.2 (c) RVIM 1.3. Color Map: Blue represents fibrous tissue, Green represents cartilaginous tissue, Yellow represents bone.

5.5.4 Combined influence of sliding and gap distance towards bone growth

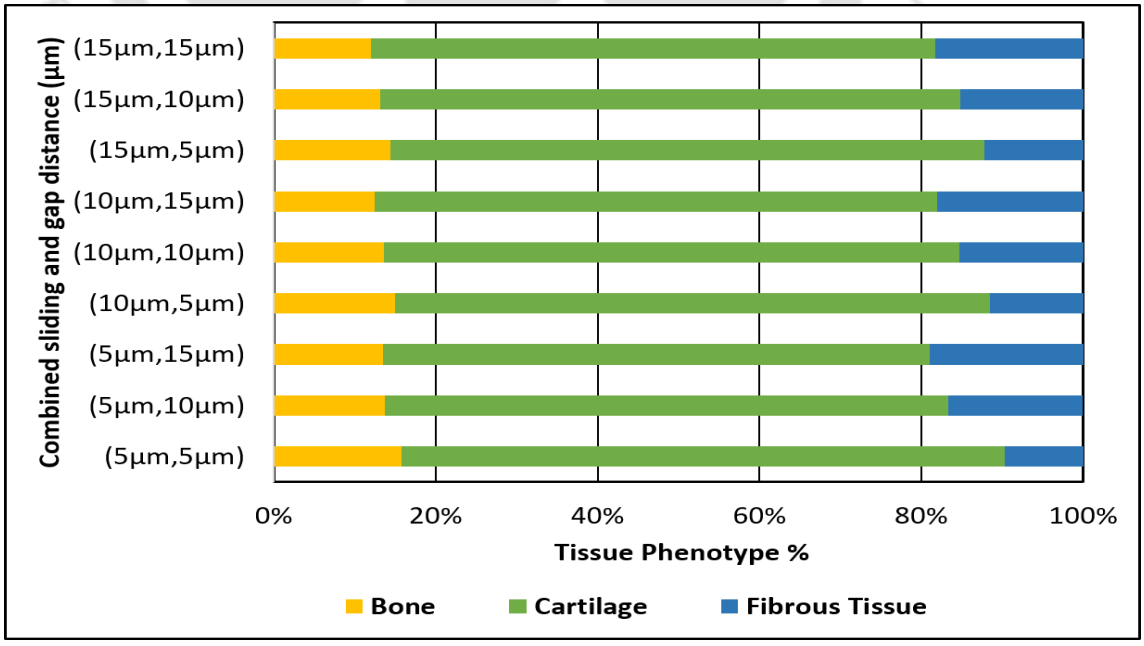

Figure 5.7 Percentage of formed tissue with combined variation in sliding distance and gap distance at the bone-implant interface

Figure 5.7 shows the differential distribution of tissue phenotypes formed for all the combinations of tangential and normal micromotions. The levels of tissue phenotype for (5 µm, 5 µm) combination of micromotions shows a bone growth of around 15.82%, while soft cartilaginous tissues formed in abundance around 74.55% and rest is fibrous tissue (9.63%). As normal micromotion values are increased incrementally, keeping the tangential micromotion constant (5 µm), amount of bone growth decreased (13.69 % for 10 µm normal micromotion, 13.51% for 15 µm normal micromotion) while increase in fibrous tissue (16.63% for 10 µm normal micromotion, 18.94% for 15 µm normal micromotion). There is also a decrease in formation of cartilage at higher normal micromotions (69.68% for 10 µm normal micromotion, 67.55% for 15 µm normal micromotion). A similar finding was observed in other cases also when the normal micromotions were increased while maintaining the tangential micromotion constant. Moreover, bone growth is also found to be inhibited with the increase in tangential micromotion from 5 µm to 15 µm, keeping the normal micromotion to a fixed value in each cases. It is also interesting to note that, simultaneous increase of both the sliding and gap distances from their previous combination say for example, from (5 µm, 5 µm) to (10 µm, 10 µm) or (10 µm, 15 µm) have also significant influence of formation of tissue phenotype at the bone-implant interface. When both the micromotion values were simultaneously increased from (5 µm, 5 µm) to (10 µm, 10 µm), bone growth and cartilage formation reduced from 15.82% to 13.66% and 74.55% to 71.03%, respectively. Fibrous tissue was observed to have increased in parallel from 9.63% for (5 µm, 5 µm) combination to 15.31% for (10 µm, 10 µm) combination. In addition, the increase of fibrous tissue for simultaneous enhancement in both the micromotion values was substantially significant as compared to reduction in growth of bone and cartilage for the same scenario. There is an increase of 58.98% in the formation of fibrous tissue as compared to 13.65% reduction of bone growth and mere 4.72% reduction of formed cartilage on simultaneous increase of micromotion from (5 µm, 5 µm) to (10 µm, 10 µm). Similar observations were identified for other similar combinations as well which has been shown in the Figure 5.7.

Formation of fibrous tissue was predominant for higher micromotion values irrespective of the direction of application of displacements (Puthumanapully 2010; Tan et al. 2017). Compared with two different combinations of micromotions, bone growth was found to be higher if any one of the micromotion values in the

combination is found to be lower than the corresponding value of the other combination as shown in Figure 5.7. This finding is well-supported by some of the previous studies (Bougherara et al. 2007; Ghavidelnia et al. 2020). On the other hand, simultaneous increase of both the shear and normal micromotion led to a significant increase in fibrous tissue and thereby fibrous encapsulation (Abu-Amer et al. 2007; He et al. 2017) over the implant surface as compared to the amount of reduction in the formation of bone and cartilage. This observation suggests that lower the values of both the directional parameters of micromotion, higher reduction in formation of fibrous tissue can be achieved. Such a reduction in micromotion can be achieved by following proper surgical protocols followed by a proper design of implant. However, it is noteworthy that, completely eliminating both the components of micromotion at the bone-implant interface might have negative influence on bone growth and implant stability (Ghavidelnia et al. 2020). Although both the shear and normal micromotion plays an important role in deciding the type and amount of tissue phenotype formed at the bone-implant interface, however, the directional component with the lower value of displacement (Ghavidelnia et al. 2020) in each case plays the pivotal role in formation of different tissue phenotypes.

5.6 Clinical significance of the study

Distance osteogenesis (Kuzyk and Schemitsch 2011) was seen in the current research, showing the progression towards long-term secondary stability of the implant (Fig. 5.4 and Fig. 5.6). This observation is well-supported by earlier animal studies (Berglundh et al. 2003; Sennerby et al. 1993) on bone formation around endosseous implants studied on Labrador dogs (Berglundh et al. 2003) and tissue response on implantation in a rabbit tibial bone (Sennerby et al. 1993). Berglundh et al. (2003) reported continuous appositional bone formation at the site of the parent bone progressing towards the implant surfaces. Sennerby et al. (1993) also observed woven bone mineralization at the boundary of the healthy bone and slowly extending towards the smooth implant surface. According to an earlier study (Choi et al. 2017), distance and contact osteogenesis are not mutually exclusive. However, contact osteogenesis was not seen in the current research due to the lack of a surface coating and roughened surface over the smooth surface topologies.

5.7 Validation of the present study

The present study predicted levels of bone growth ranging around 15% ± 5% for a shear displacement of 20 µm. This finding is well-supported by previous numerical investigation on tissue-differentiation over beaded porous coated implant (Puthumanapully 2010). For a similar loading and boundary conditions, Puthumanapully (2010) reported a bone growth of around 16% over beaded implant surface. There is a scarcity of previous experimental and clinical data to back up the current study's prediction. Difference in models involving surface topology and dimensions may account for a somewhat variation in magnitude of projected bone growth in the current study. However, the evidence from this qualitative investigation performed earlier (Puthumanapully 2010) thus provide sufficient confidence to the results obtained from the present study.

It should also be highlighted that there is currently no obvious link between real healing time in months or years and iterative pseudo time-scale (Huiskes et al. 1987; Chennimalai Kumar et al. 2010; Avval et al. 2016). Due to the lack of experimental evidences, the numerical time scale for the simulation was set to 120 iterations, which corresponded to 120 days of healing phase, which has been described as the maximum period for stromal cells to achieve maximal cell density in the interfacial gap (Frost 1989; Lacroix et al. 2002).

5.8 Limitations

The FE models used in the present investigation to predict the amount of tissue growth is a simplification of a realistic bone-implant model, that is further influenced by anatomic topology of the bone, anisotropic material property of the bone (Dickinson et al. 2012), design of implant (Chanda et al. 2016), inter-patient variability (Mukherjee and Gupta 2016) and loading conditions under daily activities (Chanda et al. 2016). Failure of an orthopaedic implant also depends upon proportion of bone-remodelling (Huiskes et al. 1987; Chanda et al. 2020), tribological aspects (Ghavidelnia et al. 2020) and variation of surgical protocols which are not accounted in the present numerical model.

The diffusion model used in this study to simulate the processes of migration of stem cells, however, does not include the reaction terms which might account for other cellular activities (Lacroix et al. 2002). Nonetheless, even if reaction terms were included to the diffusion equation, the underlying patterns of tissue

differentiation would not be anticipated to change significantly (Lacroix et al. 2002). In addition, a prior investigation (Mukherjee and Gupta 2017b) reported that both the phenomenological algorithm used in the present study and cell-phenotype specific algorithm that incorporates cell migration, proliferation, differentiation and apoptosis seem to predict similar spatial distribution of newly formed tissue at the bone-implant interface region. Nevertheless, this computational scheme is flexible enough for comparative assessment of bone growth over multiple bone-implant interface models.

In the present study, influence of texture density on tissue growth was investigated by varying the normal component of displacement keeping the shear component constant. Although a comprehensive study with combined variation of both shear and normal loading component has been studied for a single macro-textured implant surface, further investigations on different other implant surface textures ranging from micro to macro roughened surfaces might provide a better outlook into the influence of combined directional micromotion and texture density on bone growth. However, the patterns of osteogenic tissue formation over wide range of implant designs are expected to be similar for equivalent loading and boundary conditions.

In addition, a perfectly bonded contact condition is assumed to prevail at the interfaces which might disregard the fuzzy behaviour of the interfaces. A comparative study of bone growth was performed earlier (Mukherjee and Gupta 2016) with variation in contact conditions at the interface which reported an insignificant variation in the quantitative assessment of bone growth. Although such studies might rule-out the necessity of incorporation of non-bonded contact conditions at the interfaces, there is always a room for improvement. A more realistic numerical method would incorporate continuous adaptive contact conditions, as well as coupled bone formation and remodelling processes, to analyse the growth patterns of formed tissue surrounding the implant (Fernandes et al. 1999), although at a greater computational cost.

5.9 Summary

The results presented in the study shows the influence of normal micromotion to the qualitative trends of bone growth over macro-textured implant surfaces. This is perhaps the first reported study that assess the simultaneous influence of normal micromotion and texture density to the prediction of bone growth over implant surfaces. Moreover, the present study also reported the influence of combined shear and normal loading to the type and qualitative assessment of different tissue phenotypes. Some of the conclusions drawn from this study are:

- Results show an increasing trend of bone growth at lower normal micromotions. However, higher values of normal micromotion will decrease the opening and closing gap thereby increasing the formation of fibrous tissue near the implant surface, thus destabilizing the interface leading to aseptic loosening of the implants.
- Soft cartilaginous tissue was observed to have form in abundance at lesser gap distance thus promoting endochondral ossification at long term.
- The study reported a dependence of the formed tissue on the surface texture density. However, a linear relationship between the surface texture density and tissue growth was not observed from the present investigation.
- In addition, this study also shows that both the directional components of micromotion need to be equally reduced to enhance the possibility of higher bone growth.
- Nevertheless, full-scale FE models with physiological loading conditions and material anisotropy along with clinical implications *in vivo* are necessary to gather a better understanding into the growth patterns on textured implant surfaces with change in opening/closing gap at the bone-implant interface.

CHAPTER 6

ANN based prediction of bone growth over textured implant surfaces with change in surface design parameters

Implants are widely used in the restoration of failed joints and bone fractures across the globe. The surface texture on implant surfaces is known to influence primary (mechanical) as well as secondary (biologic fixation) stability. This chapter first briefly introduces to the study related to sensitivity of bone growth to the variation in geometric control factors of the macro-textured implant surfaces. However, such *in silico* methodologies, although an efficient process to assess bone growth at the bone-implant interface, involve manually intensive modelling owing to large number of design variables and consequently, demand higher computational time. Machine Learning (ML) based approaches such as Neural Networks (NN) modelled around a wide range of experimental or computational database may be a viable alternative to minimize the complication related to tedious FE runs. This chapter further introduces the efficiency of using a trained and tested NN while predicting bone growth for unknown data of design parameters for two distinctly textured implant surfaces.

6.1 Introduction

In recent years, uncemented porous-coated implants have gained more research interest, mainly due to the long-term biologic adherence they offer between the host bone and the prosthesis compared to cemented ones. The levels of bone-growth can be estimated based on mechanoregulatory principles (Lacroix et al., 2002; Mukherjee and Gupta, 2016) of primary bone fracture healing. Surface design features such as surface roughness (Mukherjee and Gupta 2016) and macro-textures can be tailor-made to promote sufficient bone growth around a cementless prosthesis. Investigations were performed to assess the influence of surface morphology over implant surface on bone growth. The influence of surface macro-texture of an implant on the secondary stability of the bone-implant interface has been reported in Chapter 4 and Chapter 5. However, these investigations reported are based on FE models of generalized bone-implant interface models. In addition, no studies have been performed to study the sensitivity of bone growth to variation in implant geometric design variables.

6.2 Objective of this study

The primary aim of this computational investigation has been to study the sensitivity of bone growth to geometric parameters of implant macro-textures using suitable 'design of experiments (DoE)' technique.

6.3 Problem definition

Having understood the influence of macro-textured morphologies on bone growth, in this study one macro-textured implant surface model from the earlier study as discussed in Chapter 4 has been assessed for bone growth by parametrically varying the significant geometric design variables.

6.4 Materials and method

Two different representative 3D macro-textured implant models (**RVM1** and **RVM2**) were created based on commercially viable implant textures. **RVM1** contains uniformly spaced rectangular ribs which partially mimics the proximal

anterior-posterior surfaces of CORAIL hip stem. On the contrary, **RVM2** contains equally spaced hemispherical grooves of equal radius which represents the proximal region of SP-CL hip stem. **RVM#** stands for Representative Volume Model 'Number'. Solid models were initially developed in CATIA® v5R20 software (Dassault Systèmes, France), as shown in Fig 6.1b, and thereafter imported into ANSYS V14.5 FE software (ANSYS Inc., Canonsburg, PA, USA). FE models were discretized with coupled linear elastic eight-noded hexahedral elements (SOLID185). Mesh sensitivity analysis was carried out for each of the FE models to obtain definitive grid sizes to obtain acceptable accuracy in the results.

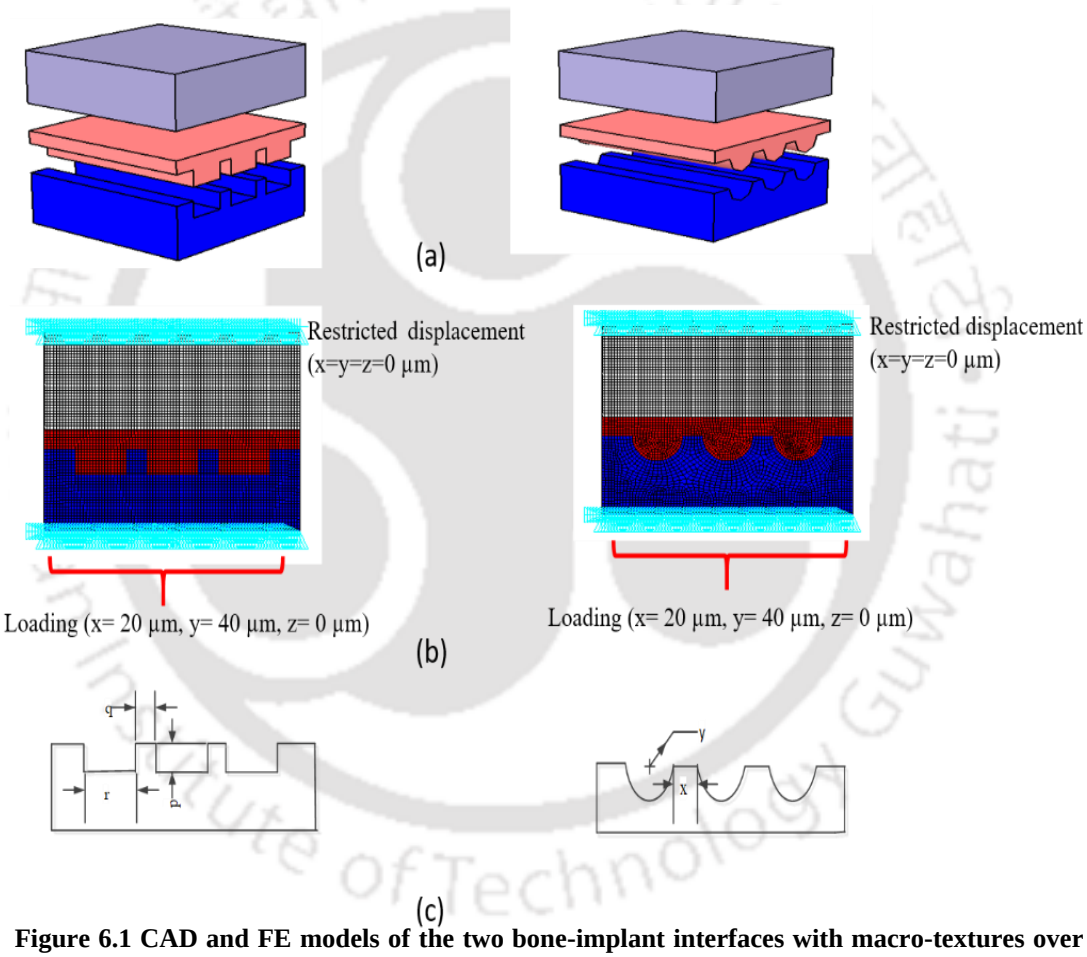

Figure 6.1 CAD and FE models of the two bone-implant interfaces with macro-textures over the implant surfaces: (a) RVM1, (b) RVM2 (Mapped colors: Blue for Implant; Red for granulation tissue; Grey for Bone).

The significant dimensions for the 3D parametric models were identified from a radiological image of implanted CLS Spotorno extracted through an image processing tool, ImageJ v1.53a (National Institutes of Health and Laboratory for Optical and Computational Instrumentation, University of Wisconsin, USA) so as to maintain clinical admissibility. All the three components of the model, i.e. host

bone, implant and granulation tissue, were assumed to be linearly elastic, homogeneous and isotropic. The Young's moduli of host bone tissue, implant and the granulation tissue were considered as 500 MPa, 210 GPa and 1 MPa, respectively. Poisson's ratio for bone and implant was taken as 0.3, whereas that of granulation tissue was taken as 0.167. All the interfaces of the model were considered perfectly bonded in nature. The top surface of the host bone was restrained in all directions, whereas a radial (gap opening/closing) displacement of 20 µm and a tangential (bone-implant micromotion) displacement 20 µm, were given to the bottom implant surface (Simmons et al., 2001; Mukherjee and Gupta, 2014).

The boundary of the bone interface was assumed to be rich in MSCs. Bone growth percentage was predicted by updating material properties at the bone-tissue interface region iteratively through the mechanoregulation based tissue differentiation algorithm (Lacroix et al., 2002; Lacroix and Prendargast, 2002a, 2002b) as discussed in Chapter 3. As reported by Claes and Heigele, 1999, mechanoregulation based tissue differentiation is governed by local hydrostatic pressure and deviatoric strain. Two design control factors "*x*" and "*y*" were chosen with two levels of dimensions based upon clinical admissibility, wherein $1 \leq x \leq 2$ and $1 \leq y \leq 2.5$ as shown in Table 6.1. A 2^k full-factorial based design of experiments was performed computationally to assess the levels of bone growth over 120 days of initial-healing period following the scheme as discussed in Chapter 3 (Lacroix et al., 2002; Lacroix and Prendargast, 2002a, 2002b).

Table 6.1 Control factors in each of the designs based on 2^k full-factorial design

MODELS	**Control Factors**	
	x	***y***
MODEL 1.1	1	1
MODEL 1.2	2	1
MODEL 1.3	1	2.5
MODEL 1.4	2	2.5

6.5 Results and Discussion

Results from present study show (Fig 6.2) a gradual declining trend in the percentage of bone growth from 15% in MODEL 1.1 to 14.1% in MODEL 1.2 with the increase in the control factor "*x*" considering the control factor "*y*" constant. Similar findings are observed for the percentage of bone growth from 13% in MODEL 1.3 to 12.5% in MODEL 1.4. Bone growth levels were also found to be decreasing from 15% in MODEL 1.1 to 13% in MODEL 1.3 with the increase in the control factor "*y*" considering the control factor "*x*" constant. Similar findings are observed for the percentage of bone growth from 14.1% in MODEL 1.2 to 12.5% in MODEL 1.4.

The present study thus focusses on the sensitivity of levels of osteogenesis to the variation in design control factors of the macro-textures on the implant surface. A gradual decline in the percentage of bone growth was estimated with the increase in inter-groove spacing. A reduction in the levels of osteogenesis was also observed with the increase in groove spacing or groove radius. Though the full-scale bone-implant model was not considered and the effect of osteogenic factors like hydroxyapatite coating, bone-morphogenetic proteins (BMPs), etc., were considered to be same in all models, notwithstanding these limitations, the present study can be useful for commercial implant manufacturers and clinicians to select trade-off implants for surgical interventions.

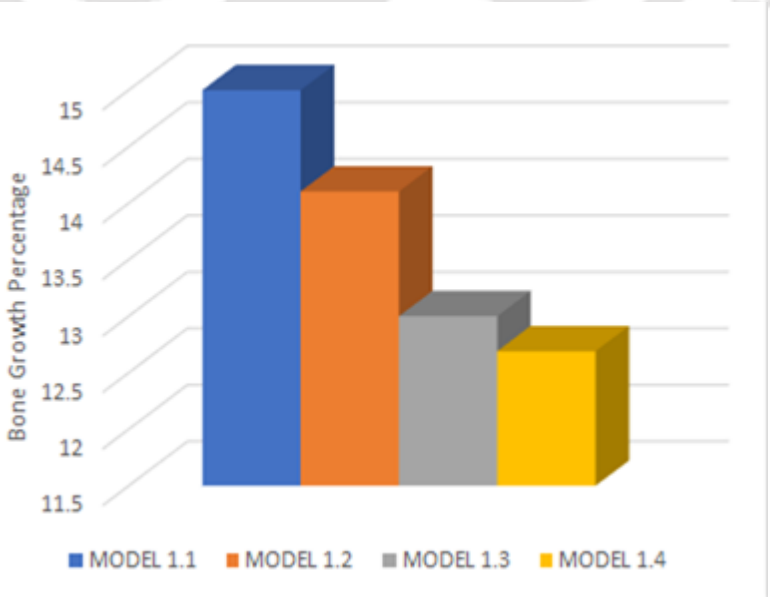

Figure 6.2 Sensitivity in bone growth levels with variation in geometric parameters based on 2^k full-factorial design.

6.6 Clinical Significance of the study

The present study can be used for further statistical analysis to predict osseointegration on multiple implant textures. A topology/shape optimization study may also be carried out further to select trade-off dimensions and shapes, considering an initial configuration of the implant. Moreover, machine learning (ML) based techniques may be employed to estimate the levels of osseointegration on a wide range of implants and implant macro-textures.

6.7 Neural network (NN) based Qualitative assessment of bone growth over macro-textured implant surfaces

6.7.1 Introduction

Lack of biological fixation is one of the major causes of aseptic loosening of cementless implants. Such failure in implant fixation can be minimized to certain extent by realistic design changes in the implant morphology. The design evaluation for a large set of implant designs with similar surface morphology need an iterative FE modeling which would be manually exhaustive and computationally expensive. In view of this, developing a predictive mathematical (Chanda et al. 2016) model might be a viable option for establishing a link between implant surface morphology and quantifiable degrees of ossification while retaining the accuracy of FE analysis.

6.7.2 State-of-the-art

The non-primitive nature of most of the surface features on implant surfaces with a range of significant design parameters might have complex non-linear relationships with the levels of ossification. Neural networks (NNs) are one of a biologically inspired machine learning (ML) algorithms which can be used efficiently as predictive mathematical models towards establishment of such complex relationships. NNs were employed in biomechanical design evaluation on many prosthesis (Cilla et al. 2017; Roy et al. 2018; Chatterjee et al. 2019) earlier. NN was used effectively by Cilla et al. (2017) to design a single objective shape optimization model for a short-stem femoral stem. Roy et al. (2018) utilized NN to convert FE results to the desirability function of an optimization problem on dental implant.

Chatterjee et al. (2019) also used a trained NN to predict microstrains of a femur-implant system from data as predicted by FE analysis.

Backpropagation algorithms are widely employed in machine learning to train NNs. Several generalization approaches, including as Bayesian regularization (BR) and Levenberg–Marquardt (LM), are employed with NNs to reduce the error associated with backpropagation procedures. Overfitting the training data is also less likely using generalization techniques. Because of their benefit in producing a reduced mean squared error, both the BR and LM techniques are often used. However, Bayesian regularization outperforms LM, with BR attaining the best correlation coefficient and the smallest sum of square errors. However, there are hardly any literatures that formulates ML techniques towards assessment of secondary stability of an cementless prosthesis based on implant design variables. Moreover, there is hardly any reported investigation on studying the efficacy of prediction of osseointegration over geometrically distinct macro-textured implant designs based on NN models.

6.7.3 Objective of this investigation

The primary goal of this study was to develop novel predictive mathematical frameworks based on a BR-BPNN to map significant design variables for two distinct, commercially viable implant surface textures to the levels of ossification considering a short-term healing period. Finally, the utility of the proposed frameworks had been extended to predict bone growth for those unlabeled data sets formed by Design of Experiment (DOE) approach.

6.7.4 Problem definition

Having understood the usefulness of NN in different biomechanical design evaluations, in this study, two macro-textured implant surface models from the earlier study as discussed in Chapter 4 have been assessed for bone growth by parametrically varying the significant geometric design variables. Thereafter, NN architectures for each of the models have been built on ML toolbox on MATLAB environment. Results obtained from trained NNs have been validated further with the results obtained from FE runs of unlabelled data.

6.7.5 Materials and method

The significant dimensions for the 3D parametric models (**RVM1** and **RVM2**) were identified as mentioned earlier in Chapter 6, Section 6.4 (Fig 6.1). The range of the parameters were decided based on average width of an intramedullary hip prosthesis inside a femoral cavity, maximum allowable gap between the bone and the implant for ossification and ease of manufacturability with the traditional manufacturing processes. The representative volumes of bone-implant interface models encompass a fabricated macro-texture covering the implant surface, while the mid-portion representing granulation tissue (which is the prime site of bone growth) and the bone representing the portion at the other side (Fig 6.1).

6.7.5.1 Dataset for "training" and "validation" of the NN

The dataset obtained for training and validation was obtained from FE-based mechanoregulatory algorithm of bone growth as discussed earlier in Chapter 3. The dataset for both the models were created based on 3 factors 4 levels full-factorial design for **RVM1** and 2 factors 4 levels full-factorial design for **RVM2**. A significance of the set of chosen parameters were analyzed using analysis of variance (ANOVA) test.

6.7.5.2 Parameterization and dataset for training model RVM1

Results obtained from 44 FE-based mechanoregulatory analyses of ossification were used as data points to train the NN. While, 20 FE-based results were used for validation. Three statistically significant design parameters ('p', 'q' and 'r') as input nodes with one output node corresponding to percentage of bone growth as obtained from FE results were chosen while training the network. 'p', 'q' and 'r' are also found to be clinically significant design parameters to estimate bone growth at bone-tissue interface. The input ($\mathbf{I_{RVM1}}$) and output ($\mathbf{O_{RVM1}}$) vectors for training the network of **RVM1** can be expressed as follows:

$$I_{RVM1} = \begin{bmatrix} p & q & r \end{bmatrix}, \mathbf{O}_{RVM1} = \begin{bmatrix} BG_{RVM1} \end{bmatrix} \tag{6.1}$$

subject to constraints:

$$1.0 \leq p \leq 2.5$$
$$1.0 \leq q \leq 2.5$$
$$2.0 \leq r \leq 5.0$$

6.7.5.3 Parameterization and dataset for training model RVM2

Results obtained from 11 FE-based mechanoregulatory analyses of ossification were used as data points to train the network, while 5 such results were used as test data cases. Two statistically significant design parameters ('*x*' and '*y*') were chosen as input nodes. Similar to the earlier model, design parameters '*x*' and '*y*' are found to be clinically significant. The input ($\mathbf{I}_{\mathbf{RVM2}}$) and output ($\mathbf{O}_{\mathbf{RVM2}}$) vectors for the network of **RVM2** can be expressed as:

$$I_{RVM\,2} = \begin{bmatrix} x & y \end{bmatrix}, \mathbf{O}_{RVM\,2} = \begin{bmatrix} BG_{RVM\,2} \end{bmatrix} \tag{6.2}$$

subject to constraints:

$$1.0 \leq x \leq 2.5$$
$$1.0 \leq y \leq 2.5$$

Table 6.2 shows the levels of design variables chosen while creating the dataset for both the models.

Table 6.2 Levels of design variables (in mm) chosen while creating the dataset for the models

RVM1		Level 1	Level 2	Level 3	Level 4
Design Parameters (mm)	*p*	1.0	1.5	2.0	2.5
	q	1.0	1.5	2.0	2.5
	r	2.0	3.0	4.0	5.0
RVM2		Level 1	Level 2	Level 3	Level 4
Design Parameters (mm)	*x*	1.0	1.5	2.0	2.5
	y	1.0	1.5	2.0	2.5

6.7.5.4 FE modelling, material properties, loading and boundary conditions

CAD models were initially developed in CATIA® v5R20 software (Dassault Systèmes, France), as shown in Figure 6.1, and thereafter imported into ANSYS V14.5 FE software (ANSYS Inc., Canonsburg, PA, USA). FE models were

discretized with coupled linear elastic eight-noded hexahedral elements (SOLID185). Mesh sensitivity analysis was carried out for each of the FE models to obtain definitive grid sizes to obtain acceptable accuracy in the results.

6.7.5.5 Material properties

Linear elastic, isotropic material properties were given to all the regions (implant, granulation tissue and host bone) of the model. The stainless steel implant material (high-nitrogen stainless steel alloy M30NW (Aubert & Duval, France)) considered in the present study was having the Young's modulus of 195 GPa. The elastic modulus of the bone material was taken as 500 MPa, while Young's modulus for granulation tissue was considered to be 1 MPa. Poisson's ratio for the bone and implant was taken as 0.3, whereas for granulation tissue was considered as 0.167. The bone-tissue and implant-tissue interfaces were assumed to be bonded in nature.

6.7.6 Loading and boundary conditions

The top surface of the host bone was restrained in all directions, whereas a radial (gap opening/closing) displacement of 40 μm and a tangential (bone-implant micromotion) displacement 20 μm, were given to the bottom implant surface.

6.7.7 Tissue differentiation based on mechanobiological principles

The evolutionary bone growth was simulated using a sequential mechanoregulatory algorithm as shown in Table 3.1, Chapter 3. The computational scheme implemented earlier (Lacroix et al. 2002; Lacroix and Prendergast 2002a, 2002b) simulated the migration of multipotent mesenchymal stem cells (MSCs) within the region of the bone-implant interface through a diffusion model (Lacroix et al. 2002; Lacroix and Prendergast 2002a, 2002b) as mentioned in Chapter 4, Equation 4.1.

Initially, the interfacial gap between the bone and the implant was considered to be filled with granulation tissue. Local mechanical signals (dilatational hydrostatic pressure and deviatoric strain) govern the differentiation of MSCs into different osteogenic cellular phenotypes. These cellular phenotypes thereafter mature into fibrous tissue, cartilage and immature bone. The effective material

properties (E_{n+1} and ν_{n+1}) of the formed tissues were estimated based on a rule of mixtures as discussed in Chapter 4, Equations. 4.2 and 4.3.

A temporal smoothing method was used to update the model's material properties following Equations. 4.4 and 4.5 as mentioned in Chapter 4. In the numeric scheme, one iterative process represents a single post-surgical day. The complete healing simulation was scheduled to run for 120 such iterations, that translates to estimated sixteen weeks' post-surgical period.

6.7.8 Process Modeling with neural network

A single hidden layer of '*N*' nodes was considered in the study for both the models. The output node is represented by the percentage of bone growth (*BG*). Initialization of weights for the datasets have been carried out to achieve better training performance. Tan-sigmoidal and linear functions were chosen as activation functions for the hidden and output layers of the network respectively. Output (O_{NN}) computed from the NN are compared with the target output (T_o) to estimate the error. The algorithm minimizes a loss function which is a linear combination of sum of squared errors and sum of squared network weights. When the computed loss function for a specific combination of errors and weights satisfies a convergence criterion, training of the NN stops, else weights were updated iteratively through back propagation of errors with LM algorithm. In the present analysis, mean squared error (*MSE*) is considered at the point of convergence for the network and estimated by:

$$MSE = \frac{1}{N}\sum_{i=1}^{N}(T_O - O_{NN})^2 \tag{6.6}$$

The NN models developed in the present study were run in MATLAB environment (MATLAB 2017a, The MathWorks Inc., Natick, MA, USA). Parametric investigations were carried out for each of the networks by trial-and-error method so as to achieve maximum predictability of the models.

6.7.9 Design of Experiment (DOE) approach to assess bone growth

Design of Experiment (DOE) is a statistical technique through controlled tests to identify the influence of several parameters to a desired output or response. There

are several types of DOE techniques used presently such as full-factorial, fractional factorial, Taguchi, Plackett-Burman and response surface methodology (RSM). Although a full-factorial DOE becomes cumbersome for a large number of parameters with their corresponding levels, it is extensively used to study the influence of all significant parameters on a desired response comprehensively. In the present study, 2^k full-factorial DOE was employed with number of input design parameters as mentioned earlier in the implant models i.e. (2^3) 8 models for **RVM1** and (2^2) 4 models for **RVM2**. Unlabeled (unseen) input data was chosen for both the models and FE analysis was performed so as to validate the results with those obtained through trained NNs.

6.7.10 Results and Discussion

6.7.10.1 Performance analysis of NN architecture

The near-optimal BPNN architecture with BR for **RVM1** was obtained through a parametric analysis as presented in Figure 6.3. BR was chosen as it can provide a better generalization and minimal over-fitting for a small and difficult dataset. While performing the parametric study, the number of neurons in the hidden layer (N) was altered in the range of (5,15). It can be observed that NN with 6 hidden neurons showed the least mean squared error (MSE) in testing (Fig 6.3). Optimal NN architecture (Fig. 6.4a) as obtained for **RVM1** is found to be 3-6-1 with training MSE to be 1.0E-13 and testing MSE to be 8.0E-14. Similarly, by altering N as shown in Figure 6.2, the optimal NN-architecture for **RVM2** (Fig 6.4b) is found to be 2-7-1 with training MSE to be 1.9E-13 and testing MSE to be 4.1E-14. Finally, significance of design parameters was analysed using ANOVA test in terms of F and p values. ANOVA test was performed at 95% confidence interval i.e. if p-value is less than 0.05, null hypothesis is rejected and all parameters are considered statistically significant. Moreover, if calculated F is more than F_{crit}, the design parameters are considered significant. Table 6.3 ANOVA test for chosen design parameters for both models. Thus, it is clear from the Table 6.3 that, p-values for all the design parameters are found to be below 0.05 thus rejecting the null hypothesis while, F-values were found to be more than F_{crit} which gives the confidence for all the design variables of the models to be statistically significant.

6.7.10.2 DOE vs trained NN for qualitative assessment of bone growth

Table 6.4 and Table 6.5 shows the comparison of the results of bone growth over implant surfaces as estimated through conventional FE analysis and the trained NNs. The results from the table clearly shows that, a trained NN is equally efficient in assessment of bone growth over implant surfaces while reducing computational cost over conventional FE based mechanoregulatory algorithms for further analysis of a large scale of implant designs.

Table 6.3 ANOVA test for chosen design parameters for both models considering percentage of bone growth

RVM1		DF	SS	MS	*F*	*p*	F_{crit}
Design Parameters	*p*	3	164.88	54.96	9.14	0.00	2.77
	q	3	161.23	52.95	9.11	0.01	2.73
	r	3	171.57	57.19	9.28	0.01	2.82
RVM2		DF	SS	MS	*F*	*p*	F_{crit}
Design Parameters	*x*	3	64.95	21.65	5.82	0.01	3.49
	y	3	64.72	19.23	5.19	0.01	3.42

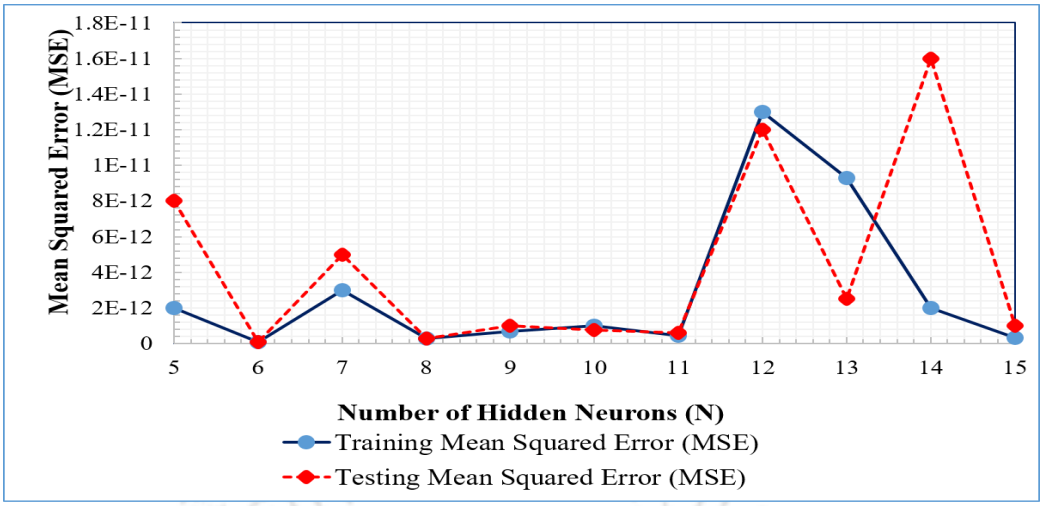

(a)

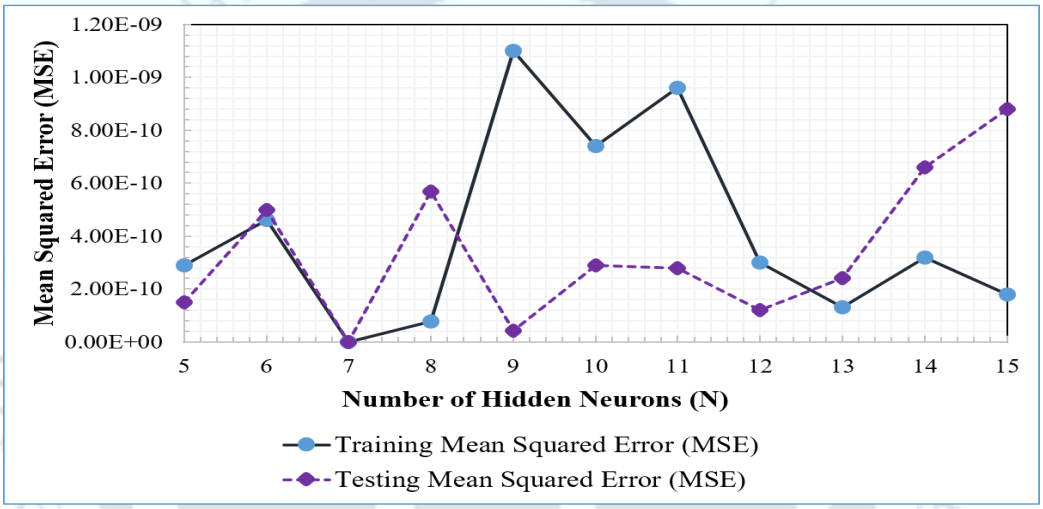

(b)

Figure 6.3 Parametric analysis to find the optimal NN architecture for models: (a) RVM1 (b) RVM2.

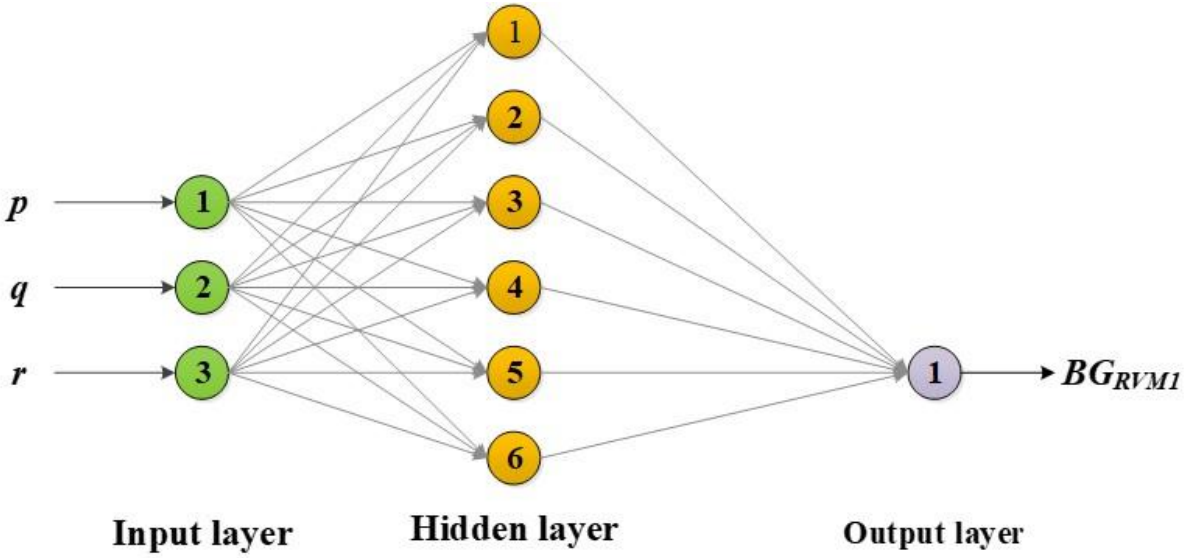

(a)

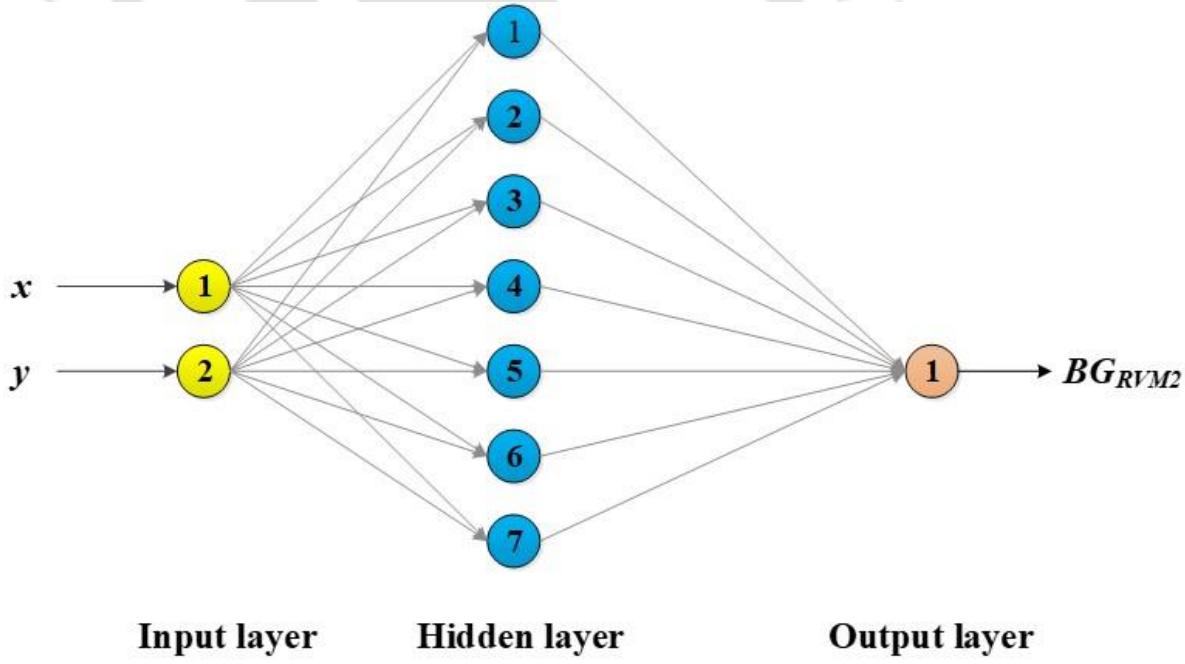

(b)

Figure 6.4 Optimal NN architectures for models: (a) RVM1 (b) RVM2.

Table 6.4 Prediction of bone growth by FE analysis vs NN for model RVM1

MODELS	Control Factors			Bone Growth %	
	p	***q***	***r***	**FE Analysis**	**From NN**
RVM1.1	1.1	2.1	4.1	10.5	10.6
RVM1.2	1.1	1.1	4.1	15.2	15.2
RVM1.3	2.1	2.1	4.1	16.2	16.1
RVM1.4	2.1	1.1	4.1	16.3	16.3
RVM1.5	1.1	2.1	3.1	16.6	16.5
RVM1.6	1.1	1.1	3.1	13.4	13.6
RVM1.7	2.1	2.1	3.1	14.4	14.1
RVM1.8	2.1	1.1	3.1	14.7	14.5

Table 6.5 Prediction of bone growth by FE analysis vs NN for model RVM2

MODELS	Control Factors		Bone Growth %	
	x	***y***	**FE analysis**	**From NN**
RVM2.1	1.8	1.1	16.9	16.8
RVM2.2	2.1	1.1	14.7	14.6
RVM2.3	1.8	2	16.3	16.3
RVM2.4	2.1	2	13.2	13.2

6.8 Summary

The present chapter first introduces to the study related to sensitivity of bone growth to the variation in geometric control factors of the macro-textured implant surfaces. Some major conclusions drawn from this study are:

- A gradual reduction in bone growth was observed with the increase in inter-groove spacing of the chosen implant section model.
- A reduction in the levels of osteogenesis was also observed with the increase in groove spacing or groove radius.
- This study further motivated to exploit the application of ML techniques such as NN to the estimation of bone growth. BR-BPNN was obtained for two distinct implant surface morphologies to test the efficacy of using NN.
- The amount of bone growth as predicted by NN was found to have significant agreement with the results obtained from FE based mechanoregulatory analysis.
- The present analysis will further assist in topology/shape optimization of implant surfaces from a wide range of implant models.

CHAPTER 7

Predictions of bone growth over optimally designed macro-textured implant surfaces using neural network and genetic algorithm

Application of finite element (FE) based mechanoregulatory schemes to estimate the amount of bone growth for a wide range of implant surface features is either manually intensive or computationally expensive. This chapter introduces a study which adopts an integrated approach combining FE, back-propagation neural network (BPNN) and genetic algorithm (GA) based search to evaluate optimum surface macro-textures from three representative implant models so as to enhance bone growth. The methodology used in this study might be used as a viable alternative to make right decision while choosing a type of implant before surgery.

7.1 Importance and objectives

Success of a load-bearing uncemented implant, like uncemented femoral stem, relies heavily on its biologic fixation (osseointegration) with the host bone (Yamada et al. 2009). In spite of the remarkable success of such uncemented implants globally, there has been a pronounced rise in the number of joint failures even after meticulous surgical interventions. The trend of increasing rate of joint arthroplasties is anticipated to continue in the forthcoming decades as well, owing primarily to the ageing population and a conspicuous improvement in medical care and health practices in developing nations (Holzwarth and Cotogno, 2012; Cilla et al. 2017). A proper combination of both primary stability (or mechanical stability) and secondary stability (consequent to biologic fixation), therefore, is a must for long-term success of uncemented implants (Chanda et al. 2016).

Previous studies have also reported that insufficient biologic adherence is one of the primary causes of aseptic loosening of uncemented implants (Pal and Gupta, 2011; Philips et al. 1990) which may be avoided by profound changes in the design of the implants (Huiskes and Boeklagen, 1988; Viceconti et al. 2001). Bone growth around an uncemented prosthesis can also be enhanced by incorporating a variety of surface features on the implant surface. There is a need for further investigation on the optimal surface features (both microscopic and macroscopic surface textures) that would further enhance osseointegration. Earlier *in silico* studies have reported the influence of microtextured (Mukherjee and Gupta, 2016) and macrotextured implant surface (ref. Chapter 3) features on bone growth, but none of the investigations have interrogated for an optimal design feature for any of the tested implant models. The design evaluation of each of the new feasible and clinically admissible surface textures would rather be a manually intensive process involving successive remeshing to generate representative FE models (Chanda et al. 2016; Harrysson et al. 2007; Bah et al. 2011). Therefore, generation of predictive, data-driven mathematical models may pose to be an efficient alternative to establish a relationship between the geometric parameters of surface features and quantified levels of bone growth.

Recently, artificial intelligence (AI) has been a boon to healthcare systems and researchers in particular. AI involves use of specialised mathematical models or

algorithms mimicking human neurological processes (Sukegawa et al. 2020). Artificial neural networks (ANNs) are one of such biologically inspired algorithms modelled on human brain activity, comprising a set of mathematical equations used to mimic biological tasks, e.g. problem-solving, learning and memorization. ANNs offer the ability to model a complex nonlinear relationship between the predictor variable and the expected outcome (Tu 1996) and have been widely trained to address a myriad of challenges that are sometimes impossible to handle using analytical methods or rule-based programming due to their adaptive layout and learning capabilities (Chanda et al. 2016).

The goal of an integrated NN-GA based methods is to first identify a pattern to establish a relationship between the input and the output parameters, and then to optimize the performance of the system by searching for optimal input parameters in the search space. Similar to NN, GA is a biologically inspired algorithm that uses some genetic operators to efficiently look for the optimal result. In addition, the GA provides a multi-solution framework and, therefore, does not require any experience of the search environment (Chanda et al. 2016). However, in many cases, unrestricted search space may lead to mathematically feasible but non-physical solution.

Establishing a relationship between different parameters while modelling human body phenomena through clinical and applied biomechanics could be a cumbersome task primarily due to non-deterministic nature of such phenomena (SchÖllhorn 2004). Therefore, approaches focused on ANN find their applications in the field of biomechanics, diagnostic imaging (Miller et al. 1992), pattern recognition (Sabbatini 1993) and other areas of bioengineering (Nayak et al. 2001). The shape of surface features on implant surfaces are generally non-primitive and unorthodox which involves a wide range of design parameters which might have complex non-linear relationships with the resulting levels of bone growth. ANNs seem to be an efficient choice to establish such relationships. Although combined FE-NN-GA based design optimization study was attempted earlier on hip implant (Chanda et al. 2016) and dental implant (Roy et al. 2018), sufficient literatures are still not available that considered predictive NN models in the design of orthopaedic implants. Moreover, to the best of authors' knowledge, there is hardly any reported

investigation on comparative study of optimized macro-textured implant designs based on combined NN-GA based design optimization.

The primary objective of this study is to establish predictive mathematical models based on a BPNN to map identified design parameters for three distinct, commercially discernible implant surface textures to the levels of post-surgical bone growth. Subsequently, a GA based search was carried out to obtain optimized surface textures for each of the reference implant macro-textures by maximizing the levels of bone growth predicted by BPNN. It may be noted here that these design parameters were identified based on their clinical significance in the process of bone growth.

7.2 Materials and method

BPNNs are generally used to form complex mathematical models based on a sample set of input-output data. In order to ascertain the input-output correlations between the geometric parameters of the macro-textures on the implants' surface and the level (in percentage) of bone growth, a near-optimal BPNN was modelled. After the BPNN was modelled and further validated, it was employed as an objective function to search for an optimized macro-texture such that the percentage bone growth was maximized.

A comparative assessment based on the above procedure was done for three different 3D macro-textured models (**MODEL A**, **MODEL B** and **MODEL C**) of the bone-implant interface similar to that described in Chapter 3. These surface texture geometries were designed based on the discernible macro textures on commercially viable femoral stems. All femoral stems considered for developing the complex models of the surface macro-textures have been clinically proven to be effective prostheses with long-term outcomes (Heyland et al. 2019). **MODEL A**, which is modelled after proximal area of CLS Spotorno, has variable height ribs to improve bone compression and provide a higher level of stimulus for osseointegration. **MODEL B**, mimicking the textures on CORAIL, as identified by rectangular ribs to allow mechanical stability. **MODEL C**, which characterizes an analogous region of SP-CL stems, also has semi-circular grooves.

The dimensions for the initial parametric model for **MODEL A** were extracted from a radiological image of implanted CLS Spotorno via an image processing tool,

ImageJ v1.53a (National Institutes of Health and Laboratory for Optical and Computational Instrumentation, University of Wisconsin, USA). The major dimensions (height of ribs/grooves, inter-groove distance, rib thickness) of the other initial models, i.e. **MODEL B** and **MODEL C**, were chosen broadly based on dimensions of **MODEL A** to provide clinical admissibility to the implant macro textures as well as to set standard measurements for the ease of comparison. A cast-in macroscopic texture covers the implant surface for each of the models, with the mid-region of the model representing granulation tissue while the other side represents bone (Fig. 7.1). In the present study, a bone-implant distance of 2 mm was considered for all the models to provide a constant thickness to the interface. The current investigation is based on the presumption that an optimal osteogenic environment exists and is consistent with all bone-implant interface models.

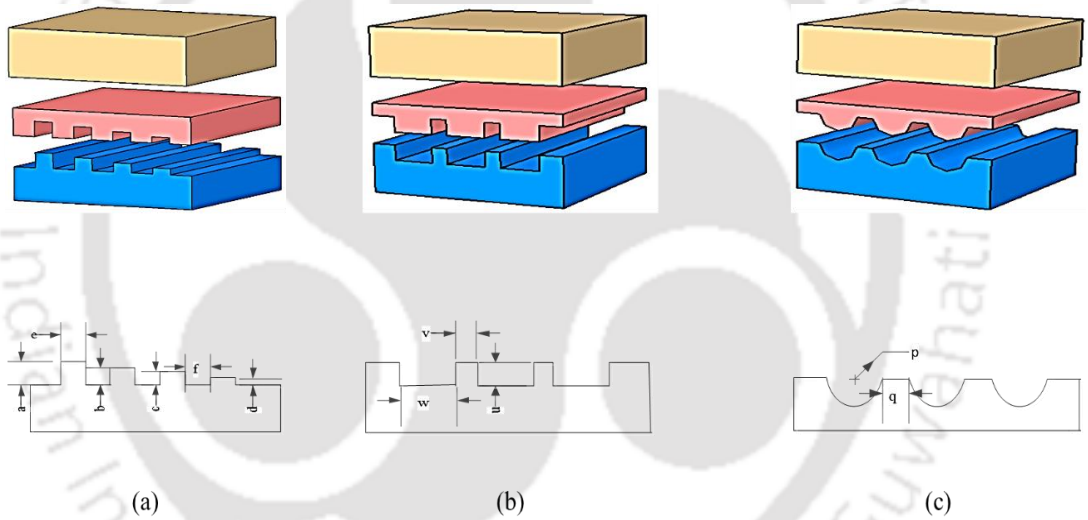

Figure 7.1 Bone-implant interface with macro-textures over representative implants for: (a) MODEL A (b) MODEL B (c) MODEL C (Colour Map: Blue for Implant; Red for granulation tissue; Yellow for Host Bone).

7.2.1 Input-output dataset for "training" the BPNN

The sample set of data used for training and validation of the neural network was obtained from the FE-based mechanoregulatory analysis of bone growth over macro-textures on implant surface at the bone-implant interface as discussed in Chapter 3. 'Semi-width' of an implant was assumed to be 5.5 mm in each of the models (based on the radiological image of **MODEL A**). It may, however, be noted that the 'semi-width' of an implant refers to the distance between the 'base' in each of the different types of models to mid-line of a standard commercial femoral stem.

7.2.1.1 Parameterization and dataset for training MODEL A

Results of 80 FE-based mechanoregulatory analyses of bone growth were used for training the BPNN, and another 12 such results were used as test data cases for validation of the network. Table 7.1 shows the dataset used for training and validation of the NN for **MODEL A**. Six significant design parameters ('*a*', '*b*', '*c*', '*d*', '*e*' and '*f*') were chosen as input parameters that characterize the shape of the macro-texture for **MODEL A** (Fig. 7.1a). '*a*', '*b*', '*c*' and '*d*' are variable heights of the ribs, whereas '*e*' and '*f*' are rib-width and inter-rib spacing, respectively. All the input parameters take values up to 1 decimal place considering design for manufacturability (DFM). The output parameter was chosen as a percentage of bone growth (BG) over the implant surface. Higher the percentage of bone growth, better will be the osseointegration. The input ($\mathbf{X_A}$) and output ($\mathbf{O_A}$) vectors for the network of **MODEL A** can be represented as follows:

$$\mathbf{X_A} = \begin{bmatrix} a & b & c & d & e & f \end{bmatrix}, \quad \mathbf{O_A} = \begin{bmatrix} BG_A \end{bmatrix} \tag{7.1}$$

subject to the geometrics constraints:

$$\begin{aligned} 4e + 3f &\leq 19.0 \\ 1.0 \leq a &\leq 2.5 \\ 1.0 \leq b &\leq 2.5 \\ 1.0 \leq c &\leq 2.5 \\ 1.0 \leq d &\leq 2.5 \\ 1.0 \leq e &\leq 2.5 \\ 2.0 \leq f &\leq 5.0 \end{aligned}$$

All the lower and upper bounds of the input parameters (in mm) were chosen in such a way so as to maintain clinical admissibility. The first constraint stands for the maximum proximal width up to which textures were allowed, which was restricted to 19 mm as per the proximal fitting requirement of CLS Spotorno stem.

Table 7.1 Dataset used to train and validate the NN for MODEL A

Training Data for MODEL A					
a	***b***	***c***	***d***	***e***	***f***
1	1	1	1	1	5
1	1	1	1.5	2.5	2
1	1	1	2	2.5	2
1	1	1	2.5	2.5	2

1	1	1.5	2.5	2.5	2
1	1	2	2.5	2.5	2
1	1	2	2.5	1	5
1	1.5	2.5	2.5	2	2
1	2	2.5	2.5	1.5	2
1	2.5	2.5	2.5	2.5	2
1.5	2.5	2.5	2.5	2.5	2
2	2.5	2.5	2.5	1	5
2.5	2.5	2.5	2.5	1	5
2.5	2	1.5	1	2.5	2
1.5	1.5	1.5	1.5	2.5	2
1.5	1.5	1.5	1	2.5	2
1.5	1.5	1.5	2	2.5	2
1.5	1.5	1.5	2.5	1	5
1.5	1.5	1	2.5	1	5
1.5	1.5	2	2.5	1	5
1.5	1.5	2.5	2.5	1	5
1.5	1	2.5	2.5	1	5
2	2	2	2	2	2
2	2	2	2.5	2	2
2	2	2	1	2	2
2	2	2	1.5	1	5
2	2	1	1.5	1	5
2	2	1.5	1.5	2	2
2	2	2.5	1.5	2	2
2	1.5	2.5	1.5	2	2
2	1	2.5	1.5	2	2
2	2.5	2.5	1.5	2	2
1	2.5	2.5	1.5	2	2
1.5	2.5	2.5	1.5	2	2
2.5	2.5	2.5	1.5	1	5
2.5	2.5	2.5	1	2.5	2
2.5	2.5	2.5	2	2.5	2
2.5	2.5	1	2	2.5	2
2.5	2.5	1.5	2	2.5	2
2.5	2.5	2	2	2.5	2
2.5	1	2	2	2	2
2.5	2	2	2	2	2
2	1	1	1.5	2	2
1.5	1	1	1	2	2
2.5	1	1	2.5	2	2
1.5	1	1	2.5	1.5	2
1.5	1	1	2	1.5	2
2	1	1	2	1.5	2
1.5	1.5	1	1	1.5	2
1.5	2	1	1	1.5	2

1.5	2.5	1	1	1	5
2.5	1.5	1	1	1	5
2.5	2.5	1	1	1	5
1	2	1	1	1	5
2	1	1	1	1	5
2	2	1	1	2	2
1	1.5	1	1	2	2
1	2.5	1	1	2	2
2	2	2.5	1	2	2
2.5	2	1	1	2	2
1	1.5	1.5	1.5	2.5	2
2	1.5	1.5	1.5	2.5	2
2.5	1.5	1.5	1.5	2.5	2
1.5	1.5	1	2	2.5	2
1.5	1.5	2	1	2.5	2
1.5	1.5	2.5	2	1	5
1.5	1.5	2	2	1	5
1	2	1.5	1.5	1	5
2	1	1.5	1.5	1	5
1.5	2	1.5	1.5	1	5
2	1.5	1.5	1.5	1.5	2
2.5	2.5	1.5	1.5	2	2
1	1	1.5	1.5	1.5	2
2	2	1.5	1.5	2	2
2.5	2	2	2.5	1.5	2
2	2.5	2	2	2	2
1	2	2	2	1.5	2
1.5	2	2	2	2	2
2.5	2	2	2	1.5	2
1	2	2	1.5	2	2

Testing Data for MODEL A

1	1	1	1	2	2
2.5	2	2	1.5	2.5	2
1	1.5	2	2	1	5
1	1	1.5	1.5	1.5	2
2.5	2.5	2.5	2.5	1.5	2
1.5	2	2	1	1	5
1.5	2.5	2.5	1	2.5	2
1.5	2.5	2.5	2	1	5
2	2.5	2.5	1.5	2.5	2
1.5	2.5	2.5	1.5	1	5
1	2.5	2.5	1	1.5	2
2	2.5	2.5	2	2.5	2

7.2.1.2 Parameterization and dataset for training MODEL B

Results of 52 FE-based mechanoregulatory analyses of bone growth were used for training the BPNN, and another 8 such results were used as test data cases. Table 7.2 shows the dataset used for training and validation of the NN for **MODEL B**. Three significant design parameters ('*u*', '*v*' and '*w*') were chosen as input parameters (in mm). '*u*', '*v*' and '*w*' are rib-height, rib-width and inter-rib spacing, respectively (Fig. 7.1b). The input ($\mathbf{X_B}$) and output ($\mathbf{O_B}$) vectors for the network of **MODEL B** can be represented as follows:

$$\mathbf{X_B} = \begin{bmatrix} u & v & w \end{bmatrix}, \ \mathbf{O_B} = \begin{bmatrix} BG_B \end{bmatrix} \tag{7.2}$$

subject to constraints:

$$\begin{aligned} 1.0 \le u \le 2.5 \\ 1.0 \le v \le 2.5 \\ 2.0 \le w \le 5.0 \end{aligned}$$

Table 7.2 Dataset used to train and validate the NN for MODEL B

Training Data for MODEL B		
u	***v***	***w***
1	1	2
1	1.5	2
1	2	2
1	2.5	2
1	1	3
1	1.5	3
1	2.5	3
1	1	4
1	2	4
1	2.5	4
1	1	5
1	1.5	5
1	2	5
1.5	1	2
1.5	2	2
1.5	2.5	2
1.5	1	3
1.5	2	3
1.5	2.5	3
1.5	1	4
1.5	1.5	4

1.5	2	4
1.5	2.5	4
1.5	1	5
1.5	1.5	5
1.5	2	5
2	1.5	2
2	2	2
2	2.5	2
2	1	3
2	2	3
2	2.5	3
2	1	4
2	1.5	4
2	2	4
2	2.5	4
2	1	5
2	1.5	5
2	2	5
2.5	1	2
2.5	1.5	2
2.5	2.5	2
2.5	1	3
2.5	2	3
2.5	2.5	3
2.5	1	4
2.5	1.5	4
2.5	2	4
2.5	2.5	4
2.5	1	5
2.5	1.5	5
2.5	2	5

Testing Data for MODEL B

1	2	3
1	1.5	4
1.5	1.5	2
1.5	1.5	3
2	1	2
2	1.5	3
2.5	2	2
2.5	1.5	3

7.2.1.3 Parameterization and dataset for training MODEL C

Results of 36 FE-based mechanoregulatory analysis of bone growth were used for training the BPNN, whereas 8 such results were used as test data cases. Table 7.3 shows the dataset used for training and validation of the NN for **MODEL C**. Two significant design parameters ('p' and 'q') were chosen as input parameters (in mm). 'p' and 'q' are groove radius and inter-groove spacing, respectively (Fig. 7.1c). The input ($\mathbf{X_C}$) and output ($\mathbf{O_C}$) vectors for the network of **MODEL C** can be represented as:

$$\mathbf{X_C} = \begin{bmatrix} p & q \end{bmatrix}, \mathbf{O_C} = \begin{bmatrix} BG_C \end{bmatrix} \tag{7.3}$$

subject to constraints:

$$1.0 \leq p \leq 2.5$$
$$1.0 \leq q \leq 2.5$$

Table 7.3 Dataset used to train and validate the NN for MODEL C

Training Data for MODEL B	
p	***q***
2.5	2
2.5	2.5
1	1
1	2.5
1.7	1.1
2	1.7
2.5	1
1.7	1.9
1.1	2.2
1.9	2
2.2	2.3
2	1.1
1.5	1.3
2.4	1.7
1.8	2.5
1.3	1.4
2.2	1.1
2.4	2
2.2	1.7
1.4	1.3
1.2	1.6
2.3	1.3

2.2	2.2
1.4	1.6
1.3	2.3
1.5	1
2.2	2.2
1.9	1.9
1.9	1.7
1.9	2
2	2
2.2	2.3
1.7	1
1.7	1.4
1.4	1.1
2.1	2
Testing Data for MODEL C	
2	1.3
2	1.9
1.4	1.9
2	2.1
1.2	2.3
1.2	2.2
1.6	2
1.1	2.3

For training the BPNN, all the input parameters and output data were normalized in the range (0.0,1.0) with reference to their corresponding lower (minimum value) and upper (maximum value) bounds. Table 7.4 shows the design parameters and their respective lower and upper bounds corresponding to each of the models.

7.2.2 FE modelling, material properties, loading and boundary conditions

The FE models for each candidate design of all three design morphologies of the bone-implant interface were developed based on the geometric constraints as stated above. All models were developed in CATIA® v5R20 software (Dassault Systèmes, France), as shown in Fig. 7.1, and subsequently imported into ANSYS V14.5 FE software (ANSYS Inc., Canonsburg, PA, USA) for analysis. Every candidate design was discretized using coupled linear elastic eight-noded hexahedral elements (Fig 7.2).

In order to obtain acceptable accuracy of FE results, mesh convergence study was carried out for each design candidate. A typical mesh convergence study for each of the models involves evaluation of peak von Mises stress at the bone-implant interface. For example: consider a data case for **MODEL C** with p = 2.5 mm, q = 2 mm, three different FE meshes ~6,372 elements (coarse mesh), ~11,676 elements (medium mesh), ~38,052 elements (fine mesh) were chosen to predict the peak Von Mises stress at the interface. Interestingly, the maximum difference in peak Von Mises stress was found to be 21% between the coarse mesh and the medium mesh and 0.5% between the medium mesh and fine mesh respectively. Considering the computational cost and efficiency, the medium mesh is found to be reliable for further computations with sufficient accuracy.

Table 7.4 Design parameters corresponding to each of the models (Fig. 7.1)

MODEL A		Lower Bound	Upper Bound
Design Parameters (mm)	*a*	1.0	2.5
	b	1.0	2.5
	c	1.0	2.5
	d	1.0	2.5
	e	1.0	2.5
	f	2.0	5.0
MODEL B		Lower Bound	Upper Bound
Design Parameters (mm)	*u*	1.0	2.5
	v	1.0	2.5
	w	2.0	5.0
MODEL C		Lower Bound	Upper Bound
Design Parameters (mm)	*p*	1.0	2.5
	q	1.0	2.5

Linear elastic, homogeneous and isotropic material properties were considered for all volumetric regions (implant, granulation tissue and host bone) of the FE model. However, the initial condition of homogeneity of granulation tissue will cease to prevail as tissue differentiation takes place in the iterative timescale. The implant material considered in the present study was a high-nitrogen stainless steel alloy M30NW (Aubert & Duval, France) having Young's modulus, E = 195 GPa. The elastic modulus of the host bone was assumed to be 500 MPa (Puthumanapully,

2010; Mukherjee and Gupta, 2014), and that for granulation tissue was considered to be 1 MPa. Poisson's ratio for both the host bone and implant material was taken as 0.3, whereas that for granulation tissue was taken as 0.167. All the interfaces in all the candidate designs were assumed to be bonded under all conditions.

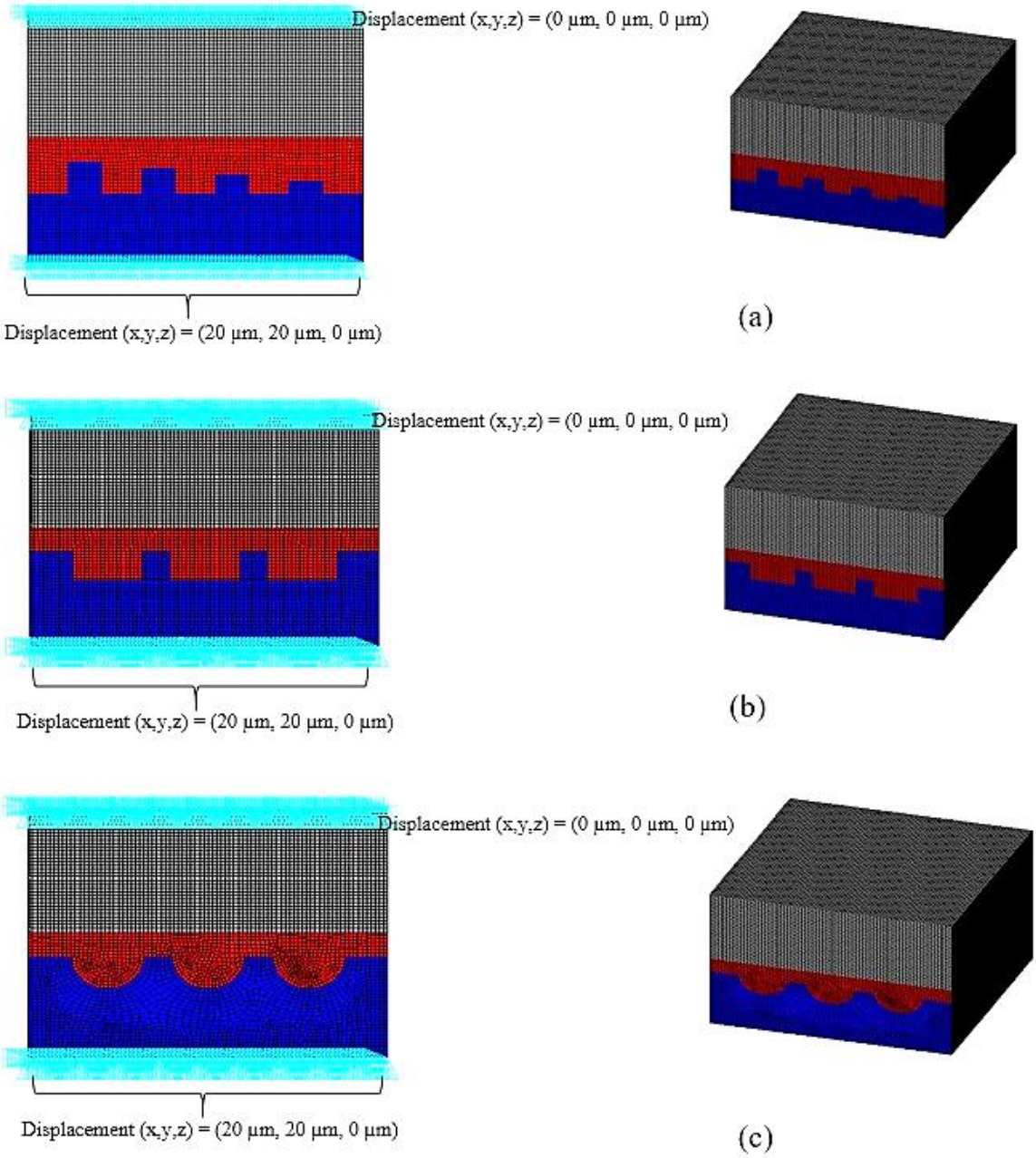

Figure 7.2 FE models of the three representative bone-implant interface with macro-textures over the representative implant surfaces: (a) MODEL A, (b) MODEL B and (c) MODEL C. (Colour Map: Blue for Implant; Red for granulation tissue; Grey for Host Bone).

The upper surface of the bone was constrained in all directions, whereas a normal (assuming a press-fit condition) and a tangential (relative bone-implant micromotion) displacement, each of 20 μm (Mukherjee and Gupta, 2014), were provided at the bottom implant surface.

7.2.3 Tissue differentiation based on mechanobiological principles

The progressive bone growth phenomenon was implemented using the mechanobiology based algorithm as discussed in Table 3.1, Chapter 3. The numerical model (Fig. 7.3) simulated the migration of mesenchymal stem cells (MSCs) within the region of the bone-implant interface through a diffusion model (Lacroix et al. 2002; Lacroix and Prendergast, 2002a, 2002b) as mentioned in Chapter 4, Equation 4.1.

Impermeable implant boundary was assumed to represent no cell loss during the cellular diffusive process. Initially, the interface region was considered to be filled with granulation tissue. Local mechanical stimuli (hydrostatic pressure and deviatoric strain) govern the differentiation of MSCs into different cellular phenotypes (Barry, 2003; Isaksson et al., 2006). Upon maturation, these cellular phenotypes modify into fibrous tissue, cartilage and bone (Claes and Heigele, 1999). The effective material properties of the newly formed tissues were predicted based on a rule of mixture as discussed in Chapter 4, Equations. 4.2 and 4.3.

For averting numerical instability, a temporal smoothing method was employed (Lacroix and Prendergast, 2002a, 2002b) to update material properties in each interface finite elements based on Equations. 4.4 and 4.5 as mentioned in Chapter 4. In this mechanoregulatory scheme, one post-surgical day was represented by each iteration. The complete procedure was scheduled to run for 120 iterations, translating to sixteen weeks' post-surgical period from the day of implantation.

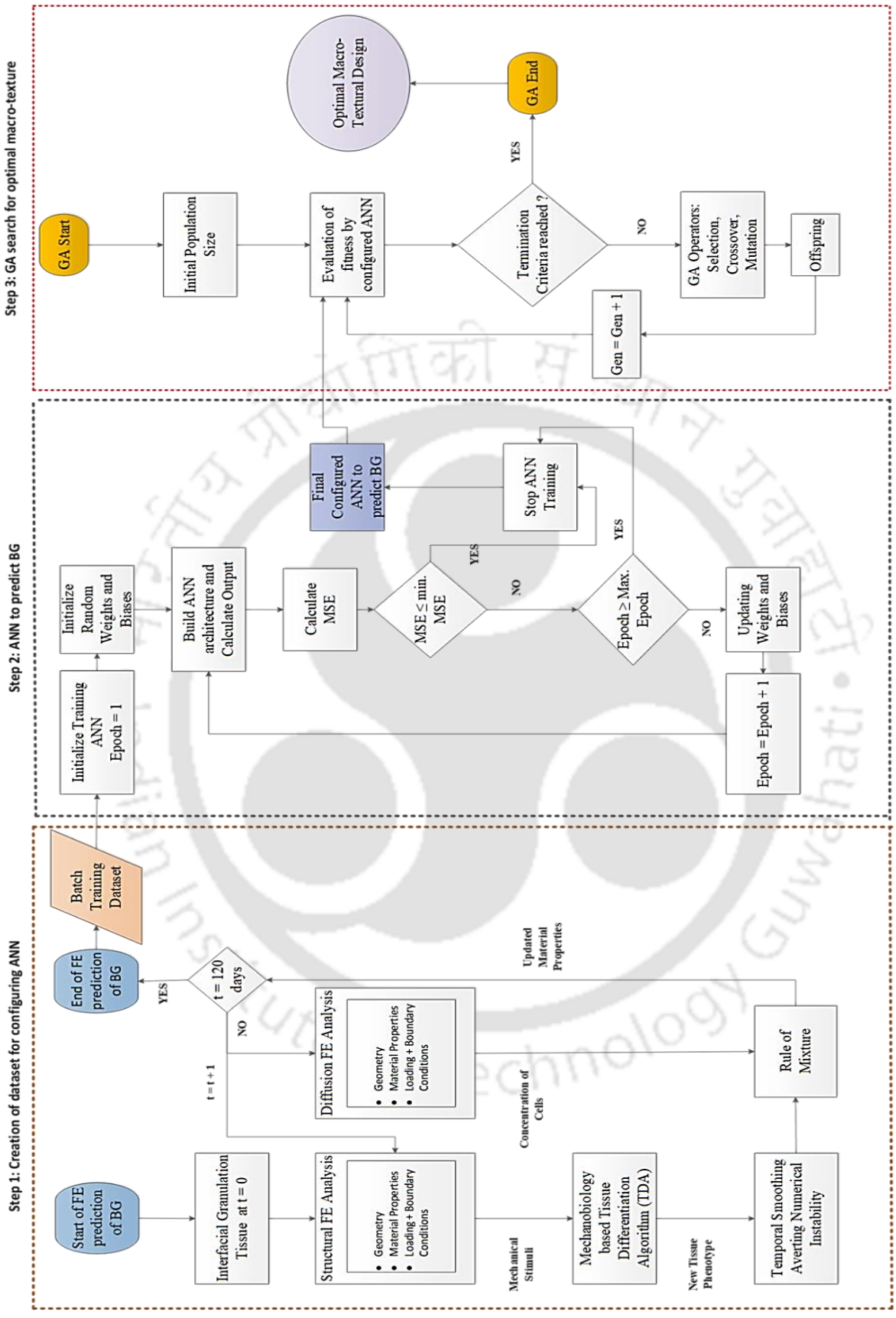

Figure 7.3 The optimization scheme comprising of FE based mechanoregulatory algorithm, ANN and GA

7.2.4 Implementation of back-propagation neural network (BPNN)

The neural network topology proposed in the present study was configured with three layers, namely input, hidden and output layers. As described, the input design variables represented by number of input neurons (m) for **MODEL A**, **MODEL B** and **MODEL C** were identified as m=6, m=3 & m=2, respectively. A single hidden layer of 'n' neurons was considered for each of the three networks. The number of neurons in the output layer (z) is one for each of the networks representing the normalized percentage of bone growth (BG). It is worth noting that a single hidden layer is considered adequate for designing an efficient neural network for a large number of real-world problems (Tu, 1996). The activation functions for input and hidden neurons were assumed to be linear and logistic-sigmoidal for all the three architectures, whereas activation function for output neuron was considered logistic-sigmoidal. A fixed bias matrix [B] of size two was added to both the hidden and output neurons. The connecting weights between the input and hidden layers were represented by a matrix [V] of size $m \times n$. In contrast, a column vector [W] of size n was used to represent the connecting weights between the hidden and output layers. Elemental values of matrices [V] and [W] were allowed in the range of -1.0 to 1.0, whereas elemental values in the bias matrix [B] ranged between 0.0 and 1.0. Initial elemental values for weights and bias matrices were randomly generated. Customized MATLAB scripts (MATLAB 2017a, The MathWorks Inc., Natick, MA, USA) were developed to model the neural networks. Subsequently, parametric studies (Chanda et al., 2016; Dutta and Pratihar, 2007; Chaki et al., 2015) were carried out for each network by altering one hyperparameter at a time, keeping the others constant to identify an optimal set of these hyperparameters (the number of hidden neurons (n), learning rate (α) and momentum constant (μ)).

7.2.5 Implementation of genetic algorithms (GA) based optimization of implant texture

The present scheme further employs a single-objective mixed-integer GA search using MATLAB Optimization Toolbox (MATLAB 2019a, The MathWorks Inc., Natick, MA, USA) to search for optimized macro-texture morphology by maximizing BG. An initial population size (P) is randomly generated for each GA

search. Each string of population contains six substrings for **MODEL A**, three substrings for **MODEL B** and two substrings for **MODEL C**. Substrings chosen in each GA scheme indicates the constraint design parameters for respective models (Chaki et al., 2015). The BG corresponding to each GA substring is predicted by the trained BPNN in order to determine the objective function, **F**. Rank scaling of objective function **F** was performed to determine the fitness function values. Crossover fraction (c) is the fraction of children, other than those elite individuals, that are generated by crossing over. The rest of the individuals are generated by mutation. The elite count was fixed at 2 across all the generations. A recent study indicated that lower values (Mishra and Shukla, 2017) of elite count results in much better optimal solutions.

The GA search in the present study employs stochastic-uniform selection algorithm with scattered cross-over fraction. Optimal GA parameters (Dutta and Pratihar, 2007; Chaki et al., 2015), e.g. crossover fraction (c), population size (P) and maximum number of generations (G) (Chanda et al., 2016) are identified through a parametric study. For reproducibility, a unique seed value was considered during the parametric study to create initial set of random population. Based on the near optimal set of GA parameters, the final GA run was performed subject to the design constraints as stated before. The final generation of the GA search yielded the optimized values of implant geometric parameters for each distinct macro-textured configuration. These optimized implant textures will hereon be referred to as OMT_A, OMT_B and OMT_C for **MODEL A**, **MODEL B** and **MODEL C**, respectively.

7.3 Results and Discussion

7.3.1 Near-optimal BPNN architecture

The near-optimal architecture of the NN for **MODEL A** was obtained through a parametric study which is presented in Figure 7.3. In the initial phase of the parametric investigation, the number of neurons in the hidden layer (n) was varied in the range of (6,16), whereas the learning rate (α) and the momentum constant (μ) were fixed to 0.4 and 0.1, respectively. It can be noted that the NN with 15 hidden neurons showed the best performance in terms of mean squared error (MSE) (Fig.

7.4). In the later phases of the parametric study, the number of neurons in the hidden layer was fixed to 15, while the values of the learning rate (α) and the momentum constant (μ) were varied in the range (0.05,0.95) for both the subsequent stages of study. Optimal NN architecture (Fig. 7.5a) as obtained for **MODEL A** is presented in Table 7.5. Similarly, by varying *n*, α and μ, the optimal NN-architectures for **MODEL B** (Fig. 7.5b) and **MODEL C** (Fig. 7.5c) are also achieved as shown in Table 7.5.

Table 7.5 Parameters of the near-optimal NN

Parameters	MODEL A	MODEL B	MODEL C
Number of Neurons in the hidden layer	15	15	16
Learning Rate (α)	0.45	0.15	0.45
Momentum Constant (μ)	0.1	0.2	0.75

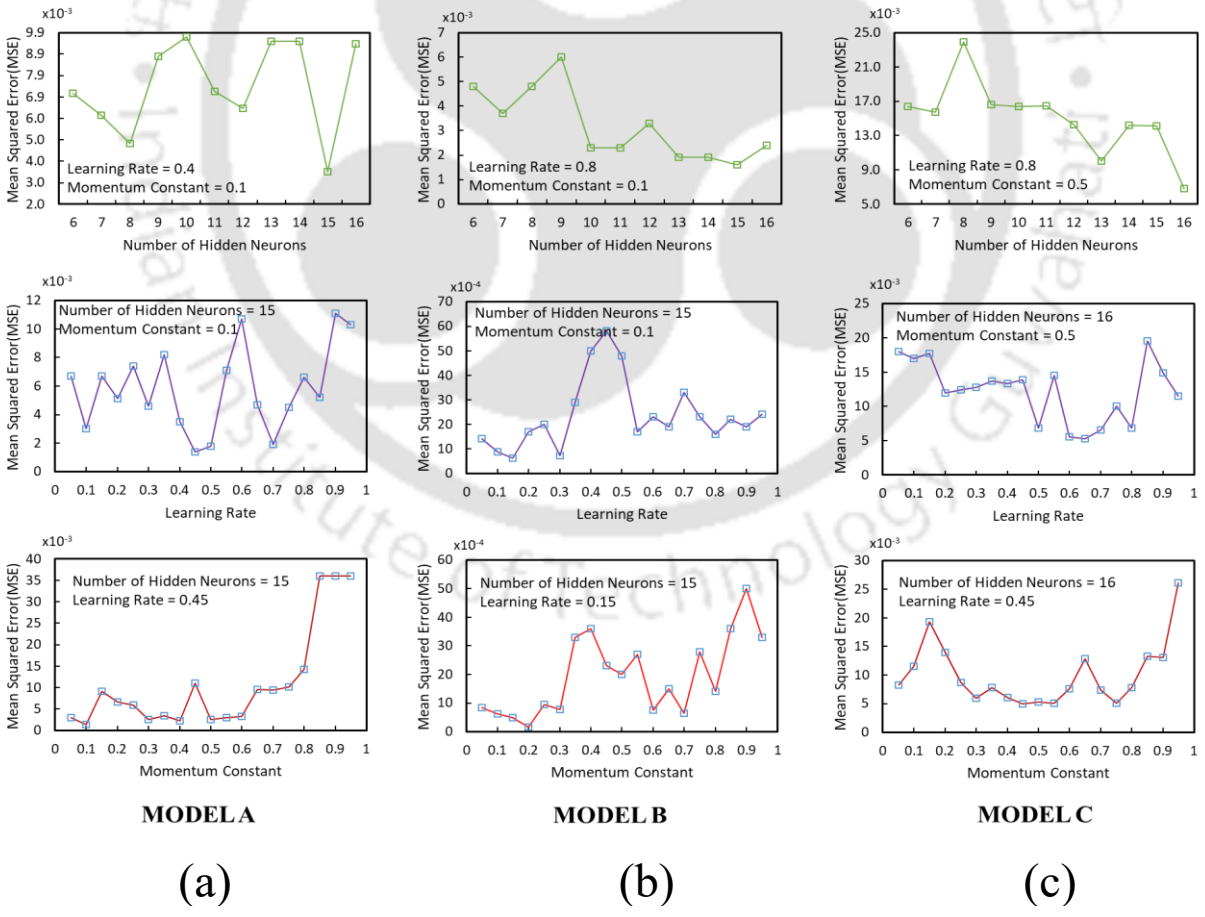

Figure 7.4 Parametric study to obtain near-optimal NN for all the *in silico* models: (a) MODEL A, (b) MODEL B and (c) MODEL C

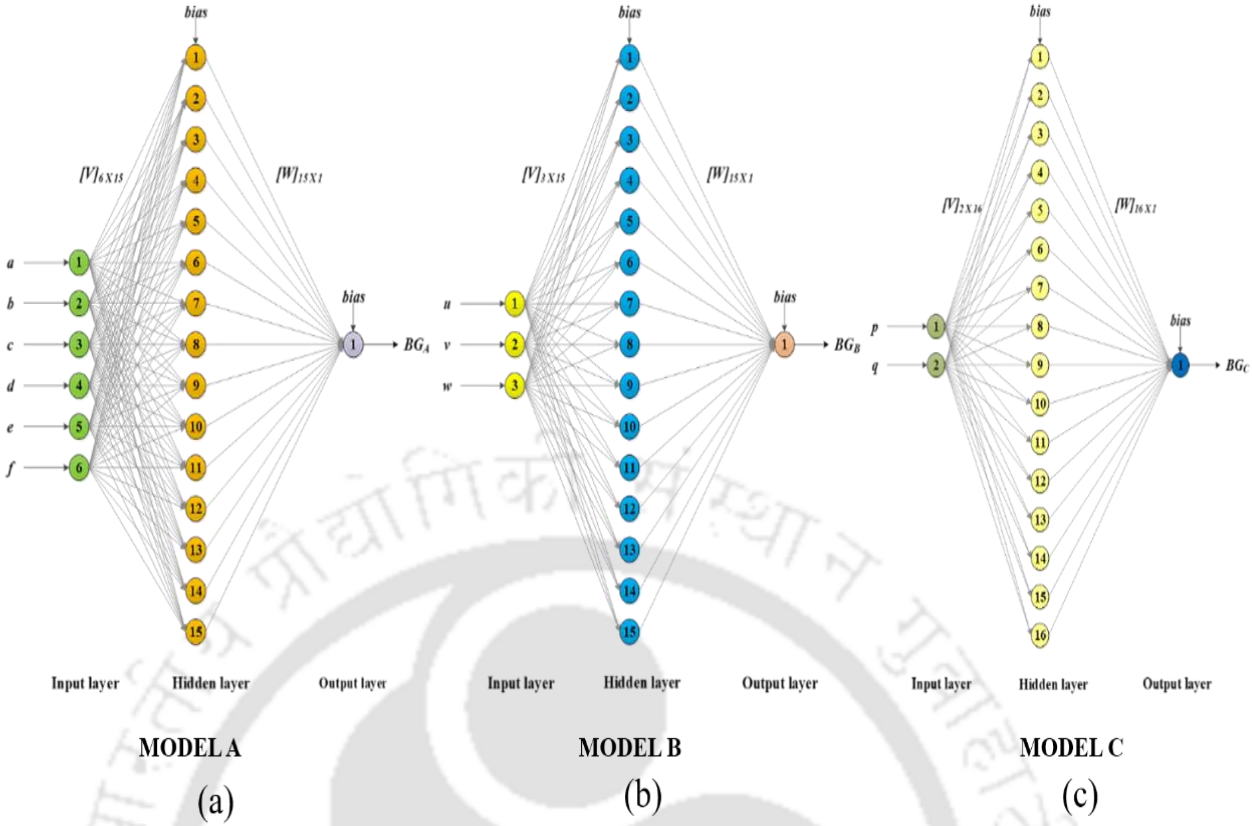

Figure 7.5 Near-optimal NN architecture for: (a) MODEL A (b) MODEL B (c) MODEL C

7.3.2 Performance analysis of NN-GA scheme

BPNNs were constructed to model a relationship between macro-textured geometric parameters and percentage bone growth (BG) at the bone-implant interface over representative uncemented prostheses having three distinct macro-textures. To select near-optimal neural networks, phase-wise parametric studies were conducted, followed by cross-validation against a suitable set of test datasets. When calculating BG for any clinically admissible input string, the NN's average computational time was estimated to be a fraction of a second. On the contrary, each simulation for prediction of BG through mechanobiology based FE analysis required more than an hour in a high-performance workstation (Windows 10 Pro, 8-core AMD Ryzen 7 3700X CPU, 64 GB RAM, speed 3.59 GHz).

Comparative analysis of the predicted output from NN and the target output for the training dataset (Fig. 7.6) as well as that for testing dataset (Fig. 7.7) of **MODEL A**, **MODEL B** and **MODEL C** are shown. Both the training (R^2 = 0.938) and testing datasets (R^2 = 0.936) in **MODEL A** had significant coefficients of determination

(R^2). The overall performance over the training dataset was also found to be significant, since the final mean squared error (MSE) was found to be 0.0014 (~0.3% of mean target values). Additionally, a consistency was observed in the training dataset as well, since only ~4.0% constituted noise readings (Fig. 7.6a). Similarly, the training (R^2 = 0.982, 0.820) and testing datasets (R^2 = 0.997, 0.810) in **MODEL B** and **MODEL C** had significant coefficients of determination (R^2) respectively. The final MSE was found to be 0.0001 (0.05 percent of mean target values) for **MODEL B** and 0.0049 (~ 0.9% of mean target values) for **MODEL C**, indicating that the overall performance over the training dataset was significant. Furthermore, a consistency was observed in the training dataset as well since only ~2% in **MODEL B** (Fig. 7.6b) and ~7.7% in **MODEL C** (Fig. 7.6c) constituted noise readings.

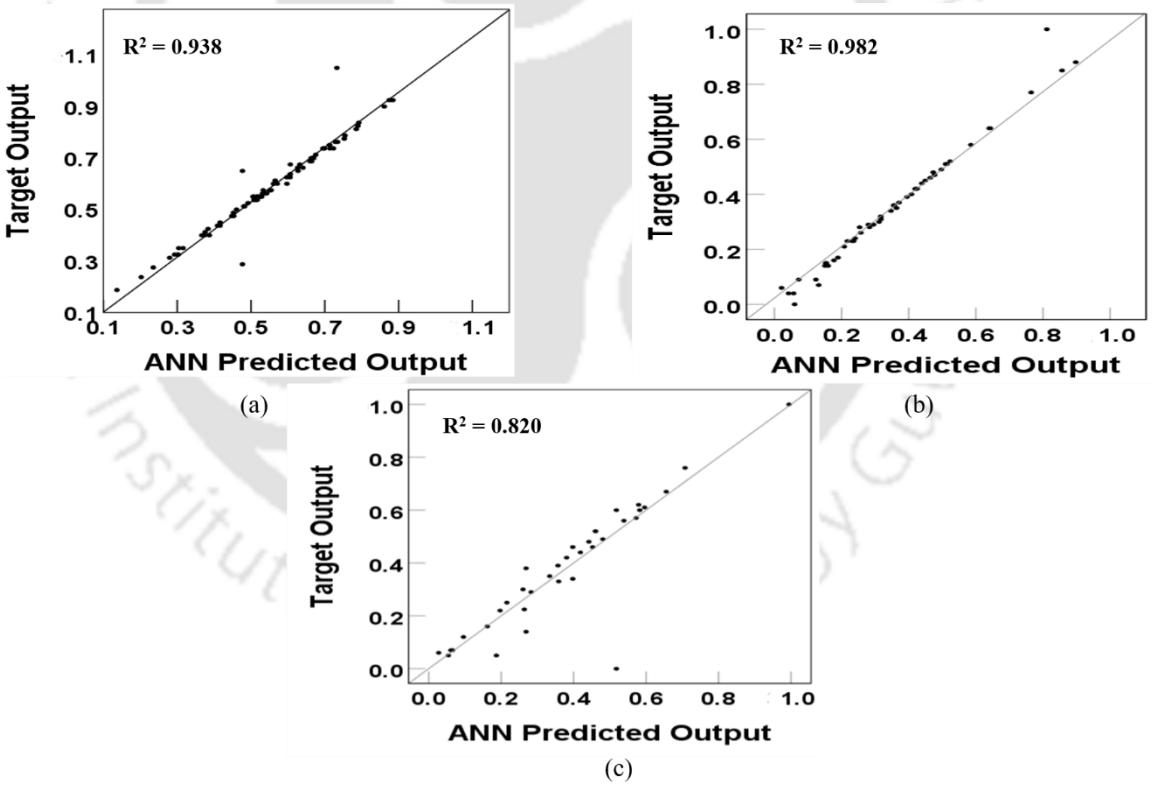

Figure 7.6 Target Output vs NN Predicted Output of the near-optimal NN for the training dataset of: (a) MODEL A (b) MODEL B (c) MODEL C

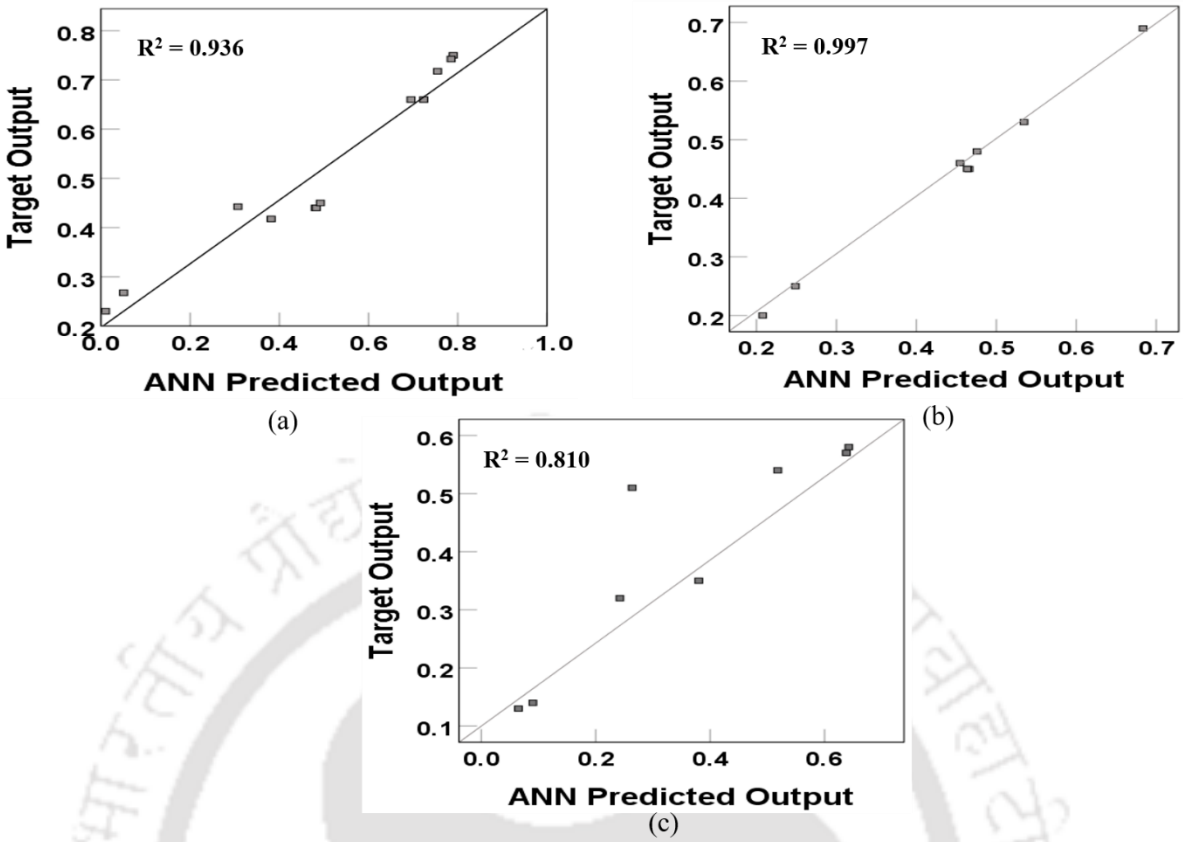

Figure 7.7 Target Output vs NN Predicted Output of the near-optimal NN for the testing dataset of: (a) MODEL A (b) MODEL B (c) MODEL C

However, unexpected correlations between the target and the predicted output have numerous statistical causes. The correlation obtained for the training dataset chosen for each of the models were closely correlated with the test dataset which provide confidence to the BPNN models developed in this study. However, as can be seen in the Figure 7.6c, the correlation obtained in the training dataset for MODEL C is relatively low (R^2=0.82) compared to that for other two geometric models (MODEL A and MODEL B) due to the presence of higher number of cross-trend outliers and quite a few fringe outliers in the dataset. This is further evidenced by the scatter-plot obtained for the test dataset (R^2=0.81) for the MODEL C as in the Figure 7.7c which shows high deviation from line of best-fit.

After construction and validation of the BPNN architectures, GA-based optimizations were performed to search for optimized macro-textured designs that would maximize bone growth thereby enhancing secondary stability (Mukherjee and Gupta, 2016; Kuzyk and Schemitsch, 2011) of the implants. A single-objective GA was executed for all the three models viz. **MODEL A**, **MODEL B** and **MODEL**

C separately with a population size of 200 over 20 generations (i.e. ~4000 design evaluations), a population size of 200 over 125 generations (i.e. ~25000 design evaluations) and a population size of 125 over 20 generations (i.e. ~2500 design evaluations), respectively, based on GA parametric studies as shown in Figure 7.8.

The optimal GA parameters for each of the models were obtained through the GA-parametric study as presented in Figure 7.8. The optimum set of GA parameters found from the GA-parametric study is presented in Table 7.6. The normalised BG predicted by NN for OMT_A, OMT_B and OMT_C were found to be -0.999992, -0.942333 and -0.99948 respectively, which on subsequent de-normalisation, predicted BG from NN for OMT_A, OMT_B and OMT_C were found to be ~14.9%, ~24.8% and ~20.5%, respectively (Fig. 7.9).

Table 7.6 Optimal GA parameters

Parameters	MODEL A	MODEL B	MODEL C
Cross-over Fraction (c)	0.85	0.65	0.75
Population Size (P)	200	200	125
Number of Generations (G)	20	125	20

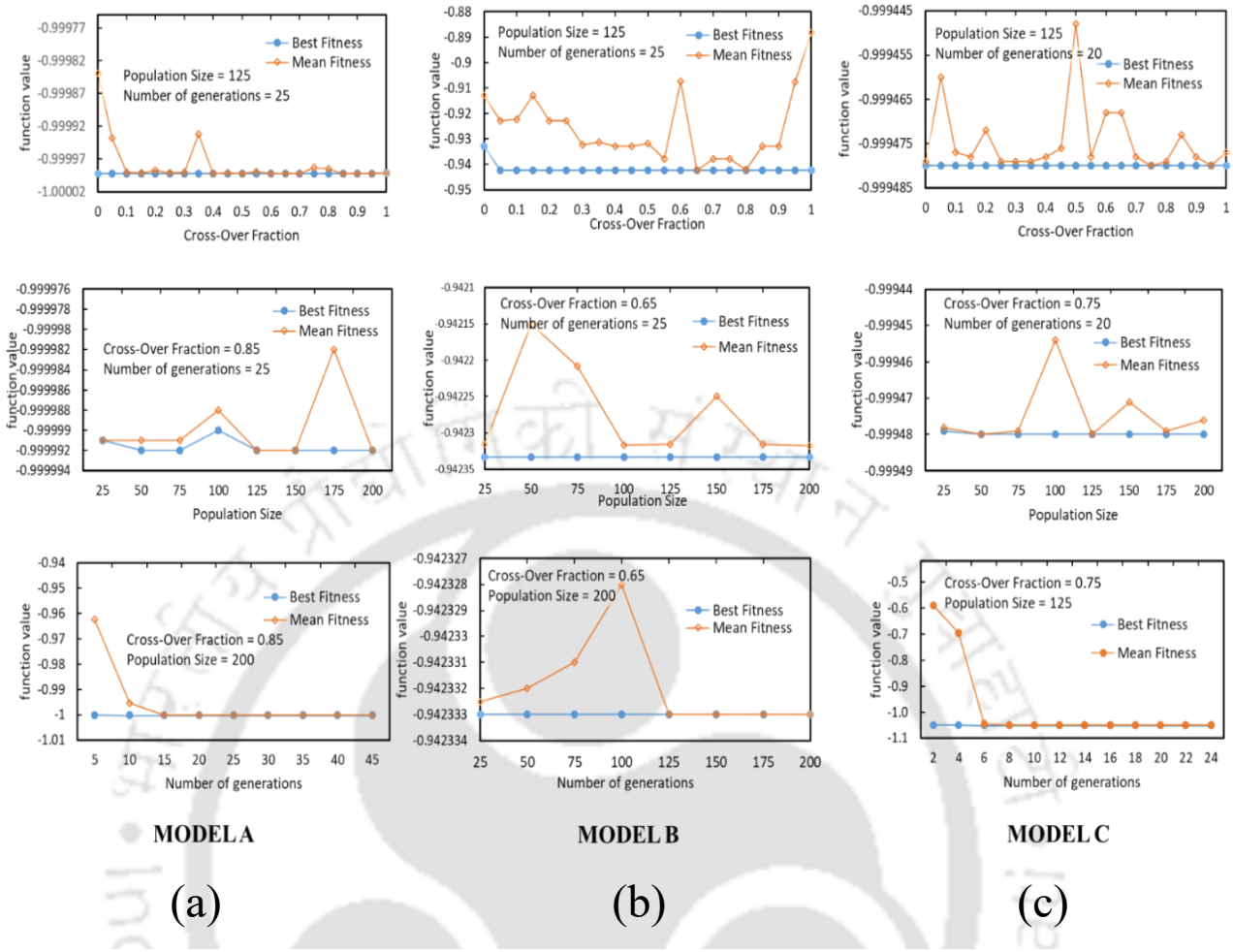

Figure 7.8 Parametric study to obtain optimal GA parameters for all the *in silico* models: (a) MODEL A, (b) MODEL B and (c) MODEL C.

A bar-chart (Fig. 7.9) presents a comparison between BG calculated from FE analysis and that predicted from NN over macro-textures for all the models. The BG calculated from FE analysis corresponding to OMT_A was found to be 14.4%, which was close to the NN predicted de-normalized BG (absolute error ~3.35%). In addition, it can be observed from Figure 7.9 that the BG (FE- calculated and NN predicted) for the OMT_A was higher compared to the initial model for **MODEL A**. The NN predicted BG for OMT_A was found to be ~4.04% higher, compared to that for the initial model.

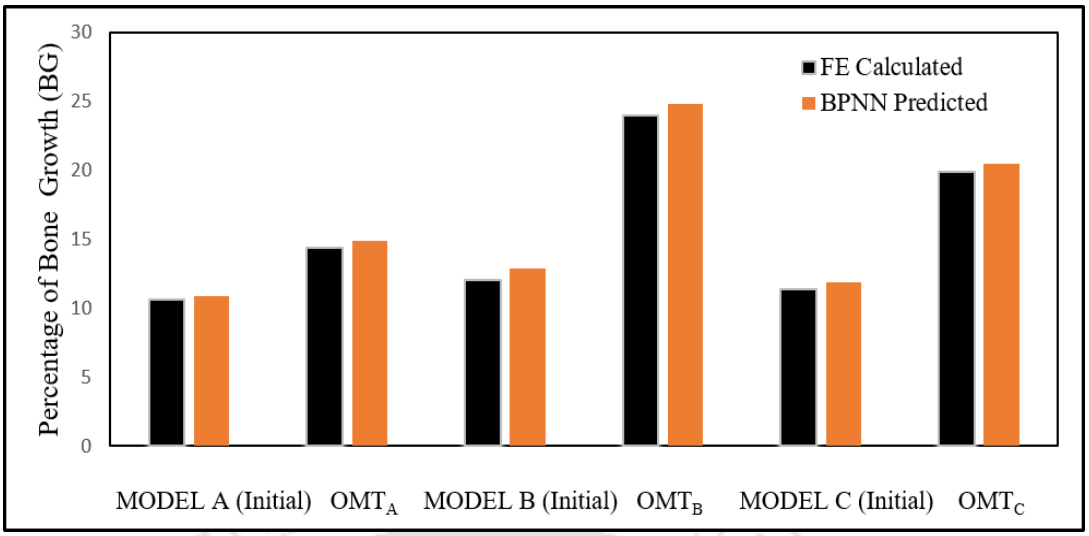

Figure 7.9 A comparison between FE-calculated and BPNN-predicted BG over macro-textures for all the initial models and their corresponding Osseointegration-maximized-textures (OMT)

Similarly, the FE-calculated BG (Fig. 7.9) corresponding to OMT_B was found to be 24%, which was close to the NN predicted de-normalized BG (absolute error ~3.22%). In addition, it can be observed from Figure 7.9 that BG (FE- calculated and NN predicted) for the OMT_B was higher compared to the initial model for **MODEL B**. The NN predicted BG for OMT_B was found to be ~11.93% higher, compared to that for the initial model.

Corresponding to OMT_C, the FE-calculated BG (Fig. 7.9) was found to be 19.9%, which was close to the NN-predicted de-normalized BG (absolute error ~2.93%). In addition, it can be observed from Figure 7.9 that BG (FE- calculated and NN predicted) for the OMT_C was higher compared to the initial model for **MODEL C**. The NN predicted BG for OMT_C was found to be ~8.64% higher, compared to that for the initial model. It is also noteworthy that, the percentage enhancement in percentage of BG was 37.2% for **MODEL A**, 92.7% for **MODEL B** and 72.85% for **MODEL C** which is found to be significantly higher as compared to that offered by their initial models.

7.3.3 Osseointegration-maximized-texture (OMT) of the implant models

The design parameters for OMT_A and initial macro-textured design for **MODEL A** are presented in Table 7.7. It has been observed that, there has been decrease in the

dimensions of parameters '*a*' and '*c*' from 2.5 mm to 1.0 mm and 1.5 mm to 1.0 mm respectively from initial design. On the contrary, there has been increase in the dimensions of parameters '*b*' and '*d*' from 2.0 mm to 2.5 mm and 1.0 mm to 2.1 mm respectively. The ridge width parameter '*e*' has been found to decrease from 2.5 mm to 1.2 mm, whereas the groove-spacing parameter '*f*' remains constant for both the models so as to maintain dimensional constraint. Similarly, the design parameters for OMT_B and initial macro-textured design for **MODEL B** are also presented in Table 7.7. It has been observed that, there has been decrease in rib height parameter '*u*' and ridge width parameter '*v*' from 2.5 mm to 1.0 mm and 2.0 mm to 1.0 mm respectively. Reduction in the inter-rib spacing or groove spacing parameter '*w*' has also been observed from 5.0 mm to 3.0 mm. The design parameters for both OMT_C and initial macro-textured design for **MODEL C** are presented in Table 7.7. It has been observed that there has been reduction in the groove spacing parameter '*p*' from 2.5 mm to 1.4 mm from initial design to OMT_C. In addition, reduction in ridge-width parameter '*q*' has also been observed from 2.0 mm to 1.2 mm.

Table 7.7 Design parameters and NN predicted bone-growth corresponding to initial and optimized designs

MODEL A		Initial Model	Optimized Model
Design Parameters (mm)	*a*	2.5	1.0
	b	2.0	2.5
	c	1.5	1.0
	d	1.0	2.1
	e	2.5	1.2
	f	3.0	3.0
NN predicted bone-growth (%)		10.86	14.9
MODEL B		Initial Model	Optimized Model
Design Parameters (mm)	*u*	2.5	1.0
	v	2.0	1.0
	w	5.0	3.0
NN predicted bone-growth (%)		12.87	24.8
MODEL C		Initial Model	Optimized Model
Design Parameters (mm)	*p*	2.5	1.4
	q	2.0	1.2
NN predicted bone-growth (%)		11.86	20.5

It is clearly evident, from Table 7.7, that OMT_A, OMT_B and OMT_C have significant geometric variations as compared to their initial models. OMT_A (corresponds to optimal macro-texture for **MODEL A)** has ribs that exhibited periodic arrangement of lower and higher rib dimensions so as to achieve uniform stress regime in the interfacial region to promote higher levels of bone growth. Both OMT_B and OMT_C have reduced ribs and groove dimensions as compared to their initial models. This improves osseointegration by reducing the formation of fibrous tissues at the groove basins. From the results of the present study, it could be observed that reduction of groove radius as well as inter-groove spacing lead to enhancement of in vitro osteogenic differentiation of MSCs which was also reported by Gui et al., 2018. Moreover, spacing ratio i.e. ratio of inter-rib spacing (w) to rib width (v) in case of the macro texture in **MODEL B** has been found to be 1:3 for the optimized model OMT_B which is also reported in an earlier study (Gui et al., 2018) which reported that similar spacing ratio promotes enhanced osteogenic differentiation. In addition, Hydrostatic stress has been found to increase with deeper ribs due to increase in stress-concentration factor (Depover et al., 2019; Pedersen, 2010). Increased hydrostatic stress promotes fibrous tissue as is relevant from mechanoregulatory tissue-differentiation algorithm (Mukherjee and Gupta, 2016; Claes and Heigele, 1999; Lacroix and Prendergast, 2002a; Chou and Müftü, 2013; Dickinson et al., 2012; Isaksson et al., 2006b; Hori and Lewis, 1982; Jurvelin et al., 1997) as mentioned in Table 3.1, Chapter 3. These results from the present study which confirm some of the earlier independent research reinforce the confidence of the present optimal results. The results in the present study also corroborates with the study results presented in Chapter 4 that higher stress-concentrations due to longer ribs and deeper grooves promotes formation of fibrous tissues.

7.4 Clinical significance of the present work

Kuroshima et al., 2017 emphasized the need for the modifications in implant macro textures to achieve better osseointegration. Vidyadhara and Rao, 2007 also stressed the importance of better proximal press-fit fixation to prevent distal stress-shielding in THA. Fig. 7.10 shows the distribution of major tissue growth over the three macro-textured optimized implant designs after 120 days of healing. From clinical significance, as observed in earlier findings (Kuzyk and Schemitsch, 2011), distance

osteogenesis (Fig. 7.10) was prevalent for all the initial as well as optimized designs which promotes attainment of secondary stability of the prosthesis. In a few other studies (Puthumanapully, 2010; Liu and Niebur, 2008; Choi et al., 2017), bone mineralization at the edge of the host bone region as well as a further progression towards the surface of the implant was observed.

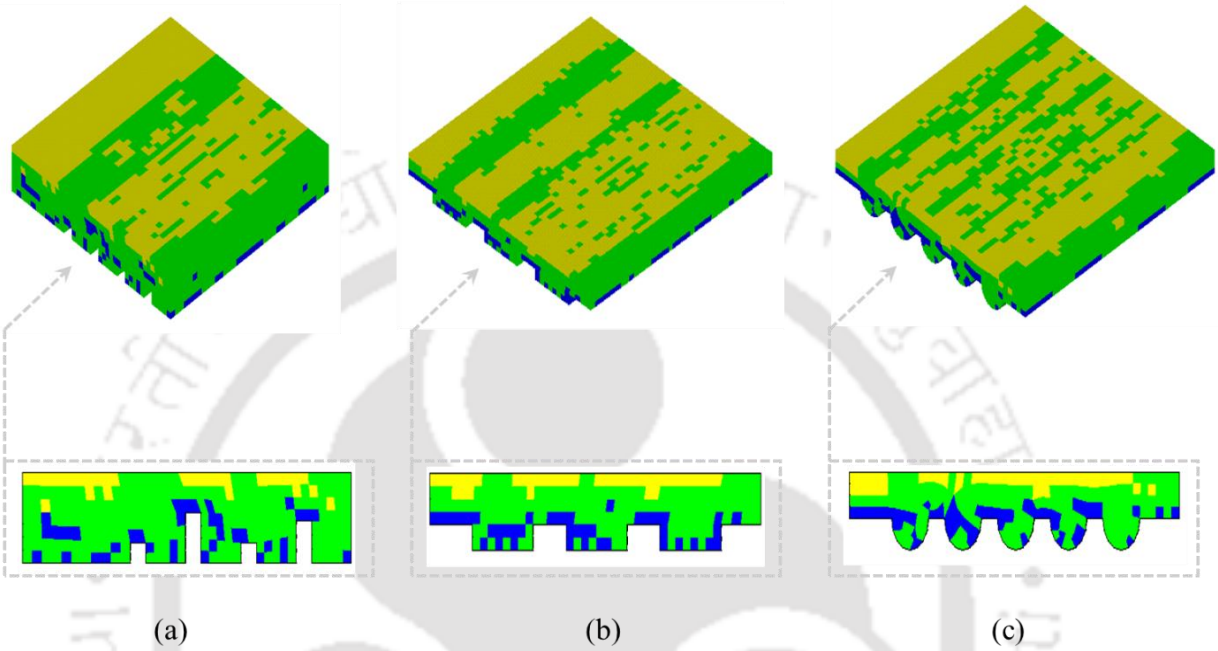

Figure 7.10 Distribution of major tissue growth over the three macro-textured optimized implant designs after 120 days of healing period: (a) MODEL A, (b) MODEL B and (c) MODEL C (Colour Map: Blue for fibrous tissue; Green for cartilaginous tissue; Yellow for Bone).

7.5 Limitations and Usefulness of the present scheme

It is to be noted that the computational scheme for predicting bone growth employed in the present study is a simplified form of realistic post-surgical bone growth phenomena, which is also influenced by other anatomic and physiological conditions, surgical techniques and osteogenic factors. In the present study, a perfectly bonded bone-implant interface condition was considered for prediction of bone growth which might disregard the fuzzy nature of the bone–implant interface. However, by comparing the bone growth between perfectly bonded and non-bonded interface condition, earlier study (Mukherjee and Gupta, 2016) reported that the difference was observed to be insignificant. In addition, it may be noted that a full-

scale bone-implant models with spatial variation in micromotion values with realistic physiological boundary conditions may provide further insight into the present computational scheme, it acts as a stopgap model with the sole purpose of methodical prediction of the secondary stability at the bone-implant interface.

Although the diffusion model has been employed in the present investigation to mimic the biological phenomena of MSC migration, but it does ignore the reaction term and hence does not comprehend cellular proliferation and other cellular activity like apoptosis (Lacroix et al., 2002). But, if reactive terms like proliferation, apoptosis etc. were included, the rate of tissue differentiation would have varied everywhere in proportion to cellular concentration. Thus, fundamentally the trends of tissue differentiation would not be expected to alter to a considerable extent as reported by Lacroix et al., 2002. Nevertheless, the outcome predicted by NN for all the three models, being a generalized one, may not predict actual bone growth condition for a wide range of patients which further necessitates long term clinical results to validate the *in silico* model, since inter-patient diversity plays a major role in design assessment of orthopaedic implants (Dopico-González et al., 2010; Pancanti et al., 2003). However, this method will definitely be useful for a specific group of implants.

The trained NN architectures may also face the consequences of being under-fit or over-fit. A sufficient quantity and quality of training dataset along with careful selection of epochs are essential for better performance of the NN architectures. Diversity of dataset influences the NN to perform better (Dorronsoro, 2002). In the present case, enough care has been taken in shuffling and splitting of the training and testing dataset so as to enhance the diversity in the dataset. The NN topologies were determined based on the average of all such shuffling cases so as to achieve the overall distribution of the available data for each of the model. The chances of bias in the datasets thus has been minimized sufficiently. In addition, the FE analysis output does not have any significant noise to influence it and the data being sufficiently spread does not allow over fitting of the NN. Even though a diversified set of training data was used in training each of the neural networks, there is always a room for improvement.

The presently developed BPNN scheme attempts to relate the levels of osseointegration with the implant macro-textures under a constant relative micromotion between implant and bone. It may be worth noting that there will be variation in quantification of bone growth with the change in loading and displacement boundary conditions at the bone-implant interface models (Puthumanapully, 2010; Andreykiv et al., 2008a). However, the present scheme proposed in this Chapter is flexible enough to incorporate variable loading and boundary conditions in a future investigation.

The present investigation is based on simplified model in the sense that it does not consider the porous coating on the implant surface, density of bone and cartilage extracellular matrices (ECMs) as well as osteogenic and chondrogenic growth factors. While incorporation of those factors makes the model more complicated but the qualitative prediction and spatial distribution of bone formation at the bone-implant interface has been reported to be not so significant (Lacroix et al., 2002; Mukherjee and Gupta, 2017a). However, the quantitative estimation of bone growth was little higher (Mukherjee and Gupta, 2017b) while considering cell-phenotype specific algorithm as compared to phenomenological algorithm. Therefore, the present model though little simplified does produce a conservative estimate of bone growth and serves the objective of determining the optimum morphology of the implant texture.

Nevertheless, this obviates the need for more robust albeit computationally expensive FE based mechanobiological predictions of osseointegration. Besides, the present work also hunts for optimized macro-textures for each model investigated, by utilizing BPNN as a method to evaluate the value of the objective function. However, the optimized macro-textures, so obtained, may not be optimal ones considering other failure mechanisms involved with uncemented arthroplasty, e.g. tribological aspects or stress-shielding phenomena. Nevertheless, the developed methodology provides sufficient flexibility to the implant manufacturers, clinicians and the scientists to explore wide range of implant designs with rational speed and accuracy, while choosing a trade-off implant for patient-specific surgical interventions.

7.6 Summary

This study presents near-optimal NN architectures framed for the purpose of predicting long-term secondary stability of uncemented prosthesis at representative bone-implant interface models having commercially viable macro-textures. This is perhaps the first reported NN-based investigation to relate geometric design parameters to the resulting percentage of bone growth. Some of the important conclusions from the present study:

- The levels of NN-predicted BG were found to have pronounced agreement with the FE-predicted results.
- The OMTs obtained based on the GA search were found to offer enhanced biologic fixation, compared to that offered by discernible textures in three distinct initial models.
- Results from the study show that reduction in the dimension of ribs/grooves promotes higher levels of bone growth.
- Moreover, periodic patterns of ribs with higher and lower rib dimensions predicted uniform stress regime at the interfacial region, thereby resulting in enhanced bone growth.
- The present NN-GA based scheme was able to speculate the amount of bone growth based on geometric parameters of the macro-textures and may, therefore, be used as a pre-clinical tool for the search of favourable implant designs.

CHAPTER 8

Qualitative assessment of growth of connective tissues on femoral stem with macro-textures

This chapter presents an in silico investigation of the qualitative trend of growth of connective tissues for a specific type of femoral implant with commercially discernible macro-textures on its proximal surfaces. Based on a CT-scan dataset, patient-specific bone material modelling and musculoskeletal loading conditions with peak forces during normal walking and stair climbing were considered in this study. Mechanoregulatory algorithm was used to qualitatively assess the spatial distribution and amount of bone growth. A comparative analysis of growth of connective tissues on femoral implant with and without proximal macro-textures were also investigated under normal walking.

8.1 Importance and Objective

As already discussed in Chapter 3, there are two modes of implant fixation in the intramedullary bone canal. Cemented fixation relies primarily on the bone cement or PMMA that acts as a void filler at the gaps between the bone and the implant. In addition, bone cement also helps in proper adherence of the implant with the host bone. Bone cement is however less reliable due to its exothermic polymerization, high stiffness and minimum reliability for a long period of time (Tai et al., 2016). On the contrary, the uncemented fixation relies on the mechanical interlocking of the surface textures on implant to the bony ridges of healthy bone as well as biologic fixation of the newly formed tissues connecting the host bone and the implant. Due to fewer limitations in uncemented implant fixation specially to younger population where bone quality is relatively good and the cancellous bone provide adequate fixation strength, this methodology is widely used in many countries including India (Puthumanapully, 2010). Classical designs of femoral implants have either have been plain surfaces or else included macro-textures on the proximal implant so as to adhere the implant with the endosteum of the proximal diaphysis. As discussed earlier in Chapter 4, when subjected to mechanical loads, the implants along with their surface morphologies have inherent ability to change the mechanical environment around the prosthesis. Variation in mechanical stimulus at the bone-implant interface further changes the growth pattern of connective tissue at the interface (Mukherjee and Gupta, 2016; Mathai and Gupta, 2022). The role of proximal surfaces of the femoral implants were often overlooked due to more emphasis on the bone-implant stability at the distal section. Furthermore, the macroscopic textures got more emphasis on mechanical interlocking rather than investigating their role in bone growth.

In the previous chapters on analysing the influence of macro-textured surfaces on bone growth, neither the whole implants were studied nor the real-life musculoskeletal loading conditions were incorporated. It is however a known fact that excessive interfacial micromotions (sliding and gap distances) lead to unstable implant fixation mostly owing to the imbalance in mechanical stability between the implant and the host bone (Sánchez et al., 2021a; Sánchez et al., 2021b). However, these relative displacements at the bone-implant interface shares a cause and effect relationship with the musculoskeletal loading conditions. The goal of hip

replacement procedure is to restore the failed hip joint and thus aid the patients towards a normal walking gait. It is however noteworthy that, the patient still shows some form of disability even after a successful hip procedure.

Normal walking and stair climbing are the two daily activities which are suggested by experienced orthopaedic surgeons after a successful hip procedure. Other sorts of routine activities are generally not recommended at least for first six weeks after implantation. Climbing of stairs causes high hip joint force and high torsional moments around the prosthesis (Bergmann et al., 1995). High magnitude of joint forces and moments may contribute to early aseptic loosening of the femoral stems (Bergmann et al., 1995). However, modifications in design of femoral stems may reduce the risk of endoprosthethic loosening by improving primary as well as secondary stability of the implants. Studies have not been performed earlier to decide whether or not macro-textured architectures on surface of femoral stem have any influence on changing the qualitative distribution of type of connective tissues at the bone-implant interface under daily routine activities. In addition, no studies have been performed to understand the qualitative assessment of growth of different tissue phenotype comparing two femoral stems with or without macro-textured architectures under daily routine activities.

As discussed in Chapter 4, after a successful hip procedure, a sequence of events take place around an uncemented prosthesis resembling the events during primary bone fracture healing (Kienapfel et al., 1999; Davies, 1996,2003). Variation in micromotion at the bone-implant interface depend on different parameters such as musculoskeletal loading conditions, stiffness of the femoral stem, quality of the bone of the patient and design of the stem. Under optimum loading, sufficient primary stability and optimum level of micromotion, bone growth occurs at the bone-implant interface gap connecting the femoral stem with the healthy bone. However, high magnitude of strains due to excessive micromotion may result in fibrous tissue formation at the gap thus weaken the interface strength (Haddad et al., 1987; Jasty et al. 1991; Jasty et al., 1997; Puthumanapully and Browne, 2010).

There has been an extensive use of commercially available femoral stems that are used clinically after years of continuous research and development but yet are considered relatively unknown commodity in terms of functional reliability and

durability (Puthumanapully, 2010). A study by Kurtz et al., 2007 reported that the demand for total hip arthroplasty (THA) is projected to grow by 174% in the United States itself by 2030. A retrospective cohort study by Bhattacharyya et al., 2007 reported that there has been an increase of patients by 216% between 2002 and 2006 who requires revision surgery for failed joint following peri-prosthetic hip fracture. With such a large scale demand for artificial hip and lack of sufficient retrieval studies for these hip stems as well as lack of clinical outcomes, *in silico* assessment of implants can provide a quicker solution towards performance of such prosthesis. Very few computational assessments (Folgado et al., 2009; Tarala et al. 2011; Mathai and Gupta, 2022) of growth of tissue phenotype over a femoral stem has been performed as yet. Folgado et al. 2009 studied the influence of hip stem geometry, material and extent of porous coating on bone growth in an uncemented THA. Tarala et al., 2011 proposed a FE methodology to study combined bone growth and remodelling for hip stems. Both these studies used magnitude of micromotion at the bone-implant interface in order to pre-clinically assess the pattern of tissue differentiation instead of using any of the mechanoregulatory principles as discussed in Chapter 2. Very recently, Mathai and Gupta, 2022 employed a multiscale framework (Mukherjee and Gupta, 2016) to pre-clinically assess the influence of musculoskeletal loading conditions on bone ingrowth into porous coated hip stems with micro-textured surfaces using mechanoregulatory principle of Claes and Heigele, 1999.

In view of the above discussions, the aim of the present study is to perform a comparative assessment of growth of connective tissue at the bone-implant interface due to a femoral stem with and without macro-textures at its proximal surfaces. In addition, qualitative trends of bone growth have also been studied for femoral stems with proximal macro-textures under daily routine activities such as normal walking and stair climbing.

8.2 Problem definition-materials and methods

The patient-specific FE models of implanted proximal left femur were developed based on a patient-specific lower limb Computed Tomography (CT) scan dataset (512 x 512 pixels; pixel size of 0.707 mm; slice thickness of 0.625 mm) of a 35-year-old female patient having 58 kg body weight (BW).

8.2.1 Development of FE model

The 3-D surface model of left proximal femur was developed using CT-scan data and imported to ANSYS V14.5 FE software (ANSYS Inc., Canonsburg, PA, USA). Values in Hounsfield Units (HU), also referred as CT number were used to express the CT gray scale value (GSV). Figure 8.1 shows a 3-D surface model of the femur. To obtain the 3-D surface model of the femur (Fig. 8.1), the CT-scan data was processed using a medical image processing software, MIMICS® (Materialise, Leuven, Belgium). Image segmentation was used within a 2-D CT-scan slice to distinguish bone from soft tissue using CT number threshold values.

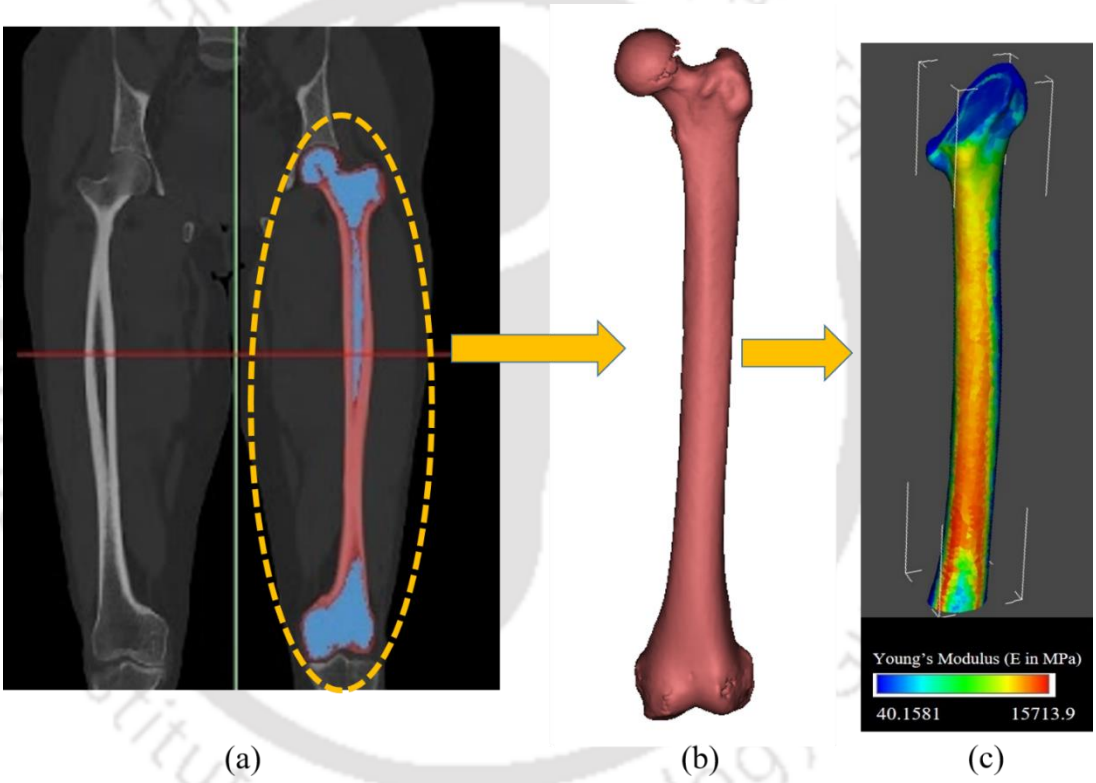

Figure 8.1 (a) Coronal view of the CT scan image of the patient; (b) 3D surface model developed in MIMICS®; (c) Site-specific isotropic material property of the bone after resection and implementation in BONEMAT

A solid model of a femoral stem considering the major dimension of a generic CORAIL hip stem (size 12 collarless) was reproduced in SolidWorks® software (DS SolidWorks Corp., Concord, MA, USA) as shown in Figure 8.2. Two such implant models were developed with one having textures on its proximal surface and another without textures on its proximal surface. From herein, one

implant will be referred as textured femoral stem (TFS) and another non-textured femoral stem (NTFS). In addition, the model of the femur and the implants were further converted into faceted surfaces (STL format) and imported into Rhinoceros® software (Rhinoceros V6.0, Robert McNeel & Associates, Seattle, USA). A layer of granulation tissue was developed around the proximal surface of the implant by uniformly exploding the implant geometry at the proximal surface by 1 mm in every direction and thereby performing Boolean subtraction operation. As discussed in Chapter 4, this additional layer of granulation tissue acts as the site of tissue growth after implantation. It is however to be noted that, the length of the original left femur was 390 mm which was further resected by 100 mm from the distal tip of the femur so as to reduce computational cost. The femur was then resected from top as well and the tissue-implant assembly was positioned virtually inside the bone canal through Boolean operations as shown in Figure 8.2. The resected angle and position of the implant inside the bone canal was kept so as to mimic surgical protocols. The femoral stem occupied a major region of proximal epiphysis, proximal metaphysis as well as portion of diaphysis.

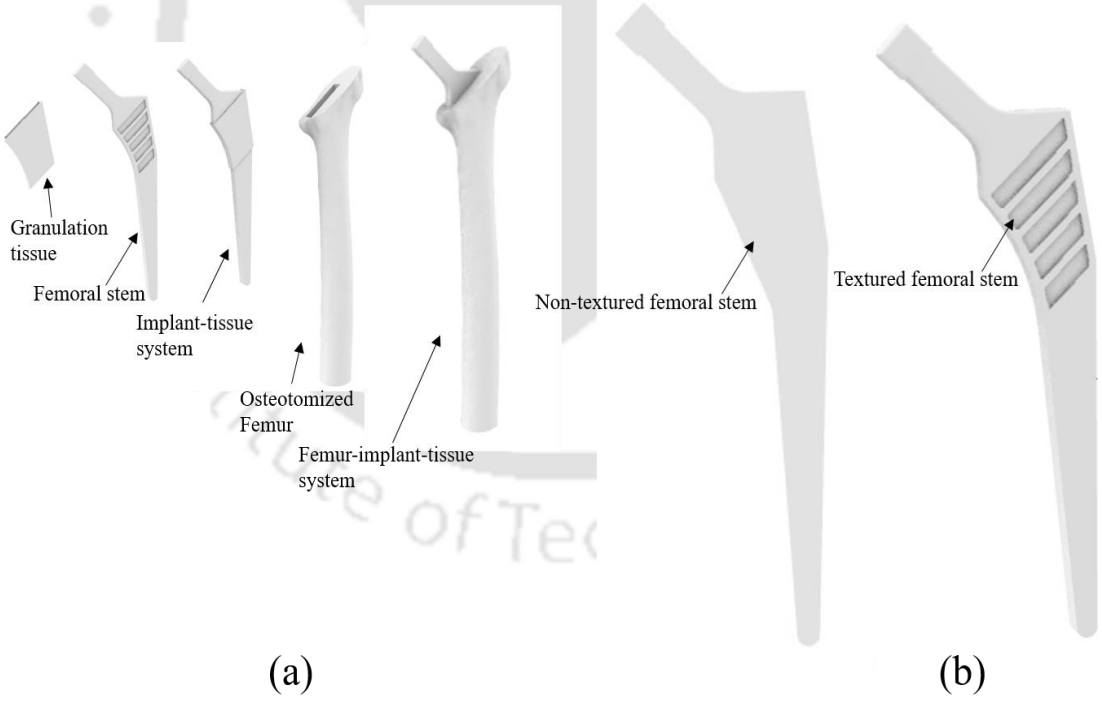

Figure 8.2 (a) 3D CAD models of the granulation tissue, femoral stem, assembled implant-tissue system, osteotomized bone and total femur-implant-tissue assembly; (b) 3D CAD models of the femoral stems (with and without texture on proximal surface)

The whole assembly in the form of tessellated surface models was then imported to ANSYS ICEM CFD V14.5 FE software (ANSYS Inc., Canonsburg, PA, USA) to

check and repair any existing faults in the geometry. Volumetric mesh was generated with 4-noded tetrahedral mesh which was imported to ANSYS Mechanical APDL V14.5 FE software (ANSYS Inc., Canonsburg, PA, USA) for further processing. It is however to be noted that, relatively finer mesh was used at the bone-implant interface region for better stress-strain estimation. 4-noded tetrahedral elements were then converted to 10-noded tetrahedral elements (SOLID 187) using an APDL script as shown in Figure 8.3. The choice of using 10-noded tetra elements in place of 4-noded tetra elements was attributed to higher convergence rate as well as they were found to produce better outcomes (Viceconti et al., 1998; Fraldi et al., 2010). In addition, a useful feature of tetrahedral elements with quadratic shape function is its excellent ability to approximate complex shapes and geometries such as biological tissues like femur (Fraldi et al., 2010).

The optimum element size to be used for the study was decided by experimenting with various mesh configurations on implanted femurs with peak loads on hip joint considering normal gait. For the femur-implant-tissue model with TFS, mesh independency was checked with three different mesh sizes containing ~76525 elements (coarse mesh), ~150558 elements (medium mesh) and ~385275 elements (fine mesh) comparing maximum deviatoric strain. The maximum difference in peak deviatoric strain was found to be 7% between coarse and medium mesh and 2.1% between medium and fine mesh. Similarly, for the femur-implant-tissue model with NTFS, mesh independency was checked with three different mesh sizes containing ~75523 elements (coarse mesh), ~153532 elements (medium mesh) and ~380273 elements (fine mesh) comparing peak deviatoric strain. The maximum difference in peak deviatoric strain was found to be 5.3% between coarse and medium mesh and 1.5% between medium and fine mesh. In the present study, peak deviatoric strain was used for the mesh convergence study as opposed to peak von Mises stress as performed in studies as discussed in earlier chapters because deviatoric strain itself is believed to be a strong predictor of tissue growth at the bone-implant interface (Isaksson et. al., 2006; Tarlochan et al, 2018; Mehboob et al., 2020; Mohandes et al., 2021).

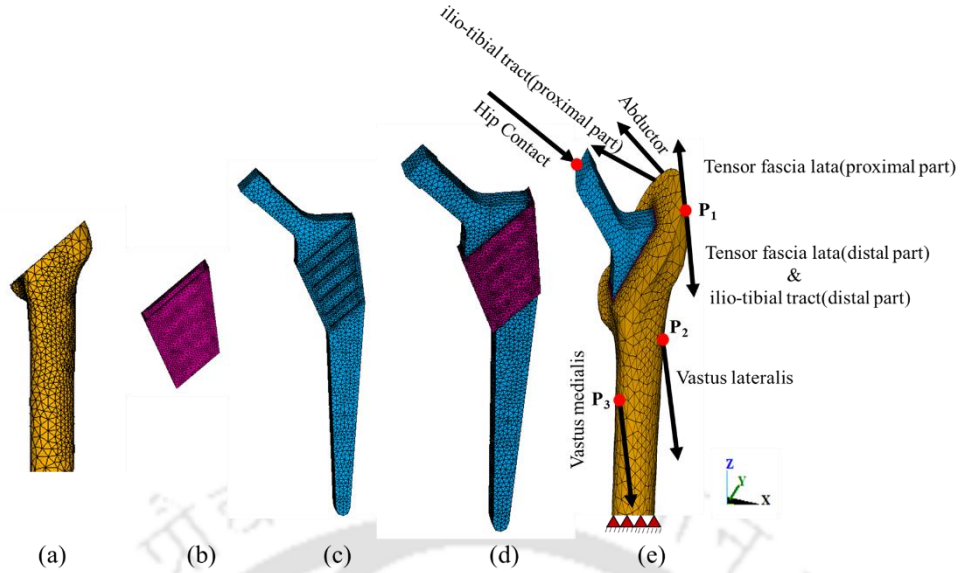

Figure 8.3 FE models of (a) resected bone; (b) granulation tissue; (c) implant (d) implant-tissue assembly; (e) total assembly of bone-tissue-implant with musculoskeletal loading and boundary condition

8.2.2 Material Properties

In the present study, bone was assumed to be linear elastic and isotropic material. However, considering an influence of local stiffness of the bone on the mechanical environment around the granulation tissue, it was critical to avoid single stiffness value for the entire bone and instead assigning element-specific properties. The site-specific material property was extracted from the patient-specific CT scan data set using a freeware software, BONEMAT V3.2, developed at the Institute Ortopedici Rizzoli, Bologna, Italy (Taddei et al., 2007). BONEMAT is a programme that connects a 3D finite element mesh to the bone radiography density (Hounsfield units, HU) obtained from a CT scan data set. The BONEMAT algorithm then uses a nonlinear relationship to assign an elastic modulus to each finite element based on the apparent bone density at the associated element location on the CT scan data set. The apparent density (ρ in g cm^{-3}) for bone at each element was computed using the following relationship:

$$\rho = \rho_1 + (\rho_2 - \rho_1) \times \frac{[HU - HU_1]}{[HU_2 - HU_1]} \tag{8.1}$$

where HU_1 and HU_2 denotes the CT numbers of no bone condition (HU_1=0 HU) and cortical bone (HU_2 = 1658HU) as obtained from CT scan data set, respectively. ρ_1(0.022 g cm^{-3}) and ρ_2(1.73 g cm^{-3}) are apparent densities of no bone condition and

cortical bone, respectively. Any CT-GSV value that was negative was considered 0 HU (no bone condition). The apparent density (in gcm^{-3}) was connected to the Young's moduli (E in MPa) of bone elements using the following relationship (Morgan et al., 2003; Chanda et al., 2016):

$$E = 7281\rho^{1.52} \tag{8.2}$$

Young's modulus for the implant material (high-nitrogen stainless steel alloy M30NW) was taken as 195 GPa (Aubert & Duval, France) and that of granulation tissue is taken as 1 MPa. Poisson's ratio for bone and implant was considered as 0.3, whereas that of granulation tissue was considered 0.167. The implant-tissue interface and bone-tissue interface were considered perfectly bonded. However, a surface-to-surface contact pair was modelled between the distal portion of the implant to the bone with a coefficient of friction of 0.5 (Mehboob et al., 2020). The contact simulation was performed using the Augmented Lagrangian Algorithm (ALA) in ANSYS Mechanical APDL V14.5 FE software (ANSYS Inc., Canonsburg, PA, USA).

8.2.3 Loading and boundary conditions

The implanted femur model was oriented laterally by 10° in the frontal plane while 9° dorsally in the sagittal plane following the orientations mentioned in ISO 7206-4:2010. The musculoskeletal forces from two routine activities such as normal walking and stair climbing were considered for FE study. A concentrated load, P_0 was applied at the center of the head of the femoral stem in every loading condition as shown in Figure 8.3e. P_1, P_2 and P_3 are the points of attachments of different associated muscles considered during each routine activities (Fig. 8.3e). Doctors advise patient not to put entire weight on the operated leg right after surgery and instead walk with walking aid at least for 6 weeks. As a result, 80 percent of the patient's BW was applied to the femoral stem for the first 6 weeks considering the swing phase of the gait cycle (Heller et al. 2005; Pedersen et al. 1997) and assuming that the subject walks on walking aid and the operated leg is in the swing phase. Thereafter, 260 percent BW was considered for following 2 weeks, assuming the usual gait cycle as shown in Table 8.1. Similarly, when stair climbing was considered, 50 percent of the patient's BW was applied to the femoral stem for the first 6 weeks considering the swing phase of the gait cycle (Heller et al. 2005; Pedersen et al. 1997) and assuming that the subject climbs on stairs with walking

aid and the operated leg is in the swing phase. Thereafter, 280 percent BW was considered for following 2 weeks, assuming the normal gait cycle as shown in Table 8.2. Fixed boundary condition was applied at the diaphysis of the femur ~50 mm below the distal tip of the femoral stem. The estimated musculoskeletal loading conditions for normal walking and stair climbing were normalized to a body weight of the patient (58 kg).

Table 8.1 Maximum loads during normal walking (Heller et al. 2005; Pedersen et al. 1997)

Post-Operative Condition (@80% BW)			
Force	**F_x(N)**	**F_y (N)**	**F_z (N)**
Hip Contact	-108	-65.6	-458.4
Abductor	116	8.6	173
Tensor fascia latae, Proximal Part	14.4	23.2	26.4
Tensor fascia latae, Distal Part	-1	-1.4	-38
Vastus Lateralis	-1.8	37	-185.8
Normal Gait Cycle (@260% BW)			
Force	**F_x(N)**	**F_y (N)**	**F_z (N)**
Hip Contact	-324	-196.8	-1375.2
Abductor	348	25.8	519
Tensor fascia latae, Proximal Part	43.2	69.6	79.2
Tensor fascia latae, Distal Part	-3	-4.2	-114
Vastus Lateralis	-5.4	111	-557.4

Table 8.2 Maximum loads during stair climbing (Heller et al. 2005; Pedersen et al. 1997)

Post-Operative Condition (@50% BW)			
Force	**F_x(N)**	**F_y (N)**	**F_z (N)**
Hip Contact	-65.2	-66.7	-259.9
Abductor	77.1	31.7	93.4
Ilio-tibial tract, Proximal Part	11.5	3.3	14.1
Ilio-tibial tract, Distal Part	-0.5	-0.9	-18.5
Tensor fascia latae, Proximal Part	3.4	5.4	3.2
Tensor fascia latae, Distal Part	-0.2	-0.3	-7.1
Vastus Lateralis	-2.4	24.6	-148.6
Vastus Medialis	-9.7	43.6	293.8
Normal Gait Cycle (@280% BW)			
Force	**F_x(N)**	**F_y (N)**	**F_z (N)**
Hip Contact	-355.8	-363.6	-1417.8
Abductor	420.6	172.8	509.4
Ilio-tibial tract, Proximal Part	63	18	76.8
Ilio-tibial tract, Distal Part	-3	-4.8	-100.8
Tensor fascia latae, Proximal Part	18.6	29.4	17.4
Tensor fascia latae, Distal Part	-1.2	-1.8	-39
Vastus Lateralis	-13.2	134.4	-810.6
Vastus Medialis	-52.8	237.6	-1602.6

8.2.4 Methodology of applying tissue differentiation algorithm

The tissue growth phenomenon was simulated using a mechanoregulatory framework as shown in Chapter 3, Figure 3.1 that simulated the dispersal of MSCs through the region of granulation tissue using a transient-diffusion model as mentioned in Chapter 4, Equation 4.1.

A cell-dispersal period of 56 days or approximately two months was chosen for the dispersal of MSCs in the present study. Zero diffusion boundary condition was considered at the implant boundary, which represents no cell diffusion from the tissue towards impermeable implant. The concentration of other cells in the granulation tissue, which are unimportant for tissue differentiation, is considered to be zero (Andreykiv et al., 2008a; Puthumanapully, 2010; Mukherjee and Gupta, 2017a). The concentration of MSCs at the bone-tissue interface (c_{max}) was assumed to be c = 1.0.

Local mechanical signals at the granulation tissue quantified as hydrostatic pressure and deviatoric strain as reported by Claes and Heigele, 1999 determine the differentiation of MSCs into fibroblasts, chondrocytes and osteoblasts (Barry, 2006; Isaksson et al., 2006a) which on maturation, form fibrous tissue, cartilage and bone (Claes and Heigele, 1999). The mechanical conditions required for formation of various tissue phenotypes in the mechanoregulatory algorithm is shown in Chapter 3, Table 3.1.

The effective tissue material properties were numerically calculated using a rule of mixture as discussed in Chapter 4, Equations. 4.2 and 4.3. In order to avoid numerical instability after every iteration, a temporal smoothing methodology was implemented to update the material properties in each finite element in the tissue layer, following Equations. 4.4 and 4.5 as mentioned in Chapter 4. The tissue differentiation algorithm was implemented through a custom script written in MATLAB environment (Matlab 2017a, The MathWorks Inc., Natick, MA, USA). Every iteration in this numerical framework represents one post-surgical day. The entire simulation was set to run for 56 iterations in a high-performance workstation (Windows 10 Pro, 8-core AMD Ryzen 7 3700X CPU, 64 GB RAM, speed 3.59 GHz).

8.3 Results and Discussion

In this study, mechanoregulation based tissue differentiation algorithm was implemented to assess the qualitative distribution of different tissue phenotypes at the bone-implant interfaces of two implanted femoral stems with and without macro-textures on their proximal surfaces following a THA. Musculoskeletal loading condition under normal walking was considered for the FE simulation. The loading condition was divided primarily into two segments: post-operative condition up to first 6 weeks followed by normal gait for the following 2 weeks. Thereafter, a separate study was performed comparing tissue distribution around implanted TFS under normal walking as well as stair climbing following similar protocol of loading condition. Based on the above investigations, results have been generated to study the influence of textured and non-textured stems on tissue growth under routine activities.

8.3.1 Influence of TFS and NTFS on tissue growth at bone-implant interface

Figure 8.4 shows the percentage of connective tissue phenotypes formed over textured and non-textured femoral stems upon normal walking. As discussed in Chapter 4, section 4.4.1, the thin tissue layer between the bone and the implant was assumed to be filled with granulation tissue, which differentiates on progressive iterations. In the femoral stem without macro-textures (NTFS), the majority of the tissue phenotype formed was found to be fibrous tissue. The formation of fibrous tissue progressively increased from 80% to 92.90% from starting day up to 6^{th} week and thereafter remained almost constant (~94%). The formation of bone (7% to 3.6% from starting day to 8^{th} week) as well as cartilage (12% to 2% from starting day to 8^{th} week) were relatively less and on continuous declining trend. Interestingly, the differentiation of MSCs to different tissue phenotypes was much quicker and almost attained zero percent within a week's time in NTFS. Although the formation of fibrous tissue was also prominent in the case of femoral stem with macro-textures (TFS), the percentage of fibrous tissue is relatively lower (71% to 85.38% from starting day to 8^{th} week) compared to that in NTFS. However, the formation of fibrous tissue has remained constant (~85.38%) from 6^{th} to 8^{th} week equivalent to the situation observed in case of NTFS. Results from the study show continuous decline in formation of cartilaginous tissue (18.41% to 3.94% from starting day to

8th week) and relatively lesser bone growth which varies from 3.39% after 1st week to 5.16% after 5th week and thereafter declined to 3.20% at the end of 8th week. However, the differentiation of MSCs were relatively slow and varied from 9.86% after 1st week to 7.48% by the end of 8th week.

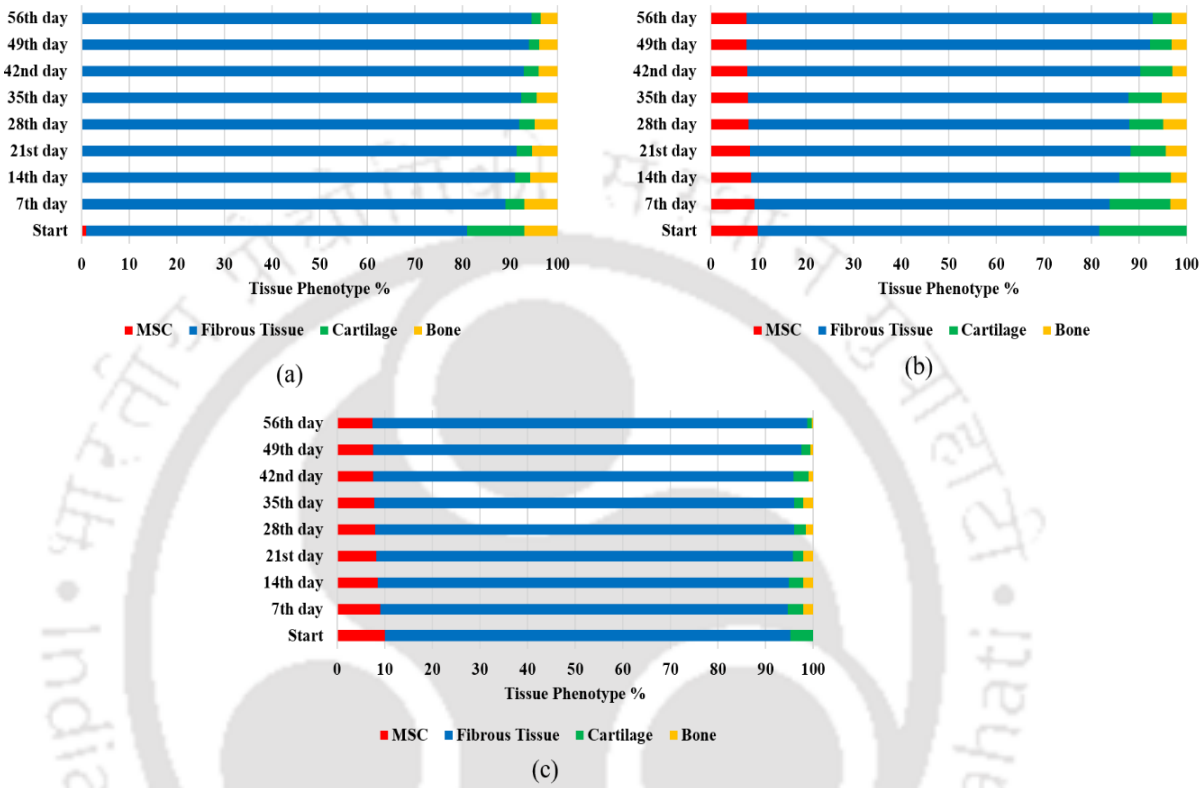

Figure 8.4 Influence of TFS and NTFS on tissue growth: (a) NTNW (b) TNW (c) TSC (NTNW: influence of NTFS upon normal walking; TNW: influence of TFS upon normal walking; TSC: influence of TFS upon stair climbing)

Figure 8.5 shows the spatial distribution of connective tissues at the interface tissue bed due to NTFS under normal walking. Gruen zones for the femoral stem are represented in Figure 8.6. Bone growth was observed primarily at latero-medial region over the GZ 1, GZ 7 and also proximal latero-medial regions of GZ 2 and GZ 6. However, major portion of anterior and posterior regions of the interface tissue was enveloped by fibrous tissue while, soft cartilaginous tissue was observed in scarce in the distal regions of the interface tissue on both anterior and posterior surfaces. The amount of cartilage in the posterior section of the interface tissue has declined after 6th week and the distribution of the same remained almost constant over the next 2 weeks.

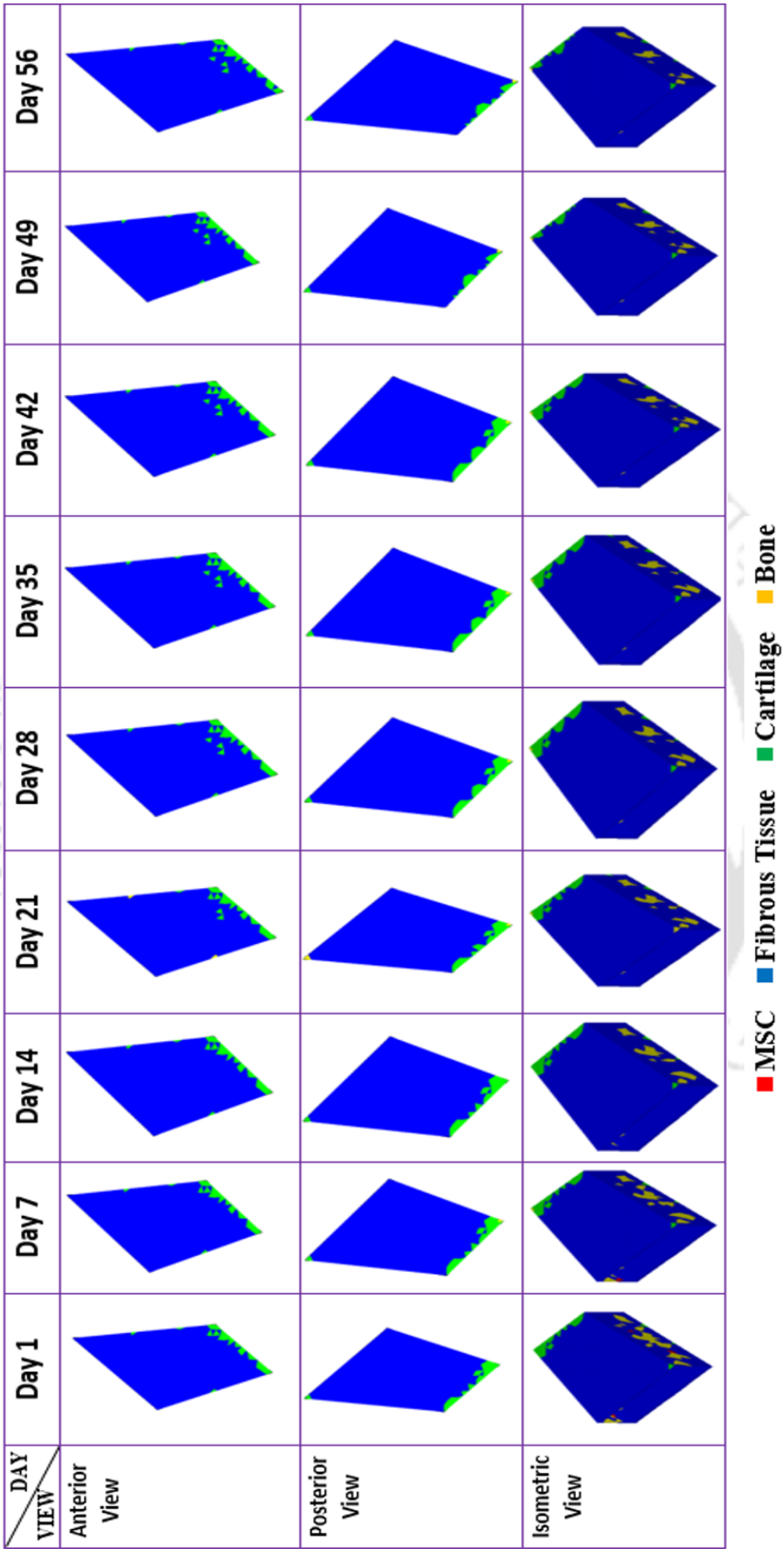

Figure 8.5 Spatial distribution of tissue growth for NTFS under normal walking (AV: Anterior View; PV: Posterior View)

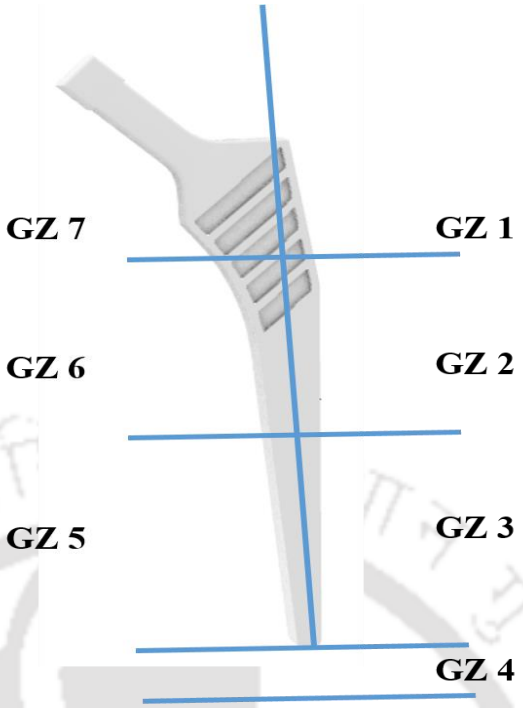

Figure 8.6 3D solid model of the femoral stem showing the Gruen Zones (GZ)

The spatial distribution of connective tissues at the interface tissue bed due to TFS under normal walking is shown in Figure 8.7. Bone growth was observed primarily at distal portion of the tissue in the regions of GZ 2 and GZ 6. However, major portion of distal anterior and posterior regions of the interface tissue was filled with cartilaginous tissue. Interestingly, the distribution of cartilage over the anterior portion has been discontinuous with bulk bands of fibrous envelope in between from 6^{th} week onwards. Small non-uniform patches of residual granulation tissue were observed in the latero-medial section of the tissue towards the bone end and the interface region attached to the implant.

Figure 8.5 and Figure 8.7 shows the presence of large amount of fibrous tissue at the proximal regions of interface layer. When categorized through gruen zones, fibrous tissue is more prominent at the GZ 1 and GZ 7. This large amount of fibrous tissue at GZ1 and GZ7 may be attributed to the high stresses and deviatoric strain at the points of attachment of the significant muscles such as abductor, tensor fascia latae, vastus lateralis as well as high hip contact force. This finding corroborates well with previous studies (Puthumanapully and Browne, 2011; Tan et al., 2017), anticipating weaker interface and inhibiting osteogenesis due to enhanced

stress regime around the prosthesis. In addition, a prior study by Giori et al. (1993) also reports that distortion of cells (deviatoric strain component) promotes formation of fibrous matrix. Moreover, fibrous encapsulation was also observed around the ridges of the macro-textures due to the excess increase of stress-concentration in those regions (Tan et al., 2017).

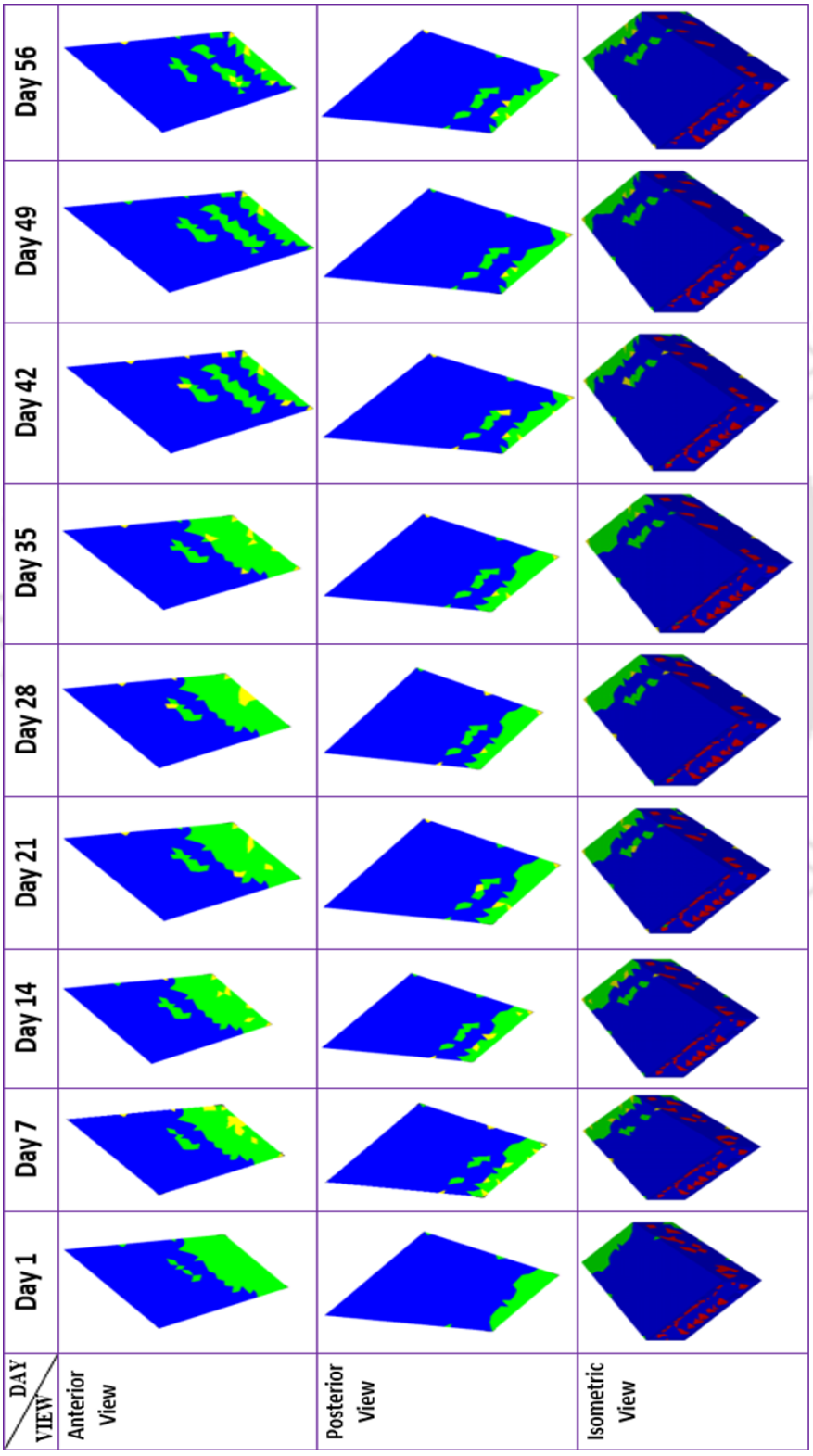

Figure 8.7 Spatial distribution of tissue growth for TPS under normal walking (AV: Anterior View; PV: Posterior View)

Presence of bone at latero-medial region over the GZ 1, GZ 7 (Fig. 8.5) and also proximal latero-medial regions of GZ 2 and GZ 6 is supported by an earlier study (Puthumanapully and Browne, 2011). However, it is interesting to note that, most of the MSCs in the case of NTFS differentiated to weaker fibrous tissues rapidly. On the contrary, macro-textures in TFS promoted differentiation of MSCs into rudimentary cartilage which may trigger endochondral ossification (Nowlan et al., 2007; Breeland et al., 2021) but at a slow pace. Such findings from the present study infer that, triggers that promote rapid differentiation of MSCs may not be beneficial for long term ossification. Moreover, regardless of the variability in morphology, macro-textures on the surfaces of femoral stems actually promote differentiation of MSCs into rudimentary cartilage and bone although at a slow pace as compared to NTFS.

Evidence of fibrous tissue at the proximal surfaces of the interface layer may promote pre-mature aseptic loosening near the region of greater trochanter. It is however true that, loosening of implant in this region of femur is highly attributed to stress-shielding and bone loss, it's impossible to rule out the possibility of a weak interface in these areas due to the growth of fibrous tissue at the interface (Puthumanapully and Browne, 2011).

The decrease in the amount of cartilage and bone over the iterative time-scale is due to continuous high load at the interface which promotes bone resorption and cartilage degeneration (Isaksson et al., 2006a) as also evidenced in earlier studies described in previous chapters. Such an observation clearly infers that even the recommended activity such as normal walking on a daily basis post-THA during early rehabilitation period induce high intermittent stress at the bone-implant interface and thus weaken the interface by bone resorption and cartilage degeneration. So an optimum level of recommended activity may be prescribed to the patient underwent THA (Bergmann et al., 1995) during early rehabilitation period.

Figure 8.8 shows the variation in average tissue stiffness for NTFS and TFS under different routine activities. Initially the stiffness of the tissue was same for both NTFS and TFS as in both the cases the interface region was filled with granulation tissue. Thereafter, post-operative increase in average tissue stiffness was

found to be much higher in TFS (ranging from ~8% to ~11%) as compared to NTFS (ranging from ~2.3% to ~7%). However, the trends in variation of average stiffness over the whole healing phase remains similar for both the types of implant with and without macro-textures. The average tissue stiffness for NTFS ranges from ~2.30% after 1st week to ~7% after 5th week and thereafter declined to ~3% by the end of 8th week. Similarly, the average tissue stiffness for TFS ranges from ~10.69% after 1st week to ~11.31% after 5th week and thereafter declined to ~7.95% by the end of 8th week.

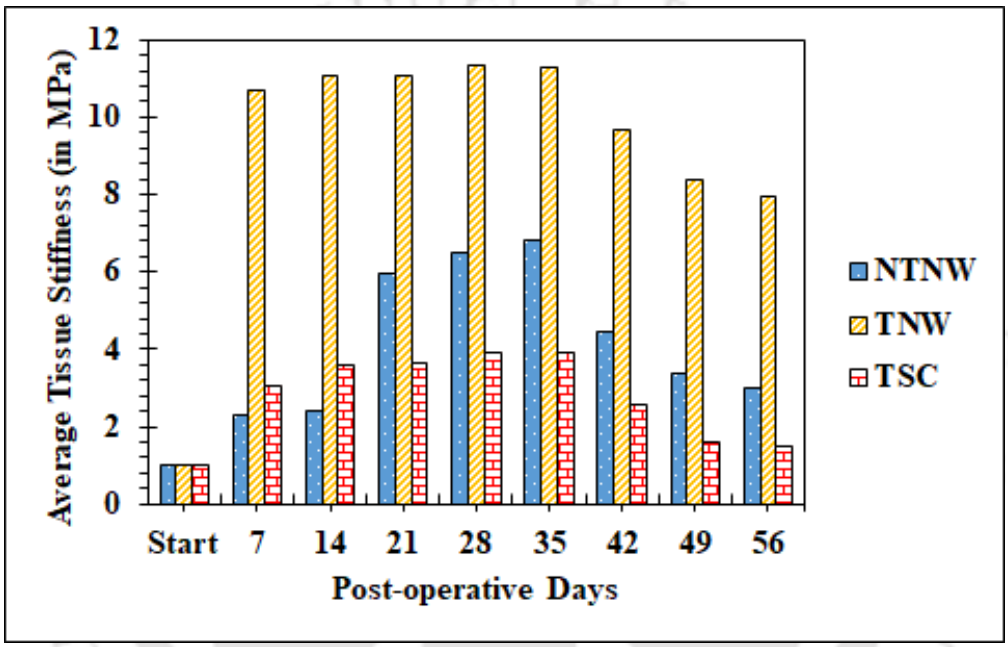

Figure 8.8 The temporal variation in average tissue stiffness at the bone-implant interface region (NTNW: Non-textured Implant normal walking case; TNW: Textured Implant normal walking case; TSC: Textured Implant Stair Climbing case)

The average tissue stiffness thus found to increase up to the end of 5th week and thereafter reduced to degenerative process. Due to the inconsistency in type of tissue formed at the interface layer, the average tissue stiffness over the whole domain was found to be much less. However, there might be presence of site-specific peaks and valleys in the magnitude of average tissue stiffness which was also evidenced by an earlier study (Puthumanapully and Browne, 2011; Mathai and Gupta, 2022).

8.3.2 Influence of routine activities on tissue growth

So far, qualitative assessment of growth of different connective tissues was performed comparing NTFS and TFS in the section 8.3.1, Chapter 8. This study was further extended to compare tissue growth in TFS under routine activities such as normal walking and stair climbing. Figure 8.4 shows the percentage of connective tissue phenotypes formed over textured femoral stems under normal walking and stair climbing. Comparative to normal walking, fibrous tissue formation was relatively higher (85% to 91% from starting day to 8th week) in case of loading under stair climbing. However, the formation of fibrous tissue has remained constant (~91%) from 6th to 8th week equivalent to the situation observed in case of NTFS and TNW. Due to high fibrous tissue, formation of cartilage (5% to 1% from starting day to 8th week) and bone (2% to 1% from starting day to 8th week) was much lower in case of TSC as compared to TNW.

The spatial distribution of connective tissues at the interface tissue bed due to TFS under stair climbing is shown in Figure 8.9. Similar to TNW, bone growth was observed in scare primarily at distal portion of the tissue in the regions of GZ 2 and GZ 6. However, unlike TNW, the distribution of cartilaginous tissue at the distal anterior and posterior regions of the interface tissue was limited. Interestingly, similar to NTFS, envelope of fibrous tissue was seen all over the major portion of anterior and posterior regions of the interface tissue. In addition, the amount of cartilage in the distal section of the interface tissue has declined after 6th week and the distribution remained almost similar up to 8th week.

Formation of fibrous tissue in case of stair climbing was higher as compared to that formed during normal walking. Although distribution of bone formed under both the activities was sporadic and often patchy (Puthumanapully and Browne, 2011), especially in case of normal walking case, the amount of bone formation during stair climbing was found to be highly reduced. This observation of high fibrous matrix and reduced bone growth during stair climbing may be attributed to very high torsional moments acting at the bone-implant interface (Bergmann et al., 1995). An *in vivo* study by Bergmann et al., (1995) reported torsional moment during stair climbing to be twice than that during normal walking. Stair climbing is susceptible to early aseptic loosening as compared to than during normal walking

due to formation of high fibrous tissue at the proximal surfaces of the interface layer in stair climbing. Thus in order to reduce the risk of aseptic loosening and failure of implant post-THA, patients should avoid stair climbing or any such activity involving high torsional loads during the early rehabilitation period. A different study on cemented prosthesis reported that isolated stair climbing is detrimental than isolated normal walking when comparing both the load cases (Stolk et al., 2002) which also provide sufficient confidence to the prescription presented in this study.

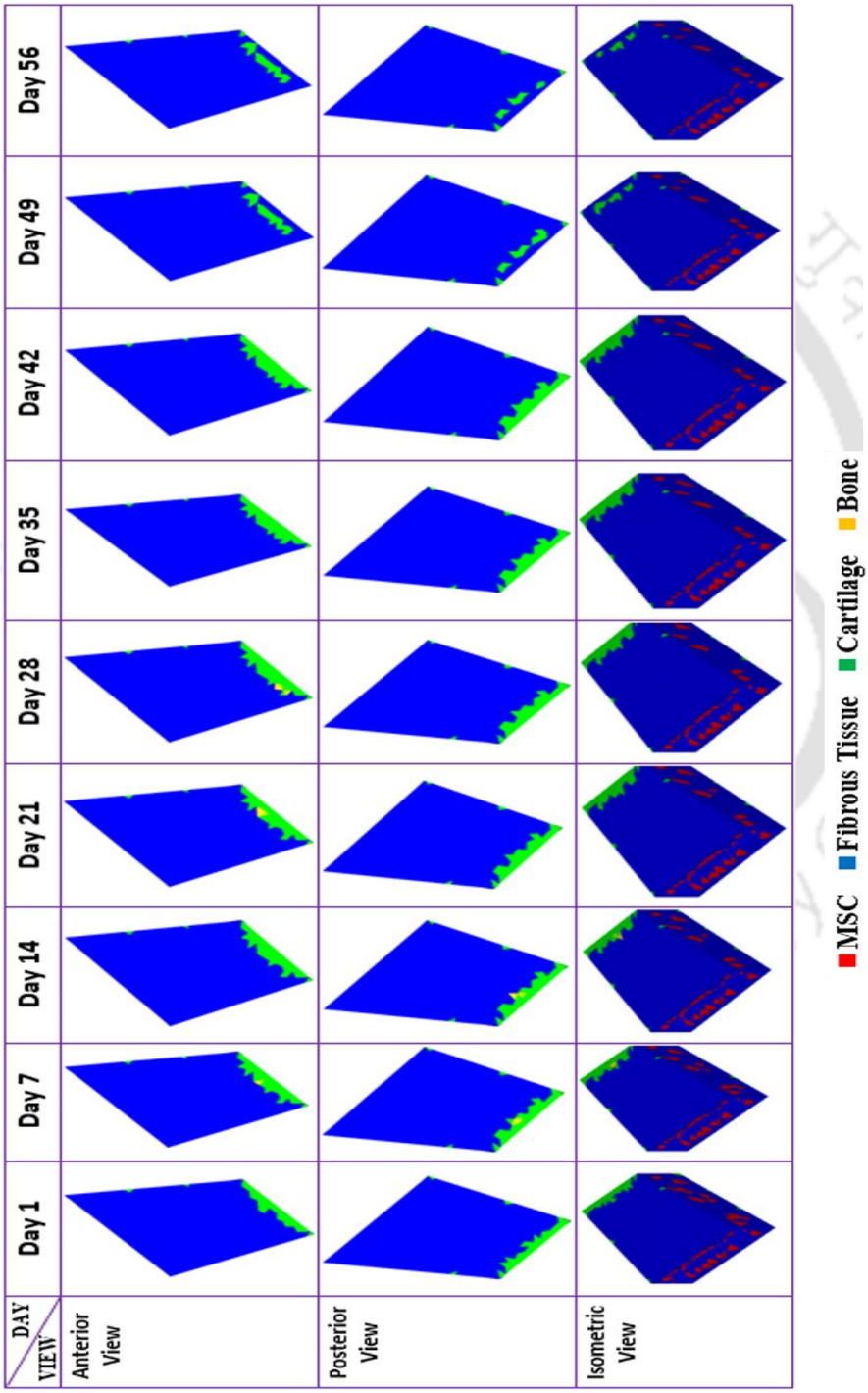

Figure 8.9 Spatial distribution of tissue growth for TFS under stair climbing (AV: Anterior View; PV: Posterior View)

Figure 8.8 shows the variation in average tissue stiffness for TFS under daily routine activities. Post-operative increase in average tissue stiffness was found to be much higher in TNW (ranging from ~8% to ~11%) as compared to TSC (ranging from ~1.5% to ~3.9%). However, the trends in variation of average stiffness over the whole healing phase remains similar under both the routine activities. Similar to NTNW and TNW, the average tissue stiffness for TSC ranges from ~3% after 1st week to ~3.9% after 5th week and thereafter declined to ~1.5% by the end of 8th week.

8.4 Clinical significance of the study

Regardless of the amount of bone formation, both contact osteogenesis (Mathai and Gupta, 2022; Mukherjee and Gupta, 2016) and distance osteogenesis (Kuzyk and Schemitsch, 2011; Burke and Kelly, 2012) was evidenced by the present study primarily in the NTFS (Fig. 8.5). This is however, contrary to the bone formation in case of TFS. Only distance osteogenesis (Fig. 8.7 and Fig 8.9) was observed in case of textured stems (TFS) which is also evidenced in the studies performed in earlier Chapters. Such an anomaly in type of osteogenesis may be attributed primarily to the design of implant surface topologies. However, an earlier study by Choi et al., 2017 reported that both these types of osteogenesis are not mutually exclusive in nature and may occur simultaneously. This finding corroborates with the finding in the present study for NTFS. Interestingly, few animal studies (Berglundh et al., 2003; Sennerby et al., 1993) on bone growth around endosseous prosthesis performed on canines (Berglundh et al., 2003) and cellular response on implantation in a tibia of a rabbit (Sennerby et al., 1993) reported appositional bone growth at the parent bone site and progresses towards the periphery of the prosthesis.

8.5 Validation of the present study

It is noteworthy that, the response of any biological tissue such as bone is site-specific as well as patient-specific which makes it difficult to compare any numerical projections with experimental outcomes (Carter et al. 1998; Mathai and Gupta 2022). However, the presence of bone in the distal end and mediolateral regions of the tissue for NTFS is well-supported by previous clinical (Santori et al., 2006a, 2006b) as well as numerical (Puthumanapully and Browne, 2011; Fernandes et al.

2002) investigations on femoral stems. Furthermore, the presence of cartilage at the distal end and fibrous envelope at the proximal surfaces is corroborated by an earlier study on short-stemmed metaphyseal loading implant (Puthumanapully and Browne, 2011) as well as by a study on bone remodelling on uncemented femoral stems (Fernandes et al. 2002). There is a dearth of early *in vivo* or clinical evidence to support the results predicted in the current investigation. However, the estimates from these clinical (Santori et al., 2006a, 2006b) and numerical investigations (Puthumanapully and Browne, 2011) performed erstwhile thus provide enough reliability to the results obtained from the current investigation.

As it is already discussed in section 5.7, Chapter 5 that there is no established relationship between the real healing period and iterative time-scale (Huiskes et al., 1987; Chennimalai Kumar et al., 2010; Avval et al., 2016) used for computation of such mechanoregulatory tissue-differentiation algorithms. However, based on clinical suggestions from an experienced orthopaedic surgeon, the time-period of healing in the present simulation was kept for 56 days or eight weeks' post-operative.

8.6 Limitations

There are still certain limitations to this present investigation. Due to poor understanding of granulation tissue, the assumption of a homogeneous isotropic media has been made, which may not be a true representation of the condition in vivo, where the presence of other inflammatory cells may influence the process of cell dispersal, proliferation, and differentiation. The present mechanoregulation based tissue differentiation scheme assumes a constant diffusion rate for MSCs despite the variations in diffusion rates that exists throughout the region of the bone-implant interface. Moreover, cell-phenotype specific mechanoregulatory algorithms might be useful to study the detailed cellular response and their subsequent implications of tissue differentiation (Isaksson et al., 2008a; Mukherjee and Gupta, 2017). However, studies reported that such explicit modelling of cell phenotype has limited influence on final outcome of distribution of different tissue phenotypes (Andreykiv et al., 2008b; Isaksson et al., 2008a; Mukherjee and Gupta, 2017). Furthermore, different mechanoregulatory algorithms will have different outcome with respect to quantitative evaluation of tissue growth (Gómez-Benito et al.,2005; Ambard and Swider, 2006; Puthumanapully and Browne, 2010). Nevertheless, the

qualitative trends of tissue growth remain similar. It is noteworthy to state that, the current study was limited to only one macro-textured surface topology without incorporating the influence of micro-roughness and different other macro-textures on tissue growth and regeneration process which might need a more robust multi-scale approach of prediction of tissue differentiation (Mathai and Gupta, 2022). Moreover, a combined bone growth and remodelling approach might be incorporated to get an overall outcome of the growth of connective tissues (Mukherjee and Gupta, 2017a). Only two loading conditions were taken in this study and other common routine activities such as standing and sitting on a chair, might be incorporated along with adaptive and dynamic loading conditions such as alternating normal walking and stair climbing in a future study. In addition, patient variability such as gender, morphology and quality of host bone, material property of the bone etc. was not accounted in this present study. Regardless of the following limitations, the present study might be useful to appreciate the influence of macro-textured implant surfaces on tissue growth around an uncemented prosthesis.

8.7 Summary

The present study implemented mechanoregulation based tissue differentiation algorithm to assess spatial distribution of different connective tissues associated with bone formation around femoral stems with and without proximal macro-textures. Some of the important conclusions drawn from the study are:

- The textured surfaces promote more cartilage as compared to non-textured stems and thus might promote endochondral ossification.
- Bone growth was prominent on GZ 2 and GZ 6 as obtained in an earlier study on short-stemmed metaphyseal loading implant.
- Formation of fibrous tissue was higher towards GZ 1 and GZ 7 in all the considered situations in the study and thus promotes aseptic loosening.
- In addition, a prescription has been documented regarding post-operative loading conditions.
- Although both normal walking and stair climbing are part of recommended activities post-THA, stair climbing might not be recommended as a part of recovery protocol as it may slow down the healing process and promote aseptic loosening by forming a fibrous envelope at the proximal implant surfaces.

CHAPTER 9

Conclusions and Scope for Future Work

This chapter introduces the key accomplishments of this dissertation along with some scope of future research studies which concludes the thesis.

9.1 Conclusions

The work in this thesis primarily developed a finite element (FE) based framework to pre-clinically assess the mechanoregulatory influences of macro-textures on ossification and bone on-growth patterns at the bone-implant interface region and over the implant surface. A comparative study on influence of three different clinically admissible macro-textured surfaces on the growth and distribution of bone and other connective tissues was investigated considering fixed radial and varying tangential micromotions. In addition, influence of sequential opening and closing of bone-implant interface gaps simulated by variable radial micromotions at the interface was also studied. Influence of texture density on growth of tissue phenotype was later investigated. A full-factorial study based on variation in significant design parameters of the macro-textures were performed and bone growth was assessed qualitatively. Based upon the results of the full-factorial based study, neural networks (NNs) were structured as predictive models of bone growth while providing implant texture dimensions as inputs. Thereafter, design optimization of such macro-textures was performed by adopting a suitable design optimization scheme supported by state-of-the-art genetic algorithms (GAs) to suggest some improved designs. Finally, one such texture was modified and modelled on a femoral stem and a comparative study between a textured and non-textured implant was performed based on a full-scale femur-implant system under two recommended routine activities post-THA.

Based on the results from the thesis some important conclusions have been drawn. While some of these conclusions have a broader significance in THA in general, some have significant clinical importance. Therefore, the conclusions from this thesis are classified as general conclusions and specific conclusions and presented accordingly.

9.1.1 General Conclusions

- It is possible to implement the currently used mechanoregulatory tissue differentiation algorithm for estimation of bone growth over macro-textured implant morphologies.
- Present study reinforced the idea generated in this dissertation that, it is not only micro and nano surface roughness but also macro roughness on the implant surface

that might promote endochondral ossification as well as influence the formation and distribution of different tissue phenotypes at the bone-implant interface gap. However, the idea presented in this thesis no way denies the influence of micro level surface roughness on bone formation but rather infer that a proper combination of micro and macro-texture on an implant surface will accelerate and enhance the amount of bone growth, which is in general believed to be only due to micro-textures.

- Textures containing filleted and chamfered edges reduces the formation of fibrous tissue thus promoting formation of soft cartilage and bone.
- Increase in texture density with sharp edges increases the probability of fibrous encapsulation.
- ML techniques such as NN can be efficiently used to formulate non-linear predictive mathematical models in qualitative prediction of bone growth with implant design parameters as inputs.
- Soft computing strategies such as combining FEA-NN-GA might be useful to establish an unsupervised learning platform for real-time cloud prediction of bone growth. Such online platforms will inherently help clinicians to choose an appropriate implant design on patient-by-patient basis.
- Non-textured implants produce more fibrous tissue compared to textured implant under similar routine activity which might trigger aseptic loosening of implant.
- Fibrous tissue formation is more under stair climbing activity compared to that under normal walking. This suggests that stair climbing immediately after a hip replacement surgery, although falls under recommended activity, appears to be detrimental to the patient compared to normal walking.
- Even low-level activity on a daily-basis might induce high level of stress at the bone-implant interface favouring fibrous matrix and thus accelerating the loosening of implants during the early rehabilitation period after a successful THA.
- A trade-off between the type of activity and activity time might be recommended by the orthopaedic registrars for proper anchorage of bone with the implant.

9.1.2 Specific Conclusions

- Higher levels of micromotion lead to a higher rate of fibrogenesis and chondrogenesis followed by a lower rate of osteogenesis resulting in weak bone-implant interface strength.
- It could be inferred that changes in the bone-implant contact area with large surfaces through grooves or macro-textures alter the mechanical environment required to trigger endochondral ossification and adherence of optimum bone growth to the implant surface.
- This study observed the presence of distance osteogenesis from the bone site towards the implant site, unlike prior studies on micro-roughened surface.
- Although an increasing trend of ossification is observed at lower normal micromotions, higher values of normal micromotion will reduce the opening and closing gap. This enhances the formation of fibrous tissue near the implant surface, thus destabilizing the interface leading to aseptic loosening of the implants.
- Soft cartilaginous tissue was observed to have form in abundance at lesser gap distance which might promote endochondral ossification at long term.
- Although a dependence of the formed tissue on the surface texture density is observed, a linear relationship between the surface texture density and tissue growth was not observed in the present investigation.
- Both the directional components of micromotion need to be equally reduced to enhance the possibility of higher bone growth.
- A gradual reduction in bone growth was observed with the increase in inter-groove spacing of the chosen implant section model.
- A reduction in the levels of osteogenesis was also observed with the increase in groove spacing or groove radius.
- Bone growth as predicted by NN was found to have a good agreement with those obtained from FE based mechanoregulatory analysis reinforcing the efficacy of the developed model.
- The optimized macro-textured surfaces obtained based on the GA search were found to offer enhanced biologic fixation and thereby better ossification, compared to that offered by discernible textures in three distinct initial models.
- Reduction in the dimension of ribs/grooves triggers faster ossification and optimal bone growth.

- Periodic patterns of ribs with higher and lower rib dimensions predicted uniform stress regime at the interfacial region, thereby resulting in enhanced ossification.
- The textured femoral stem promotes more cartilage compared to non-textured stem and thus might promote endochondral ossification.
- As reported in earlier study on short-stemmed metaphyseal loading implant, bone growth was prominent on GZ 2 and GZ 6.
- Formation of fibrous tissue was higher towards GZ 1 and GZ 7 in all the considered situations in the study which favours aseptic loosening.

9.2 Future scope

Given the growing clinical interest in uncemented intramedullary fixation implants, the scope of research in this area is broad and profound and hence, the present work could be further extended in following directions:

- Bone being a highly complex living tissue with site-specific anisotropy, a more accurate description of material model for bone might provide a better outcome of the presently available results. In this regard, further studies based on highly advanced micro-CT scan or micro-MRI images of bone from different body skeletal sections of a living subject might be attempted.
- Granulation tissue, in reality is a thin layer of inflamed tissue with remarkable number of inflammatory cells and with sufficient vascularity, which might influence the results predicted in the present study. Future studies may introduce novel material models to incorporate non-homogeneous nature of the granulation tissue.
- The present investigation also did not consider the bone adaptation, influences of micro and nano-level textures, biomaterials, growth factors such as bone morphogenetic proteins (BMPs) and wear of uncemented implants on peri-prosthetic bone growth. However, the numerical framework used in this study, could be extended to incorporate the influences of those factors to obtain a holistic picture of the assessment of bone growth around such uncemented implants.
- Studies on formulating biochemical material models of implant coating used might be attempted in future to establish a suitable relationship between material biocompatibility as well as osteoconduction.
- The NN schemes developed in the present study attempt to relate the levels of bone growth with the significant dimensions of chosen implant macro-textures under a constant relative displacement between implant and bone. Future studies may be

attempted to make an online NN platform which may be used to train input data from different such macro-textures to pre-clinically predict the type of macro-textured surface suitable on patient-by-patient basis.

- Each of the studies performed in the present thesis are based on comparative analysis of more than one design with some specific chosen design and loading parameters. Future studies may be attempted by considering inter-patient variability, surgical variability as well as the impact of differing modelling assumptions.
- It may be noted that, the full-scale study is based on static analysis considering peak load at the hip joint under normal walking and stair climbing. Moreover, the peak joint force as well as the associated muscle forces are calculated based on studies performed in different subjects. Hence, a patient-specific dynamic study of the present model considering the complete gait cycle may be more useful in gaining more insight into physiological load transfer and its impact on the bone-implant interface environment.
- It should be further emphasized that because the CT-scan dataset was based on a living patient, one-to-one validation of the numerical results was not possible. To compare the numerical results with *in vitro* observations, additional investigations including fabrication of the implants with state-of-the-art 3D printing technique followed by bone growth assays may be used. Animal trials could also help to confirm the bone growth projections. Nonetheless, clinical trials are most likely the best technique to assess the efficacy of new implant designs and, as a result, validate the numerical findings of this study.

Appendix A: Pseudo-Code for finite element structural analysis

Code for FE structural Analysis:

Ansys Parametric Design Language (APDL) pseudo-code for FE structural analysis

(A) **For first iteration:**

(A.1) **PRE-PROCESSING**

- Import/Create solid/FE model
- Formulate material models for Bone, Granulation tissue and Implant section

(A.2) **SOLUTION**

- Initiate Static Structural FE analysis
- Apply loading and boundary condition
- Solve Static FE analysis

(A.3) **POST-PROCESSING**

- Create Element tables to calculate hydrostatic pressure and deviatoric strain
- Formulate Equation for hydrostatic pressure as:

$$\sigma_{average} = \frac{\sigma_1 + \sigma_2 + \sigma_3}{3}$$ where $(\sigma_1, \sigma_2, \sigma_3)$ are 3 principal stresses

- Formulate Equation for deviatoric strain as:

$$\varepsilon_{deviatoric} = \frac{1}{1+\nu}\sqrt{\frac{(\varepsilon_1 - \varepsilon_2)^2 + (\varepsilon_2 - \varepsilon_3)^2 + (\varepsilon_3 - \varepsilon_1)^2}{2}}$$

where $(\varepsilon_1, \varepsilon_2, \varepsilon_3)$ are 3 principal strains and ν is the effective Poisson's ratio.

- Create Array to store element wise stress and strain data

- Store data to a text file for exporting it to MATLAB to run tissue differentiation algorithm.

(B) **For other iterations:**

(B.1) **PRE-PROCESSING**

- Import/Create solid/FE model
- Import element wise updated material property file from MATLAB
- Create Array in ANSYS to store updated material property data
- Formulate material models for Bone, Implant section and update new material property for Granulation tissue

(B.2) **SOLUTION**

- Initiate Static Structural FE analysis
- Apply loading and boundary condition
- Solve Static FE analysis

(B.3) **POST-PROCESSING**

- Create Element tables to calculate hydrostatic pressure and deviatoric strain
- Formulate Equation for hydrostatic pressure as:

$$\sigma_{average} = \frac{\sigma_1 + \sigma_2 + \sigma_3}{3}$$ where $(\sigma_1, \sigma_2, \sigma_3)$ are 3 principal stresses

- Formulate Equation for deviatoric strain as:

$$\varepsilon_{deviatoric} = \frac{1}{1+\nu}\sqrt{\frac{(\varepsilon_1 - \varepsilon_2)^2 + (\varepsilon_2 - \varepsilon_3)^2 + (\varepsilon_3 - \varepsilon_1)^2}{2}}$$

where $(\varepsilon_1, \varepsilon_2, \varepsilon_3)$ are 3 principal strains and ν is the effective Poisson's ratio.

- Create Array to store element wise stress and strain data
- Store data to a text file for exporting it to MATLAB to run tissue differentiation algorithm.

Appendix B: Pseudo-Code for mechanoregulation based tissue differentiation algorithm

MATLAB pseudo-code for mechanoregulation based tissue differentiation algorithm

B.1 Mechanoregulatory tissue differentiation code

for iteration = 1 to number of finite elements in the bone-implant gap size

if {Hydrostatic Pressure = 0 and Deviatoric Strain = 0}

Young's Modulus =1;

Poisson's Ratio =0.167;

elseif {Hydrostatic Pressure > 0.15 and Deviatoric Strain > 0}

Young's Modulus = 2;

Poisson's Ratio =0.167;

elseif {Hydrostatic Pressure > 0.15 and Deviatoric Strain < 0}

Young's Modulus = 2;

Poisson's Ratio =0.167;

elseif {Hydrostatic Pressure > -0.15 and Deviatoric Strain > 0.05}

Young's Modulus = 2;

Poisson's Ratio =0.167;

elseif {Hydrostatic Pressure > -0.15 and Deviatoric Strain < -0.05}

Young's Modulus = 2;

Poisson's Ratio =0.167;

elseif {Hydrostatic Pressure < -0.15}

if {Deviatoric Strain < -0.15 or Deviatoric Strain > 0.15}

Young's Modulus = 10;

Poisson's Ratio =0.167;

else

Young's Modulus = 1000;

Poisson's Ratio =0.3;

end

elseif {Hydrostatic Pressure >= -0.15 and Hydrostatic Pressure <= 0.15 and Deviatoric Strain >= -0.05 and Deviatoric Strain <= 0.05}

Young's Modulus = 6000;

Poisson's Ratio =0.3;

else

warning ('Current values of hydrostatic pressure and deviatoric strain not covered by simulation')

end

end

B.2 Code for Temporal smoothing and Rule of Mixture for Young's Modulus

(A) **For first iteration:**

Initialize an array A (number of finite elements x 10) with Young's Modulus of granulation tissue

for iter = 1 to number of finite elements in the bone-implant gap size

for X= 2 to 10

A (iter, X-1) = A(iter, X);

end

A(iter,10) = Young's Modulus (iter,1);

Smoothed Young's Modulus = Summation (A,2)/10;

end

for iter = 1 to number of finite elements in the bone-implant gap size

Updated Young's Modulus = ((1 – element specific cell-concentration) * Young's Modulus of granulation tissue) + (element specific cell-concentration * Smoothed Young's Modulus);

end

(B) **For other iterations:**

for iter = 1 to number of finite elements in the bone-implant gap size

for X= 2 to 9

A (iter, X-1) = A (iter, X);

end

A(iter,9) = Updated Young's Modulus (iter,1);

A(iter,10) = Young's Modulus (iter,1);

Smoothed Young's Modulus = Summation (A,2)/10;

end

for iter = 1 to number of finite elements in the bone-implant gap size

Updated Young's Modulus = ((1 – element specific cell-concentration) * Young's Modulus of granulation tissue) + (element specific cell-concentration * Smoothed Young's Modulus);

end

B.3 Code for Temporal smoothing and Rule of Mixture for Poisson's Ratio

(A) **For first iteration:**

Initialize an array B (number of finite elements x 10) with Zeros

for iter = 1 to number of finite elements in the bone-implant gap size

for Y= 1 to 10

B (iter, Y) = Poisson's Ratio of granulation tissue;

end

end

for iter = 1 to number of finite elements in the bone-implant gap size

for Y= 2 to 10

B (iter, Y-1) = B(iter, Y);

end

B(iter,10) = Poisson's Ratio(iter,1);

Smoothed Poisson's Ratio = Summation (B,2)/10;

end

for iter = 1 to number of finite elements in the bone-implant gap size

Updated Poisson's Ratio = ((1 – element specific cell-concentration) * Poisson's Ratio of granulation tissue) + (element specific cell-concentration * Smoothed Poisson's Ratio);

end

(B) **For other iterations:**

for iter = 1 to number of finite elements in the bone-implant gap size

for Y= 2 to 9

B (iter, Y-1) = B (iter, Y);

end

B(iter,9) = Updated Poisson's Ratio (iter,1);

B(iter,10) = Poisson's Ratio (iter,1);

Smoothed Poisson's Ratio = Summation (B,2)/10;

end

for iter = 1 to number of finite elements in the bone-implant gap size

Updated Poisson's Ratio = ((1 – element specific cell-concentration) * Poisson's Ratio of granulation tissue) + (element specific cell-concentration * Smoothed Poisson's Ratio);

end

Appendix C: Pseudo-Code for forward and backward calculation for neural network

MATLAB pseudo-codes for forward and backward calculation for BPNN

C.1 Forward step code

(A) **MAIN PROGRAM-General Input:** Normalized Input, Normalized Output

(B) **MAIN PROGRAM-Input for Forward calculation:**

- number of epochs,
- learning rate,
- momentum constant,
- number of input layer neurons,
- number of hidden layer neurons,
- number of output neuron,
- initialize bias for hidden and output layer,
- initialize weights connecting input to hidden neurons,
- initialize weights connecting hidden to output neuron

(C) **MAIN FUNCTION-Choice of activation functions for hidden and output layer:**

- **Function:** logistic-sigmoid function
  - **Input:** inputs from hidden layer when hidden layer activation function is calculated else input from output layer when output layer activation function is calculated
  - **Output:** logistic-sigmoid function value for either hidden layer or output layer

(D) **MAIN PROGRAM-For loop:**

For every epoch,

- Input layer output = input + bias;
- Hidden layer input = input * weights connecting input to hidden layer +bias;
- Hidden layer output = Call function (logistic-sigmoid function with input hidden layer input);
- Output layer input = Hidden layer output * weights connecting hidden to output layer +bias;
- Output layer output = Call function (logistic-sigmoid function with input as hidden layer input);

End for

C.2 Backward step code

(A) **MAIN FUNCTION-Gradients of activation functions for hidden and output layer:**

- **Function:** gradient_logistic-sigmoid function
  - **Input:** Hidden layer output and Output layer output
  - **Output:** gradient of logistic-sigmoid function for either hidden layer or output layer

(B) **MAIN PROGRAM**- Initialize change in weights for hidden and output layers

(C) **Calculation of Mean Squared Error:**

For every epoch,

- Error Signal= Normalized Output - Output layer output;
- Mean Squared error = [Sum over k=1 to k=ξ{(Error)^2}]/(2*ξ), where ξ= number of training cases;

(D) **Update of weights in each layer:**

If Mean Squared error > ε where ε = error limit

- Gradient of output layer = Call function (gradient_logistic_sigmoid function with input as output layer output);
- Gradient of hidden layer = Call function (gradient_logistic_sigmoid function with input as hidden layer output);
- Adjustment in weights connecting hidden and output layer at epoch = - {Gradient of output layer * Error * Hidden layer output * learning rate} + {Adjustment in weights connecting hidden and output layer at epoch^{--} * momentum constant};
- Adjustment in weights connecting input and hidden layer at epoch = - {Gradient of output layer * Error * weights connecting hidden and output layer * Gradient of Hidden layer * input * learning rate} + {Adjustment in weights connecting input and hidden layer at epoch^{--} * momentum constant};
- New weights connecting hidden and output layer for epoch^{++} = [weights connecting hidden and output layer at epoch + Adjustment in weights connecting hidden and output layer at epoch];
- New weights connecting input and hidden layer for epoch^{++} = [weights connecting input and hidden layer at epoch + Adjustment in weights connecting input and hidden layer at epoch];

End If

End for

References

Abu-Amer Y, Darwech I, Clohisy JC. Aseptic loosening of total joint replacements: mechanisms underlying osteolysis and potential therapies. *Arthritis Research & Therapy*.2007;9 Suppl 1(Suppl 1):S6. doi: 10.1186/ar2170.

Albrektsson T, Johansson C. Osteoinduction, osteoconduction and osseointegration. *European Spine Journal*. 2001 Oct;10 Suppl 2(Suppl 2): S96-101. doi: 10.1007/s005860100282.

Allen Q, Raeymaekers B. Surface Texturing of Prosthetic Hip Implant Bearing Surfaces: A Review. *Journal of Tribology*. 2021 Apr 1;143(4):040801. doi: 10.1115/1.4048409.

Altman GH, Horan RL, Martin I, Farhadi J, Stark PR, Volloch V, Richmond JC, Vunjak-Novakovic G, Kaplan DL. Cell differentiation by mechanical stress. *FASEB Journal*. 2002 Feb;16(2):270-2. doi: 10.1096/fj.01-0656fje.

Ambard D, Swider P.A predictive mechano-biological model of the bone-implant healing. *European Journal of Mechanics- A/Solids*. 2006 Nov 1;25(6):927-37. doi: 10.1016/j.euromechsol.2006.02.006.

Amstutz HC, Campbell P, Kossovsky N, Clarke IC. Mechanism and clinical significance of wear debris-induced osteolysis. *Clinical Orthopaedics and Related Research*. 1992 Mar;(276):7-18.

Andreaus U, Colloca M, Iacoviello D, Pignataro M. Optimal-tuning PID control of adaptive materials for structural efficiency. *Structural and Multidisciplinary Optimization*. 2011; 43(1):43-59. doi: 10.1007/s00158-010-0531-9

Andreaus U, Colloca M, Iacoviello D. An optimal control procedure for bone adaptation under mechanical stimulus. *Control Engineering Practice*. 2012;20(6):575-583. doi: 10.1016/j.conengprac.2012.02.002

Andreaus U, Colloca M, Iacoviello D. Modeling of Trabecular Architecture as Result of an Optimal Control Procedure. In: Andreaus U, Iacoviello D. (eds) Biomedical Imaging and Computational Modeling in Biomechanics. Lecture Notes in Computational Vision and Biomechanics 2013; 4, *Springer International Publishing*. doi: 10.1007/978-94-007-4270-3_2

Andreaus U, Colloca M, Iacoviello D. Optimal bone density distributions: numerical analysis of the osteocyte spatial influence in bone remodeling. *Computer*

Methods and Programs in Biomedicine.2014;113(1):80-91. doi: 10.1016/j.cmpb.2013.09.002

Andreaus U, Colloca M. Prediction of micromotion initiation of an implanted femur under physiological loads and constraints using the finite element method. *Proceedings of the Institution of Mechanical Engineers, Part H: Journal of Engineering in Medicine*. 2009 Jul;223(5):589-605. doi: 10.1243/09544119JEIM559

Andreaus U, Giorgio I, Lekszycki T. A 2-D continuum model of a mixture of bone tissue and bio-resorbable material for simulating mass density redistribution under load slowly variable in time. *Journal of Applied Mechanics and Medicine*. 2014; 94:978-1000. doi: 10.1002/zamm.201200182

Andreaus U, Giorgio I, Madeo A. Modeling of the interaction between bone tissue and resorbable biomaterial as linear elastic materials with voids. *Journal of Applied Mechanics and Physics*. 2015; 66:209-237. doi: 10.1007/s00033-014-0403-z

Andreykiv A, van Keulen F, Prendergast PJ. Computational mechanobiology to study the effect of surface geometry on peri-implant tissue differentiation. *Journal of Biomechanical Engineering*. 2008a Oct;130(5):051015. doi: 10.1115/1.2970057.

Andreykiv A, van Keulen F, Prendergast PJ. Simulation of fracture healing incorporating mechanoregulation of tissue differentiation and dispersal/proliferation of cells. *Biomechanics and Modeling in Mechanobiology*. 2008b Dec;7(6):443-61. doi: 10.1007/s10237-007-0108-8.

Angele P, Yoo JU, Smith C, Mansour J, Jepsen KJ, Nerlich M, Johnstone B. Cyclic hydrostatic pressure enhances the chondrogenic phenotype of human mesenchymal progenitor cells differentiated in vitro. *Journal of Orthopaedic Research*.2003 May;21(3):451-7. doi: 10.1016/S0736-0266(02)00230-9.

Ansari JS, Takahashi T, Pandit H. Uncemented hips: current status. Journal of Orthopaedic Trauma.2018 Feb 32(1):20-26. doi: 10.1016/j.mporth.2017.11.005.

Ashman RB, Cowin SC, Van Buskirk WC, Rice JC. A continuous wave technique for the measurement of the elastic properties of cortical bone. *Journal of Biomechanics*. 1984;17(5):349-61. doi: 10.1016/0021-9290(84)90029-0.

Avval PT, Samiezadeh S, Bougherara H. Long-term response of femoral density to hip implant and bone fracture plate: Computational study using a mechano-biochemical model. *Medical Engineering & Physics*.2016 Feb;38(2):171-80. doi: 10.1016/j.medengphy.2015.11.013.

Bagge M. A model of bone adaptation as an optimization process. *Journal of Biomechanics*. 2000 Nov;33(11):1349-57. doi: 10.1016/s0021-9290(00)00124-x.

Barry FP. Biology and clinical applications of mesenchymal stem cells. *Birth Defects Research C Embryo Today*. 2003 Aug;69(3):250-6. doi: 10.1002/bdrc.10021.

Beaupré GS, Orr TE, Carter DR. An approach for time-dependent bone modeling and remodeling-application: a preliminary remodeling simulation. *Journal of Orthopaedic Research*.1990 Sep;8(5):662-70. doi: 10.1002/jor.1100080507.

Behrens BA, Nolte I, Wefstaedt P, Stukenborg-Colsman C, Bouguecha A. Numerical investigations on the strain-adaptive bone remodelling in the periprosthetic femur: influence of the boundary conditions. *BioMedical Engineering OnLine*. 2009 Apr 16;8:7. doi: 10.1186/1475-925X-8-7.

Belmont PJ Jr, Powers CC, Beykirch SE, Hopper RH Jr, Engh CA Jr, Engh CA. Results of the anatomic medullary locking total hip arthroplasty at a minimum of twenty years. A concise follow-up of previous reports. *The Journal of Bone & Joint Surgery*. 2008 Jul;90(7):1524-30. doi: 10.2106/JBJS.G.01142.

Berahmani S, Hendriks M, de Jong JJA, van den Bergh JPW, Maal T, Janssen D, Verdonschot N. Evaluation of interference fit and bone damage of an uncemented femoral knee implant. *Clinical Biomechanics*.(Bristol, Avon). 2018 Jan;51:1-9. doi: 10.1016/j.clinbiomech.2017.10.022.

Berglundh T, Abrahamsson I, Lang NP, Lindhe J. De novo alveolar bone formation adjacent to endosseous implants. *Clinical Oral Implants Research*. 2003 Jun;14(3):251-62. doi: 10.1034/j.1600-0501.2003.00972.x.

Bergmann G, Bender A, Dymke J, Duda G, Damm P. Standardized Loads Acting in Hip Implants. *PLoS One*. 2016 May 19;11(5):e0155612. doi: 10.1371/journal.pone.0155612.

Bergmann G, Deuretzbacher G, Heller M, Graichen F, Rohlmann A, Strauss J, Duda GN. Hip contact forces and gait patterns from routine activities. *Journal of*

Biomechanics. 2001 Jul;34(7):859-71. doi: 10.1016/s0021-9290(01)00040-9.

Bergmann G, Graichen F, Rohlmann A. Hip joint loading during walking and running, measured in two patients. *Journal of Biomechanics*. 1993 Aug;26(8):969-90. doi: 10.1016/0021-9290(93)90058-m.

Bergmann G, Graichen F, Rohlmann A. Is staircase walking a risk for the fixation of hip implants? *Journal of Biomechanics*. 1995 May;28(5):535-53. doi: 10.1016/0021-9290(94)00105-d.

Bhattacharyya T, Chang D, Meigs JB, Estok DM 2nd, Malchau H. Mortality after periprosthetic fracture of the femur. *The Journal of Bone & Joint Surgery*. 2007 Dec;89(12):2658-62. doi: 10.2106/JBJS.F.01538.

Bonfoh N, Novinyo E, Lipinski P. Modeling of bone adaptative behavior based on cells activities. *Biomechanics and Modeling in Mechanobiology*. 2011 Oct;10(5):789-98. doi: 10.1007/s10237-010-0274-y.

Bougherara H, Bureau M, Campbell M, Vadean A, Yahia L. Design of a biomimetic polymer-composite hip prosthesis. *Journal of Biomedical Materials Research Part A*. 2007 Jul;82(1):27-40. doi: 10.1002/jbm.a.31146.

Bouguecha A, Weigel N, Behrens BA, Stukenborg-Colsman C, Waizy H. Numerical simulation of strain-adaptive bone remodelling in the ankle joint. *BioMedical Engineering OnLine*. 2011 Jul 5; 10:58. doi: 10.1186/1475-925X-10-58.

Breeland G, Sinkler MA, Menezes RG (2021) Embryology, Bone Ossification. In: StatPearls [Internet]. Treasure Island (FL): *StatPearls Publishing*.

Brown SR, Davies WA, DeHeer DH, Swanson AB. Long-term survival of McKee-Farrar total hip prostheses. *Clinical Orthopaedics and Related Research*. 2002 Sep;(402):157-63. doi: 10.1097/00003086-200209000-00013.

Burke DP, Kelly DJ. Substrate stiffness and oxygen as regulators of stem cell differentiation during skeletal tissue regeneration: a mechanobiological model. *PLoS One*. 2012;7(7): e40737. doi: 10.1371/journal.pone.0040737.

Calvo-Echenique A, Bashkuev M, Reitmaier S, Pérez-Del Palomar A, Schmidt H. Numerical simulations of bone remodelling and formation following nucleotomy. *Journal of Biomechanics*. 2019 May 9;88:138-147. doi: 10.1016/j.jbiomech.2019.03.034.

Carter DR, Beaupré GS, Giori NJ, Helms JA. Mechanobiology of skeletal regeneration. *Clinical Orthopaedics and Related Research*. 1998 Oct;(355 Suppl):S41-55. doi: 10.1097/00003086-199810001-00006.

Carter DR, Blenman PR, Beaupré GS. Correlations between mechanical stress history and tissue differentiation in initial fracture healing. *Journal of Orthopaedic Research*.1988;6(5):736-48. doi: 10.1002/jor.1100060517.

Carter DR, Caler WE, Spengler DM, Frankel VH. Uniaxial fatigue of human cortical bone. The influence of tissue physical characteristics. *Journal of Biomechanics*. 1981;14(7):461-70. doi: 10.1016/0021-9290(81)90096-8.

Carter DR, Orr TE, Fyhrie DP. Relationships between loading history and femoral cancellous bone architecture. *Journal of Biomechanics*. 1989;22(3):231-44. doi: 10.1016/0021-9290(89)90091-2.

Carter DR, Wong M. The role of mechanical loading histories in the development of diarthrodial joints. *Journal of Orthopaedic Research*.1988;6(6):804-16. doi: 10.1002/jor.1100060604.

Carter DR. Anisotropic analysis of strain rosette information from cortical bone. *Journal of Biomechanics*. 1978;11(4):199-202. doi: 10.1016/0021-9290(78)90013-1.

Carter DR. Mechanical loading histories and cortical bone remodeling. *Calcified Tissue International*. 1984;36 Suppl 1:S19-24. doi: 10.1007/BF02406129.

Causey GC, Picha GJ, Price J, Pelletier MH, Wang T, Walsh WR. In-Vivo response to a novel pillared surface morphology for osseointegration in an ovine model. *Journal of the Mechanical Behaviour of Biomedical Materials*. 2021 Jul; 119:104462. doi: 10.1016/j.jmbbm.2021.104462.

Chaki S, Shanmugarajan B, Ghosal S, Padmanabham G. Application of integrated soft computing techniques for optimisation of hybrid CO2 laser-MIG welding process. *Applied Soft Computing*.2015;30:365-374. https://doi.org/10.1016/j.asoc.2015.01.045.

Chanda S, Gupta S, Kumar Pratihar D. A genetic algorithm based multi-objective shape optimization scheme for cementless femoral implant. *Journal of Biomechanical Engineering*. 2015 Mar;137(3). doi: 10.1115/1.4029061.

Chanda S, Gupta S, Pratihar DK. A combined neural network and genetic algorithm based approach for optimally designed femoral implant having improved primary stability. *Applied Soft Computing*.2016; 38:296–307.

Chanda S, Gupta S, Pratihar DK. Effects of interfacial conditions on shape optimization of cementless hip stem: an investigation based on a hybrid framework. *Structural and Multidisciplinary Optimization*. 2016 53:1143–1155. doi: 10.1007/s00158-015-1382-1.

Chanda S, Mukherjee K, Gupta S, Pratihar DK. A comparative assessment of two designs of hip stem using rule-based simulation of combined osseointegration and remodelling. *Proceedings of the Institution of Mechanical Engineers, Part H: Journal of Engineering in Medicine*. 2020 Jan;234(1):118-128. doi: 10.1177/0954411919890998.

Chang PB, Williams BJ, Bhalla KS, Belknap TW, Santner TJ, Notz WI, Bartel DL. Design and analysis of robust total joint replacements: finite element model experiments with environmental variables. *Journal of Biomechanical Engineering*. 2001 Jun;123(3):239-46. doi: 10.1115/1.1372701.

Chang PB, Williams BJ, Santner TJ, Notz WI, Bartel DL. Robust optimization of total joint replacements incorporating environmental variables. *Journal of Biomechanical Engineering*. 1999 Jun;121(3):304-10. doi: 10.1115/1.2798325.

Charnley J. Total hip replacement by low-friction arthroplasty. *Clinical Orthopaedics and Related Research*. 1970 Sep-Oct; 72:7-21.

Chatterjee S, Dey S, Majumder S, RoyChowdhury A, Datta S. Computational intelligence based design of implant for varying bone conditions. *International Journal for Numerical Methods in Biomedical Engineering*. 2019 Jun;35(6): e3191. doi: 10.1002/cnm.3191.

Checa S, Prendergast PJ. A mechanobiological model for tissue differentiation that includes angiogenesis: a lattice-based modeling approach. *Annals of Biomedical Engineering*. 2009 Jan;37(1):129-45. doi: 10.1007/s10439-008-9594-9.

Chen G, Pettet GJ, Pearcy M, McElwain DL. Modelling external bone adaptation using evolutionary structural optimization. *Biomechanics and Modeling in Mechanobiology*. 2007 Jul;6(4):275-85. doi: 10.1007/s10237-006-0055-9.

Cheng YC, Jiang CP, Lin DH. Finite element based optimization design for a one-piece zirconia ceramic dental implant under dynamic loading and fatigue life validation. *Structural and Multidisciplinary Optimization*. 2019; 59:835–849. doi: 10.1007/s00158-018-2104-2.

Chennimalai Kumar N, Dantzig JA, Jasiuk IM, Robling AG, Turner CH. Numerical modeling of long bone adaptation due to mechanical loading: correlation with experiments. *Annals of Biomedical Engineering*. 2010 Mar;38(3):594-604. doi: 10.1007/s10439-009-9861-4.

Cheong VS, Blunn GW, Coathup MJ, Fromme P. A novel adaptive algorithm for 3D finite element analysis to model extracortical bone growth. *Computer Methods in Biomechanics and Biomedical Engineering*. 2018 Feb;21(2):129-138. doi: 10.1080/10255842.2018.1425997.

Choi JY, Sim JH, Yeo IL. Characteristics of contact and distance osteogenesis around modified implant surfaces in rabbit tibiae. *Journal of Periodontal & Implant Science*. 2017 Jun;47(3):182-192. doi: 10.5051/jpis.2017.47.3.182.

Chou HY, Müftü S. Simulation of peri-implant bone healing due to immediate loading in dental implant treatments. *Journal of Biomechanics*. 2013; 46(5): 871-878. https://doi.org/10.1016/j.jbiomech.2012.12.023.

Chun HJ, Cheong SY, Han JH, Heo SJ, Chung JP, Rhyu IC, Choi YC, Baik HK, Ku Y, Kim MH. Evaluation of design parameters of osseointegrated dental implants using finite element analysis. *Journal of Oral Rehabilitation*. 2002 Jun;29(6):565-74. doi: 10.1046/j.1365-2842.2002.00891.x.

Cilla M, Borgiani E, Martínez J, Duda GN, Checa S. Machine learning techniques for the optimization of joint replacements: Application to a short-stem hip implant. *PLoS One*. 2017 Sep 5;12(9): e0183755. doi: 10.1371/journal.pone.0183755.

Claes LE, Heigele CA. Magnitudes of local stress and strain along bony surfaces predict the course and type of fracture healing. *Journal of Biomechanics*. 1999 Mar;32(3):255-66. doi: 10.1016/s0021-9290(98)00153-5.

Cochran DL, Schenk RK, Lussi A, Higginbottom FL, Buser D. Bone response to unloaded and loaded titanium implants with a sandblasted and acid-etched surface: a histometric study in the canine mandible. *Journal of Biomedical Materials Research*. 1998 Apr;40(1):1-11. doi: 10.1002/(sici)1097-4636(199804)40:1<1::aid-jbm1>3.0.co;2-q.

Corso LL, Spinelli Lde F, Schnaid F, Zanrosso CD, Marczak RJ. Optimization of a Cemented Femoral Prosthesis Considering Bone Remodeling. *Journal of Biomechanical Engineering*. 2016 Jan;138(1). doi: 10.1115/1.4031938.

Cowin SC, Hegedus DH. Bone remodeling I: theory of adaptive elasticity. *Journal of Elasticity*. 1976; 6:313–326. doi: 10.1007/BF00041724.

Cowin SC. Wolff's law of trabecular architecture at remodeling equilibrium. *Journal of Biomechanical Engineering*. 1986 Feb;108(1):83-8. doi: 10.1115/1.3138584.

Crawford RW, Murray DW. Total hip replacement: indications for surgery and risk factors for failure. *Annals of the Rheumatic Diseases*. 1997 Aug;56(8):455-7. doi: 10.1136/ard.56.8.455.

Cristofolini L, Varini E, Viceconti M. In-vitro method for assessing femoral implant-bone micromotions in resurfacing hip implants under different loading conditions. *Proceedings of the Institution of Mechanical Engineers, Part H: Journal of Engineering in Medicine*. 2007 Nov;221(8):943-50. doi: 10.1243/09544119JEIM278.

Crowninshield RD, Johnston RC, Andrews JG, Brand RA. A biomechanical investigation of the human hip. *Journal of Biomechanics*. 1978;11(1-2):75-85. doi: 10.1016/0021-9290(78)90045-3.

Currey JD. The mechanical adaptations of bones. Princeton NJ USA *Princeton University Press*. 1984.

Dalstra M, Huiskes R, van Erning L. Development and validation of a three-dimensional finite element model of the pelvic bone. *Journal of Biomechanical Engineering*. 1995 Aug;117(3):272-8. doi: 10.1115/1.2794181.

Davies JE. In vitro modeling of the bone/implant interface. *The Anatomical Record*. 1996 Jun;245(2):426-45. doi: 10.1002/(SICI)1097-0185(199606)245:2<426::AID-AR21>3.0.CO;2-Q.

Davies JE. Understanding peri-implant endosseous healing. *Journal of Dental Education*. 2003 Aug;67(8):932-49.

de Beus AM, Hoeltzel DA, Eftekhar NS. Design optimization of a prosthesis stem reinforcing shell in total hip arthroplasty. *Journal of Biomechanical Engineering*. 1990 Aug;112(3):347-57. doi: 10.1115/1.2891195.

Deb K, Pratap A, Agarwal S, Meyarivan T. A fast and elitist multiobjective genetic algorithm: NSGA-II. *IEEE Transactions on Evolutionary Computation*.2002; 6(2):182−197.

Depover T, Hertelé S, Verbeken K. The effect of hydrostatic stress on the hydrogen induced mechanical degradation of dual phase steel: A combined experimental and numerical approach. *Engineering Fracture Mechanics*. 2019; 221:106704.

Dickinson A, Taylor A, Browne M. Implant-bone interface healing and adaptation in resurfacing hip replacement. *Computer Methods in Biomechanics and Biomedical Engineering*. 2012; 15(9): 935-947. https://doi.org/10.1080/10255842.2011.567269.

Doblaré M, García JM. Anisotropic bone remodelling model based on a continuum damage-repair theory. *Journal of Biomechanics*. 2002 Jan;35(1):1-17. doi: 10.1016/s0021-9290(01)00178-6.

Dong XN, Guo XE. The dependence of transversely isotropic elasticity of human femoral cortical bone on porosity. *Journal of Biomechanics*. 2004 Aug;37(8):1281-7. doi: 10.1016/j.jbiomech.2003.12.011.

Dopico-González C, New AM, Browne M. Probabilistic finite element analysis of the uncemented hip replacement – effect of femur characteristics and implant design geometry. *Journal of Biomechanics*. 2010; 43 (3): 512–520.

Dorronsoro J. Artificial neural networks, in: Icann: Intl. Conf., *Springer*, Madrid,2002.

Dowson D, Seedhom BB, Johnson GR. Biomechanics of the lower limb. In: An introduction to the biomechanics of joint and joint replacement. Eds: Dowson D Wright. 1981:68–84.

Duda GN, Brand D, Freitag S, Lierse W, Schneider E. Variability of femoral muscle attachments. *Journal of Biomechanics*. 1996 Sep;29(9):1185-90. doi: 10.1016/0021-9290(96)00025-5.

Duda GN, Heller M, Albinger J, Schulz O, Schneider E, Claes L. Influence of muscle forces on femoral strain distribution. *Journal of Biomechanics*. 1998 Sep;31(9):841-6. doi: 10.1016/s0021-9290(98)00080-3.

Dunbar MJ. Cemented femoral fixation: the North Atlantic divide. *Orthopedics*. 2009 Sep;32(9):orthosupersite.com/view.asp?rID=42832. doi: 10.3928/01477447-20090728-07.

Duncan RL, Turner CH. Mechanotransduction and the functional response of bone to mechanical strain. *Calcified Tissue International*. 1995 Nov;57(5):344-58. doi: 10.1007/BF00302070.

Dutta P, Pratihar DK. Modeling of TIG welding process using conventional regression analysis and neural network-based approaches. *Journal of Materials Processing Technology*. 2007; 184 (1–3):56–68.

Elleuch S, Jrad H, Kessentini A, Wali M, Dammak F. Design optimization of implant geometrical characteristics enhancing primary stability using FEA of stress distribution around dental prosthesis. *Computer Methods in Biomechanics and Biomedical Engineering*. 2021 Jul;24(9):1035-1051. doi: 10.1080/10255842.2020.1867112.

Engh CA, McGovern TF, Bobyn JD, Harris WH. A quantitative evaluation of periprosthetic bone-remodeling after cementless total hip arthroplasty. *The Journal of Bone & Joint Surgery*. 1992 Aug;74(7):1009-20.

Evans JT, Evans JP, Walker RW, Blom AW, Whitehouse MR, Sayers A. How long does a hip replacement last? A systematic review and meta-analysis of case series and national registry reports with more than 15 years of follow-up. *Lancet*. 2019 Feb 16;393(10172):647-654. doi: 10.1016/S0140-6736(18)31665-9.

Evans SL, Gregson PJ. Numerical optimization of the design of a coated, cementless hip prosthesis. *Journal of Materials Science: Materials in Medicine*. 1994 Aug;5(8):507-510. doi: 10.1007/BF00124881.

Fernandes P, Rodrigues H, Jacobs C. A Model of Bone Adaptation Using a Global Optimization Criterion Based on the Trajectorial Theory of Wolff. *Computer Methods in Biomechanics and Biomedical Engineering*. 1999;2(2):125-138. doi: 10.1080/10255849908907982.

Fernandes PR, Folgado J, Jacobs C, Pellegrini V. A contact model with ingrowth control for bone remodelling around cementless stems. *Journal of Biomechanics*. 2002 Feb;35(2):167-76. doi: 10.1016/s0021-9290(01)00204-4.

Fernandes PR, Folgado J, Ruben RB. Shape optimization of a cementless hip stem for a minimum of interface stress and displacement. *Computer Methods in Biomechanics and Biomedical Engineering*. 2004 Feb;7(1):51-61. doi: 10.1080/10255840410001661637.

Folgado J, Fernandes PR, Jacobs CR, Pellegrini VD Jr. Influence of femoral stem geometry, material and extent of porous coating on bone ingrowth and atrophy in cementless total hip arthroplasty: an iterative finite element model.

Computer Methods in Biomechanics and Biomedical Engineering. 2009 Apr;12(2):135-45. doi: 10.1080/10255840903081123.

Fraldi M, Esposito L, Perrella G, Cutolo A, Cowin SC. Topological optimization in hip prosthesis design. *Biomechanics and Modeling in Mechanobiology*. 2010 Aug;9(4):389-402. doi: 10.1007/s10237-009-0183-0.

Frost HM. Bone "mass" and the "mechanostat": a proposal. *The Anatomical Record*. 1987 Sep;219(1):1-9. doi: 10.1002/ar.1092190104.

Frost HM. The biology of fracture healing. An overview for clinicians. *Part II. Clinical Orthopaedics and Related Research*. 1989 Nov;(248):294-309.

Frost HM. The laws of bone structure. Springfield Illionis USA *Charles C Thomas Publisher*. 1964.

Fyhrie DP, Carter DR. A unifying principle relating stress to trabecular bone morphology. *Journal of Orthopaedic Research*.1986;4(3):304-17. doi: 10.1002/jor.1100040307.

Garcia JM, Martínez MA, Doblaré M. An anisotropic internal-external bone adaptation model based on a combination of CAO and continuum damage mechanics technologies. *Computer Methods in Biomechanics and Biomedical Engineering*. 2001;4(4):355-77. doi: 10.1080/10255840108908014.

Gardner TN, Mishra S, Marks L. The role of osteogenic index, octahedral shear stress and dilatational stress in the ossification of a fracture callus. *Medical Engineering & Physics*.2004 Jul;26(6):493-501. doi: 10.1016/j.medengphy.2004.03.009.

Gardner TN, Stoll T, Marks L, Mishra S, Knothe Tate M. The influence of mechanical stimulus on the pattern of tissue differentiation in a long bone fracture--an FEM study. *Journal of Biomechanics*. 2000 Apr;33(4):415-25. doi: 10.1016/s0021-9290(99)00189-x.

Garijo N, Fernández JR, Pérez MA, García-Aznar JM. Numerical stability and convergence analysis of bone remodeling model. *Computer Methods in Applied Mechanics and Engineering*. 2014 Apr 1; 271: 253-268.doi: 10.1016/j.cma.2013.12.014.

Gebert A, Peters J, Bishop NE, Westphal F, Morlock MM. Influence of press-fit parameters on the primary stability of uncemented femoral resurfacing

implants. *Medical Engineering & Physics*.2009 Jan;31(1):160-4. doi: 10.1016/j.medengphy.2008.04.007.

Geng JP, Ma QS, Xu W, Tan KB, Liu GR. Finite element analysis of four thread-form configurations in a stepped screw implant. *Journal of Oral Rehabilitation*. 2004 Mar;31(3):233-9. doi: 10.1046/j.0305-182X.2003.01213.x.

Geraldes DM, Phillips AT. A comparative study of orthotropic and isotropic bone adaptation in the femur. *International Journal for Numerical Methods in Biomedical Engineering*. 2014 Sep;30(9):873-89. doi: 10.1002/cnm.2633.

Geramizadeh M, Katoozian H, Amid R, Kadkhodazadeh M. Three-dimensional optimization and sensitivity analysis of dental implant thread parameters using finite element analysis. *Journal of the Korean Association of Oral and Maxillofacial Surgeons*. 2018 Apr;44(2):59-65. doi: 10.5125/jkaoms.2018.44.2.59.

Ghavidelnia N, Bodaghi M, Hedayati R. Femur Auxetic Meta-Implants with Tuned Micromotion Distribution. *Materials (Basel)*. 2020 Dec 29;14(1):114. doi: 10.3390/ma14010114.

Ghaziani AO, Soheilifard R, Kowsar S. The effect of functionally graded materials on bone remodeling around osseointegrated trans-femoral prostheses. *Journal of the Mechanical Behavior of Biomedical Materials*.2021 Jun; 118:104426. doi: 10.1016/j.jmbbm.2021.104426.

Ghimire S, Miramini S, Edwards G, Rotne R, Xu J, Ebeling P, Zhang L. The investigation of bone fracture healing under intramembranous and endochondral ossification. *Bone Reports*. 2020 Dec 15;14:100740. doi: 10.1016/j.bonr.2020.100740.

Ghosh R, Gupta S. Bone remodelling around cementless composite acetabular components: the effects of implant geometry and implant-bone interfacial conditions. *Journal of the Mechanical Behavior of Biomedical Materials*.2014 Apr; 32:257-269. doi: 10.1016/j.jmbbm.2014.01.010.

Ghosh R, Mukherjee K, Gupta S. Bone remodelling around uncemented metallic and ceramic acetabular components. *Proceedings of the Institution of Mechanical Engineers, Part H: Journal of Engineering in Medicine*. 2013 May;227(5):490-502. doi: 10.1177/0954411913478703.

Ghosh R, Pratihar DK, Gupta S. Towards the optimal design of an uncemented acetabular component using genetic algorithms. *Engineering Optimization*. 2015; 47(12):1587-1601, doi: 10.1080/0305215X.2014.971779.

Gibson LJ. The mechanical behaviour of cancellous bone. *Journal of Biomechanics*. 1985;18(5):317-28. doi: 10.1016/0021-9290(85)90287-8.

Giorgio I, Andreaus U, Alzahrani F, Hayat T, Lekszycki T. A Diffusion Model for Stimulus Propagation in Remodeling Bone Tissues. In: Altenbach H, Müller W, Abali B. (eds) Higher Gradient Materials and Related Generalized Continua, Advanced Structured Materials 2019;120, *Springer International Publishing*. doi: 10.1007/978-3-030-30406-5_5

Giorgio I, Andreaus U, Scerrato D, dell'Isola F. A visco-poroelastic model of functional adaptation in bones reconstructed with bio-resorbable materials. *Biomechanics and Modeling in Mechanobiology*. 2016 Oct;15(5):1325-43. doi: 10.1007/s10237-016-0765-6

Giori NJ, Beaupré GS, Carter DR. Cellular shape and pressure may mediate mechanical control of tissue composition in tendons. *Journal of Orthopaedic Research*. 1993 Jul;11(4):581-91. doi: 10.1002/jor.1100110413.

Giori NJ, Ryd L, Carter DR. Mechanical influences on tissue differentiation at bone-cement interfaces. *Journal of Arthroplasty*. 1995 Aug;10(4):514-22. doi: 10.1016/s0883-5403(05)80154-8.

Gittens RA, Olivares-Navarrete R, Schwartz Z, Boyan BD. Implant osseointegration and the role of microroughness and nanostructures: lessons for spine implants. *Acta Biomaterialia*.2014 Aug;10(8):3363-71. doi: 10.1016/j.actbio.2014.03.037.

Goda I, Ganghoffer JF, Maurice G. Combined bone internal and external remodeling based on Eshelby stress. *International Journal of Solids and Structures*. 2016 Sep; 94:138-157. doi: 10.1016/j.ijsolstr.2016.04.036.

Gómez-Benito MJ, García-Aznar JM, Kuiper JH, Doblaré M. Influence of fracture gap size on the pattern of long bone healing: a computational study. *Journal of Theoretical Biology*. 2005 Jul 7;235(1):105-19. doi: 10.1016/j.jtbi.2004.12.023.

Gray H. Anatomy of the human body. *Philadelphia Lea & Febiger*. 1918.

Gui N, Xu W, Myers DE, Shukla R, Tang HP, Qian M. The effect of ordered and partially ordered surface topography on bone cell responses: a review. *Biomaterials Science*. 2018 Jan 30;6(2):250-264. doi: 10.1039/c7bm01016h.

Guo XE. Mechanical properties on cortical and cancellous bone tissue. In: Bone Mechanics handbook Ed: Cowin SC New York *Informa Healthcare*.2008.

Haddad RJ Jr, Cook SD, Thomas KA. Biological fixation of porous-coated implants. *The Journal of Bone & Joint Surgery*. 1987 Dec;69(9):1459-66.

Haider IT, Speirs AD, Beaulé PE, Frei H. Influence of ingrowth regions on bone remodelling around a cementless hip resurfacing femoral implant. *Computer Methods in Biomechanics and Biomedical Engineering*. 2015;18(12):1349-57. doi: 10.1080/10255842.2014.903931.

Hambli R, Katerchi H, Benhamou CL. Multiscale methodology for bone remodelling simulation using coupled finite element and neural network computation. *Biomechanics and Modeling in Mechanobiology*. 2011 Feb;10(1):133-45. doi: 10.1007/s10237-010-0222-x.

Harris WH, Schiller AL, Scholler JM, Freiberg RA, Scott R. Extensive localized bone resorption in the femur following total hip replacement. *The Journal of Bone & Joint Surgery*. 1976 Jul;58(5):612-8.

Harrysson OLA, Hosni YA, Nayfeh JF. Custom-designed orthopedic implants evaluated using finite element analysis of patient-specific computed tomography data: femoral-component case study. *BMC Musculoskeletal Disorders*.2007;8 (91):1-10. http://dx.doi.org/10.1186/1471-2474-8-91.

Hart RT, Davy DT, Heiple KG. Mathematical modeling and numerical solutions for functionally dependent bone remodeling. *Calcified Tissue International*. 1984;36 Suppl 1:S104-9. doi: 10.1007/BF02406142.

He R, Lu Y, Ren J, Wang Z, Huang J, Zhu L, Wang K. Decreased fibrous encapsulation and enhanced osseointegration in vitro by decorin-modified titanium surface. *Colloids and Surfaces B: Biointerfaces*. 2017 Jul 1; 155:17-24. doi: 10.1016/j.colsurfb.2017.03.055.

Hedia HS, Abdel-Shafi AA, Fouda N. Shape optimization of metal backing for cemented acetabular cup. *Bio-Medical Materials and Engineering*. 2000;10(2):73-82.

Hedia HS, Barton DC, Fisher J, Elmidany TT. A method for shape optimization of a hip prosthesis to maximize the fatigue life of the cement. *Medical*

Engineering & Physics.1996 Dec;18(8):647-54. doi: 10.1016/s1350-4533(96)00025-2.

Hedia HS, Barton DC, Fisher J, Ibrahim A. Shape optimization of a Charnley prosthesis based on the fatigue notch factor. *Bio-Medical Materials and Engineering*. 1996;6(3):199-217.

Heller MO, Bergmann G, Deuretzbacher G, Dürselen L, Pohl M, Claes L, Haas NP, Duda GN. Musculo-skeletal loading conditions at the hip during walking and stair climbing. *Journal of Biomechanics*. 2001 Jul;34(7):883-93. doi: 10.1016/s0021-9290(01)00039-2.

Heller MO, Bergmann G, Kassi JP, Claes L, Haas NP, Duda GN. Determination of muscle loading at the hip joint for use in pre-clinical testing. *Journal of Biomechanics*. 2005 May;38(5):1155-63. doi: 10.1016/j.jbiomech.2004.05.022.

Heyland M, Checa S, Kendoff D, Duda GN. Anatomic grooved stem mitigates strain shielding compared to established total hip arthroplasty stem designs in finite-element models. *Scientific Reports-UK*. 2019; 9(1):1-11. 10.1038/s41598-018-36503-z.

Hirabayashi S, Iwamoto M. Finite element analysis of biological soft tissue surrounded by a deformable membrane that controls transmembrane flow. *Theoretical Biology and Medical Modelling*. 2018 Dec 10;15(1):21. doi: 10.1186/s12976-018-0094-9.

Hollister SJ, Brennan JM, Kikuchi N. A homogenization sampling procedure for calculating trabecular bone effective stiffness and tissue level stress. *Journal of Biomechanics*. 1994 Apr;27(4):433-44. doi: 10.1016/0021-9290(94)90019-1.

Holzwarth U, Cotogno G. Total Hip Arthroplasty. State of the Art, Challenges and Prospects. Brussels: European Commission. 2012.

Hori RY, Lewis J. Mechanical properties of the fibrous tissue found at the bone cement interface following total joint replacement. *Journal of Biomedical Materials Research*.1982; 16(6): 911-927. https://doi.org/10.1002/jbm.820160615.

Huiskes R, Boeklagen R. Mathematical shape optimization of hip prosthesis design. *Journal of Biomechanics*. 1989;22(8-9):793-804. doi: 10.1016/0021-9290(89)90063-8.

Huiskes R, Boeklagen R. The application of numerical shape optimization to artificial-joint design. In *Computational Methods in Bioengineering: Presented at the Winter Annual Meeting of the American Society Mechanical Engineers*. 1988;9:185-197.

Huiskes R, Ruimerman R, van Lenthe GH, Janssen JD. Effects of mechanical forces on maintenance and adaptation of form in trabecular bone. *Nature*. 2000 Jun 8;405(6787):704-6. doi: 10.1038/35015116.

Huiskes R, Van Driel WD, Prendergast PJ, Søballe K. A biomechanical regulatory model for periprosthetic fibrous-tissue differentiation. *Journal of Materials Science: Materials in Medicine*. 1997 Dec;8(12):785-8. doi: 10.1023/a:1018520914512.

Huiskes R, Weinans H, Dalstra M. Adaptive bone remodeling and biomechanical design considerations for noncemented total hip arthroplasty. *Orthopedics*. 1989 Sep;12(9):1255-67.

Huiskes R, Weinans H, Grootenboer HJ, Dalstra M, Fudala B, Slooff TJ. Adaptive bone-remodeling theory applied to prosthetic-design analysis. *Journal of Biomechanics*. 1987;20(11-12):1135-50. doi: 10.1016/0021-9290(87)90030-3.

Huiskes R, Weinans H, van Rietbergen B. The relationship between stress shielding and bone resorption around total hip stems and the effects of flexible materials. *Clinical Orthopaedics and Related Research*. 1992 Jan;(274):124-34.

Huiskes R. Failed innovation in total hip replacement. Diagnosis and proposals for a cure. *Acta Orthopaedica Scandinavica*. 1993 Dec;64(6):699-716. doi: 10.3109/17453679308994602.

Irandoust S, Müftü S. The interplay between bone healing and remodeling around dental implants. *Scientific Reports*. 2020 Mar 9;10(1):4335. doi: 10.1038/s41598-020-60735-7.

Isaksson H, van Donkelaar CC, Huiskes R, Ito K. A mechano-regulatory bone-healing model incorporating cell-phenotype specific activity. *Journal of Theoretical Biology*. 2008 May 21;252(2):230-46. doi: 10.1016/j.jtbi.2008.01.030.

Isaksson H, van Donkelaar CC, Huiskes R, Ito K. Corroboration of mechanoregulatory algorithms for tissue differentiation during fracture

healing: Comparison with in vivo results. *Journal of Orthopaedic Research*. 2006 May;24(5):898-907. doi: 10.1002/jor.20118.

Isaksson H, van Donkelaar CC, Huiskes R, Yao J, Ito K. Determining the most important cellular characteristics for fracture healing using design of experiments methods. *Journal of Theoretical Biology*. 2008 Nov 7;255(1):26-39. doi: 10.1016/j.jtbi.2008.07.037.

Isaksson H, van Donkelaar CC, Ito K. Sensitivity of tissue differentiation and bone healing predictions to tissue properties. *Journal of Biomechanics*. 2009 Mar 26;42(5):555-64. doi: 10.1016/j.jbiomech.2009.01.001.

Isaksson H, Wilson W, van Donkelaar CC, Huiskes R, Ito K. Comparison of biophysical stimuli for mechano-regulation of tissue differentiation during fracture healing. *Journal of Biomechanics*. 2006a;39(8):1507-16. doi: 10.1016/j.jbiomech.2005.01.037.

Ishida T, Nishimura I, Tanino H, Higa M, Ito H, Mitamura Y. Use of a genetic algorithm for multiobjective design optimization of the femoral stem of a cemented total hip arthroplasty. *Artificial Organs*. 2011 Apr;35(4):404-10. doi: 10.1111/j.1525-1594.2010.01117.x.

Jacobs CR, Levenston ME, Beaupré GS, Simo JC, Carter DR. Numerical instabilities in bone remodeling simulations: the advantages of a node-based finite element approach. *Journal of Biomechanics*. 1995 Apr;28(4):449-59. doi: 10.1016/0021-9290(94)00087-k.

Jacobs CR, Simo JC, Beaupré GS, Carter DR. Adaptive bone remodeling incorporating simultaneous density and anisotropy considerations. *Journal of Biomechanics*. 1997 Jun;30(6):603-13. doi: 10.1016/s0021-9290(96)00189-3.

Jang IG, Kim IY, Kwak BB. Analogy of strain energy density based bone-remodeling algorithm and structural topology optimization. *Journal of Biomechanical Engineering*. 2009 Jan;131(1):011012. doi: 10.1115/1.3005202.

Jang IG, Kim IY. Computational study of Wolff's law with trabecular architecture in the human proximal femur using topology optimization. *Journal of Biomechanics*. 2008 Aug 7;41(11):2353-61. doi: 10.1016/j.jbiomech.2008.05.037.

Jansen KA, Donato DM, Balcioglu HE, Schmidt T, Danen EH, Koenderink GH. A guide to mechanobiology: Where biology and physics meet. *Biochimica et Biophysica Acta*. 2015 Nov;1853(11 Pt B):3043-52. doi: 10.1016/j.bbamcr.2015.05.007.

Jasty M, Bragdon C, Burke D, O'Connor D, Lowenstein J, Harris WH. In vivo skeletal responses to porous-surfaced implants subjected to small induced motions. *The Journal of Bone & Joint Surgery*. 1997 May;79(5):707-14. doi: 10.2106/00004623-199705000-00010.

Jasty M, Bragdon CR, Maloney WJ, Haire T, Harris WH. Ingrowth of bone in failed fixation of porous-coated femoral components. *The Journal of Bone & Joint Surgery*. 1991 Oct;73(9):1331-7.

Jasty MJ, Floyd WE 3rd, Schiller AL, Goldring SR, Harris WH. Localized osteolysis in stable, non-septic total hip replacement. *The Journal of Bone & Joint Surgery*. 1986 Jul;68(6):912-9.

Jee WSS. Integrated bone tissue physiology: anatomy and physiology. In: Bone Mechanics Handbook Ed: Cowin SC New York *Informa Healthcare*. 2008.

Jurvelin JS, Buschmann MD, Hunziker EB. Optical and mechanical determination of Poisson's ratio of adult bovine humeral articular cartilage. *Journal of Biomechanics*. 1997; 30(3): 235-241. https://doi.org/10.1016/S0021-9290(96)00133-9.

Katoozian H, Davy DT. Effects of loading conditions and objective function on three-dimensional shape optimization of femoral components of hip endoprostheses. *Medical Engineering & Physics*.2000 May;22(4):243-51. doi: 10.1016/s1350-4533(00)00030-8.

Kelly DJ, Prendergast PJ. Mechano-regulation of stem cell differentiation and tissue regeneration in osteochondral defects. *Journal of Biomechanics*. 2005 Jul;38(7):1413-22. doi: 10.1016/j.jbiomech.2004.06.026.

Kelly DJ, Prendergast PJ. Prediction of the optimal mechanical properties for a scaffold used in osteochondral defect repair. *Tissue Engineering*. 2006 Sep;12(9):2509-19. doi: 10.1089/ten.2006.12.2509.

Khayyeri H, Checa S, Tägil M, Prendergast PJ. Corroboration of mechanobiological simulations of tissue differentiation in an in vivo bone chamber using a lattice-modeling approach. *Journal of Orthopaedic Research*.2009 Dec;27(12):1659-66. doi: 10.1002/jor.20926.

Kienapfel H, Sprey C, Wilke A, Griss P. Implant fixation by bone ingrowth. *Journal of Arthroplasty*. 1999 Apr;14(3):355-68. doi: 10.1016/s0883-5403(99)90063-3.

Kim JT, Yoo JJ. Implant Design in Cementless Hip Arthroplasty. *Hip Pelvis*. 2016 Jun;28(2):65-75. doi: 10.5371/hp.2016.28.2.65.

Koh YG, Lee JA, Lee HY, Chun HJ, Kim HJ, Kang KT. Design optimization of high tibial osteotomy plates using finite element analysis for improved biomechanical effect. *Journal of Orthopaedic Surgery and Research*. 2019 Jul 16;14(1):219. doi: 10.1186/s13018-019-1269-8.

Kowalczyk P. Design optimization of cementless femoral hip prostheses using finite element analysis. *Journal of Biomechanical Engineering*. 2001 Oct;123(5):396-402. doi: 10.1115/1.1392311.

Kuiper JH, Huiskes HWJ. Numerical optimization of hip-prosthetic stem material. In Middleton J, Pande GN, Williams KR, editors, Recent advances in computer methods in biomechanics and biomedical engineering ams. *Swansea: Books and Journals International*. 1992.

Kung PC, Chien SS, Tsou NT. A Hybrid Model for Predicting Bone Healing around Dental Implants. *Materials (Basel)*. 2020 Jun 25;13(12):2858. doi: 10.3390/ma13122858.

Kuroshima S, Nakano T, Ishimoto T, Sasaki T, Inoue M, Yasutake M, et al. Optimally oriented grooves on dental implants improve bone quality around implants under repetitive mechanical loading. *Acta Biomaterialia*. 2017; 48: 433-444. 10.1016/j.actbio.2016.11.021.

Kurtz S, Ong K, Lau E, Mowat F, Halpern M. Projections of primary and revision hip and knee arthroplasty in the United States from 2005 to 2030. *The Journal of Bone & Joint Surgery*. 2007 Apr;89(4):780-5. doi: 10.2106/JBJS.F.00222.

Kuzyk PR, Schemitsch EH. The basic science of peri-implant bone healing. *Indian Journal of Orthopaedics*. 2011 Mar;45(2):108-15. doi: 10.4103/0019-5413.77129.

Lacroix D, Prendergast PJ, Li G, Marsh D. Biomechanical model to simulate tissue differentiation and bone regeneration: application to fracture healing. *Medical & Biological Engineering & Computing*. 2002; 40(1):14-21. https://doi.org/10.1007/bf02347690.

Lacroix D, Prendergast PJ. A mechano-regulation model for tissue differentiation during fracture healing: analysis of gap size and loading. *Journal of Biomechanics*. 2002a; 35(9):1163-1171. https://doi.org/10.1016/S0021-9290(02)00086-6.

Lacroix D, Prendergast PJ. Three-dimensional simulation of fracture repair in the human tibia. *Computer Methods in Biomechanics and Biomedical Engineering*. 2002b; 5(5):369-376. https://doi.org/10.1080/1025584021000025014.

Learmonth ID, Gheduzzi S, Vail TP. Clinical experience with metal-on-metal total joint replacements: indications and results. *Proceedings of the Institution of Mechanical Engineers, Part H: Journal of Engineering in Medicine*. 2006 Feb;220(2):229-37. doi: 10.1243/095441105X69123.

Li J, Li H, Shi L, Fok AS, Ucer C, Devlin H, Horner K, Silikas N. A mathematical model for simulating the bone remodeling process under mechanical stimulus. *Dental Materials*. 2007 Sep;23(9):1073-8. doi: 10.1016/j.dental.2006.10.004.

Li MJ, Kung PC, Chang YW, Tsou NT. Healing Pattern Analysis for Dental Implants Using the Mechano-Regulatory Tissue Differentiation Model. *International Journal of Molecular Sciences*. 2020 Dec 2;21(23):9205. doi: 10.3390/ijms21239205.

Lin D, Li Q, Li W, Swain M. Dental implant induced bone remodeling and associated algorithms. *Journal of the Mechanical Behavior of Biomedical Materials*.2009 Oct;2(5):410-32. doi: 10.1016/j.jmbbm.2008.11.007.

Liu X, Niebur GL. Bone ingrowth into a porous coated implant predicted by a mechano-regulatory tissue differentiation algorithm. *Biomechanics and Modeling in Mechanobiology*. 2008 Aug;7(4):335-44. doi: 10.1007/s10237-007-0100-3.

Loboa EG, Wren TA, Beaupré GS, Carter DR. Mechanobiology of soft skeletal tissue differentiation--a computational approach of a fiber-reinforced poroelastic model based on homogeneous and isotropic simplifications. *Biomechanics and Modeling in Mechanobiology*. 2003 Nov;2(2):83-96. doi: 10.1007/s10237-003-0030-7.

Lombardi AV Jr, Berend KR, Mallory TH, Skeels MD, Adams JB. Survivorship of 2000 tapered titanium porous plasma-sprayed femoral components. *Clinical*

Orthopaedics and Related Research. 2009 Jan;467(1):146-54. doi: 10.1007/s11999-008-0568-x.

Lu X, Wu Z, Xu K, Wang X, Wang S, Qiu H, Li X, Chen J. Multifunctional Coatings of Titanium Implants Toward Promoting Osseointegration and Preventing Infection: Recent Developments. *Frontiers in Bioengineering and Biotechnology*. 2021 Dec 7; 9:783816. doi: 10.3389/fbioe.2021.783816.

Luo ZP, An KN. A theoretical model to predict distribution of the fabric tensor and apparent density in cancellous bone. *Journal of Mathematical Biology*. 1998 Jun;36(6):557-68. doi: 10.1007/s002850050114.

Maloney WJ, Jasty M, Rosenberg A, Harris WH. Bone lysis in well-fixed cemented femoral components. *The Journal of Bone & Joint Surgery*. 1990 Nov;72(6):966-70. doi: 10.1302/0301-620X.72B6.2246299.

Marieb EN, Hoehn K. Human anatomy & physiology. *Pearson education*. 2013.

Martini FH, Bartholomew EF. Essentials of anatomy and physiology. *Pearson education*. 2016.

Mathai B, Dhara S, Gupta S. Orthotropic bone remodelling around uncemented femoral implant: a comparison with isotropic formulation. *Biomechanics and Modeling in Mechanobiology*. 2021 Jun;20(3):1115-1134. doi: 10.1007/s10237-021-01436-6.

Mathai B, Gupta S. Bone Ingrowth Around an Uncemented Femoral Implant Using Mechanoregulatory Algorithm: A Multiscale Finite Element Analysis. *Journal of Biomechanical Engineering*. 2022 Feb 1;144(2):021004. doi: 10.1115/1.4052227.

Matheron G. The intrinsic random functions and their applications. *Advances in Applied Probability*. 1973 Dec; 5(3):439-468. doi:10.2307/1425829.

Matsoukas G, Kim IY. Design optimization of a total hip prosthesis for wear reduction. *Journal of Biomechanical Engineering*. 2009 May;131(5):051003. doi: 10.1115/1.3049862.

Matsuda N, Morita N, Matsuda K, Watanabe M. Proliferation and differentiation of human osteoblastic cells associated with differential activation of MAP kinases in response to epidermal growth factor, hypoxia, and mechanical stress in vitro. *Biochemical and Biophysical Research Communications*. 1998 Aug 19;249(2):350-4. doi: 10.1006/bbrc.1998.9151.

McKellop H, Park SH, Chiesa R, Doorn P, Lu B, Normand P, Grigoris P, Amstutz H. In vivo wear of three types of metal on metal hip prostheses during two decades of use. *Clinical Orthopaedics and Related Research*. 1996 Aug;(329 Suppl):S128-40. doi: 10.1097/00003086-199608001-00013.

McNamara BP, Prendergast PJ, Taylor D. Prediction of bone adaptation in the ulnar-osteotomized sheep's forelimb using an anatomical finite element model. *Journal of Biomedical Engineering*. 1992 May;14(3):209-16. doi: 10.1016/0141-5425(92)90054-o.

McNamara LM, Prendergast PJ. Bone remodelling algorithms incorporating both strain and microdamage stimuli. *Journal of Biomechanics*. 2007;40(6):1381-91. doi: 10.1016/j.jbiomech.2006.05.007.

Mehboob H, Ahmad F, Tarlochan F, Mehboob A, Chang SH. A comprehensive analysis of bio-inspired design of femoral stem on primary and secondary stabilities using mechanoregulatory algorithm. *Biomechanics and Modeling in Mechanobiology*. 2020 Dec;19(6):2213-2226. doi: 10.1007/s10237-020-01334-3.

Mendonça G, Mendonça DB, Aragão FJ, Cooper LF. Advancing dental implant surface technology--from micron- to nanotopography. *Biomaterials*. 2008 Oct;29(28):3822-35. doi: 10.1016/j.biomaterials.2008.05.012.

Miller AS, Blott BH, Hames TK. Review of neural network applications in medical imaging and signal processing. *Medical & Biological Engineering & Computing*. 1992;30 (5):449–464.

Mishra A, Shukla A. Analysis of the effect of elite count on the behaviour of genetic algorithms: a perspective. *IEEE 7th International Advance Computing Conference (IACC)*. 2017; 835-840. 10.1109/IACC.2017.0172.

Mohandes Y, Tahani M, Rouhi G, Tahami M. A mechanobiological approach to find the optimal thickness for the locking compression plate: Finite element investigations. *Proceedings of the Institution of Mechanical Engineers, Part H: Journal of Engineering in Medicine*. 2021 Apr;235(4):408-418. doi: 10.1177/0954411920985757.

Mondal S, Ghosh R. Bone remodelling around the tibia due to total ankle replacement: effects of implant material and implant-bone interfacial conditions. *Computer Methods in Biomechanics and Biomedical*

Engineering. 2019 Dec;22(16):1247-1257. doi: 10.1080/10255842.2019.1661385.

Mont MA, Seyler TM, Marker DR, Marulanda GA, Delanois RE. Use of metal-on-metal total hip resurfacing for the treatment of osteonecrosis of the femoral head. *The Journal of Bone & Joint Surgery*. 2006 Nov;88 Suppl 3:90-7. doi: 10.2106/JBJS.F.00543.

Morgan EF, Bayraktar HH, Keaveny TM. Trabecular bone modulus-density relationships depend on anatomic site. *Journal of Biomechanics*. 2003 Jul;36(7):897-904. doi: 10.1016/s0021-9290(03)00071-x.

Morgan EF, Keaveny TM. Dependence of yield strain of human trabecular bone on anatomic site. *Journal of Biomechanics*. 2001 May;34(5):569-77. doi: 10.1016/s0021-9290(01)00011-2.

Mukherjee K, Gupta S. Bone ingrowth around porous-coated acetabular implant: a three-dimensional finite element study using mechanoregulatory algorithm. *Biomechanics and Modeling in Mechanobiology*. 2016 Apr;15(2):389-403. doi: 10.1007/s10237-015-0696-7.

Mukherjee K, Gupta S. Combined Bone Ingrowth and Remodeling Around Uncemented Acetabular Component: A Multiscale Mechanobiology-Based Finite Element Analysis. *Journal of Biomechanical Engineering*. 2017 Sep 1;139(9). doi: 10.1115/1.4037223.

Mukherjee K, Gupta S. Influence of Implant Surface Texture Design on Peri-Acetabular Bone Ingrowth: A Mechanobiology Based Finite Element Analysis. *Journal of Biomechanical Engineering*. 2017a Mar 1;139(3). doi: 10.1115/1.4035369.

Mukherjee K, Gupta S. Mechanobiological simulations of peri-acetabular bone ingrowth: a comparative analysis of cell-phenotype specific and phenomenological algorithms. *Medical & Biological Engineering & Computing*. 2017b; 55: 449-465. doi: 10.1007/s11517-016-1528-3.

Mukherjee K, Gupta S. Simulation of tissue differentiation around acetabular cups: the effects of implant-bone relative displacement and polar gap. *Advances in biomechanics and applications*. 2014; 1(2):95-109. https://doi.org/10.12989/aba.2014.1.2.095.

Mullender M, El Haj AJ, Yang Y, van Duin MA, Burger EH, Klein-Nulend J. Mechanotransduction of bone cells in vitro: mechanobiology of bone tissue.

Medical & Biological Engineering & Computing. 2004 Jan;42(1):14-21. doi: 10.1007/BF02351006.

Munhoz AM, Clemens MW, Nahabedian MY. Breast Implant Surfaces and Their Impact on Current Practices: Where We Are Now and Where Are We Going? *Plastic and Reconstructive Surgery – Global Open*. 2019 Oct 15;7(10):e2466. doi: 10.1097/GOX.0000000000002466.

Nagel T, Kelly DJ. Mechano-regulation of mesenchymal stem cell differentiation and collagen organization during skeletal tissue repair. *Biomechanics and Modeling in Mechanobiology*. 2010 Jun;9(3):359-72. doi: 10.1007/s10237-009-0182-1.

Nayak R, Jain LC, Ting BKH. Artificial Neural Networks in Biomedical Engineering: A Review. in: *Asia-Pacific Conference on Advance Computation*, Sydney, Australia,2001.

Nicolella DP, Thacker BH, Katoozian H, Davy DT. The effect of three-dimensional shape optimization on the probabilistic response of a cemented femoral hip prosthesis. *Journal of Biomechanics*. 2006;39(7):1265-78. doi: 10.1016/j.jbiomech.2005.03.010.

Nishimura I, Yuhta T, Ikubo K, Shimooka T, Murabayashi S, Mitamura Y. Modification of the frictional surfaces of artificial joints. *ASAIO Journal*. 1993 Jul-Sep;39(3):M762-6.

Nobari S, Katoozian HR, Zomorodimoghadam S. Three-dimensional design optimization of patient-specific femoral plates as a means of bone remodelling reduction. *Computer Methods in Biomechanics and Biomedical Engineering*. 2010 Dec;13(6):819-27. doi: 10.1080/10255841003630645.

Nomura S, Takano-Yamamoto T. Molecular events caused by mechanical stress in bone. *Matrix Biology*. 2000 May;19(2):91-6. doi: 10.1016/s0945-053x(00)00050-0.

Nordin M, Frankel VH. Basic biomechanics of the musculoskeletal system. *Lippincott Williams & Wilkins*. 2001.

Nowlan NC, Murphy P, Prendergast PJ. Mechanobiology of embryonic limb development. *Annals of the New York Academy of Sciences*. 2007 Apr; 1101:389-411. doi: 10.1196/annals.1389.003.

Olivares-Navarrete R, Hyzy SL, Hutton DL, Erdman CP, Wieland M, Boyan BD, Schwartz Z. Direct and indirect effects of microstructured titanium substrates

on the induction of mesenchymal stem cell differentiation towards the osteoblast lineage. *Biomaterials*. 2010 Apr;31(10):2728-35. doi: 10.1016/j.biomaterials.2009.12.029.

Ostadi Moghaddam A, Mahjoob M, Nazarian A. Bone Remodeling under Vibration: A Computational Model of Bone Remodeling Incorporating the Modal Behavior of Bone. *Journal of Biomechanical Engineering*. 2018 Sep 25; 140(12):121003. doi: 10.1115/1.4040602.

Özkaya N, Leger D, Goldsheyder D, Nordin M. Mechanical properties of biological tissues. In: *Fundamentals of Biomechanics*. 2017.

Özkaya N, Nordin M. Fundamentals of biomechanics: equilibrium motion and deformation. New York *Springer Verlag*. 1999.

Pachore JA, Vaidya SV, Thakkar CJ, Bhalodia HK, Wakankar HM. ISHKS joint registry: A preliminary report. *Indian Journal of Orthopaedics*. 2013 Sep;47(5):505-9. doi: 10.4103/0019-5413.118208.

Pal B, Gupta S. The effect of primary stability on load transfer and bone remodelling within the uncemented resurfaced femur. *Proceedings of the Institution of Mechanical Engineers, Part H: Journal of Engineering in Medicine*. 2011; 225:549–561.

Pancanti A, Bernakiewicz M, Viceconti M. The primary stability of a cement-less stem varies between subjects as much as between activities. *Journal of Biomechanics*. 2003; 36 (6): 777–785.

Pandit HG, Hand CJ, Ramos JL, Pradhan NS, Hobbs NJ. Early Aseptic Loosening in One Design (3M-Capital) of Cemented Total Hip Replacement. *HIP International*. 2000 Jan 1;10(1):38-42. doi:10.1177/112070000001000105.

Parfitt AM. The cellular basis of bone remodeling: the quantum concept reexamined in light of recent advances in the cell biology of bone. *Calcified Tissue International*. 1984;36 Suppl 1:S37-45. doi: 10.1007/BF02406132.

Pauwels F. [A new theory on the influence of mechanical stimuli on the differentiation of supporting tissue. The tenth contribution to the functional anatomy and causal morphology of the supporting structure]. Z Anat Entwicklungsgesch. 1960; 121:478-515. German.

Pedersen DR, Brand RA, Davy DT. Pelvic muscle and acetabular contact forces during gait. *Journal of Biomechanics*. 1997 Sep;30(9):959-65. doi: 10.1016/s0021-9290(97)00041-9.

Pedersen NL. Stress concentrations in keyways and optimization of keyway design. *Journal of Strain Analysis for Engineering Design*. 2010; 45(8):593-604.

Petrie CS, Williams JL. Shape optimization of dental implant designs under oblique loading using the p-version finite element method. *Journal of Mechanics in Medicine and Biology*. 2002 Sep 1;2(03n04):339-345. doi: 10.1142/S0219519402000435.

Philips TW, Messieh SS, McDonald PD. Femoral stem fixation in hip replace-ment. A biomechanical comparison of cementless and cemented prostheses. *Journal of Bone & Joint Surgery*. 1990; 72 (3):431–434.

Pilliar RM. Overview of surface variability of metallic endosseous dental implants: textured and porous surface-structured designs. *Implant Dentistry*. 1998;7(4):305-14. doi: 10.1097/00008505-199807040-00009.

Pivonka P, Zimak J, Smith DW, Gardiner BS, Dunstan CR, Sims NA, Martin TJ, Mundy GR. Model structure and control of bone remodeling: a theoretical study. *Bone*. 2008 Aug;43(2):249-63. doi: 10.1016/j.bone.2008.03.025.

Prados-Privado M, Martínez-Martínez C, Gehrke SA, Prados-Frutos JC. Influence of Bone Definition and Finite Element Parameters in Bone and Dental Implants Stress: A Literature Review. *Biology (Basel)*. 2020 Aug 14;9(8):224. doi: 10.3390/biology9080224.

Prendergast PJ, Huiskes R, Søballe K. ESB Research Award 1996. Biophysical stimuli on cells during tissue differentiation at implant interfaces. *Journal of Biomechanics*. 1997 Jun;30(6):539-48. doi: 10.1016/s0021-9290(96)00140-6.

Prendergast PJ, Taylor D. Prediction of bone adaptation using damage accumulation. *Journal of Biomechanics*. 1994 Aug;27(8):1067-76. doi: 10.1016/0021-9290(94)90223-2.

Puthumanapully PK, Browne M. Tissue differentiation around a short stemmed metaphyseal loading implant employing a modified mechanoregulatory algorithm: a finite element study. *Journal of Orthopaedic Research*. 2011 May;29(5):787-94. doi: 10.1002/jor.21305.

Puthumanapully PK. Simulation of tissue differentiation in uncemented hip implants based on a mechanoregulatory hypothesis. Dissertation, 2010, *University of Southampton*.

Qin YX, McLeod KJ, Guilak F, Chiang FP, Rubin CT. Correlation of bony ingrowth to the distribution of stress and strain parameters surrounding a porous-coated implant. *Journal of Orthopaedic Research*.1996 Nov;14(6):862-70. doi: 10.1002/jor.1100140604.

Roux W. Der zuchtende Kampf der Teile,oder die Teilauslese' im Organismus. (Theorie der funktionellen Anpassung'). *Wilhelm Engelmann*, Leipzig. 1881.

Roy S, Dey S, Khutia N, Chowdhury AR, Datta S. Design of patient specific dental implant using FE analysis and computational intelligence techniques. *Applied Soft Computing*.2018; 65:272–279. https://doi.org/10.1016/j.asoc.2018.01.025.

Ruben RB, Fernandes PR, Folgado J. On the optimal shape of hip implants. *Journal of Biomechanics*. 2012 Jan 10;45(2):239-46. doi: 10.1016/j.jbiomech.2011.10.038.

Ryu HS, Namgung C, Lee JH, Lim YJ. The influence of thread geometry on implant osseointegration under immediate loading: a literature review. *Journal of Advanced Prosthodontics*. 2014 Dec;6(6):547-54. doi: 10.4047/jap.2014.6.6.547.

Sabbatini RME. Neural networks for classification and pattern recognition of biological signals. *In: Proceedings of the 15th Annual International Conference of the IEEE Engineering in Medicine and Biology Societ*, Los Alamitos, IEEE Press, San Diego, CA, 1993.

Saeidi M, Gubaua JE, Kelly P, Kazemi M, Besier T, Dicati GWO, Pereira JT, Neitzert T, Ramezani M. The influence of an extra-articular implant on bone remodelling of the knee joint. *Biomechanics and Modeling in Mechanobiology*. 2020 Feb;19(1):37-46. doi: 10.1007/s10237-019-01193-7.

Saikko VO. Wear of polyethylene acetabular cups against alumina femoral heads. 5 prostheses compared in a hip simulator for 35 million walking cycles. *Acta Orthopaedica Scandinavica*. 1993 Oct;64(5):507-12. doi: 10.3109/17453679308993680.

Sánchez E, Schilling C, Grupp TM, Giurea A, Verdonschot N, Janssen D. No effect in primary stability after increasing interference fit in cementless TKA tibial components. *Journal of the Mechanical Behaviour of Biomedical Materials*. 2021b Jun; 118:104435. doi: 10.1016/j.jmbbm.2021.104435.

Sánchez E, Schilling C, Grupp TM, Giurea A, Wyers C, van den Bergh J, Verdonschot N, Janssen D. The effect of different interference fits on the primary fixation of a cementless femoral component during experimental testing. *Journal of the Mechanical Behaviour of Biomedical Materials*. 2021a Jan; 113:104189. doi: 10.1016/j.jmbbm.2020.104189.

Sandino C, Lacroix D. A dynamical study of the mechanical stimuli and tissue differentiation within a CaP scaffold based on micro-CT finite element models. *Biomechanics and Modeling in Mechanobiology*. 2011 Jul;10(4):565-76. doi: 10.1007/s10237-010-0256-0.

Santori N, Albanese CV, Learmonth ID, Santori FS. Bone preservation with a conservative metaphyseal loading implant. *Hip International*. 2006b; 16 Suppl 3:16-21. doi: 10.5301/hip.2009.3327.

Santori N, Lucidi M, Santori FS. Proximal load transfer with a stemless uncemented femoral implant. *Journal of Orthopaedics and Traumatology*. 2006a; 7(3):154-160. doi:10.1007/s10195-006-0141-x.

SchÖllhorn WI. Applications of artificial neural nets in clinical biomechanics. *Clinical Biomechanics*. 2004;19:876–898.

Sennerby L, Thomsen P, Ericson LE. Early tissue response to titanium implants inserted in rabbit cortical bone. *Journal of Materials Science: Materials in Medicine*. 1993; 4:240-250. https://doi.org/10.1007/BF00122275.

Simmons CA, Meguid SA, Pilliar RM. Mechanical regulation of localized and appositional bone formation around bone-interfacing implants. *Journal of Biomedical Materials Research*. 2001 Apr;55(1):63-71. doi: 10.1002/1097-4636(200104)55:1<63::aid-jbm90>3.0.co;2-v.

SMITH-PETERSEN MN. Evolution of mould arthroplasty of the hip joint. *The Journal Bone & Joint Surgery*. 1948 Feb;30B(1):59-75.

Snell RS. Clinical anatomy by regions. *Lippincott Williams & Wilkins*. 2011 Oct 28.

Søballe K, Hansen ES, Brockstedt-Rasmussen H, Bünger C. Hydroxyapatite coating converts fibrous tissue to bone around loaded implants. *The Journal Bone & Joint Surgery*. 1993 Mar;75(2):270-8. doi: 10.1302/0301-620X.75B2.8444949.

Speirs AD, Slomczykowski MA, Orr TE, Siebenrock K, Nolte LP. Three-dimensional measurement of cemented femoral stem stability: an in vitro

cadaver study. *Clinical Biomechanics*.(Bristol, Avon). 2000 May;15(4):248-55. doi: 10.1016/s0268-0033(99)00079-0.

Steigenga J, Al-Shammari K, Misch C, Nociti FH Jr, Wang HL. Effects of implant thread geometry on percentage of osseointegration and resistance to reverse torque in the tibia of rabbits. *Journal of Periodontology*. 2004 Sep;75(9):1233-41. doi: 10.1902/jop.2004.75.9.1233.

Stolk J, Verdonschot N, Huiskes R. Stair climbing is more detrimental to the cement in hip replacement than walking. *Clinical Orthopaedics and Related Research*. 2002 Dec;(405):294-305. doi: 10.1097/00003086-200212000-00037.

Stoltz JF, Magdalou J, George D, Chen Y, Li Y, Isla ND, He X, Remond V. Influence of mechanical forces on bone: Introduction to mechanobiology and mechanical adaptation concept. *Journal of Cellular Immunotherapy*. 2018 Sept 12; 4(1):10-12. doi:10.1016/j.jocit.2018.09.003.

Sukegawa S, Yoshii K, Hara T, Yamashita K, Nakano K, Yamamoto N, et al. Deep Neural Networks for Dental Implant System Classification. *Biomolecules*. 2020; 10(7):984. doi: 10.3390/biom10070984.

Taddei F, Schileo E, Helgason B, Cristofolini L, Viceconti M. The material mapping strategy influences the accuracy of CT-based finite element models of bones: an evaluation against experimental measurements. *Medical Engineering & Physics*. 2007 Nov;29(9):973-9. doi: 10.1016/j.medengphy.2006.10.014.

Tai CL, Lai PL, Lin WD, Tsai TT, Lee YC, Liu MY, Chen LH. Modification of Mechanical Properties, Polymerization Temperature, and Handling Time of Polymethylmethacrylate Cement for Enhancing Applicability in Vertebroplasty. *BioMed Research International*. 2016; 2016:7901562. doi: 10.1155/2016/7901562.

Tan F, Wang C, Yang C, Huang Y, Fan Y. Biomechanical Effects of Various Bone-Implant Interfaces on the Stability of Orthodontic Miniscrews: A Finite Element Study. *Journal of Healthcare Engineering*. 2017; 2017:7495606. doi: 10.1155/2017/7495606.

Tarala M, Janssen D, Verdonschot N. Balancing incompatible endoprosthetic design goals: a combined ingrowth and bone remodeling simulation. *Medical Engineering & Physics*. 2011 Apr;33(3):374-80. doi: 10.1016/j.medengphy.2010.11.005.

Tarlochan F, Mehboob H, Mehboob A, Chang SH. Influence of functionally graded pores on bone ingrowth in cementless hip prosthesis: a finite element study using mechano-regulatory algorithm. *Biomechanics and Modeling in Mechanobiology*. 2018 Jun;17(3):701-716. doi: 10.1007/s10237-017-0987-2.

Taylor SJ, Perry JS, Meswania JM, Donaldson N, Walker PS, Cannon SR. Telemetry of forces from proximal femoral replacements and relevance to fixation. *Journal of Biomechanics*. 1997 Mar;30(3):225-34. doi: 10.1016/s0021-9290(96)00141-8.

Tu JV. Advantages and disadvantages of using artificial neural networks versus logistic regression for predicting medical outcomes. *Journal of Clinical Epidemiology*. 49(11) (1996) 1225-1231. doi: 10.1016/s0895-4356(96)00002-9.

Turner CH, Anne V, Pidaparti RM. A uniform strain criterion for trabecular bone adaptation: do continuum-level strain gradients drive adaptation? *Journal of Biomechanics*. 1997 Jun;30(6):555-63. doi: 10.1016/s0021-9290(97)84505-8.

Turner CH, Pavalko FM. Mechanotransduction and functional response of the skeleton to physical stress: the mechanisms and mechanics of bone adaptation. *Journal of Orthopaedic Science*. 1998;3(6):346-55. doi: 10.1007/s007760050064.

Vaidya SV, Jogani AD, Pachore JA, Armstrong R, Vaidya CS. India Joining the World of Hip and Knee Registries: Present Status-A Leap Forward. *Indian Journal of Orthopaedics*. 2020 Sep 16;55(Suppl 1):46-55. doi: 10.1007/s43465-020-00251-y.

van den Bogert AJ, Read L, Nigg BM. An analysis of hip joint loading during walking, running, and skiing. *Medicine & Science in Sports & Exercise*. 1999 Jan;31(1):131-42. doi: 10.1097/00005768-199901000-00021.

Van Rietbergen B, Huiskes R, Weinans H, Sumner DR, Turner TM, Galante JO. ESB Research Award 1992. The mechanism of bone remodeling and resorption around press-fitted THA stems. *Journal of Biomechanics*. 1993 Apr-May;26(4-5):369-82. doi: 10.1016/0021-9290(93)90001-u.

Viceconti M, Bellingeri L, Cristofolini L, Toni A. A comparative study on different methods of automatic mesh generation of human femurs. *Medical*

Engineering & Physics. 1998 Jan;20(1):1-10. doi: 10.1016/s1350-4533(97)00049-0.

Viceconti M, Monti L, Muccini R, Bernakiewicz M, Toni A. Even a thin layer of soft tissue may compromise the primary stability of cementless hip stems. *Clinical Biomechanics*. 2001; 16(9):765-775. https://doi.org/10.1016/s0268-0033(01)00052-3.

Vidyadhara S, Rao SK. Uncemented primary press-fit total hip arthroplasty: a 3 to 6 years of experience. *Journal of Orthopaedic Surgery* (Hong Kong). 2007; 15(1): 50-55. doi: 10.1177/230949900701500112.

Waizy H, Behrens BA, Radtke K, Almohallami A, Stukenborg-Colsman C, Bouguecha A. Bone cyst formation after ankle arthroplasty may be caused by stress shielding. A numerical simulation of the strain adaptive bone remodelling. *Foot* (Edinb). 2017 Dec; 33:14-19. doi: 10.1016/j.foot.2017.07.001.

Wang X, Thomas CD, Clement JG, Das R, Davies H, Fernandez JW. A mechanostatistical approach to cortical bone remodelling: an equine model. *Biomechanics and Modeling in Mechanobiology*. 2016 Feb;15(1):29-42. doi: 10.1007/s10237-015-0669-x.

Watanabe S, Hiroyasu T, Miki M. Neighborhood cultivation genetic algorithm for multi-objective optimization problems. *In Proceedings of the 4th Asia-Pacific conference on simulated evolution and learning (SEAL-2002)* 2002 Nov 18:198-202.

Weinans H, Huiskes R, Grootenboer HJ. The behavior of adaptive bone-remodeling simulation models. *Journal of Biomechanics*. 1992 Dec;25(12):1425-41. doi: 10.1016/0021-9290(92)90056-7.

Weinans H, Huiskes R, van Rietbergen B, Sumner DR, Turner TM, Galante JO. Adaptive bone remodeling around bonded noncemented total hip arthroplasty: a comparison between animal experiments and computer simulation. *Journal of Orthopaedic Research*.1993 Jul;11(4):500-13. doi: 10.1002/jor.1100110405.

Weinans H, Prendergast PJ. Tissue adaptation as a dynamical process far from equilibrium. *Bone*. 1996 Aug;19(2):143-9. doi: 10.1016/8756-3282(96)00143-3.

Weinbaum S, Cowin SC, Zeng Y. A model for the excitation of osteocytes by mechanical loading-induced bone fluid shear stresses. *Journal of Biomechanics*. 1994 Mar;27(3):339-60. doi: 10.1016/0021-9290(94)90010-8.

WILES P. The surgery of the osteoarthritic hip. *British Journal of Surgery*. 1958 Mar 18;45(193):488-97. doi: 10.1002/bjs.18004519315.

Willing R, Kim IY. Design optimization of a total knee replacement for improved constraint and flexion kinematics. *Journal of Biomechanics*. 2011 Apr 7;44(6):1014-20. doi: 10.1016/j.jbiomech.2011.02.009.

Willing R, Kim IY. Three dimensional shape optimization of total knee replacements for reduced wear. *Structural and Multidisciplinary Optimization*. 2009 38:405–414. doi: 10.1007/s00158-008-0281-0.

Wolff J. The law of bone remodelling. translated by p. maquet and r. furlong. New York, *Springer*. 1986.

Wolff, J. Das Gesetz der transformation der knochen, Berlin, *Hirshwald*. 1892.

Yamada H, Yoshihara Y, Henmi O, Morita M, Shiromoto Y, Kawano T, et al. Cementless total hip replacement: past, present, and future. *Journal of Orthopaedic Science*. 2009; 14(2): 228-241. https://dx.doi.org/10.1007%2Fs00776-008-1317-4.

Yoon YS, Jang GH, Kim YY. Shape optimal design of the stem of a cemented hip prosthesis to minimize stress concentration in the cement layer. *Journal of Biomechanics*. 1989;22(11-12):1279-84. doi: 10.1016/0021-9290(89)90231-5.

Zhang B, Huang W, Wang J, Wang X. Comparison of the effects of surface texture on the surfaces of steel and UHMWPE. *Tribology International* 2013; 65:138-145.https://doi.org/10.1016/j.triboint.2013.01.004.

List of Publications

List of publications from the present thesis:

Journal Publications

1. **Ghosh R**, Chanda S, Chakraborty D. The influence of macro-textural designs over implant surface on bone on-growth: A computational mechanobiology based study. *Computers in Biology and Medicine*. 2020 Sep; 124:103937. doi: 10.1016/j.compbiomed.2020.103937.
2. **Ghosh R**, Chanda S, Chakraborty D. Qualitative predictions of bone growth over optimally designed macro-textured implant surfaces obtained using NN-GA based machine learning framework. *Medical Engineering & Physics*. 2021 Sep; 95:64-75. doi: 10.1016/j.medengphy.2021.08.002.
3. **Ghosh R**, Chanda S, Chakraborty D. Influence of sequential opening/closing of interface gaps and texture density on bone growth over macro-textured implant surfaces using FE based mechanoregulatory algorithm. *Computer Methods in Biomechanics and Biomedical Engineering*, 2022, July; 25(9):985-999. doi: 10.1080/10255842.2021.1994960.
4. **Ghosh R**, Chanda S, Chakraborty D. Application of finite element analysis to tissue differentiation and bone remodelling approaches and their use in design optimization of orthopaedic implants: A review. *International Journal for Numerical Methods in Biomedical Engineering*, 2022, Oct; 38(10):e3637. doi: 10.1002/cnm.3637.
5. **Ghosh R**, Hazra A, Chanda S, Chakraborty D. Computational assessment of growth of connective tissues around textured hip stem subjected to daily activities after THA. *Medical & Biological Engineering & Computing*, 2023, Feb; 61(2):525-540. doi: 10.1007/s11517-022-02729-3.

Book Chapter

1. **Ghosh R**, Chanda S, Chakraborty D. Neural Network (NN) Based Qualitative Assessment of Bone Growth over Textured Implant Surfaces. In: Popat, K.C., Kanagaraj, S., Sreekanth, P.S.R., Kumar, V.M.R. (eds) *Advances in Mechanical Engineering and Material Science. ICAMEMS 2022. Lecture Notes in Mechanical Engineering*. *Springer, Singapore.* doi: 10.1007/978-981-19-0676-3_13.

Conference Publications

1. **Ghosh R**, Chanda S, Chakraborty D. Mechanobiology-based microscale study of influence of surface texture design on periacetabular bone ingrowth. *Orthopaedic Proceedings*, Vol 101, The British Editorial Society of Bone & Joint Surgery, *International Society for Technology in Arthroplasty (ISTA) 31st Annual Congress*, London, England, UK, Oct 2018.
2. **Ghosh R**, Chanda S, Chakraborty D. Sensitivity Of Osseointegration To The Variation In Geometric Control Factors Of The Macro-textures On The Implant Surface. Vol 46:0536, *Orthopaedic Research Society (ORS), Orthopaedic Research Society(ORS) Annual Meeting*, San Francisco, USA, Feb 2021.
3. **Ghosh R**, Chanda S, Chakraborty D. Neural Network (NN) Based Qualitative Assessment of Bone Growth over Textured Implant Surfaces. *International Conference on advances in mechanical engineering and material science (ICAMEMS)*, Amaravati, Andhra Pradesh, India**,** Jan 2022.
4. **Ghosh R**, Chanda S, Chakraborty D. Combined influence of material properties of bone and implant on bone growth over macro-textured implant surface. North East Research Conclave (NERC), IIT Guwahati, Assam, India, May 2022.
5. **Ghosh R**, Hazra A, Chanda S, Chakraborty D. Biomechanical assessment of bone growth over femoral implant with proximal macro-textured surfaces. *World Congress of Biomechanics (WCB)*, Taipei, Taiwan, July 2022.

About the Author

Rajdeep Ghosh was born on the eighth day of January, 1992, in Udaipur, Tripura, India. He has completed his schooling from Ramakrishna Mission Vidyalaya, Viveknagar, Agartala, Tripura, India. In the year 2008 and 2010, he passed the AISSE and AISSCE Examination respectively, with first division, under Central Board of Secondary Education. He has been a prestigious Jagadis Bose National Science Talent Search (JBNSTS)scholar in the year 2008. He completed his Bachelor's in Mechanical Engineering from National Institute of Technology Agartala in 2015 with first class. Thereafter, he joined the Kirloskar Brothers Limited, Pune, India for a short span of one year as a Graduate Engineer Trainee (GET). Thereafter, he joined Indian Institute of Technology Guwahati, for pursuing a Doctoral study in the field of orthopaedic biomechanics in 2016. Being motivated by Dr Debabrata Chakraborty, Department of Mechanical Engineering, Indian Institute of Technology Guwahati he continued his doctoral research under the supervision of Dr Debabrata Chakraborty, Department of Mechanical Engineering, Indian Institute of Technology Guwahati and Dr Souptick Chanda, Department of Biosciences and BioEngineering, Indian Institute of Technology Guwahati. He is an associate member of Orthopaedic Research Society as well as a student member of International Society of Biomechanics. He has served as a peer-reviewer for 2 reputed SCIE journals in the field of biomedical engineering during his doctoral studies. In 2018, he was awarded a travel grant for attending ISTA annual congress held in London, UK. His doctoral research study on 'Biomechanical assessment and design optimization of macro-textured implant surfaces and their application in proximal surface of femoral implant' lasted until June, 2022.